

NON-REACTING FLOW CHARACTERISTICS AND  
EMISSIONS REDUCTION ON BLENDS OF COAL AND DAIRY BIOMASS IN  
30 KW<sub>T</sub> LOW NO<sub>x</sub> DOWN-FIRED FURNACE

A Thesis

by

TIYAWUT TIYAWONGSAKUL

Submitted to the Office of Graduate and Professional Studies of  
Texas A&M University  
in partial fulfillment of the requirements for the degree of

MASTER OF SCIENCE

Chair of Committee,	Kalyan Annamalai
Committee Members,	Adonios Karpetis
	Devesh Ranjan
Head of Department,	Andreas A. Polycarpou

August 2014

Major Subject: Mechanical Engineering

Copyright 2014 Tiyawut Tiyawongsakul

## ABSTRACT

Recently, coal-fired power plants have considered either to retire themselves or to use natural gas as the main energy source instead of coal due to more stringent air pollution regulations for nitrogen oxides ( $\text{NO}_x$ ), mercury (Hg) and more recently the required  $\text{CO}_2$  reduction of 30% by 2030. Clean coal technology must be continuously developed in order to prevent people from losing their jobs and to decrease the negative impacts of firing coal on environment. The present research focuses on  $\text{NO}_x$  emissions which arise mainly due to oxidation of fuel-bound nitrogen using low  $\text{NO}_x$  burner (LNB) when fired with Wyoming Powder River Basin coal (PRB) and blends of coal and dairy biomass (DB). The DB was selected as co-fired fuel for possible elimination of DB from dairy feedlots which result in land, air and water pollution if not properly disposed of. LNB adopts staged air introduction in order to limit the availability of oxygen when nitrogen from fuel is released. To achieve the objective, the mixing patterns between fuel particle and air were predicted using non-reacting flow (NRF) simulation inside the cylindrical combustion chamber. The effects of varying burner parameters, fuel particle sizes, main burner equivalence ratios ( $\text{ER}_{\text{mb}}$ ) and overall equivalence ratios ( $\text{ER}_{\text{oa}}$ ) on mixing characteristics were investigated. Then, the LNB components were modified based on the results from NRF simulation. The modified main burner is a partially premixed swirl burner (fuel mixes with the primary air inside the fuel/primary air nozzle, and the secondary air is swirled by the straight-vane swirler) whose swirl angle and secondary air swirl number are  $59^\circ$  and 1.42 respectively. The circular over-fire air

(OFA) nozzles are located 484 mm below the main burner exit, and the OFA is injected into the combustion chamber in the radial direction. The fuels used in the research were: 1) pure PRB and 2) the fuel blend of PRB and DB with the PRB-to-DB ratio of 90 to 10 on mass basis (90-10 PRB-DB blend). Fuel characteristics were first obtained, and empirical chemical formulae were deduced. The  $\text{CO}_2$ ,  $\text{O}_2$  and  $\text{NO}$  were measured as a function of  $\text{ER}_{\text{oa}}$  and  $\text{ER}_{\text{mb}}$  ( $\text{ER}_{\text{mb}}$  based on air flow without inclusion of OFA). The gas analyses were used to obtain the burnt fraction, respiratory quotient ( $\text{RQ}_s = \text{CO}_2$  moles produced/ $\text{O}_2$  moles consumed) and equivalence ratio which is then checked against measured values. Uncertainty analyses were also performed.

The optimum conditions for minimum  $\text{NO}_x$  emission that pass the EPA limit (210 g/GJ) were obtained as follows. With  $\text{ER}_{\text{oa}} = 0.95$ , firing pure PRB produced  $\text{NO}_x$  220 g/GJ without OFA, and 179 g/GJ with OFA ( $\text{ER}_{\text{mb}} = 1.10$ ) which is about 18.6 % reduction. Under same conditions, the co-firing of 90-10 PRB-DB blend decreased  $\text{NO}_x$  by 3.6% without OFA, and 22.2% with OFA ( $\text{ER}_{\text{mb}} = 1.10$ ) compared to firing pure PRB at  $\text{ER}_{\text{oa}} = 0.95$  without OFA. Furthermore, co-firing 90-10 PRB-DB blend with OFA at  $\text{ER}_{\text{mb}} = 1.10$  and  $\text{ER}_{\text{oa}} = 0.95$  (excess air 5.26%) emitted  $\text{NO}_x$  approximately 171 g/GJ whilst firing pure PRB without OFA at  $\text{ER}_{\text{oa}} = 0.85$  (excess air 17.65%) emitted  $\text{NO}_x$  approximately 330 g/GJ which is 48% reduction and less than 210 g/GJ (the current EPA limit). This reduction could benefit 500-MWt power plants approximately \$113,500 per year in case the efficiency of power plants is 35% and  $\text{NO}_x$  are traded at \$15.89 per short ton.

## DEDICATION

This thesis is dedicated to my parents, Somboon and Sansanee Tiyawongsakul, and my older sister, Pasaweepitch Sornakkharapha, for all of their love and support.

Although this work is only one stepping stone toward my ultimate goal, it is a very big one. I truly hope that people who are interested in combustion science and engineering will find this work useful and use it to strengthen their research.

## ACKNOWLEDGEMENTS

I would like to thank my academic advisor who is also my committee chair, Prof. Annamalai, and my committee members, Assoc. Prof. Karpetis and Asst. Prof. Ranjan, for their guidance and support throughout the past two years. I will always keep your advice in mind.

All of my allowances, tuitions and fees, and expenses for studying and conducting research at Texas A&M University were supported by SCG Chemicals. So, I would like to thank SCG Chemicals for believing in my potential and being my sponsor. Moreover, I would like to extend my thanks to my mentors, friends, colleagues, and subordinates at SCG Chemicals who always helped me get through tough times and encouraged me to pursue my graduate studies in the U.S.A.

Thank Siva Sankar Thannapal for teaching me how to use instruments in laboratories. I am proud to have you as my labmate.

Finally, I would like to thank my parents and my sister who always love me and encourage me to get up every time I fall down.

## NOMENCLATURE

A	Amount of air
$A_{\text{actual}}$	Actual amount of air
$A_{\text{eff}}$	Effective flow area
$A_{\text{eff, pa}}$	Effective flow area of the primary airflow
$A_{\text{eff, sa}}$	Effective flow area of the secondary airflow
Ar	Argon gas
$A_{\text{stoich}}$	Stoichiometric amount of air
ASTM	American Society for Testing and Materials
A/F	Air-to-fuel ratio
B	Pre-exponential factor or frequency factor
BF	Burnt Fraction
C	Carbon atom
c	Number of carbon atoms
CABEL	Coal and Biomass Energy Laboratory
CFD	Computational Fluid Dynamics
CH <sub>4</sub>	Methane
CO	Carbon monoxide
CO <sub>2</sub>	Carbon dioxide
CRZ	Central Recirculation Zone
CW	Clockwise

CCW	Counter clockwise
CWF	Cumulative Weight Fraction
C <sub>3</sub> H <sub>8</sub>	Propane
d <sub>ps</sub>	Particle size
d <sub>ps, char</sub>	Characteristic particle size
d <sub>s</sub>	Size of sieve aperture
DAF	Dry and ash-free
DB	Dairy biomass
D <sub>chb</sub>	Inside diameter of combustion chamber
DTG	Derivative thermogravimetric analysis
E <sub>a</sub>	Activation energy
EIA	Energy Information Administration
EPA	Environmental Protection Agency
ER	Equivalence ratio
ER <sub>mb</sub>	Main burner equivalence ratio
ER <sub>oa</sub>	Overall equivalence ratio
ERZ	External Recirculation Zone
F	Amount of fuel
F <sub>actual</sub>	Actual amount of fuel
FC	Fixed carbon
F <sub>stoich</sub>	Stoichiometric amount of fuel
g	Gram

$G_{\text{ang}}$	Axial flux of angular momentum
$G_{\text{ax}}$	Axial flux of axial momentum
GHG	Greenhouse gas
GJ	Gigajoule
$\text{GW}_t$	Gigawatt of thermal energy
H	Hydrogen atom
h	Number of hydrogen atoms
HCN	Hydrogen cyanide
HR	Heating rate
HHV	Higher heating value
$\text{HHV}_{\text{air}}$	Higher heating value based on stoichiometric air
$\text{HHV}_{\text{O}_2}$	Higher heating value based on stoichiometric oxygen
HV	Heating value
$\text{HV}_{\text{fc}}$	Heating value of fixed carbon
$\text{HV}_{\text{fuel}}$	Heating value of fuel
$\text{HV}_{\text{vm}}$	Heating value of volatile matter
$\text{H}_2\text{O}$	Water
H/C	Atomic hydrogen-to-carbon ratio
IDF	Induced draft fan
kg	Kilogram
kmol	Kilomole
$\text{kW}_t$	Kilowatt of thermal energy



LADB	Low-ash Dairy Biomass
LNB	Low NO <sub>x</sub> burner
LPM	Liter per minute
L <sub>rev</sub>	Length that fuel particle can penetrate into the recirculation zone before being reversed
L <sub>rz</sub>	Length of recirculation zone
L <sub>sr</sub>	Swirl recess length
MATS	Mercury and Air Toxics Standards
MVR	Maximum volatile release
M <sub>fuel</sub>	Molecular weight of fuel
M <sub>air</sub>	Molecular weight of air
m <sub>vm</sub>	Mass of volatile matter
N	Nitrogen atom
n	Number of nitrogen atoms or order of pyrolysis
N <sub>conv</sub>	Fuel-bound nitrogen conversion efficiency
NH	Nitrogen hydride
NO	Nitric oxide
NO <sub>x</sub>	Nitrogen oxides
NO <sub>2</sub>	Nitrogen dioxide
NO <sub>3</sub>	Nitrogen trioxide
N <sub>2</sub>	Diatomic nitrogen or nitrogen gas
N <sub>2</sub> O	Nitrous oxide

N/C	Atomic nitrogen-to-carbon ratio
O	Oxygen atom
o	Number of oxygen atoms
O <sub>2</sub>	Diatomic oxygen
OFA	Over-fire air
OFA <sub>actual</sub>	Actual amount of over-fire air
OH	Hydroxide
O/C	Atomic oxygen-to-carbon ratio
PA <sub>actual</sub>	Actual amount of primary air
PRB	Wyoming Powder River Basin coal
PSA	Particle Size Analysis
PSD	Particle Size Distribution
P <sub>stat</sub>	Static pressure
r <sub>h</sub>	Hub radius or the outer radius of the fuel/primary air nozzle
RQ	Respiratory Quotient
RRD	Rosin-Rammler distribution
R <sub>u</sub>	Universal gas constant
r <sub>v</sub>	Radius of the swirler vane
RZ	Recirculation zone
S	Sulfur atom
s	Number of sulfur atoms
SA <sub>actual</sub>	Actual amount of secondary air

SCR	Selective catalytic reduction
SN	Swirl number
SN'	Swirl number without static pressure
SN' <sub>sa</sub>	Secondary air swirl number
SO <sub>2</sub>	Sulfur dioxide
SR	Stoichiometric ratio
SRM	Single reaction modelling
T	Temperature
TAMU	Texas A&M University
T <sub>c</sub>	Flow Temperature at the center of the combustion chamber
TGA	Thermogravimetric analysis
T <sub>ign</sub>	Ignition temperature
T <sub>pyr, peak</sub>	Peak temperature of the pyrolysis process
T <sub>w</sub>	Temperature at the wall of the combustion chamber
VM	Volatile Matters
v	Flow velocity
v <sub>s</sub>	Swirled flow velocity
v <sub>us</sub>	Unswirled flow velocity
W	Weight
w <sub>cs</sub>	Base width of the coal spreader
α <sub>v</sub>	Swirl angle
α <sub>dstr</sub>	Distribution parameter in Rosin-Rammler distribution

## TABLE OF CONTENTS

	Page
ABSTRACT .....	ii
DEDICATION .....	iv
ACKNOWLEDGEMENTS .....	v
NOMENCLATURE.....	vi
TABLE OF CONTENTS .....	xii
LIST OF FIGURES.....	xiv
LIST OF TABLES .....	xx
1. INTRODUCTION.....	1
2. LITERATURE REVIEW .....	6
2.1 Fuels and Fuel Analyses.....	6
2.2 NO <sub>x</sub> Emissions .....	19
2.3 NO <sub>x</sub> Reduction Technologies.....	21
2.4 Flow Simulation .....	32
3. OBJECTIVE AND TASKS .....	34
4. NON-REACTING FLOW (NRF) SIMULATION .....	36
5. EXPERIMENTAL FACILITIES AND PROCEDURES .....	39
5.1 Thermochemical Properties of Coal and Dairy Biomass .....	39
5.2 Fluid Dynamic Characteristic.....	42
5.3 Burner Modification.....	45
5.4 Experimental Studies .....	45
6. LOW NO <sub>x</sub> BURNER (LNB) MODIFICATIONS.....	53
6.1 Background .....	53
6.2 Pre-Existing LNB Components Measurement and Inspection .....	57
6.3 Modifications of LNB Components.....	63

	Page
7. RESULTS AND DISCUSSION .....	73
7.1 Fuel Analyses .....	73
7.2 Results of Particle Size Analysis.....	84
7.3 Experimental Results .....	87
8. CONCLUSIONS .....	129
9. FUTURE WORK .....	131
REFERENCES.....	133
APPENDIX A .....	140
APPENDIX B .....	141
APPENDIX C .....	147
APPENDIX D .....	153
APPENDIX E.....	162
APPENDIX F .....	168
APPENDIX G .....	198
APPENDIX H .....	209
APPENDIX I.....	211
APPENDIX J.....	216
APPENDIX K .....	224
APPENDIX L.....	235
APPENDIX M.....	237
APPENDIX N .....	239
APPENDIX O .....	240
APPENDIX P .....	242

## LIST OF FIGURES

	Page
Figure 1 Illustration of a conventional burner .....	3
Figure 2 Illustration of a low NO <sub>x</sub> burner.....	3
Figure 3 Regions of several types of solid fuels on Van Krevelen diagram .....	8
Figure 4 Example of TGA curve .....	13
Figure 5 Example of DTG curve .....	14
Figure 6 Determination of ignition temperature using the point where TGA curve in an oxidizing carrier gas starts separating from TGA curve in an inert carrier gas.....	15
Figure 7 Determination of ignition temperature using TGA-DTG method .....	16
Figure 8 CO concentration versus ER .....	22
Figure 9 Control volumes of: a) primary combustion zone and b) entire chamber.....	25
Figure 10 Illustration of the swirl recess length .....	27
Figure 11 Velocity profiles between radial and non-radial OFA injections.....	28
Figure 12 Location of OFA injection .....	29
Figure 13 Various types of OFA nozzles .....	30
Figure 14 Configurations of reburn fuel injector.....	32
Figure 15 Flow characteristics from NRF and reacting flow simulations.....	33
Figure 16 Schematic of SDT Q600 setup .....	40
Figure 17 Illustration of reference and sample pans of SDT Q600.....	41
Figure 18 Ro-Tap model B testing sieve shaker and sieve arrangement.....	42
Figure 19 The 30kW <sub>t</sub> down-fired furnace in CABEL .....	54

	Page
Figure 20 Partially premixed burner: a) an illustration of old partially premixed burner, b) the auger blade attached to the outer surface of the fuel/primary air nozzle as the swirler for secondary air, and c) the auger blades attached to the outer surface of the secondary air nozzle as the swirler for tertiary air .....	54
Figure 21 Pre-existing helix-vane swirler with the swirl angle ( $\alpha$ ) of 33 degrees and the swirl recess length ( $L_{sr}$ ) of 24 mm .....	56
Figure 22 LNB system setups: a) Gomez’s setup, and b) Lawrence’s setup .....	56
Figure 23 Two pieces of 1/4” 90-degree galvanized installed inside the combustion chamber .....	56
Figure 24 Illustration of the pre-existing LNB furnace components.....	59
Figure 25 Illustration of: a) swirl burner components, b) cross-sectional view of a swirl burner, and c) base width of a coal spreader .....	59
Figure 26 Illustration of combustion chamber components .....	60
Figure 27 Illustration of: a) burner diffuser half angle ( $\theta_{bd}$ ) and b) quarl half angle ( $\theta_{quarl}$ ).....	60
Figure 28 Straight-vane swirler with $\alpha$ of 45 degrees and $L_{sr}$ of 24 mm.....	61
Figure 29 Rough welding seams of the pre-existing helix-vane swirler .....	62
Figure 30 Coal spreaders: a) fin-type coal spreader (consists of two thin plates), and b) v-shaper coal spreader .....	62
Figure 31 Melted OFA outlet nozzles .....	63
Figure 32 Modified swirler .....	65
Figure 33 Main burner and OFA setup after modification .....	68
Figure 34 Piping diagrams of secondary air system: a) Lawrence’s setup, and b) present setup .....	69
Figure 35 The modified secondary air piping system attached to the main burner.....	70
Figure 36 Top view of the piping diagram for the OFA system: a) previous system, and b) present system .....	71

	Page
Figure 37 Current piping system of the air staging in the LNB .....	72
Figure 38 Proximate analysis of PRB, DB, and 90-10 PRB-DB blend on DAF basis.....	75
Figure 39 Van Krevelen diagram of PRB, DB, and 90-10 PRB-DB .....	79
Figure 40 TGA curves of PRB, DB, and 90-10 PRB-DB .....	81
Figure 41 DTG curves of PRB, DB, and 90-10 PRB-DB in inert carrier gas.....	82
Figure 42 Particle flow characteristics of PRB when: a) $d_{ps,PRB} = \{25 \mu\text{m}\}$ , b) $d_{ps,PRB} = \{50 \mu\text{m}, 75 \mu\text{m}, 100 \mu\text{m}, 125 \mu\text{m}, 150 \mu\text{m}\}$ , and c) $d_{ps,PRB} = \{175 \mu\text{m}, 200 \mu\text{m}\}$ .....	86
Figure 43 CO <sub>2</sub> and O <sub>2</sub> in flue gas from firing PRB at various ER <sub>oa</sub> .....	88
Figure 44 CO <sub>2</sub> and O <sub>2</sub> in flue gas from co-firing 90-10 PRB-DB at various ER <sub>oa</sub> .....	89
Figure 45 NO <sub>x</sub> in g/GJ from firing PRB and 90-10 PRB-DB at various ER <sub>oa</sub> .....	90
Figure 46 NO <sub>x</sub> from firing PRB and co-firing 90-10 PRB-DB blend at various ER without OFA.....	92
Figure 47 NO <sub>x</sub> emissions in g/GJ from firing PRB and co-firing 90-10 PRB-DB blend by setting ER <sub>oa</sub> at 0.85 and varying ER <sub>mb</sub> .....	93
Figure 48 NO <sub>x</sub> emissions in g/GJ from firing PRB and co-firing 90-10 PRB-DB blend by setting ER <sub>oa</sub> at 0.90 and varying ER <sub>mb</sub> .....	94
Figure 49 NO <sub>x</sub> emissions in g/GJ from firing PRB and co-firing 90-10 PRB-DB blend by setting ER <sub>oa</sub> at 0.95 and varying ER <sub>mb</sub> .....	95
Figure 50 NO <sub>x</sub> emissions in g/GJ from firing PRB and co-firing 90-10 PRB-DB blend at various ER <sub>oa</sub> with fixed ER <sub>mb</sub> of 1.10.....	97
Figure 51 NO <sub>x</sub> emissions in g/GJ from firing PRB and co-firing 90-10 PRB-DB blend at various ER <sub>oa</sub> with fixed ER <sub>mb</sub> of 1.05.....	98
Figure 52 NO <sub>x</sub> emissions in g/GJ from firing PRB and co-firing 90-10 PRB-DB blend at various ER <sub>oa</sub> with fixed ER <sub>mb</sub> of 1.00.....	99
Figure 53 CO emission in g/GJ from firing PRB and co-firing 90-10 PRB-DB blend at various ER <sub>oa</sub> .....	101



	Page
Figure 54 CO emission in g/GJ from firing PRB and co-firing 90-10 PRB-DB blend at various $ER_{oa}$ without OFA .....	102
Figure 55 CO emission in g/GJ from firing PRB and co-firing 90-10 PRB-DB blend at various $ER_{oa}$ with $ER_{mb}$ of 1.10.....	103
Figure 56 CO emission in g/GJ from firing PRB and co-firing 90-10 PRB-DB blend at various $ER_{oa}$ with $ER_{mb}$ of 1.05.....	104
Figure 57 CO emission in g/GJ from firing PRB and co-firing 90-10 PRB-DB blend at various $ER_{oa}$ with $ER_{mb}$ of 1.00.....	105
Figure 58 $NO_x$ versus CO in g/GJ from firing PRB and co-firing 90-10 PRB-DB blend at various $ER_{oa}$ .....	107
Figure 59 $NO_x$ versus CO emissions from firing PRB in g/GJ at various $ER_{oa}$ .....	108
Figure 60 $NO_x$ versus CO emissions from co-firing 90-10 PRB-DB blend in g/GJ ....	109
Figure 61 BF of firing PRB and co-firing 90-10 PRB-DB blend under various conditions .....	112
Figure 62 Fuel N conversion efficiency of firing PRB and co-firing 90-10 PRB-DB blend under various conditions.....	114
Figure 63 Average fuel N conversion efficiency of lean combustion under various conditions ( $ER_{oa}$ ranged from 0.85 to 0.95) .....	115
Figure 64 Illustration of thermocouples arrangement .....	117
Figure 65 Location of thermocouples for measuring: a) $T_c$ and b) $T_w$ .....	118
Figure 66 $T_c$ profile of firing PRB without OFA at various $ER_{oa}$ .....	119
Figure 67 $T_w$ profile of firing PRB without OFA at various $ER_{oa}$ .....	120
Figure 68 $T_c$ profile of co-firing 90-10 PRB-DB blend without OFA at various $ER_{oa}$ .....	121
Figure 69 $T_w$ profile of co-firing 90-10 PRB-DB blend without OFA at various $ER_{oa}$ .....	122
Figure 70 Average $T_c$ of firing PRB in lean regime by varying $ER_{mb}$ .....	124

	Page
Figure 71 Average $T_w$ of firing PRB in lean regime by varying $ER_{mb}$ .....	124
Figure 72 Average $T_c$ of co-firing 90-10 PRB-DB in lean regime by varying $ER_{mb}$ ...	125
Figure 73 Average $T_w$ of co-firing 90-10 PRB-DB in lean regime by varying $ER_{mb}$ .....	126
Figure 74 Results of DTA in inert gas of PRB and 90-10 PRB-DB blend .....	127
Figure 75 HHV based on stoichiometric $O_2$ of PRB, DB and other types of C-H-O fuels compared to the atomic H/C and O/C .....	145
Figure 76 Determination of $T_{ign}$ using Method I .....	154
Figure 77 Determination of $T_{ign}$ by using Method II.....	155
Figure 78 $T_{ign}$ of PRB determined by Method I .....	156
Figure 79 $T_{ign}$ of DB determined by Method I .....	156
Figure 80 $T_{ign}$ of 90-10 PRB-DB blend determined by Method I .....	157
Figure 81 $T_{ign}$ of PRB determined by Method II with the oxidizing gas.....	157
Figure 82 $T_{ign}$ of DB determined by Method II with the oxidizing gas.....	158
Figure 83 $T_{ign}$ of 90-10 PRB-DB determined by Method II with the oxidizing gas ....	158
Figure 84 $T_{ign}$ of PRB determined by Method II with the inert gas .....	159
Figure 85 $T_{ign}$ of DB determined by Method II with the inert gas .....	159
Figure 86 $T_{ign}$ of 90-10 PRB-DB determined by Method II with the inert gas .....	160
Figure 87 Plots of PSA by sieving on PRB and DB.....	167
Figure 88 Method of $L_{rev}$ determination .....	175
Figure 89 Ash solidified in the quarl zone.....	189
Figure 90 Method of $L_{rz}$ determination .....	196
Figure 91 Geometry of burner for deriving $SN'_{sa}$ .....	200
Figure 92 Plot of $SN'_{sa}$ versus $\alpha_v$ .....	201

	Page
Figure 93 Burner geometry with very thin-walled fuel/primary air nozzle and v-shaped coal spreader.....	202
Figure 94 Illustration of the base width and the half angle of the v-shaped coal spreader .....	203
Figure 95 Burner geometry with thick-walled fuel/primary air nozzle and v-shaped coal spreader.....	206
Figure 96 Plot of $SN'_{oa, vt}$ versus $\alpha_v$ .....	208
Figure 97 Illustration of gas travelling through sections of combustion chamber .....	210
Figure 98 The system for $U_{oa}$ consideration .....	225
Figure 99 Coordinate for $T_{\infty, hg}$ calculation .....	225

## LIST OF TABLES

		Page
Table 1	ASTM standards for proximate analysis.....	9
Table 2	ASTM standards for ultimate analysis.....	11
Table 3	ASTM standards for heating value analysis.....	12
Table 4	Examples of kinetics constants using maximum VM release method with the pyrolysis order of one.....	18
Table 5	Examples of kinetics constants using maximum VM release method with the pyrolysis order of n.....	19
Table 6	Examples of the mesh refinement, the resolution of the result and the approximate processing time of three levels of initial mesh.....	38
Table 7	Fixed and variable parameters for parametric studies.....	44
Table 8	Results of firing PRB and 90-10 PRB-DB by using Lawrence’s model.....	55
Table 9	Dimensions of the pre-existing LNB furnace components.....	58
Table 10	Dimensions of the modified LNB components.....	64
Table 11	Summary of coal spreader parameters before and after modification.....	66
Table 12	Proximate analysis of PRB, DB, and 90-10 PRB-DB blend.....	74
Table 13	Ultimate analysis of PRB, DB, and 90-10 PRB-DB blend.....	76
Table 14	Atomic H/C and O/C of PRB, DB, and 90-10 PRB-DB blend.....	76
Table 15	Empirical formulae of PRB, DB, and 90-10 PRB-DB blend.....	77
Table 16	HHV of PRB, DB, and 90-10 PRB-DB blend on various bases.....	78
Table 17	N, S, and ash loadings of PRB, DB, and 90-10 PRB-DB blend.....	79
Table 18	Comparison of data between proximate analysis and TGA.....	81
Table 19	Significant temperatures in pyrolysis of PRB, DB, and 90-10 PRB-DB.....	83

	Page
Table 20	Summary of kinetics constants of PRB, DB, and 90-10 PRB-DB blend.....84
Table 21	Equations for predicting the amount of NO <sub>x</sub> or CO ..... 110
Table 22	Average BF of firing PRB and 90-10 PRB-DB in lean region (ER <sub>oa</sub> ranged from 0.85 to 0.95)..... 111
Table 23	RQ of PRB, DB and 90-10 PRB-DB blend ..... 116
Table 24	Percentages of the mass flow rates of OFA to the main airflow..... 123
Table 25	Overall uncertainties of flue gas measurement from firing PRB under various conditions ..... 128
Table 26	Overall uncertainties of flue gas measurement from co-firing 90-10 PRB-DB blend under various conditions ..... 128
Table 27	Empirical formulae of PRB, DB, and 90-10 PRB-DB on DAF basis..... 140
Table 28	Normalized empirical formulae of PRB, DB, and 90-10 PRB-DB ..... 140
Table 29	Heating Values of PRB, DB, and 90-10 PRB-DB ..... 141
Table 30	Comparison between the HHV <sub>meas</sub> and the HHV <sub>pred</sub> using Boie equation ..... 143
Table 31	Comparison between HHV on as-received basis using and the predicted HHV by Mesroghli, Jorjani, Chelgani's correlation ..... 144
Table 32	HHV based on stoichiometric air and O <sub>2</sub> ..... 145
Table 33	HV <sub>vm</sub> of PRB and DB..... 146
Table 34	Stoichiometric coefficients for stoichiometric, rich, and lean combustion processes ..... 150
Table 35	A/F <sub>mass</sub> on DAF and as-received bases of PRB and DB at various ER..... 151
Table 36	A/F <sub>mass</sub> on as-received basis of 90-10 PRB-DB blend at various ER ..... 151
Table 37	Required mass flow rates for firing PRB and co-firing 90-10 PRB-DB blend at various ER ..... 151

	Page
Table 38	Required volume flow rates for firing PRB and co-firing 90-10 PRB-DB blend at various ER.....152
Table 39	Fuel loadings of PRB and 90-10 PRB-DB blend.....152
Table 40	$T_{ign}$ of PRB, DB, and 90-10 PRB-DB estimated by various methods .....160
Table 41	$T_{ign}$ of PRB and DB with various particle sizes .....161
Table 42	Size of sieve aperture of each mesh number .....164
Table 43	Result from PSA by sieving on PRB .....166
Table 44	Result from PSA by sieving on DB .....166
Table 45	Summary of PSA by sieving on PRB and DB .....167
Table 46	Details of pipe sizes and flow areas for various numbers of secondary air inlet nozzles.....168
Table 47	Streamlines and velocity profiles of secondary airflow through one secondary air inlet nozzle at various secondary air volume flow rates.....171
Table 48	Streamlines and velocity profiles of secondary airflow through two secondary air inlet nozzles at various secondary air volume flow rates .....172
Table 49	Streamlines and velocity profiles of secondary airflow through four secondary air inlet nozzles at various volume flow rates.....173
Table 50	Particle flow characteristics of injecting PRB particle through fin-type coal spreader with 1-mm base width at various particle sizes .....176
Table 51	Particle flow characteristics of injecting PRB particle through fin-type coal spreader with 3-mm base width at various particle sizes .....178
Table 52	Particle flow characteristics of injecting PRB particle through v-shaped coal spreader with 3-mm base width at various particle sizes .....180
Table 53	Velocity and primary air distribution profiles by setting swirl angle at 35 degrees and varying $L_{sr}$ .....183
Table 54	Velocity and primary air distribution profiles by setting swirl angle at 40 degrees and varying $L_{sr}$ .....184

	Page
Table 55	Velocity and primary air distribution profiles by setting swirl angle at 45 degrees and varying $L_{sr}$ .....185
Table 56	Velocity and primary air distribution profiles by setting swirl angle at 50 degrees and varying $L_{sr}$ .....186
Table 57	Velocity and primary air distribution profiles by setting swirl angle at 55 degrees and varying $L_{sr}$ .....187
Table 58	Velocity and primary air distribution profiles by setting swirl angle at 60 degrees and varying $L_{sr}$ .....188
Table 59	Effects of burner diffuser on NRF characteristics at various volume flow rates .....190
Table 60	Conditions for investigating the effects of OFA on NRF characteristics.....192
Table 61	Front view of velocity profiles of airflows under various conditions .....193
Table 62	Top view of mass fraction profiles of OFA under various conditions.....194
Table 63	Front view of mass fraction profiles of OFA under various conditions.....195
Table 64	$L_{rz}$ at 300 K and 1,500 K under various conditions .....197
Table 65	Mean residence times at various equivalence ratios .....210
Table 66	Particle Stokes numbers of PRB ( $St_{p,PRB}$ ) at various particle sizes and equivalence ratios .....213
Table 67	Particle Stokes numbers of DB ( $St_{p,DB}$ ) at various particle sizes and equivalence ratios .....213
Table 68	Particle Reynolds number from particle study on PRB ( $Re_{p,PRB}$ ) .....214
Table 69	Particle Reynolds number from particle study on DB ( $Re_{p,DB}$ ).....214
Table 70	Particle relaxation time of PRB ( $\tau_{pr,PRB}$ ) at various particle sizes and equivalence ratios .....215
Table 71	Particle relaxation time of DB ( $\tau_{pr,DB}$ ) at various particle sizes and equivalence ratios .....215
Table 72	Experimental results of firing PRB .....217

	Page
Table 73	Experimental results of co-firing 90-10 PRB-DB blend .....218
Table 74	NO <sub>x</sub> and CO emissions in g/GJ .....219
Table 75	Estimated percentage of N <sub>2</sub> in dry flue gas .....220
Table 76	T <sub>c</sub> profiles of firing PRB .....226
Table 77	T <sub>w</sub> profiles of firing PRB.....227
Table 78	T <sub>c</sub> profiles of co-firing 90-10 PRB-DB blend .....228
Table 79	T <sub>w</sub> profiles of co-firing 90-10 PRB-DB blend .....229
Table 80	Maximum temperature of firing PRB and co-firing 90-10 PRB-DB blend .....230
Table 81	Equations of T <sub>c</sub> profiles, T <sub>∞,hg</sub> and U <sub>oa</sub> from firing PRB.....231
Table 82	Equations of T <sub>w</sub> profiles, T <sub>w,hg</sub> and U <sub>oa</sub> from firing PRB .....232
Table 83	Equations of T <sub>c</sub> profiles, T <sub>∞,hg</sub> and U <sub>oa</sub> from co-firing 90-10 PRB-DB blend .....233
Table 84	Equations of T <sub>w</sub> profiles, T <sub>w,hg</sub> and U <sub>oa</sub> from co-firing 90-10 PRB-DB blend .....234
Table 85	Results of burnt fraction estimation .....236
Table 86	Results of fuel N conversion efficiency calculation.....238
Table 87	N <sub>conv, avg</sub> of lean combustion (ER ranged from 0.85 to 0.95) .....238
Table 88	Benefit of NO <sub>x</sub> reduction in various scenarios.....241
Table 89	Overall uncertainties of airflows and temperature components .....242
Table 90	Standard errors in measuring flue gas composition from firing PRB .....243
Table 91	Standard errors in measuring flue gas composition from co-firing 90- 10 PRB-DB blend.....244



## 1. INTRODUCTION

Recently, operators of coal-fired power plants have planned to shut their plants down because they have to incur a large amount of expenses on pollution control technologies in order to satisfy air pollution regulations such as U.S. Environmental Protection Agency's (EPA) Mercury and Air Toxics Standards (MATS) that will be enforced in 2016. Additionally, the projection from U.S. Energy Information Administration (EIA) shows that approximately 60 GW<sub>t</sub> of coal-fired capacity will retire at the time MATS is obliged (U.S. EIA 2014).

Another factor that drives the retirement of coal-fired power plants is the emerging of shale gas. Shale gas is claimed to be cleaner than coal because the major composition of shale gas is methane (CH<sub>4</sub>); thus, it is mercury-, ash- and particulate-free fuel. In addition, the greenhouse-gas (GHG) footprint of shale gas is only about a half of the GHG footprint of coal (Cathles III, et al. 2012). Nonetheless, the usage of carbon neutral energy sources such as biomass in coal-fired power plants is arising according to the current goal of carbon reduction which is 30% by 2030 (Koch 2014). Therefore, clean coal technology should be continuously developed in order to make coal and biomass ones of the sustainable energy resources.

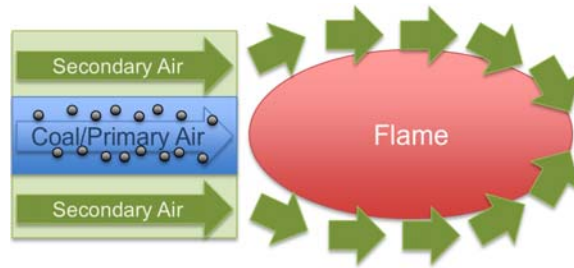
Besides carbon monoxide (CO) and carbon dioxide (CO<sub>2</sub>), nitrogen oxides (NO<sub>x</sub>) are ones of the main pollutant emissions that are regulated by U.S. EPA. NO<sub>x</sub> are known to be harmful to environment because it could irritate the respiratory system of human being, mix with moisture in atmosphere and cause acid rain, or destroy the ozone layer

in the upper atmosphere. The limit of NO<sub>x</sub> emissions depends on fuel type. For instance, the limit for sub-bituminous coal such as Wyoming Powder River Basin coal (PRB) is 210 g/GJ of heat input (U.S. EPA 2012).

Typically, the NO<sub>x</sub> emissions are due to: 1) thermal NO<sub>x</sub> where atmospheric nitrogen (N<sub>2</sub>) reacts with oxygen to produce trace amounts of NO<sub>x</sub> particularly at high temperature, 2) fuel NO<sub>x</sub> where the fuel-bound nitrogen (fuel N) reacts with oxygen and produce NO<sub>x</sub> with significant fraction of oxidizer to NO<sub>x</sub> (almost 30%), and 3) prompt NO<sub>x</sub> where hydrocarbon (HC) fragments such as HCN produced in the fuel-rich regime react with oxygen and form NO<sub>x</sub>. For coal, fuel NO<sub>x</sub> dominates the others.

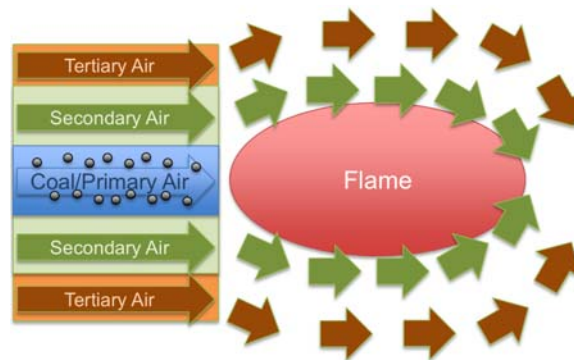
Generally, the NO<sub>x</sub> emission can be controlled by using: 1) low NO<sub>x</sub> burner (LNB) where air is introduced in stage to reduce availability of O<sub>2</sub> for fuel N oxidation 2) selective catalytic reduction (SCR) where NO<sub>x</sub> is reduced to N<sub>2</sub> using catalysts, and 3) reburn system where natural gas is injected downstream of main burner to form N compounds with HC fragments which reduced NO<sub>x</sub> to N<sub>2</sub>.

In a conventional swirl burner (Figure 1), coal and primary air are injected through a coal/primary air nozzle. Then, secondary air is injected through a secondary air nozzle and mixes with the mix of coal and primary air at the burner exit. Hence, coal, primary air, and secondary air are burned at the same interface. This is so-called a partially-premixed burner. Additionally, the secondary air is swirled by a swirler in order to create swirl beyond the burner exit. The swirl creates suction forces at the center of the swirl due to the pressure gradient and draws air from the far field to the near field of the burner. Consequently, a recirculation zone (RZ) is formed, and flame is stabilized.



**Figure 1 – Illustration of a conventional burner**

On the other hand, in LNB (Figure 2), the oxygen concentration inside the primary combustion zone is decreased by delaying the air until the downstream of the primary combustion zone. In other words, mass flow rate of secondary air is decreased whilst mass flow rate of tertiary air is increased. Decrease of oxygen concentration inside the primary combustion zone creates a fuel-rich zone which prohibits fuel NO<sub>x</sub> mechanisms. As a result, fuel N reacts with each other and forms N<sub>2</sub> rather than NO<sub>x</sub>.



**Figure 2 – Illustration of a low NO<sub>x</sub> burner**

NO<sub>x</sub> could also be traded in emissions markets like carbon credits. So, coal-fired power plants that do not want to invest in new technologies could buy NO<sub>x</sub> credits from other plants. NO<sub>x</sub> price for emissions trading was about \$15.89 per short ton in 2011 although it was as high as \$776.04 per short ton in 2007 (U.S. EIA 2012).

Despite the fact that NO<sub>x</sub> credits have been traded at low price recently, NO<sub>x</sub> reduction is still one of the challenging tasks particularly when post combustion treatments such as SCR might not be an option because of its low cost effectiveness. SCR units could have operating costs per ton of NO<sub>x</sub> reduced as high as \$3,148 whilst low NO<sub>x</sub> burners (LNB) could have operating costs approximately \$332 per ton of NO<sub>x</sub> reduced. Furthermore, the capital expenditure of an SCR unit alone is about \$860,000; meanwhile, the capital expenditure of LNB is only \$130,000 or about 15% of the SCR unit (McAdams, Reed and Itse 2001). The current research, therefore, focuses on LNB development for coal-fired power plants.

This thesis consists of eight sections and 15 appendices. To start with, Literature Review section provides the overview and brief knowledge of fuel analyses, NO<sub>x</sub> formation mechanisms, LNB system for coal-fired power plant, previous studies on co-firing of blends between coal and dairy biomass (DB), benefits of DB on NO<sub>x</sub> reduction, effects of over-fire air (OFA) injection, flow simulation inside a combustion chamber, and numbers related to combustion and fluid dynamic such as equivalence ratio (ER), swirl number (SN), etc. Then, tasks required for achieving the overall objective of the current research are proposed in Objective and Tasks section.

The details of non-reacting flow (NRF) simulation on SolidWorks program are given in Non-Reacting Flow Simulation section in order to develop the LNB system prior to fabrication. The NRF characteristics which are the results of the NRF simulation are given in Appendix F.

All of the experimental facilities used in the present research are listed in Experimental Facilities and Procedures section. The procedure used for each facility is given in this section, so all of experiments could be repeated with the same exact procedure. The summary of parametric studies is also included in this section. Next, the burner parts that were modified based on the results from the NRF simulation are detailed in LNB Modifications section.

Then, CO, CO<sub>2</sub>, and NO<sub>x</sub> emissions were determined by analyzing flue gas from firing pure PRB and blends of PRB and DB at various ER. In addition, the flow temperatures at the center and at the wall along the vertical section of combustion chamber were measured. Results of fuel analyses and flue gas analysis such as burnt fraction (BF), fuel N conversion efficiency ( $N_{conv}$ ) and respiratory quotients (RQ) are presented in Results and Discussion section. All of the significant results are summarized in Conclusion section. Lastly, future tasks for broadening horizons of NO<sub>x</sub> reduction are proposed in Future Work section.

## 2. LITERATURE REVIEW

This section provides brief and basic knowledge for conducting the current research. First, fuel properties and methods used in analyzing them are explained in order to provide the basic understanding of the fuels used in the current research. Second, important components of LNB system are described altogether with some typical values used in industries such as equivalence ratio (ER) and swirl number (SN). Third, the effects of the over-fire air (OFA) system and co-firing blends of PRB and DB on NO<sub>x</sub> reduction are briefly explained. Lastly, brief details of reacting and NRF simulations are given in order to compare the pros and cons of each type of simulation.

### 2.1 Fuels and Fuel Analyses

Understanding of fuels is the first priority before starting anything else. This subsection will provide some basic knowledge of fuels used in the present research and how to find their thermochemical properties.

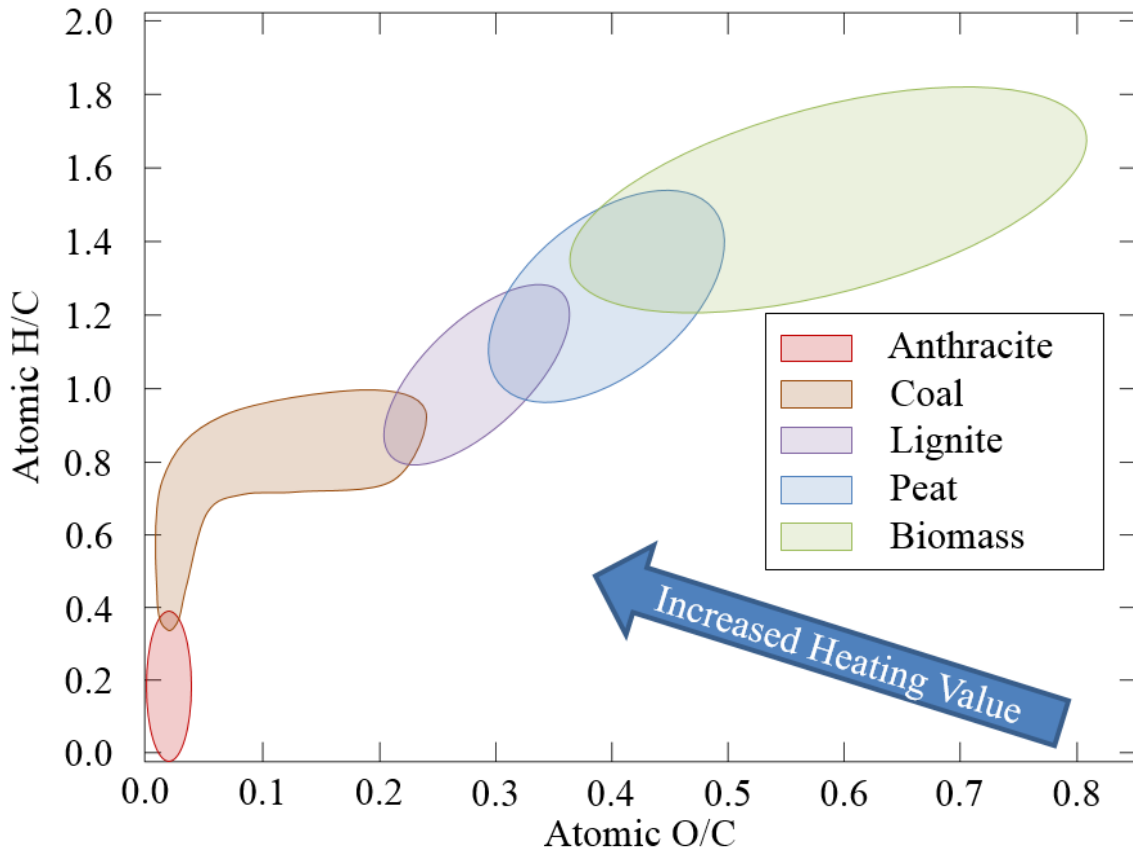
#### 2.1.1 Coal and Dairy Biomass (DB)

Coal is a combustible matter in a solid form. It comprises of Carbon (C), Hydrogen (H), Oxygen (O), Nitrogen (N), and Sulfur (S) where C content dominates the other contents. Coal originates from compressed and fossilized carbon, i.e. fossil fuel, in rock layers over a long period of time. To be more specific, coal originates from dead plants that gradually turn into peat, and peat gradually converts into lignite, sub-bituminous, bituminous and anthracite coal respectively while it is exposed to high

temperature and pressure. The fraction of C content increases when coal is exposed to high temperature and pressure because volatile matter (VM) releases from the matrix of coal. Thus, different coal rank means different age and different C content. For instance, anthracite which is the oldest type of coal has C content approximately 86%-97% whilst lignite which is the lowest rank of coal contains C only 25%-35% (U.S. EIA 2014).

In addition, the relation between the atomic H-to-C ratio (H/C) and the atomic O-to-C ratio (O/C) of the solid fuels on Van Krevelen diagram as shown in Figure 3 shows that the heating value (HV) of fuels will increase when O/C decreases and H/C increases (Van Loo and Koppejan 2007). For example, consider CH<sub>4</sub> which does not have O content (H/C = 4.0 and O/C = 0) and anthracite which is the highest rank of coal (H/C ≈ 0.2 and O/C ≈ 0.02). The higher heating value (HHV) of CH<sub>4</sub> is approximately 55,530 kJ per kg which is much higher than anthracite whose HHV is 34,000 kJ per kg approximately. This indicates that the blue arrow in Figure 3 is correct.

Cattle manure or DB is a by-product from livestock that can pollute the environment such as air, water, and soil if there is no proper treatment or management before disposing it to the environment. Besides utilizing DB as fertilizer, DB can be used as either gaseous fuel (biogas) or solid fuel depends on application. Actually, a large portion of cattle manure is the undigested feed such as grains. Therefore, when raw cattle manure is dried out, the undigested feed can be ground and used as an alternative solid fuel. DB is also considered as one of potential alternative energy resources because it is C neutral. Hence, co-firing the fuel blends of coal and DB will benefit C emission.



**Figure 3 – Regions of several types of solid fuels on Van Krevelen diagram (adapted from Van Loo and Koppejan 2007)**

### 2.1.2 Proximate, Ultimate, and Heating Value Analyses

Proximate analysis provides the moisture, ash, VM, and fixed carbon (FC) contents in solid fuels. A result from proximate analysis is also able to classify a rank of a coal sample because proximate analysis can estimate the FC content in the sample. American Society for Testing and Materials (ASTM) sets the standards for proximate analysis as shown in Table 1, and the procedures of determining the aforementioned contents in a sample are described below.



**Table 1 – ASTM standards for proximate analysis**

Content	ASTM Standards	
	Coal	Biomass
<u>Proximate Analysis</u>	D3172	
- Moisture	D3173	E871
- VM	D3175	E872 and E897
- Ash	D3174	D1102 and E830
- FC	By difference	By difference

<u>Standard Code</u>	<u>Description</u>
D1102	Standard Test Method for Ash in Wood
D3172	Standard Practice for Proximate Analysis of Coal and Coke
D3173	Standard Test Method for Moisture in the Analysis Sample of Coal and Coke
D3174	Standard Test Method for Ash in the Analysis Sample of Coal and Coke from Coal
D3175	Standard Test Method for Volatile Matter in the Analysis Sample of Coal and Coke
E830	Standard Test Method for Ash in the Analysis Sample of Refuse Derived Fuel
E871	Standard Test Method for Moisture Analysis of Particulate Wood Fuel
E872	Standard Test Method for Volatile Matter in the Analysis of Particulate Wood Fuels
E897	Standard Test Method for Volatile Matter in the Analysis Sample of Refuse Derived Fuel

First, a sample of a solid fuel will be naturally dried (air dried) in order to remove the moisture from the surface of the sample. The sample, then, is weighed and recorded as the surface moisture. Next, the remaining sample is evenly split into three batches. The first batch is dried in an oven (oven dried) in order to remove the moisture inside the structure of the sample (subsurface moisture). After that, the sample of the first batch is

weighed in order to determine how much the moisture is driven off during the drying process i.e. the amount of subsurface moisture. Summation of the surface moisture amount and the subsurface moisture amount is the total amount of moisture content in the sample. Second, the second batch obtained from the previous step is heated in an inert atmosphere such as argon (Ar) or nitrogen, N<sub>2</sub>, in order to extract VM from the sample. This step follows standard D3175, E872, or E897 from American Society for Testing and Materials (ASTM). Hence, this step is used to determine VM content of the sample. Third, the third batch obtained from the first step is used for determining the ash content by heating it in an oxidizing atmosphere such as air until the weight of the sample remains constant. The remaining weight of the heated sample determined the ash content in the sample. Finally, FC content in the sample is determined by the difference between the initial weight of the batched sample and sum of the subsurface moisture, VM, and ash contents. These four values (moisture, VM, FC, and ash) are the results of the proximate analysis on the as-received basis.

Ultimate analysis, as known as elemental analysis, is the method to determine the elementary contents in the sample such as C, H, N, S, and O. Because many solid fuels do not have specific chemical formulae, knowing their C, H, N, S, and O contents could help developing the chemical formulae and determining the stoichiometric air-to-fuel ratios. The ASTM standards for conducting ultimate analysis as shown in Table 2 are applied to determine the C, H, N, S, and O contents.

**Table 2 – ASTM standards for ultimate analysis**

Content	ASTM Standards	
	Coal	Biomass
<u>Ultimate Analysis</u>	D3176	
C and H	D5373	E777
N	D5373	E778
S	D4239	E775
O	By difference	By difference
<u>Standard Code</u>	<u>Description</u>	
D3176	Standard Practice for Ultimate Analysis of Coal and Coke	
D4239	Standard Test Method for Sulfur in the Analysis Sample of Coal and Coke Using High-Temperature Tube Furnace Combustion	
D5373	Standard Test Methods for Determination of Carbon, Hydrogen and Nitrogen in Analysis Samples of Coal and Carbon in Analysis Samples of Coal and Coke	
E775	Standard Test Methods for Total Sulfur in the Analysis Sample of Refuse-Derived Fuel	
E777	Standard Test Method for Carbon and Hydrogen in the Analysis Sample of Refuse-Derived Fuel	
E778	Standard Test Methods for Nitrogen in the Analysis Sample of Refuse-Derived Fuel	

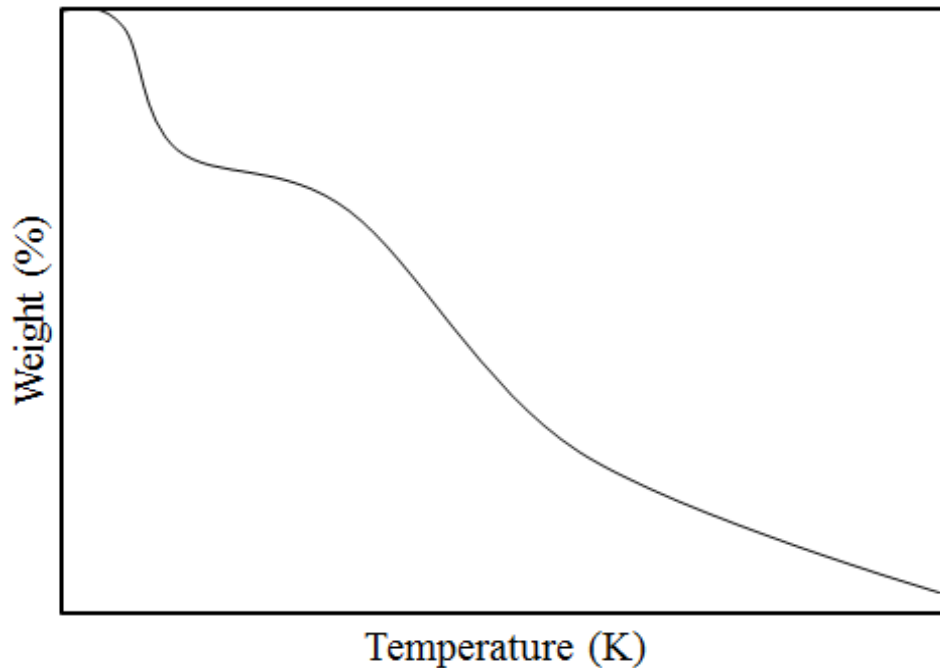
HV is the amount of heat released by a unit of fuel in stoichiometric combustion. In addition, HHV or gross calorific value is the heating value where water occurs in the products of combustion reaction in gas phase. Typically, bomb calorimeter is used to find HHV of fuels according to ASTM D5865 and E711 as shown in Table 3. HHV of solid fuels on as-received mass will be used to determine the amount of heat input. Further details and calculations are given in Appendix C where empirical equation such as Boie equation is used to estimate HHV of fuels using elemental analysis.

**Table 3 – ASTM standards for heating value analysis**

Content	ASTM Standards	
	Coal	Biomass
Heating Value Analysis	D5865	E711
<u>Standard Code</u>	<u>Description</u>	
D5865	Standard Test Method for Gross Calorific Value of Coal and Coke	
E711	Standard Test Method for Gross Calorific Value of Refuse Derived Fuel by the Bomb Calorimeter	

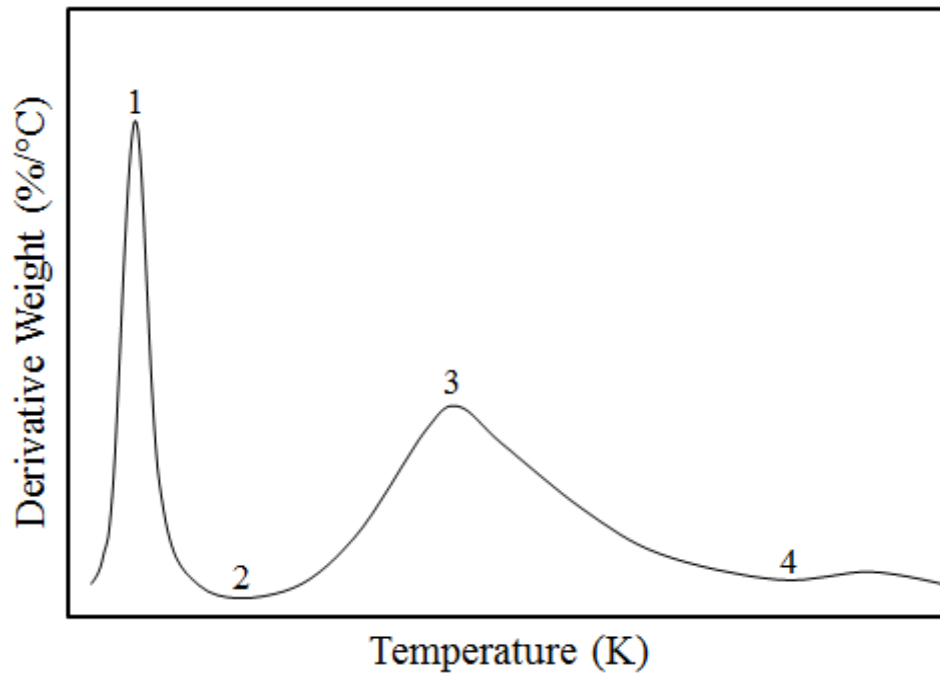
### 2.1.3 Thermogravimetric and Derivative Thermogravimetric Analyses

Thermogravimetric analysis (TGA) is the method used to measure the weight (W) changes relative to temperature (T) changes. TGA curve is the plot of percentage of remaining weight on the sample pan relative to the initial weight versus temperature (%W vs T) as shown in Figure 4. Some basic properties of solid fuels such as moisture, ash, etc., could be determined by setting procedure as prescribed in other literatures. For example, Mayoral, et al. (2001) proposed the following steps for determining ash contents in the sample with a deviation of  $\pm 0.5\%$ : 1) drying the sample with the constant heating rate (HR) at  $20^{\circ}\text{C}/\text{min}$  until temperature is  $105^{\circ}\text{C}$ , 2) maintaining temperature at  $105^{\circ}\text{C}$  for 3 minutes, 3) replacing the inert carrier gas by oxygen gas ( $\text{O}_2$ ), and 4) heating the sample from  $105^{\circ}\text{C}$  to  $850^{\circ}\text{C}$  by setting the HR of the final step at  $50^{\circ}\text{C}/\text{min}$ .



**Figure 4 – Example of TGA curve**

Derivative thermogravimetric analysis (DTG) is simply defined as the derivative of weight on the sample crucible with respect to the change of sample temperature at one instant ( $dW/dT$ ). DTG curve as shown in Figure 5 shows  $dW/dT$  versus  $T$ . This curve is useful for determining the maximum point where the maximum weight change appears or the minimum point where the minimum weight change appears. For example, in Figure 5, if the curve is plotted from DTG of coal, point 1 is the maximum point of moisture loss, point 2 is the point where the moisture is completely dried out and starts pyrolysis, point 3 represents the maximum VM release (MVR), and point 4 where the weight change is approximately constant is the end of pyrolysis.

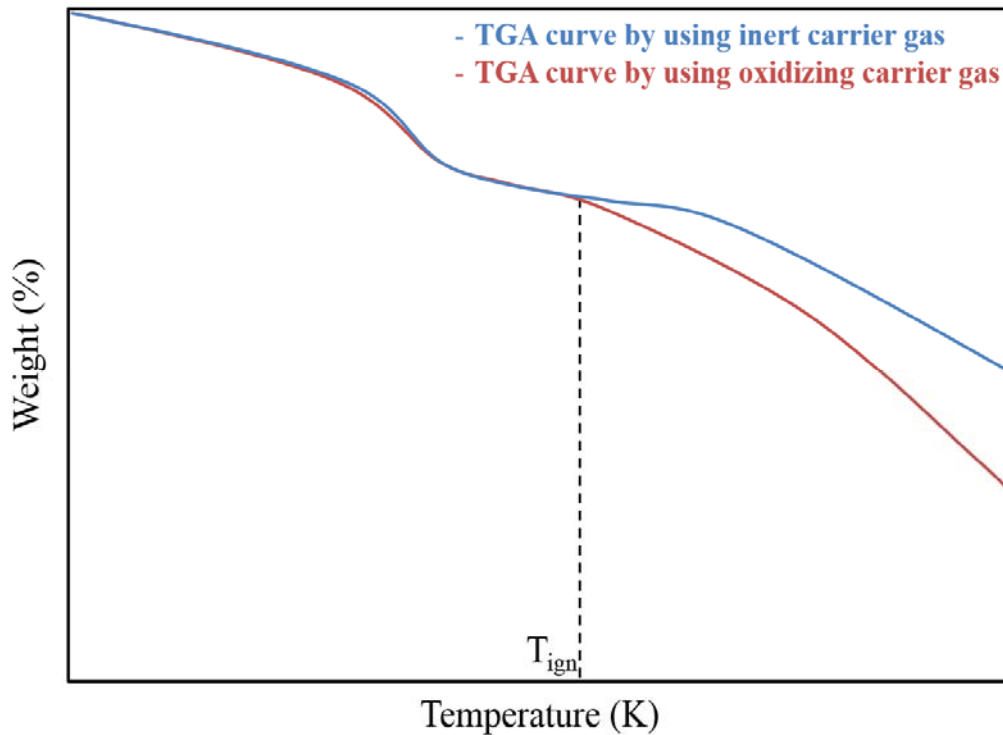


**Figure 5 – Example of DTG curve**

#### *2.1.4 Determination of Ignition Temperature*

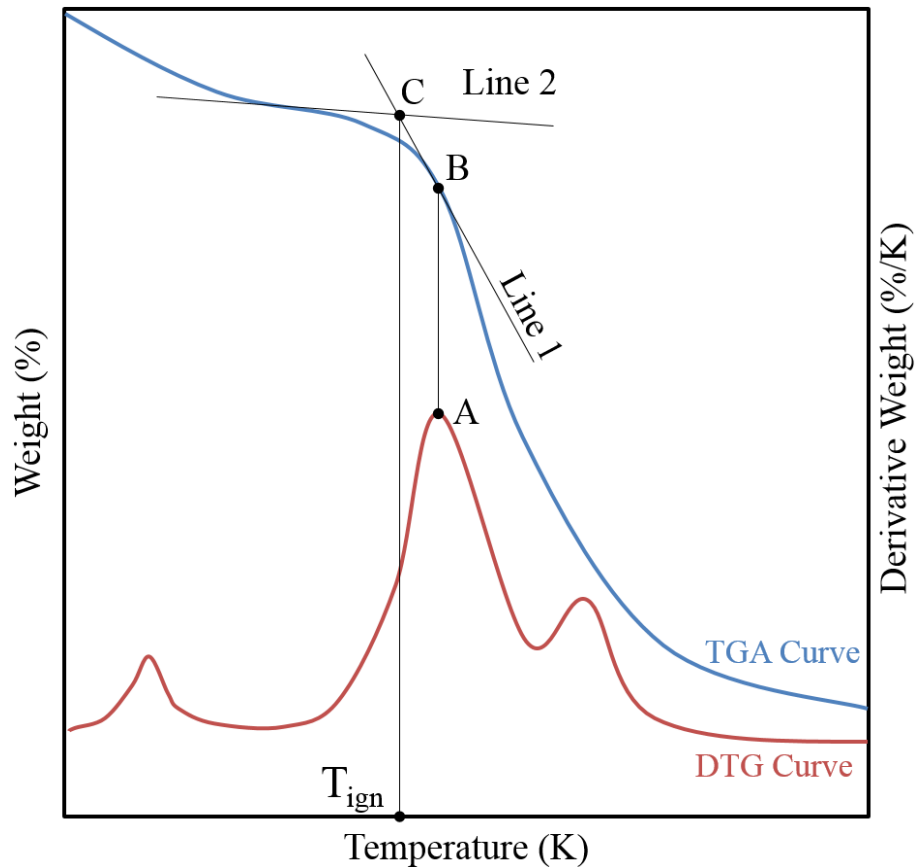
Ignition temperature ( $T_{\text{ign}}$ ) is the minimum temperature that causes a combustible substance to start burning and continue burning without supplying external heat source to it. Many methods have been developed in order to determine  $T_{\text{ign}}$  by using the results from TGA and DTG. Follows are the examples of methods used to determine  $T_{\text{ign}}$ .

First,  $T_{\text{ign}}$  could be determined when the TGA curve plotted by using an oxidizing gas (air or mixture of  $\text{N}_2$  and  $\text{O}_2$  with  $\text{N}_2$ -to- $\text{O}_2$  ratio of 79 to 21 on a volume basis) as the carrier gas starts separating from the TGA curve plotted by using an inert gas as the carrier gas as shown in Figure 6 (Tognotti, et al. 1985).



**Figure 6 – Determination of ignition temperature using the point where TGA curve in an oxidizing carrier gas starts separating from TGA curve in an inert carrier gas (adapted from Tognotti, et al. 1985)**

Second, curves generated by using the results from TGA and DTG could be used to determine  $T_{ign}$ . This is so-called TGA-DTG method. Li, et al. (2012) described this method as follows. In Figure 7, point A on the DTG curve is specified by the point of MVR. Then, point B is marked by projecting vertical line from point A to the TGA curve, and the line that is tangent to point B on the TGA curve is drawn and named as line 1. Next, the line that is tangent to the base of TGA curve during the moisture-volatile transition is drawn and named as line 2. The temperature at the cross point between line 1 and line 2 is the  $T_{ign}$ .



**Figure 7 – Determination of ignition temperature using TGA-DTG method (adapted from Li, et al. 2012)**

### 2.1.5 Kinetics Constants of Pyrolysis

The current research focuses on use of coal and DB, so the consideration on kinetics constants is mainly related to pyrolysis of coal and DB. VM that resides in coal and DB starts releasing at the beginning of pyrolysis process i.e. after the moisture is completely dried out. The process of VM release is called devolatilization. TGA and DTG curves could be used to estimate the amount of devolatilization and the point at MVR as shown in Figure 4 and Figure 5. For instance, Biagini, Fantozzi, and Tognotti (2004) mentioned that high-VM coal (coal Kema with VM of 28.7%) starts



devolatilization at 613 K and has MVR at 748 K. The amount of VM released during devolatilization is also affected by the HR ( $dT/dt$ ). To be more specific, when the higher HR is applied, the fuel will release more amount of VM during devolatilization (Biagini, Fantozzi and Tognotti 2004).

Devolatilization rate with the constant HR for single reaction modelling (SRM) could be expressed as equation (2.1) where  $m_{vm}$  is the mass of VM at time  $t$  that excludes the moisture and ash contents,  $n$  is the order of reaction,  $B$  is the pre-exponential factor or frequency factor in 1/min or 1/s,  $E_a$  is the activation energy in kJ/kmol, and  $R_u$  is the universal gas constant (8.314 kJ/kmol·K) (Martin 2006). Integrating equation (2.1) from the initial condition (denoted by “o”) to the final condition (denoted by “∞”) leads to equation (2.2), and differentiating equation (2.1) with respect to temperature yields equation (2.3).

$$-\frac{dm_{vm}}{dT} = \frac{B}{HR} m_{vm}^n \exp\left(-\frac{E_a}{R_u T}\right) \quad (2.1)$$

$$-\int_{m_{vm,o}}^{m_{vm,\infty}} \frac{dm_{vm}}{m_{vm}^n} = \frac{B}{HR} \int_{T_o}^{T_\infty} \exp\left(-\frac{E_a}{R_u T}\right) dT \quad (2.2)$$

$$-\frac{d^2 m_{vm}}{dT^2} = \frac{B}{HR} m_{vm}^{n-1} \exp\left(-\frac{E_a}{R_u T}\right) \left[ n \frac{dm_{vm}}{dT} + \left(\frac{E_a}{R_u T^2}\right) m_{vm} \right] \quad (2.3)$$

When the order of reaction is equal to one ( $n = 1$ ), equations (2.3) becomes equations (2.4). By utilizing the MVR method where the second derivative of  $m_{vm}$  with respect to  $T$  equals to zero ( $(d^2 m_{vm}/dT^2)_{\max} = 0$ ) and the data from TGA and DTG,  $E_a$

could be estimated by equation (2.5). Eventually, B could be calculated by inserting  $E_a$  obtained from the MVR method and data at the MVR into equation (2.1) as shown in equation (2.6).

$$-\frac{d^2 m_{vm}}{dT^2} = \frac{B}{HR} \exp\left(-\frac{E_a}{R_u T}\right) \left[ \frac{dm_{vm}}{dT} + \left(\frac{E_a}{R_u T^2}\right) m_{vm} \right] \quad (2.4)$$

$$E_a = -\left(\frac{dm_{vm}}{dT}\right)_{max} \left(\frac{R_u T^2}{m_{vm}}\right)_{\left(\frac{dm_{vm}}{dT}\right)_{max}} \quad (2.5)$$

$$B = -HR \left(\frac{dm_{vm}}{dT}\right)_{max} \left[ m_{vm} \exp\left(-\frac{E_a}{R_u T}\right) \right]_{\left(\frac{dm_{vm}}{dT}\right)_{max}}^{-1} \quad (2.6)$$

The MVR method is one of the easiest methods to roughly estimate B and  $E_a$ .

Table 4 and Table 5 are examples of kinetics constants obtained from the MVR method with the pyrolysis order of one and n respectively. Other methods used to estimate kinetics constants are detailed in other literatures; for example, distributed activation energy model (Martin 2006), approximations in exponential integrals (Annamalai and Puri 2007), dynamic heating (Lam, et al. 2011), etc.

**Table 4 – Examples of kinetics constants using maximum VM release method with the pyrolysis order of one (excerpted data from Martin 2006)**

Kinetics Constants	High-Ash Partially-Composted Feedlot Biomass	Low-Ash Partially-Composted Feedlot Biomass	Texas Lignite Coal
B (1/min)	3.72	494.46	3.42
$E_a$ (kJ/kmol)	$1.52 \times 10^7$	$3.59 \times 10^7$	$1.86 \times 10^7$

**Table 5 – Examples of kinetics constants using maximum VM release method with the pyrolysis order of n (excerpted data from Hoffmann 2011)**

Fuel Type	B (1/min)	E <sub>a</sub> (kJ/kmol)	n
DB	7.68×10 <sup>6</sup>	89,642	1.853
Lignite Coal	3.98×10 <sup>12</sup>	183,297	3.563
Juniper	2.25×10 <sup>4</sup>	66,527	0.328
Sorghum	8.06×10 <sup>9</sup>	122,571	0.900
Mesquite	1.65×10 <sup>6</sup>	85,193	0.564

## 2.2 NO<sub>x</sub> Emissions

NO<sub>x</sub> are by –products from combustion process. NO<sub>x</sub> mainly compose of nitric oxide (NO) and nitrogen dioxide (NO<sub>2</sub>). Actually, there are many other species such as nitrogen trioxide (NO<sub>3</sub>), nitrous oxide (N<sub>2</sub>O), etc., but the amount of NO and NO<sub>2</sub> dominates the others. Typically, in case all other species are considered negligible, the NO-to-NO<sub>2</sub> ratio is approximately 95 to 5 (Yaverbaum 1979).

NO<sub>x</sub> are generally produced in the combustion process when an oxidizer used in the process contains N. However, in case pure O<sub>2</sub> is used as the oxidizer (as known as oxy-fuel combustion), NO<sub>x</sub> can still be generated by the fuel N. The reactions between N and O particularly occur when O<sub>2</sub> concentration and temperature of the system are high. The following three mechanisms are well known for explaining how NO<sub>x</sub> generate during the combustion process.

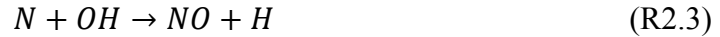
First is the fuel-bound mechanism. Fuel N can directly react with O<sub>2</sub> in the oxidizer and form NO or NO<sub>2</sub>. NO<sub>x</sub> generated by this mechanism are also called fuel NO<sub>x</sub>. Hence, this mechanism is not important for fuels that do not contain N such as

CH<sub>4</sub>, propane (C<sub>3</sub>H<sub>8</sub>), etc. So, only the fuels that contain N such as coal, biomass, etc., will take this mechanism into account. Typically, more fuel N means more NO<sub>x</sub>.

However, the ratio of NH<sub>3</sub> to HCN (NH<sub>3</sub>/HCN) in VM of coal can affect the amount of NO<sub>x</sub> formation because NH<sub>3</sub> and HCN have different reaction routes depend on type of combustion. The atomic nitrogen-to-carbon ratio (N/C) could also be used to predict NH<sub>3</sub>/HCN. When N/C is high, NH<sub>3</sub>/HCN is high (Chang, Feng and Xie 2005). This implies that solid fuels with higher N/C have more NH<sub>3</sub> than HCN in their VM.

Second is the thermal mechanism. NO<sub>x</sub> generated by this mechanism is also known as thermal NO<sub>x</sub>. Thermal mechanism is the predominant mechanism in combustion process when fuel without N content such as CH<sub>4</sub> is burned. Thermal NO<sub>x</sub> consumes N<sub>2</sub> in the oxidizer and forms NO<sub>2</sub> under high temperature condition. This mechanism is temperature sensitive; in addition, they could be exponentially generated when the temperature is above 1,370 K (C. Baukal 2005). Hence, any action that increase the flame temperature such as preheating air prior to mixing with the fuel has high possibility to increase the amount of thermal NO<sub>x</sub> generation.

Moreover, Zeldovich mechanism is the famous model for describing how thermal NO<sub>x</sub> can be formed. This model consists of three main reactions and two equilibriums as detailed from reactions (R2.1) to (R2.5). Furthermore, based on these reactions, thermal NO<sub>x</sub> will be less important if the temperature is less than 1,800 K because they require high E<sub>a</sub> to break the bonds between N<sub>2</sub>.



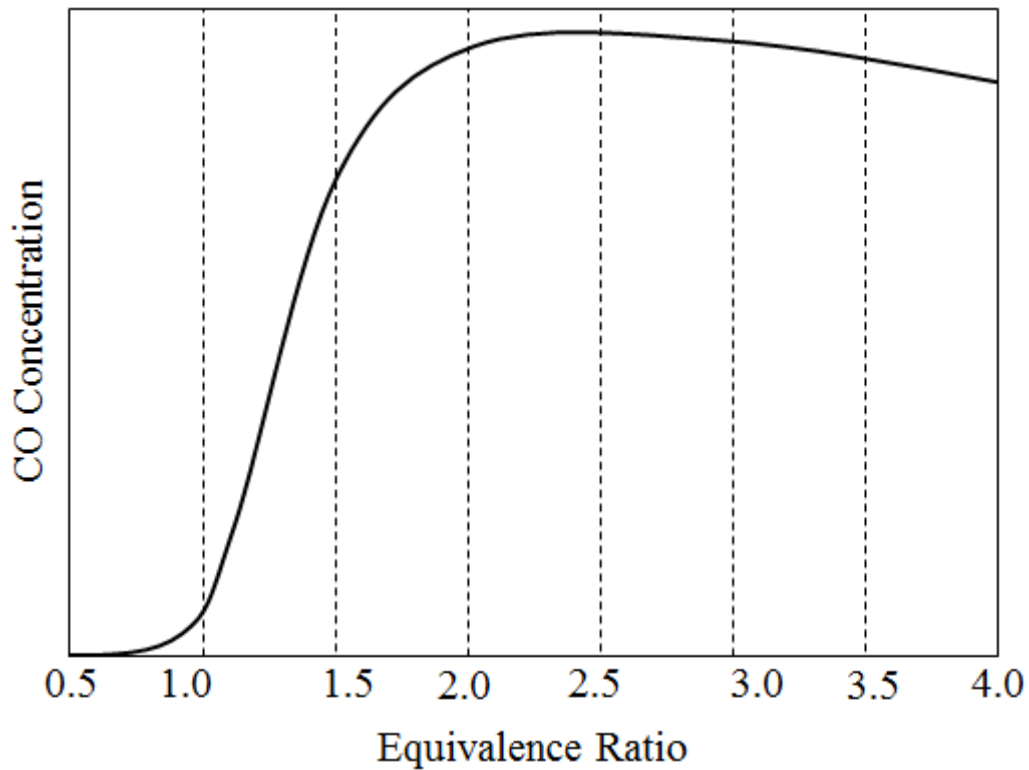
Third is the prompt mechanism. This is the rapid mechanism that changes the HC intermediates or radicals in the flame zone into hydrogen cyanide (HCN) and nitrogen hydride (NH) (Fenimore 1971). Then, HCN and NH could turn into NO<sub>x</sub> or so-called prompt NO<sub>x</sub> particularly when the combustion occurs at lower temperature and in fuel-rich condition.

### **2.3 NO<sub>x</sub> Reduction Technologies**

Nowadays, there are many technologies for NO<sub>x</sub> reduction because NO<sub>x</sub> have been ones of the main issues in pollution control for very long time. Each technique has its own advantages and disadvantages, and also, each technique has limitation depends on what aspect it is being considered such as economic, structure, etc. There are two main streams for NO<sub>x</sub> reduction technologies: combustion modifications and post-combustion treatments. Combustion modifications are techniques related to creating the environment in the primary combustion zone that could inhibit NO<sub>x</sub> formation. On the other hand, post-combustion treatments are techniques that mainly decrease NO<sub>x</sub> in the flue gas. Follows are examples of the current NO<sub>x</sub> reduction technologies.

### 2.3.1 Low Excess Air

Lowering the amount of excess air in the primary combustion zone where the flame temperature is highest could decrease the amount of  $\text{NO}_x$  formation because of lower  $\text{O}_2$  concentration. However, lower excess air could lead to flame instability problem because of changes in combustion aerodynamics. By the way, the major disadvantage of this technique is CO level increases when less air is introduced into the primary combustion zone because CO level increases when ER increases as illustrated by Baukal (2013) in Figure 8.



**Figure 8 – CO concentration versus ER (adapted from Baukal 2013)**

### 2.3.2 Flue Gas Recirculation

This technology draws a portion of flue gas from the stack or from the area around the burner to the primary combustion zone in order to dilute the local O<sub>2</sub> concentration. Moreover, flue gas recirculation can also decrease the flame temperature because flue gas has lower temperature than flame temperature. As a result of lower O<sub>2</sub> concentration and lower temperature, thermal NO<sub>x</sub> and fuel NO<sub>x</sub> are inhibited.

### 2.3.3 Staged Combustion

Staged combustion separates the combustion zone into two stages. The first stage is operated under fuel-rich condition. Only primary air and a portion of secondary air are consumed in the primary combustion zone. Since O<sub>2</sub> is deficient, fuel N reacts with each other and forms N<sub>2</sub> instead of NO. As a result, the combustion is incomplete, and NO<sub>x</sub> are decreased. Then, the remaining secondary air is mixed with the primary products in the second stage in order to complete the combustion process; thus, this stage is operated under fuel-lean condition. Because the second stage has lower temperature compared to the first stage. NO<sub>x</sub> mechanisms are inhibited.

### **Main burner equivalence ratio (ER<sub>mb</sub>) and overall equivalence ratio (ER<sub>oa</sub>)**

ER is generally defined as the ratio of the stoichiometric air-to-fuel ratio (A:F<sub>stoich</sub>) to the actual air-to-fuel ratio (A:F<sub>actual</sub>) as shown in equation (2.7). In case the amounts of fuel in A:F<sub>stoich</sub> and A:F<sub>actual</sub> are fixed, i.e. fixed heat input, ER can be adjusted by varying the actual amount of air (A<sub>actual</sub>) as expressed in equation (2.8).

$$ER = \frac{A:F_{stoich}}{A:F_{actual}} \quad (2.7)$$

$$ER = \frac{A_{stoich}}{A_{actual}} \quad (2.8)$$

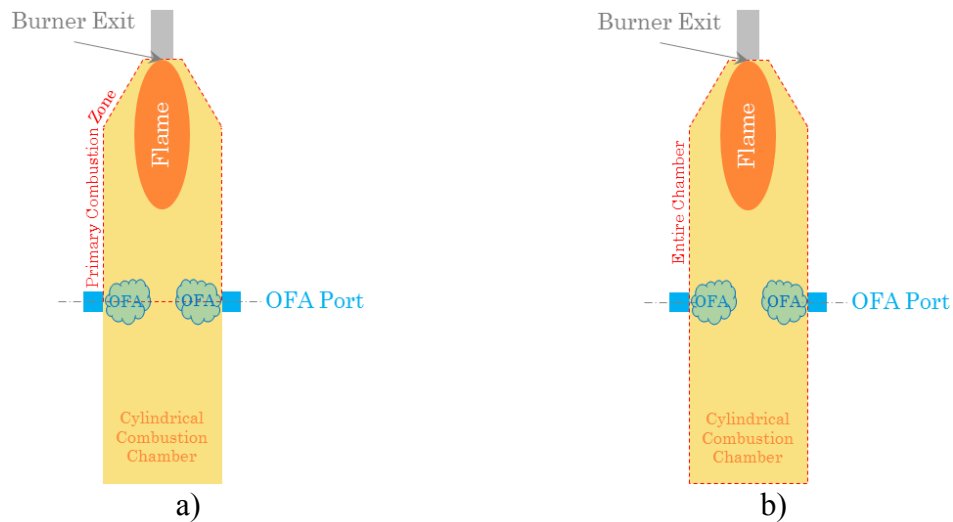
The  $ER_{mb}$  as defined in equation (2.9) is used to identify the ER inside the primary combustion zone which accounts for primary air ( $PA_{actual}$ ) and secondary air ( $SA_{actual}$ ) as illustrated in Figure 9-a.

$$ER_{mb} = \frac{A_{stoich}}{PA_{actual} + SA_{actual}} \quad (2.9)$$

On the other hand, the overall equivalence ratio ( $ER_{oa}$ ) as defined in equation (2.10) is used to indicate the ER inside the entire chamber. Thus, the control volume for calculating  $ER_{oa}$  will cover the entire combustion chamber as illustrated in Figure 9-b, and  $A_{actual}$  used in determining  $ER_{oa}$  is the sum of  $PA_{actual}$ ,  $SA_{actual}$  and the actual amount of OFA ( $OFA_{actual}$ ).

$$ER_{oa} = \frac{A_{stoich}}{PA_{actual} + SA_{actual} + OFA_{actual}} \quad (2.10)$$





**Figure 9 – Control volumes of: a) primary combustion zone and b) entire chamber**

#### 2.3.4 Swirl Burners

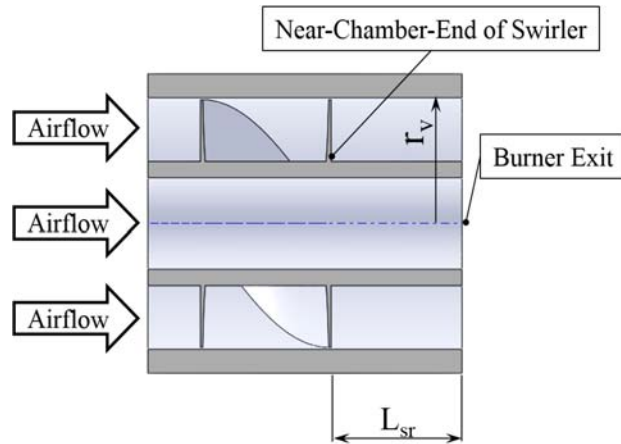
Swirler is attached to the burner in order to increase flame stability by creating recirculation zone beyond the burner. Typically, there are two types of swirler: straight vane swirler and profiled vane swirler. The straight vane swirler is easy to fabricate but has low efficiency whilst the profiled vane swirler has higher efficiency but is more difficult to construct (Syred and Beér 1974). Thus, the fabrication should concern the quality of work piece and also workmanship.

When the supplied air is swirled, it generates a bluff body at the center of the swirl. The pressure at the center of the swirl will be less than the surrounding. This causes pressure gradient and suction force that induce flow beyond the swirl into the center of the swirl. This is called the recirculation zone. The strength of the swirl could be determined by swirl number (SN). The criteria for determining the strength of the swirl are as follows (Tomeczek 1994):

$SN < 0.2$	-	Low swirl
$0.2 \leq SN < 0.6$	-	Moderate swirl
$SN \geq 0.6$	-	Strong swirl

The swirl burner could benefit not only the flame stability but also  $NO_x$  reduction. Bhimani, et al. (2013) mentioned that secondary air swirl number ( $SN'_{sa}$ ) at 1.4 could decrease  $NO_x$  more than  $SN'_{sa}$  of 1.0 when liquid fuel (canola oil) was fired because the stronger swirl could enhance mixing between air and fuel inside the combustion zone. However, the result will be opposite if the primary combustion zone is operated under fuel-lean condition. Thus, lower SN should be applied in case the primary combustion zone is fuel-lean condition (Cheng and Levinsky 2008).

Moreover, the swirl recess length ( $L_{sr}$ ) is the length measured from the near-chamber-end of the swirler to the burner exit as illustrated in Figure 10. The strength of the swirled flow generated by the swirler will gradually deteriorate along the  $L_{sr}$ . The typical ratio of  $L_{sr}$  to the radius of the swirler vane ( $r_v$ ) for low swirl burner ranges from one to four ( $1 < L_{sr}/r_v < 4$ ), and this ratio is less than one when it is high swirl burner (Cheng and Levinsky 2008).



**Figure 10 – Illustration of the swirl recess length**

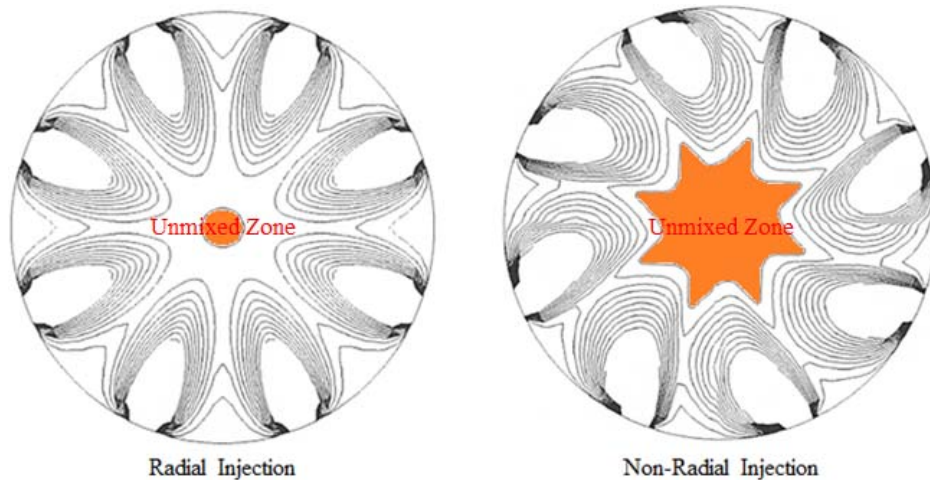
### 2.3.5 Low $NO_x$ Burners (LNB)

LNB system is considered as a cost-effective method for tackling  $NO_x$  emissions (McAdams, Reed and Itse 2001). Each unit of LNB consolidates many  $NO_x$  reduction technologies such as swirl burner, flue gas recirculation, staged combustion, etc. The amount of  $O_2$  used for operating LNB is normally low, so LNB system uses OFA to complete combustion. The facility for the current research is a 30  $kW_t$  low  $NO_x$  down-fired furnace that is located at Coal and Biomass Energy Laboratory (CABEL), Texas A&M University (TAMU). Details of its previous development could be found in Thien's (2002), Gomez's (2009), and Lawrence's (2013) papers.

### 2.3.6 Over-Fire Air (OFA) Injection

When the primary combustion zone is operated under fuel-rich condition, the amount of  $NO_x$  emissions is decreased. However, the amount of CO emissions will increase due to the incomplete combustion. Hence, the OFA is injected into the system in order to reduce CO content and to complete the combustion process.

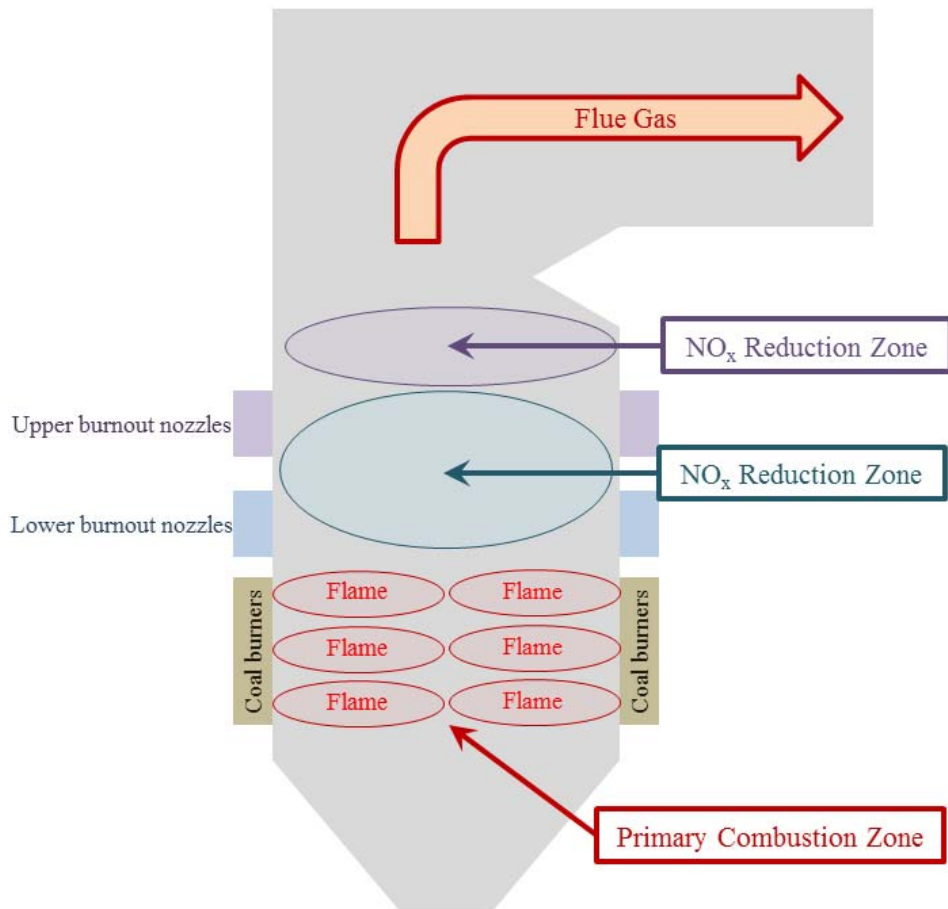
Direction of OFA injection is one of important factors that impact mixing characteristics between the gas flow from the main burner and the OFA. Vanormelingen and Van Den Bulck (1999) mentioned that non-radial OFA injection resulted in poorer mixing of the straight flow from the main burner and the OFA compared to radial OFA injection. Furthermore, the non-radial OFA injection could not penetrate into the center of the straight flow from the main burner because the non-radial OFA injection created a large unmixed zone (orange zone in Figure 11) throughout the cylindrical combustion chamber. Hence, the OFA should be injected in the radial direction.



**Figure 11 – Velocity profiles between radial and non-radial OFA injections (Adapted from Vanormelingen and Van Den Bulck 1999)**

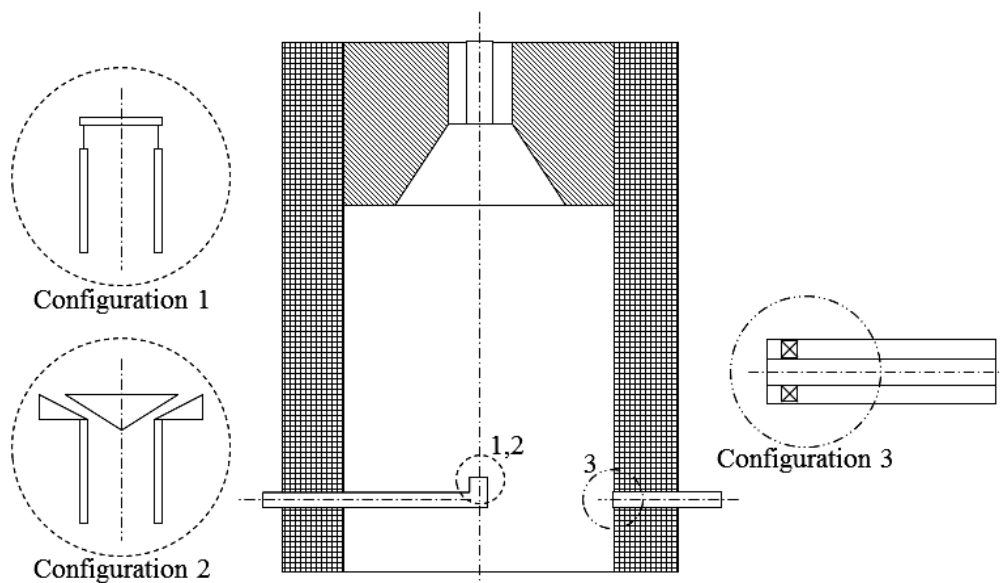
Location of the OFA injection and the volume flow rate of the OFA are interrelated (Fan, et al. 2010); for instance, in Figure 12, the amount of NO<sub>x</sub> emissions when the OFA is entrained into the combustion chamber through the upper burnout nozzles is less than when it is entrained through the lower burnout nozzles. When the

distance between the burner exit and the OFA nozzles increases, the amount of  $\text{NO}_x$  emissions decreases because the residence time inside the fuel-rich primary combustion zone increases (Ribeirete and Costa 2009). More residence time could decrease the amount of  $\text{NO}_x$  emissions under fuel-rich combustion process because the fuel N has more opportunity to bind with each other and form  $\text{N}_2$ .



**Figure 12 – Location of OFA injection (Adapted from Fan, et al. 2010)**

Ribeirete and Costa (2009) deduced that configurations of the OFA nozzles as shown in Figure 13 do not play the significant role on  $\text{NO}_x$  reduction unlike the direction of the OFA injection and the location of the OFA nozzles. Nonetheless, the amount of CO emissions still depends on the configuration of the OFA nozzles because the shape of the nozzles could impact the mixing characteristics between the OFA and the flow from the main burner.



**Figure 13 – Various types of OFA nozzles (Adapted from Ribeirete and Costa 2009)**

### 2.3.6 Co-Firing Blends of Coal and Dairy Biomass

Co-firing is one of the  $\text{NO}_x$  reduction techniques. Coal and DB are blended together prior to supplying them to the system. The reason that co-firing could decrease  $\text{NO}_x$  formation is the local  $\text{O}_2$  concentration in the primary combustion zone is decreased by VM released from biomass; hence,  $\text{NO}_x$  formations could be suppressed. However,

the amount of DB used in co-firing must be enough to cause such a decrease in O<sub>2</sub>; otherwise, introducing insufficient amount of DB particularly those with high N content will increase the amount of NO<sub>x</sub> emissions instead of lowering NO<sub>x</sub> (Li, et al. 2008).

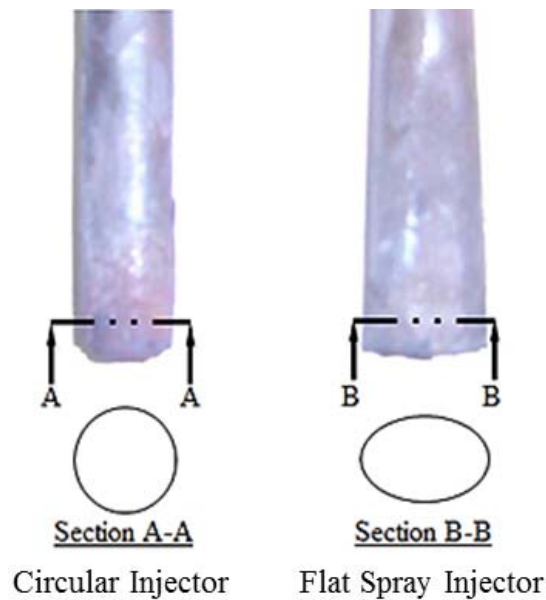
The effects of co-firing PRB and low-ash dairy biomass (LADB) on NO<sub>x</sub> reduction by using different types of swirler and air staging system were investigated by Gomez (2009) and Lawrence (2013). Gomez (2009) attached two auger blade swirlers inside secondary and tertiary air channels in order to generate swirled secondary and tertiary airflows. However, this design could not decrease NO<sub>x</sub> by using co-firing technique under fuel-lean combustion region; in contrast, NO<sub>x</sub> even increased by approximately 33% in rich combustion process.

Then, Lawrence (2013) changed the design of the swirler vane to helix vane, and relocated the tertiary air nozzle from the top of the furnace to 484 mm below the burner exit. The tertiary air or OFA was injected in the tangential direction to generate the OFA swirl for the purpose of enhancing mixing between the OFA and product gases from the main burner. However, by co-firing 90% of PRB and 10% of LADB on mass basis and using 20% of the combustion air as the OFA, NO<sub>x</sub> could be decreased by 16.5%.

### *2.3.7 Reburn*

Reburn technique can suppress NO<sub>x</sub> by injecting reburn fuel in the downstream of the combustion process. There are various types of reburn fuel such as CH<sub>4</sub>, DB, etc. Goughnour (2006) and Oh (2008) showed that DB could benefit reburn technology because using DB as the reburn fuel could reduce NO<sub>x</sub> from firing pure DB over 90% with the reburn equivalence ratio of 1.10.

Arumugam (2004) found that the amount of  $\text{NO}_x$  emissions could be reduced by using the flat spray outlet nozzles as the reburn fuel injectors instead of using the circular outlet nozzles. The configurations of the reburn fuel injectors are shown in Figure 14. He cited that the flat spray reburn fuel injectors could enhance the mixing between the reburn fuel and the main flow from the main burner. Thus, mixing between fuel and gases is one of the key factors in  $\text{NO}_x$  reduction.



**Figure 14 – Configurations of reburn fuel injector (adapted from Arumugam 2004)**

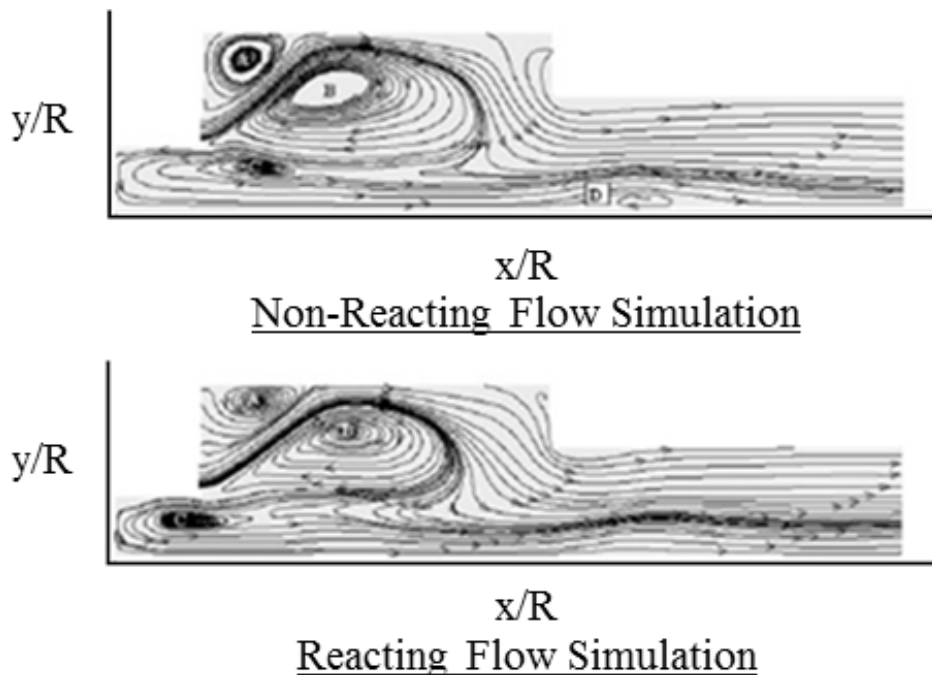
## 2.4 Flow Simulation

Computational Fluid Dynamics (CFD) program is one of useful tools to simulate flow characteristics. Generally, there are two main types of flow simulation. The first one is the NRF simulation, and the other one is the reacting flow simulation. As shown in Figure 15, the NRF characteristic inside a combustion chamber is similar to the



reacting flow characteristic whereas the reacting flow simulation could generate more elaborate contours than the NRF simulation (Orbay, et al. 2013). Nonetheless, the major disadvantage of the reacting flow simulation is it takes longer time than NRF simulation to obtain one result. To be more specific, the reacting flow simulation could take about six hours per simulation to obtain a result for a 2D model with a half of the primary combustion zone (M. Sami 2000). Without reactions, the simulation could run faster.

All in all, the number of flow characteristics generated by the NRF simulation is more than the number of flow characteristics generated by the reacting flow simulation within the same timeframe.



**Figure 15 – Flow characteristics from NRF and reacting flow simulations (Adapted from Orbay, et al. 2013)**

### 3. OBJECTIVE AND TASKS

The overall objective of the current research is to configure the LNB geometry and operating parameters that could lead to NO<sub>x</sub> emissions reduction with the aid of NRF simulation and to experimentally study the effects of change in operating parameters on NO<sub>x</sub> emissions. The essential tasks for achieving the main objective and supporting data interpretation are proposed as follows:

1. Obtain thermochemical properties of PRB and DB by:
  - 1 Sending two 225-gram samples of PRB and DB to Hazen Research Inc., for conducting proximate, ultimate and HV analyses.
  - 2 Developing the empirical chemical formulae of PRB and DB by using the results from the ultimate analysis and present additional properties of fuels
  - 3 Running TGA and DTG on PRB and DB in an inert gas and in an oxidizing gas by using TA instruments Thermal Analyzer SDT Q600 in order to acquire the following values:
    - Ignition temperature ( $T_{\text{ign}}$ ) of PRB and DB
    - Temperature at start of pyrolysis and end of pyrolysis
    - Temperature of pyrolysis at peak of volatile release ( $T_{\text{pyr, peak}}$ )
    - Kinetics constants
  - 4 Studying particle size distribution of PRB and DB by using sieving analysis and Rosin-Rammler distribution to find the distribution parameter ( $\alpha_{\text{dstr}}$ ) and characteristic particle size ( $d_{\text{ps, char}}$ )

2. Develop the fluid dynamic characteristic of LNB on SolidWorks program by running the NRF simulation on SolidWorks program regarding parametric studies detailed in the Experimental Procedure section to obtain:
  - 1 Velocity profiles of airflows inside the combustion chamber
  - 2 Approximate lengths of the recirculation zone (RZ) in various cases
  - 3 Mass fraction profiles of the primary air and the OFA from the front and top views
  - 4 Particle flow characteristics below the burner exit
  - 5 Particle Reynolds numbers ( $Re_p$ )
3. Modify LNB based on results from task 2.
4. Conduct co-firing combustion experiments to:
  - 1 Study the effects of varying main burner equivalence ratios ( $ER_{mb}$ ) and overall equivalence ratios ( $ER_{oa}$ ) by adjusting volume flow rates of secondary air and OFA on  $NO_x$  emissions.
  - 2 Obtain center and wall temperatures ( $T_c$  and  $T_w$  respectively) profiles along the vertical section of the combustion chamber.
  - 3 Determine burnt fraction (BF), fuel N conversion efficiency ( $N_{conv}$ ), and respiratory quotient (RQ) using exhaust gas analyses and/or chemical formulae.
5. Perform uncertainty analysis.

#### 4. NON-REACTING FLOW (NRF) SIMULATION

Flow Simulation, an add-in program in SolidWorks program, was used to run NRF simulation in various conditions in order to obtain the flow characteristics inside the combustion chamber. The NRF simulations at 300 K and 1,500 were conducted in order to simulate and predict the flow characteristics inside the combustion chamber.

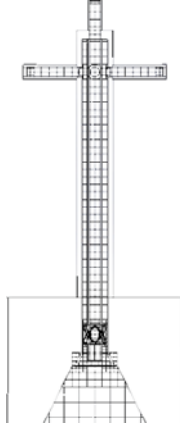
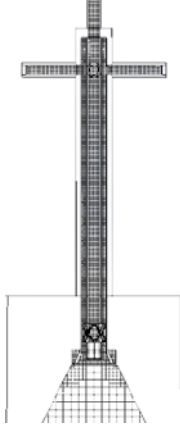
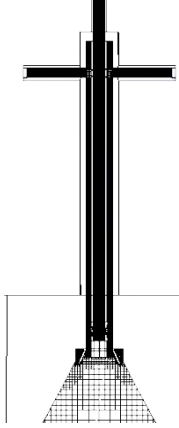
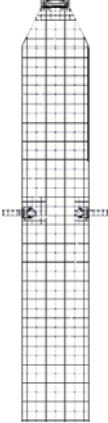
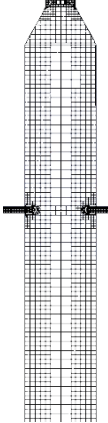
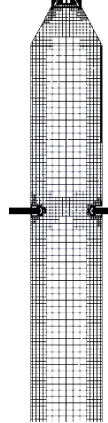

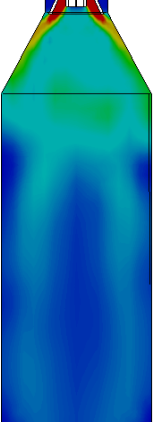
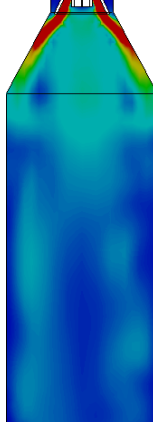
Another advantage of Flow Simulation is it can mix fluids inside the considering space up to 10 species. In addition, users can apply either pre-defined fluids in the engineering database of SolidWorks such as air, helium, blood, water, etc., or user-defined fluids. In the current research, three types of fluids e.g. primary air, secondary air, and OFA were defined based on properties of air. After finishing furnace modeling, all parameters and boundary conditions for running NRF simulation were specified on Flow Simulation as follows.

First, since the flow characteristics of the current research occurred inside the combustion chamber, the analysis type used was the internal analysis type. Second, the properties of primary air, secondary air, and OFA based on air properties were defined and saved in SolidWorks' engineering database as the user-defined fluids. In this step, if the users choose to use the pre-defined fluids instead of defining them manually, the users would not be able to distinguish the contour of mass fraction of primary air from the others. Third, the flow was specified as laminar and turbulent flow in order to know how flow could develop from the small flow areas such as the air inlet nozzles to the larger flow areas such as the combustion chamber. Fourth, the thermodynamic

parameters such as pressure and temperature of the flow were identified by using the same pressure and temperature as the conditions used in the actual 30 kW<sub>t</sub> LNB furnace. Fifth, the level of initial mesh which indicates mesh refinement was selected at level six where level one has the coarsest mesh refinement, and level eight has the finest mesh refinement. Table 6 shows the examples of the mesh refinement, the resolution of the result and the approximate processing time of each level of initial mesh. For the furnace model in the current research, level eight took approximately nine hours to obtain only one flow characteristic. Nonetheless, the resolution of flow characteristics at level three which had the least processing time was not sufficient for flow characteristic study. Hence, level six which had finer resolution than level three and used only one-tenth of the processing time of level eight was the most appropriate level in this research. Finally, the boundary conditions such as outlet pressure, mass flow rates of primary air, secondary air, OFA, etc., were applied at the inlet and outlet nozzles of the furnace model.

The results from NRF simulation show that the pre-existing LNB system could not generate symmetric RZ below the main burner. Moreover, OFA injected in the tangential direction could not penetrate into the center of the combustion chamber. As a result, the mixing between OFA and product gases occurred only around the wall of combustion chamber. So, the LNB system was developed with the aid of NRF simulation. Other significant results from NRF simulation are given in Appendix F.

**Table 6 – Examples of the mesh refinement, the resolution of the result and the approximate processing time of three levels of initial mesh**

Level of initial mesh	3	6	8
Approximate Processing time	3 minutes	54 minutes	540 minutes
Mesh refinement of the main burner			
Mesh refinement of the chamber part			
Resolution of the result			

## 5. EXPERIMENTAL FACILITIES AND PROCEDURES

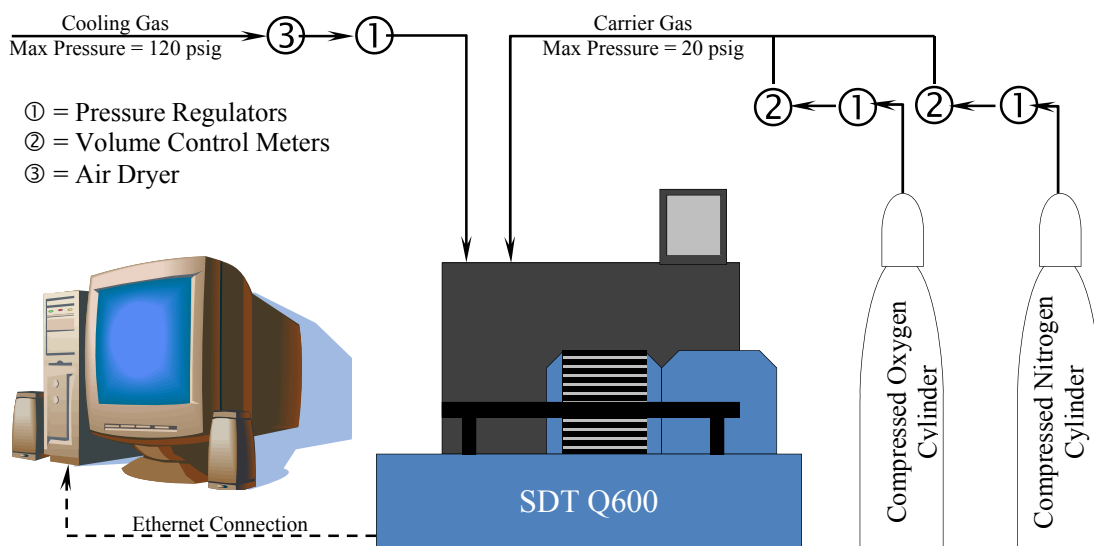
This section describes the experimental procedure required for completing the proposed tasks. Proximate and ultimate analyses were crucial tasks for obtaining the elementary composition and developing the chemical formulae of the fuels. Then, TGA and DTG studies were performed in order to determine  $T_{ign}$  and kinetics constants of PRB and DB for the pyrolysis process. Furthermore, particle size analysis by sieving was carried out in order to obtain distribution parameters and the characteristic particle sizes of PRB and DB. Also, the particle size distribution was used to simulate particle flow characteristics on SolidWorks program. The LNB design and modeling were used in developing NRF characteristics and burner fabrication. Finally, flue gas composition from co-firing blends of PRB and DB at various ER was measured by using E-Instruments E-8500 gas analyzer and was used in determining BF,  $N_{conv}$ , and RQ.

### 5.1 Thermochemical Properties of Coal and Dairy Biomass

The results of proximate and ultimate analyses were obtained from Hazen Research Inc., and used to determine the chemical formulae of PRB and DB. Since HV of fuel ( $HV_{fuel}$ ) is the sum of HV of VM ( $HV_{vm}$ ) and HV of FC ( $HV_{fc}$ ) as expressed in equation (5.1), the  $HV_{vm}$  for both PRB and DB can be determined. Furthermore, N, S and ash loading per unit energy input can also be determined.

$$HV_{fuel} = (HV_{vm} \times VM) + (HV_{fc} \times FC) \quad (5.1)$$

TA instruments Thermal Analyzer SDT Q600 is used in performing TGA and DTG. The setup of SDT Q600 is illustrated in Figure 16. SDT Q600 is connected to a computer via Ethernet connection, and signals from the analyzer are transferred to the TA Instruments controller program on the computer. The signals, then, are periodically collected on the computer's hard drive.

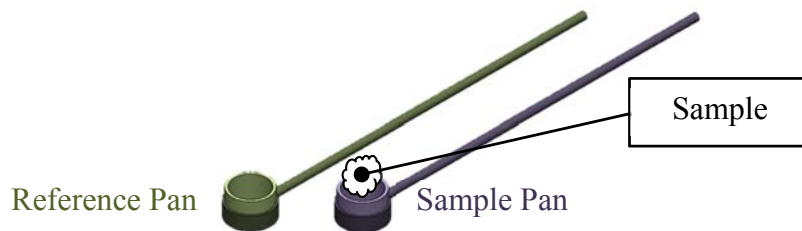


**Figure 16 – Schematic of SDT Q600 setup**

Ten milligrams of a sample are loaded into the sample pan, and the reference pan is left empty as shown in Figure 17. Each sample will be heated from room temperature to 1,273 K with the constant HR of 20 K per minute. SDT Q600 will simultaneously measure the remaining weight of the sample in the sample pan and temperature difference between the sample pan and the reference pan. The TGA results from both pyrolysis (inert medium as carrier gas) and combustion (air as carrier gas) processes will



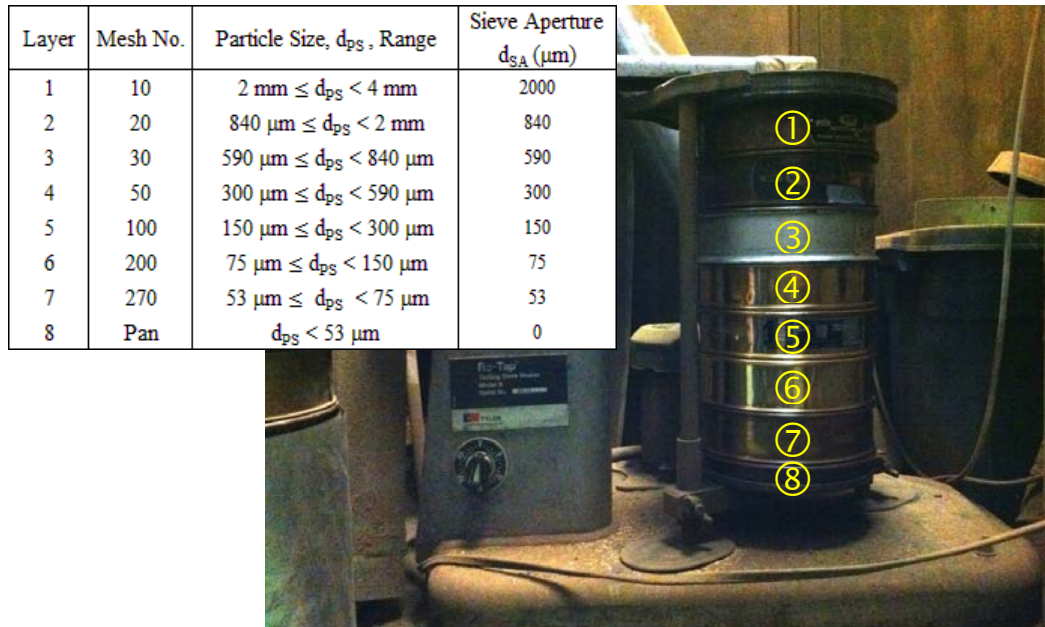
be plotted on the same chart by setting the x-axis as temperature and the y-axis as the weight percentage. The TGA and DTG curves of pyrolysis and combustion processes, then, can be used to determine  $T_{ign}$  of the sample as described earlier in Literature Review section. Meanwhile, the DTG results from pyrolysis can be used in estimating kinetics constants i.e. activation energy ( $E_a$ ), pre-exponential factor (B), and order of pyrolysis (n).



**Figure 17 – Illustration of reference and sample pans of SDT Q600**

Particle size analysis by sieving can be performed by loading one hundred grams of sample on the top sieve of a Ro-Tap model B testing sieve shaker and shaken as shown in Figure 18 for 30 minutes. There are seven layers of sieve and one layer of pan used in this study as shown in Figure 18. Sieves are arranged from top to bottom by the ascending mesh number; in other words, the least mesh number is located on the top of the stack, and the finest sieve is located at the bottom of the stack before the pan. The remaining sample on each layer will be collected and weighted. Then, Rosin-Rammler distribution will be used for determining the characteristic particle size of the sample. In other words, there is 63.12 percent of the sample that is less than or equal to  $d_{ps, char}$ . The

particle size distribution will also be used in particle flow studies on SolidWorks program.



**Figure 18 – Ro-Tap model B testing sieve shaker and sieve arrangement**

## 5.2 Fluid Dynamic Characteristic

The LNB of the pre-existing 30 kW<sub>t</sub> furnace at CABEL was modeled using SolidWorks program which has been developed by Dassault Systèmes SolidWorks Corporation. This program is one of 3D computer aided design (CAD) programs that can directly export data such as dimensions of a 3D model to a computer numerical control (CNC) cutting machine. Thus, SolidWorks program can help users create the real item just after the design has been finished.

The model was primarily based on the measured dimensions of the pre-existing LNB at CABEL. Then, the parameters listed in Table 7 were studied in order to ensure the stability of the airflows inside the combustion chamber. Effects of adjusting parameters in Table 7 on flow characteristics were investigated by using NRF simulation.

Fluid dynamic characteristic inside the combustion chamber plays the crucial role on enhancing flame stability and gas-particle mixing. In addition to the burner design and modelling, SolidWorks program has an add-in program called Flow Simulation which can mix fluids up to 10 species and simulate NRF characteristic as described in NRF Simulation section. Therefore, this add-in program can be used to investigate the results from varying each parameter given in Table 7 instead of running real experiments. This can optimize time and money in developing burners.

The NRF simulation was carried out at temperature of 300 K which is equal to room temperature because the furnace compressor draws air from the room temperature. As well, the NRF simulation was conducted at the flow temperature of 1,500 K in order to predict the flow characteristics at the estimated operating temperature.

Velocity and mass fraction profiles of airflows generated by SolidWorks Flow Simulation were used for justifying which component designs can yield the flow stability over the considering range of ER. Using velocity profile, the length of the RZ could be estimated by measuring the distance from the burner exit to the end of the RZ. Lastly, the  $Re_p$  can be determined by running the particle flow studies on SolidWorks Flow Simulation. Parametric studies are necessary to present the scope of work. Every

parameter that could impact the flow characteristics is listed and categorized as fixed or variable parameter as shown in Table 7. Some parameters such as height of the furnace, diameter of the combustion chamber and diameter of the primary air nozzle are kept as the pre-existing dimensions because of space and geometry limitation.

**Table 7 – Fixed and variable parameters for parametric studies**

No.	Parameter	Fixed	Variable
1	Fuel		
1.1	Type		✓
1.2	Higher heating value		✓
1.3	Coal-to-animal-waste ratio on a mass basis	✓	
2	Burner Components		
2.1	Swirler		
2.1.1	+ Vane radius	✓	
2.1.2	+ Profile of vane		✓
2.1.3	+ Hub radius	✓	
2.1.4	+ Swirl angle		✓
2.1.5	+ Swirl recess length		✓
2.2	Coal spreader		
2.2.1	+ Type		✓
2.2.2	+ Base width		✓
2.3	Burner diffuser		
2.3.1	+ Half angle	✓	
2.3.2	+ Length	✓	
2.3.3	+ Diameter	✓	
2.4	Fuel/primary air components		
2.4.1	+ Inside diameter of fuel/primary air nozzle	✓	
2.4.2	+ Outside diameter of fuel/primary air nozzle	✓	
2.5	Secondary air components		
2.5.1	+ Number of the inlet nozzles		✓
2.5.2	+ Inside diameter of the inlet nozzles		✓
2.5.3	+ Inside diameter of the main pipe	✓	
2.6	Over-fire air components		
2.6.1	+ Number of nozzles	✓	
2.6.2	+ Inside diameter of nozzles		✓
2.6.3	+ Configuration of nozzles		✓
2.6.4	+ Level of nozzles		✓
2.6.5	+ Orientation of nozzles		✓

**Table 7 Continued**

No.	Parameter	Fixed	Variable
3	Furnace Components		
3.1	Combustion chamber		
3.1.1	+ Height of the vertical section	✓	
3.1.2	+ Length of the horizontal section	✓	
3.1.3	+ Inside diameter	✓	
3.2	Quarl		
3.2.1	+ Half angle	✓	
3.2.2	+ Length	✓	
3.2.3	+ Diameter	✓	
4	Operating Conditions		
4.1	Heat input	✓	
4.2	Mass flow rate of fuel		✓
4.3	Main burner equivalence ratio		✓
4.4	Overall equivalence ratio		✓
4.5	Volume flow rate of primary air	✓	
4.6	Volume flow rate of secondary air		✓
4.7	Volume flow rate of over-fire air		✓
4.8	Pressure inside combustion chamber	✓	

### 5.3 Burner Modification

The LNB was modified based on the results from the fluid dynamic characteristic. A CNC machine was used to fabricate small and complicated parts such as swirler, coal spreader, etc. The other parts such as pipes and fittings were purchased by using ones available in market. Full details of burner modifications are given in LNB Modifications section.

### 5.4 Experimental Studies

The furnace used in the current research can be operated by firing pure coal or co-firing fuel blends. The diameter and thickness of the cylindrical combustion chamber is 152.4 mm and 50.8 mm respectively. The chamber consists of two sections. The first section is the vertical section whose height is 2.61 m. The second section is the horizontal section, and the distance from the center of the vertical section to the point

where the flue gas will be measured is 1.47 m. The horizontal combustion chamber was added for the purpose of increasing the residence time of the gas flow inside the chamber (B. D. Lawrence 2013). An induced draft fan (IDF) was installed at the top of the flue gas stack for safety purpose. While IDF is being operated, the pressure inside the combustion chamber becomes negative (less than the atmosphere). As a result, exhaust gas inside the chamber cannot leak out to the surrounding. The distance from the burner exit to the OFA nozzles is at set value.

PRB and DB were ground by using Vortec Impact Mill. The as-received PRB was directly loaded into the Schenck-AccuRate Mechatron gravity feeder prior to furnace preheating. For the fuel blends, PRB and DB were mixed in a bucket with the PRB-to-DB ratio of 90 to 10 on a mass basis prior to loading the fuel blend into the feeder.

Fuel particle dropped by the feeder mixes with the primary air inside the fuel/primary air nozzle before entering the combustion chamber. (This type of burner is so-called partially pre-mixed burner.) Theoretical energy input is fixed at 30 kW<sub>t</sub>; therefore, mass flow rate of the fuel depends on the as-received HHV of the fuel obtained from the HV analysis. The volume flow rate of the primary air will be maintained at 100 LPM. The swirled secondary air mixes with the fuel and the primary air at the burner exit. The ER<sub>mb</sub> (sum of primary air and secondary air) was varied from 1.00 to 1.10 in order to perform rich combustion in the primary combustion zone. Next, the OFA was injected into the combustion chamber below the burner exit in order to complete the combustion process. The ER<sub>oa</sub> (sum of primary air, secondary air, and

OFA) was varied from 0.85 to 1.05. The flue gas composition from firing PRB at the  $ER_{oa}$  of 0.85 without OFA injection was used as the base case for the present research.

The flue gas composition such as  $O_2$ ,  $CO_2$ ,  $CO$ , and  $NO_x$  from firing PRB and co-firing 90-10 PRB-DB blend at various ER was measured by using E-Instruments E-8500 gas analyzer. The values of  $NO_x$  and  $CO$  emissions were converted from ppm into g/GJ units in order to compare them with the limits set by EPA (210 g/GJ). Temperature at the center of the flow ( $T_c$ ) and temperature at the wall of the combustion chamber ( $T_w$ ) along the vertical section of the combustion chamber were measured by using type-K thermocouples. Lastly, BF,  $N_{conv}$ , and RQ were analyzed by using the data of flue gas composition.

The experimental procedure for operating the 30 kW<sub>t</sub> down-fired furnace in CABEL in the current research has four major steps: preheating the furnace, operating the furnace, varying ER while the furnace is being operated, and cooling down the furnace.

#### *5.4.1 Preheating the Furnace*

The steps to preheating the furnace by using natural gas are as follows:

1. Fully open the gate damper at the exhaust stack.
2. Open the observation port.
3. Arrange all thermocouples, so they measure the temperatures at the center of the combustion chamber.
4. Turn on the induced draft fan.
5. Check manometer.

Note: The pressure inside the combustion chamber must be negative, or the water level of the atmosphere side is lower than the chamber side. If the pressure is positive i.e. the water level of the atmosphere side is higher than the chamber side, the hot gas may vent out from the pilot burner port and cause harm to an operator.

6. Adjust the secondary air flow rate to 150 SLPM.

Note: Higher secondary air flow rate could blow off the flame from the pilot burner.

7. Check temperatures inside combustion chamber on LabVIEW program.
8. Record the initial temperatures inside the combustion chamber.
9. Light up the propane pilot burner.
10. Insert the propane pilot burner into the chamber at the lower observation port.
11. Open the valve of the natural gas line.
12. Adjust the volume flow rate of the natural gas to 20 SLPM.
13. Monitor temperatures inside the combustion chamber on LabVIEW program, again.
14. Close the valve at the propane tank while the temperature is sharply rising up.
15. Remove the propane pilot burner.
16. Close the observation port tightly.
17. Adjust the gate damper at the exhaust stack to set the pressure inside the chamber at -0.1 inch of water.
18. Calibrate the E-8500 gas analyzer.



19. Gradually increase the natural gas flow rate approximately 5 SLPM every 30 minutes while maintaining the secondary air flow rate at the equivalence ratio of 0.85 until the natural gas flow rate is 40 SLPM.
20. Monitor the exhaust O<sub>2</sub> at the end of the bottom of the exhaust stack.  
  
Note: The exhaust O<sub>2</sub> at the equivalence ratio of 0.85 while burning methane should be approximately 3.5%.
21. Wait until the peak temperature is approximately 1,400 K prior to beginning the next step.

#### *5.4.2 Operating the Furnace at the Target ER*

The procedure for operating the furnace with coal or fuel blends at the target ER is provided below:

1. Adjust the volume flow rate of the secondary to the target main burner ER.
2. Open the valve of the supplied OFA.
3. Set the pressure of OFA to 20 psi.
4. Adjust the volume flow rate of OFA air to the target overall ER
5. Check the peak temperature again.
6. Adjust the volume flow rate of the natural gas to maintain the peak temperature at 1,400 K.
7. Turn on the valve of the coal line.

8. Open the valve of the supplied primary air.

Note: The valve of the coal line must be opened before injecting the primary air; otherwise, the pressure force inside the coal line will be higher than the pipeline can withstand.

9. Set the pressure of the primary air at the pressure control valve to 20 psi.
10. Adjust the volume flow rate of the primary air to 100 SLPM.
11. Zero the natural gas flow rate.
12. Close the valve of the natural gas line to prevent coal accumulation inside the natural gas line.
13. Begin feeding coal at the target fuel flow rate depends on the HHV of the fuel.
14. Monitor flame temperature for the next 15 minutes to ensure that everything is in the steady state steady flow condition.
15. Monitor O<sub>2</sub> and CO<sub>2</sub> percentages of the exhaust gas by using the gas analyzer E-8500.
16. Adjust the flow rates of secondary air and OFA to reach the target O<sub>2</sub> percentage if operating under fuel-lean region or CO<sub>2</sub> percentage under stoichiometric or fuel-rich conditions.  
  
Note: The fuel mass flow rate might slightly drop while the feeder is feeding the fuel.
17. Begin recording the exhaust gas emissions at the bottom of the stack by using the gas analyzer E-8500.

18. Rearrange the position of the thermocouples to measure the wall temperatures 15 minutes after step 16.
19. Continue measuring the wall temperatures for 15 minutes.
20. Stop recording the exhaust gas emissions.

#### *5.4.3 Varying the ER*

Prior to changing from one ER to another ER, the combustion system should be adjusted to the initial condition (peak temperature = 1,400 K). The procedure that is given below is for varying the ER while the furnace is being operated:

1. Open the valve of the natural gas line.
2. Inject the natural gas into the furnace again by setting the flow rate at 20 SLPM as same as the beginning of the preheating step.
3. Shut down the fuel feeder.
4. Recalibrate the gas analyzer.
5. Purge the coal line by the primary air for 5 minutes.
6. Shut off the valve of the coal line.
7. Continue cooling down the furnace by using the natural gas until the peak temperature is 1,400 K.
8. Maintain the peak temperature at 1,400 K for 20 minutes.
9. Repeat step 1 to 20 in subsection 5.4.2.

#### *5.4.4 Cooling Down the Furnace*

The furnace should not be rapidly cooled down in order to avoid problems that might occur with furnace and burner components such as crack, material degradation, etc. The steps to cooling down the furnace are as follows:

1. Close the gas analyzer.
2. Shut down the fuel feeder.
3. Fully open the gate damper at the exhaust stack.
4. Purge the coal line by the primary air for 5 minutes.
5. Zero the primary air flow rate.
6. Close the valve of the coal line.
7. Adjust the volume flow rate of the secondary air to 300 SLPM.
8. Adjust the volume flow rate of the tertiary air to 100 SLPM.
9. Zero OFA flow rate two hours after the previous step.
10. Close the valve of the supplied OFA pipeline.
11. Continue cooling down by secondary air at 300 SLPM for one hour.
12. Open the observation port to entrain the surrounding air into the chamber.
13. Decrease the secondary airflow to approximately 40 SLPM.
14. Stop the LabVIEW program.

## 6. LOW NO<sub>x</sub> BURNER (LNB) MODIFICATIONS

LNB facilities at CABEL have been continuously developed since 2009, and various burner geometries have been applied in order to develop NO<sub>x</sub> reduction efficiency. This section shows the history of LNB modifications and how LNB components such as swirler, coal spreader, and piping system were modified according to the NRF simulation results.

### 6.1 Background

Gomez (2009) completed the construction of LNB system in CABEL as shown in Figure 19. The furnace design was basically based on the furnace with a conventional burner system that was constructed by Thien (2002). The main burner is a partially premixed burner (coal and primary air) with channels for swirled secondary and swirled tertiary airflows as shown in Figure 20. The tertiary air in this LNB system was also called the staged air. Both secondary and tertiary airflows were swirled in the clockwise direction (observing from top of burner) while they were passing through the auger-blade swirlers. The swirl numbers for the secondary airflow and the tertiary airflow were 0.54 and 0.53 (uncorrected) respectively. This burner system with tertiary air injection was able to decrease NO<sub>x</sub> emissions by 12% in the fuel-lean region compared to the system without the tertiary air injection.

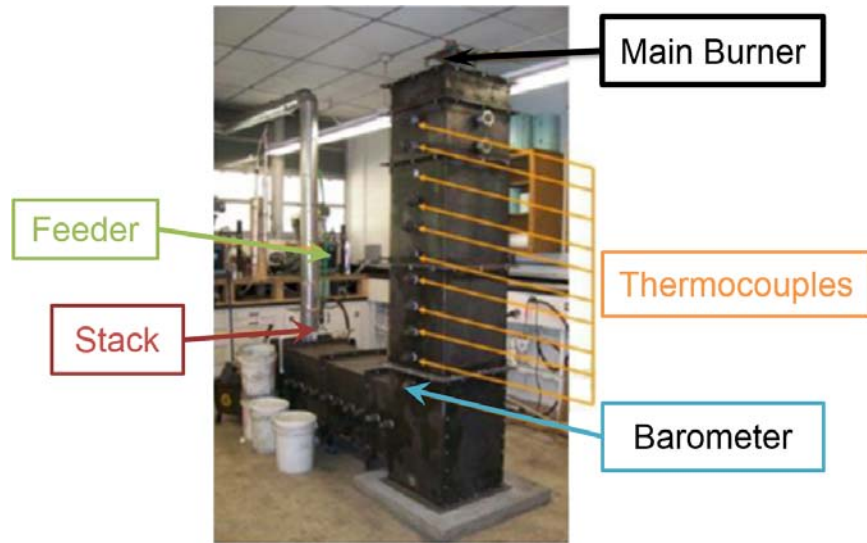


Figure 19 – The 30kW<sub>t</sub> down-fired furnace in CABEL (adapted from Gomez 2009)

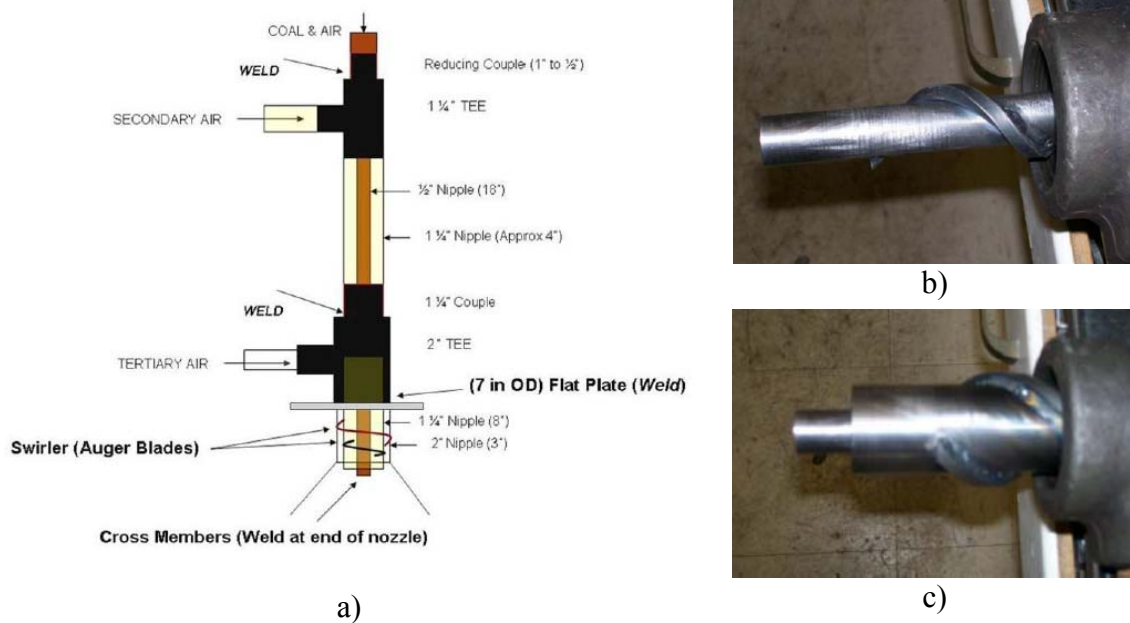
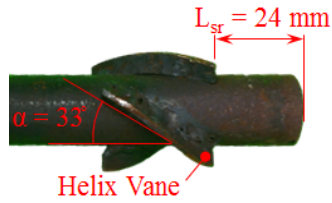


Figure 20 – Partially premixed burner (adapted from Gomez 2009): a) an illustration of old partially premixed burner, b) the auger blade attached to the outer surface of the fuel/primary air nozzle as the swirler for secondary air, and c) the auger blades attached to the outer surface of the secondary air nozzle as the swirler for tertiary air

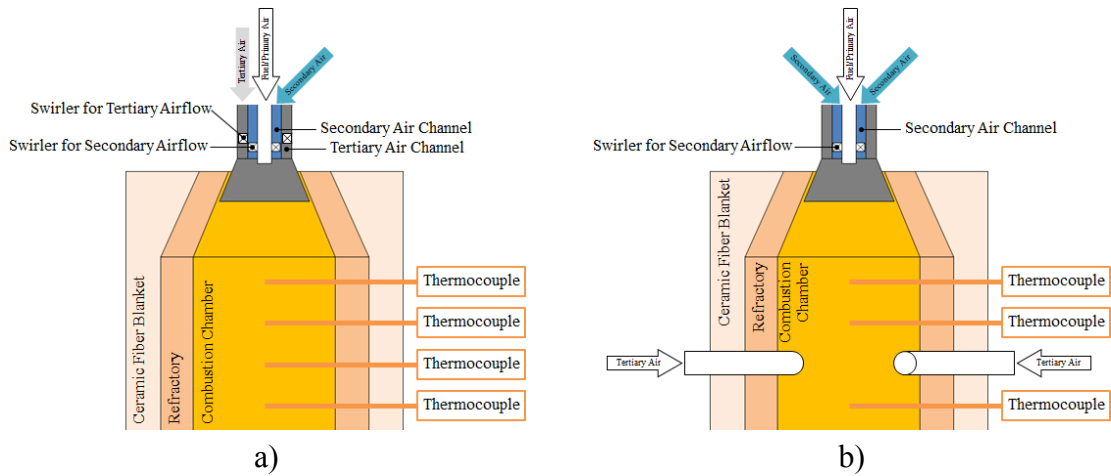
Then, Lawrence (2013) changed the type of the swirler and the air staging system. The swirler for the secondary air was changed from the auger-blade type to the helix-vane type as shown in Figure 21 with the uncorrected swirl number of 0.7, and the tertiary air nozzle was relocated from the top of the furnace as shown in Figure 22-a to the point that was below the main burner exit as shown in Figure 22-b and renamed as over-fire air (OFA). Furthermore, OFA was injected in the tangential direction downstream of main burner through two pieces of 1/4" 90-degree galvanized steel elbow as shown in Figure 23 in order to generate OFA swirl. The swirl generated by OFA (OFA swirl) had the same direction of rotation as the swirl generated by the flow from the main burner, and OFA swirl was supposed to enhance the mixing between OFA and the swirling flow from the main burner. Indeed, the staged air was supposed to mix with the mixture of combustion products from the main burner combustion zone. Some of his experimental results from firing pure PRB and 90-10 PRB-LADB given in Table 8 showed that NO<sub>x</sub> could be decreased by increasing ER<sub>oa</sub> and utilizing staged air; however, firing 90-10 PRB-LADB generated higher NO<sub>x</sub> level in lean region.

**Table 8 – Results of firing PRB and 90-10 PRB-DB by using Lawrence’s model (excerpted data from B. D. Lawrence 2013)**

Fuel type	ER <sub>oa</sub>	% OFA	NO <sub>x</sub> (g/GJ)
PRB	0.85	0	381
	0.95	0	304
	0.95	20	189
90-10 PRB-LADB	0.85	0	478
	0.95	0	395
	0.95	20	230



**Figure 21 – Pre-existing helix-vane swirler with the swirl angle ( $\alpha$ ) of 33 degrees and the swirl recess length ( $L_{sr}$ ) of 24 mm**



**Figure 22 – LNB system setups (adapted from Barth 2009): a) Gomez's setup, and b) Lawrence's setup**



**Figure 23 – Two pieces of 1/4" 90-degree galvanized installed inside the combustion chamber (adapted from Barth, 2009)**



However, according to Seebold (2013), the typical targets of NO<sub>x</sub> reduction systems are approximately 50% for LNB systems, and approximately 70% for ultra-low NO<sub>x</sub> burner (ULNB) systems with extremely fine ground coal. The current research is an attempt to develop a LNB system for the 30kW<sub>t</sub> furnace in CABEL fired with a blend of PRB and DB so that the NO<sub>x</sub> reduction could reach the target at 50% and also help carbon reduction because DB is a carbon neutral energy source. The following subsections describe the procedures and modifications performed in developing the LNB system for this furnace.

## **6.2 Pre-Existing LNB Components Measurement and Inspection**

The pre-existing LNB components modified by B. D. Lawrence (2013) were disassembled in order to measure the dimensions of the pre-existing burner. The measured dimensions of each part are given in Table 9. Figure 24 to Figure 27 illustrate components of LNB system and symbols defined in Table 9. All of the dimensions were used in furnace modeling and NRF simulations on SolidWorks program as described in NRF Simulation section.

Next, conditions of furnace components such as swirler, quarl, burner diffuser, etc., were thoroughly inspected. The inspection is necessary for modifications and materials selection because some materials or geometries may be suitable for some combustion applications but not suitable for some other applications. The following subsections show significant results from the inspection.

**Table 9 – Dimensions of the pre-existing LNB furnace components**

Components of	Symbol	Unit	Measured Value
<b>Swirl Burner</b>			
<u>Fuel/Primary Air Nozzle</u>			
- Inner radius	$r_{pa,i}$	mm	7.75
- Outer radius	$r_{pa,o}$	mm	10.25
<u>Main Secondary Air Nozzle</u>			
- Inner radius	$r_{sa,i}$	mm	17.75
- Outer radius	$r_{sa,o}$	mm	20.25
<u>Secondary Air Inlet Nozzle</u>			
- Nominal pipe size	NPS	Inch	1
- Schedule	Sch	-	40s
<u>OFA Nozzles</u>			
- Nominal pipe size	NPS	Inch	0.375
<u>Swirler</u>			
- Vane radius	$r_v$	mm	16.25
- Hub radius	$r_h$	mm	10.25
- Swirl angle	$\alpha$	Degree	33
- Swirl recess length	$L_{sr}$	mm	24
- Swirl number of secondary air	$SN'_{sa}$	-	0.54
<u>Coal Spreader</u>			
- Type	-	-	Fin
- Base width	-	mm	1
- Half angle	$\theta_{cs}$	Degree	0
<b>Combustion Chamber</b>			
- Inside diameter	$D_{chb}$	mm	152.4
- Thickness of refractory	$Thk_{ref}$	mm	50.8
- Thickness of insulation	$Thk_{ins}$	mm	50.8
<b>Other Components</b>			
- Burner diffuser half angle	$\theta_{bd}$	Degree	22.5
- Quarl half angle	$\theta_{quarl}$	Degree	26.5

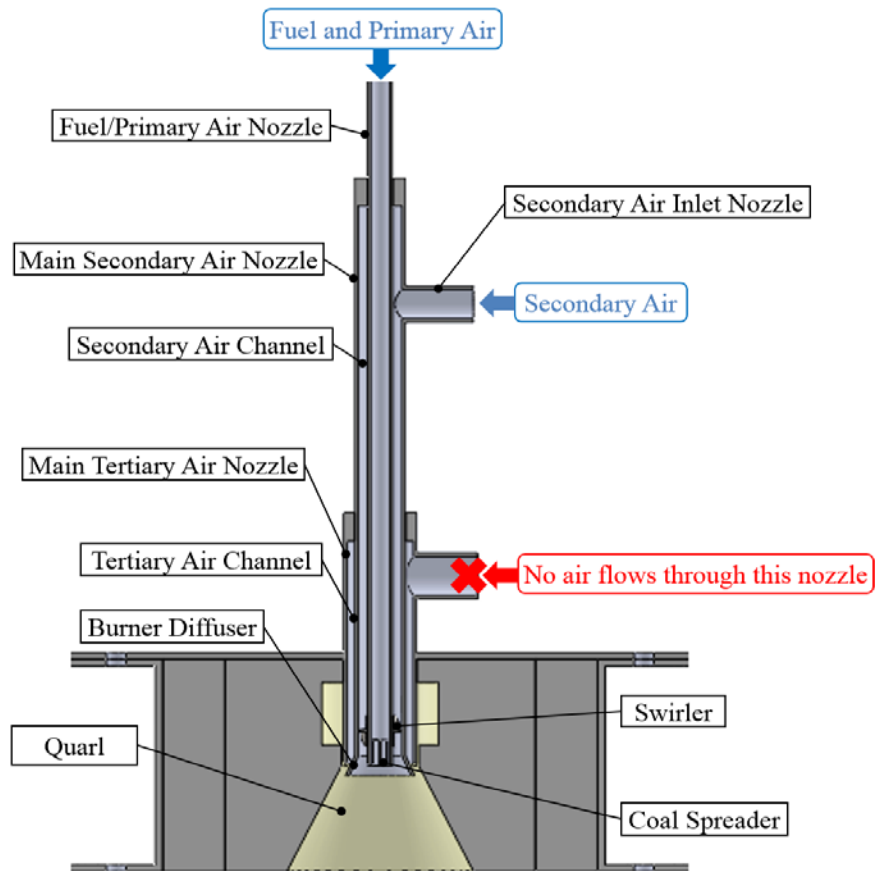


Figure 24 – Illustration of the pre-existing LNB furnace components

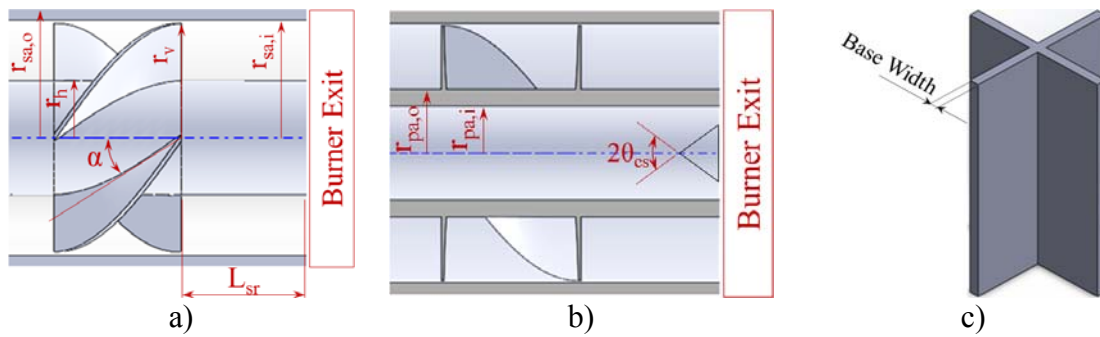


Figure 25 – Illustration of: a) swirl burner components, b) cross-sectional view of a swirl burner, and c) base width of a coal spreader

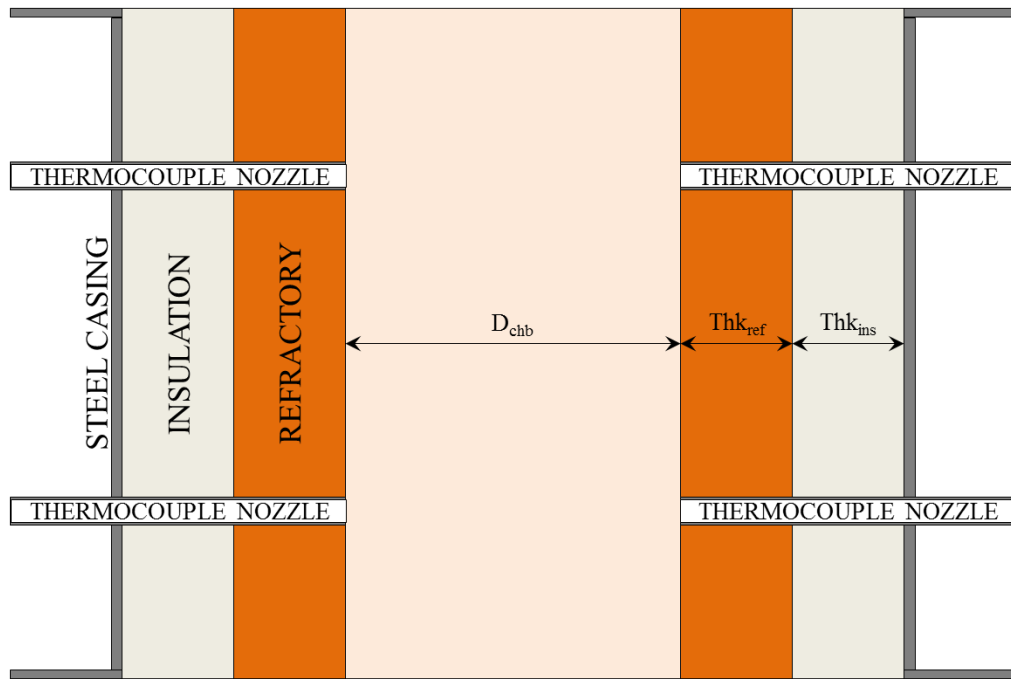


Figure 26 – Illustration of combustion chamber components

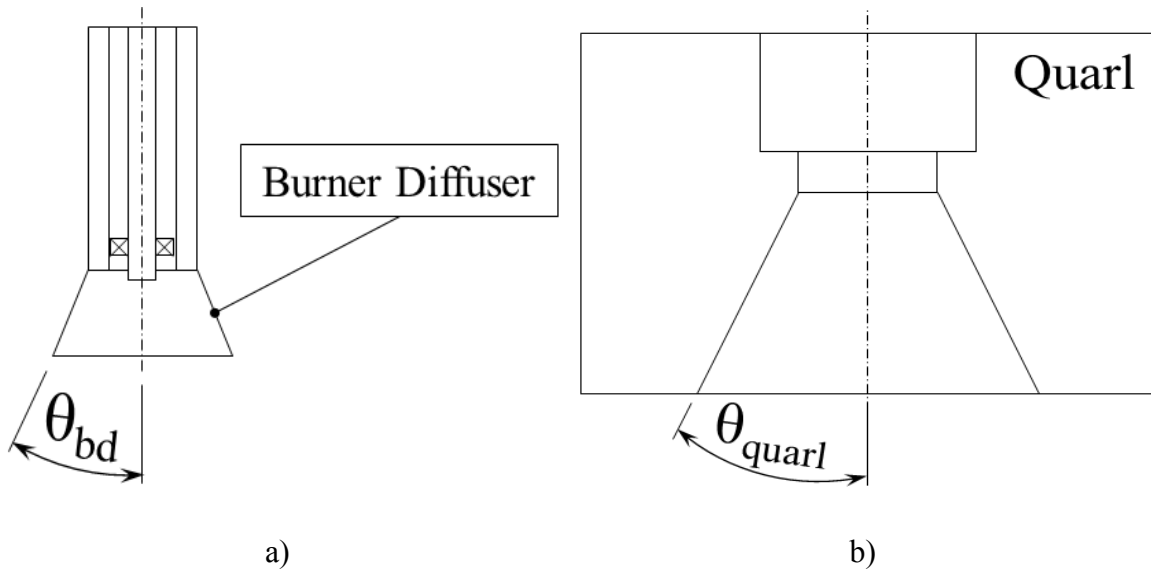
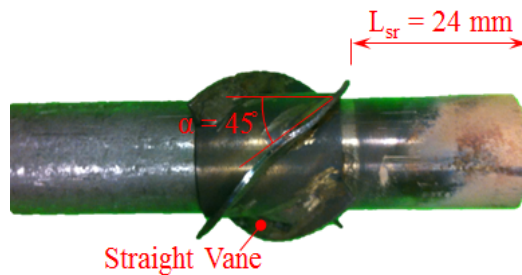


Figure 27 – Illustration of: a) burner diffuser half angle ( $\theta_{bd}$ ) and b) quarl half angle ( $\theta_{quarl}$ )

### 6.2.1 Pre-Existing Swirler

The pre-existing swirler, as shown in Figure 21, consisted of four helix vanes attached to the outer surface of the fuel/primary air nozzle with the mean measured swirl angle ( $\alpha$ ) of 33 degrees. This swirler generated the swirling flow in the clockwise rotation (observing from the top view) with the secondary air swirl number,  $SN'_{sa}$ , of 0.7 (B. D. Lawrence 2013). This  $SN'_{sa}$  was identical to  $SN'_{sa}$  of Thien's (2002) swirler which had the straight vane with  $\alpha$  of 45 degrees as shown in Figure 28. The swirl recess lengths ( $L_{sr}$ ) of both burners were 24 mm.

The major disadvantage of small scale helix-vane swirlers is they are difficult to be fabricated. Each helix vane must have the same profile and angle which require high quality of tool and workmanship. For instance, the welding seams of the pre-existing helix-vane swirler had bad surface finishing. The welding seams had many pores, and their roots were not smooth as shown in Figure 29. This problem might affect flow characteristics of the secondary airflow. Hence, a new straight-vane swirler was fabricated instead of using the helix-vane type. The details of swirler design are discussed in next subsection.



**Figure 28 – Straight-vane swirler with  $\alpha$  of 45 degrees and  $L_{sr}$  of 24 mm**



**Figure 29 – Rough welding seams of the pre-existing helix-vane swirler**

### 6.2.2 Pre-Existing Coal Spreader

The pre-existing coal spreader was a fin type and was attached to the inner surface of the fuel/primary air nozzle as shown in Figure 30-a, for the purpose of distributing fuel particle uniformly across the cross-sectional area prior to entering the RZ, whereas Thien (2002) used a v-shaped coal spreader as shown in Figure 30-b. Flow simulation was carried out to indicate which type of the coal spreaders could distribute particle into the combustion chamber more uniformly. The conditions and results of the flow simulation are given in next subsection.



a)



b)

**Figure 30 – Coal spreaders: a) fin-type coal spreader (consists of two thin plates), and b) v-shaped coal spreader**

### 6.2.3 Pre-Existing OFA Nozzles

The outlet nozzles of OFA, as shown in Figure 23, were melted as shown in Figure 31, i.e. elbows for tangential injection melted away. This problem might stem from material-related issues. Because the nozzles were made by using ASTM 197 (standard for malleable irons) whose melting temperature is approximately 1,477 K (OnlineMetals.com), it is possible that the galvanized steel nozzles could not withstand in high temperature gas flow.



**Figure 31 – Melted OFA outlet nozzles**

### 6.3 Modifications of LNB Components

The problems listed above were solved by modifying some components according to the simulation results. Moreover, the material of the components that expose to high temperature, i.e. components inside the combustion chamber, was changed from galvanized steel to stainless steel 316 whose melting temperature is approximately 1,644 K (AK Steel Corporation 2013) in order to prevent melting problem of components. Both design and measured dimensions of the modified LNB components are given in Table 10.

**Table 10 – Dimensions of the modified LNB components**

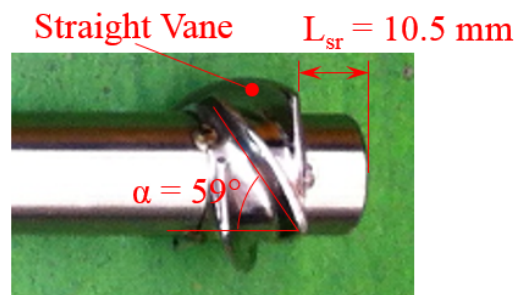
Components of	Symbol	Unit	Design	Measured
<b>Swirl Burner</b>				
<u>Fuel/Primary Air Nozzle</u>				
- Inner radius	$r_{pa,i}$	mm	7.88	8.25
- Outer radius	$r_{pa,o}$	mm	10.25	10.25
<u>Main Secondary Air Nozzle</u>				
- Inner radius	$r_{sa,i}$	mm	17.54	17.65
- Outer radius	$r_{sa,o}$	mm	21.1	21.1
<u>Secondary Air Inlet Nozzle</u>				
- Nominal pipe size	NPS	Inch	0.5	0.5
- Schedule	Sch	-	80s	80s
<u>OFA Nozzles</u>				
- Nominal pipe size	NPS	Inch	0.5	0.5
- Schedule	Sch	-	40s	40s
<u>Swirler</u>				
- Vane radius	$r_v$	mm	16.25	16.15
- Hub radius	$r_h$	mm	11.25	11.15
- Swirl angle	$\alpha_v$	Degree	60	59
- Swirl recess length	$L_{sr}$	mm	10.25	10.5
- Swirl number of secondary air	$SN'_{sa}$	-	1.48	1.42
<u>Coal Spreader</u>				
- Type	-	-	V-Shaped	V-Shaped
- Base Width	-	mm	3	3
<b>Other Components</b>				
- Burner diffuser half angle	$\theta_{bd}$	Degree	22.5	22.5

### 6.3.1 Swirler Modification

The swirler had two major changes. First, the profile of the swirler was changed from the helix vane to the straight vane as shown in Figure 32, and it was fabricated by using machining method in order to prevent rough welding seams as mentioned earlier.



Second,  $\alpha_v$  was changed from 33 degrees to 59 degrees, so  $SN'_{sa}$  calculated by using the measured dimensions given in Table 9 and Table 10 was increased from 0.54 to 1.42. Actually, the overall swirl number is not constant because it must consider the momentums of both primary and secondary airflows. The details of swirl number calculation for various cases are given in Appendix G.



**Figure 32 – Modified swirler**

### 6.3.2 Coal Spreader Modification

The type of coal spreader was changed from the fin type to the v-shaped type because the v-shaped coal spreaders can distribute fuel particle more uniformly compared to the fin-type coal spreaders especially when the particle size is large according to the particle flow simulation results shown in Appendix H. Moreover, the axial velocity of fuel/primary air flow exits from the v-shaped coal spreaders is less than from the fin-type coal spreaders in case the base width is kept constant because the fuel/primary air velocity vector exits from the v-shaped coal spreaders could be separated into axial and tangential directions; meanwhile, the fuel/primary air velocity vector exits from the fin-type coal spreaders has only the axial direction. As a result, the

axial flow velocity that exits from the v-shaped coal spreaders is less than from the fin-type ones. Thus, the v-shaped coal spreaders are superior to the fin-type ones.

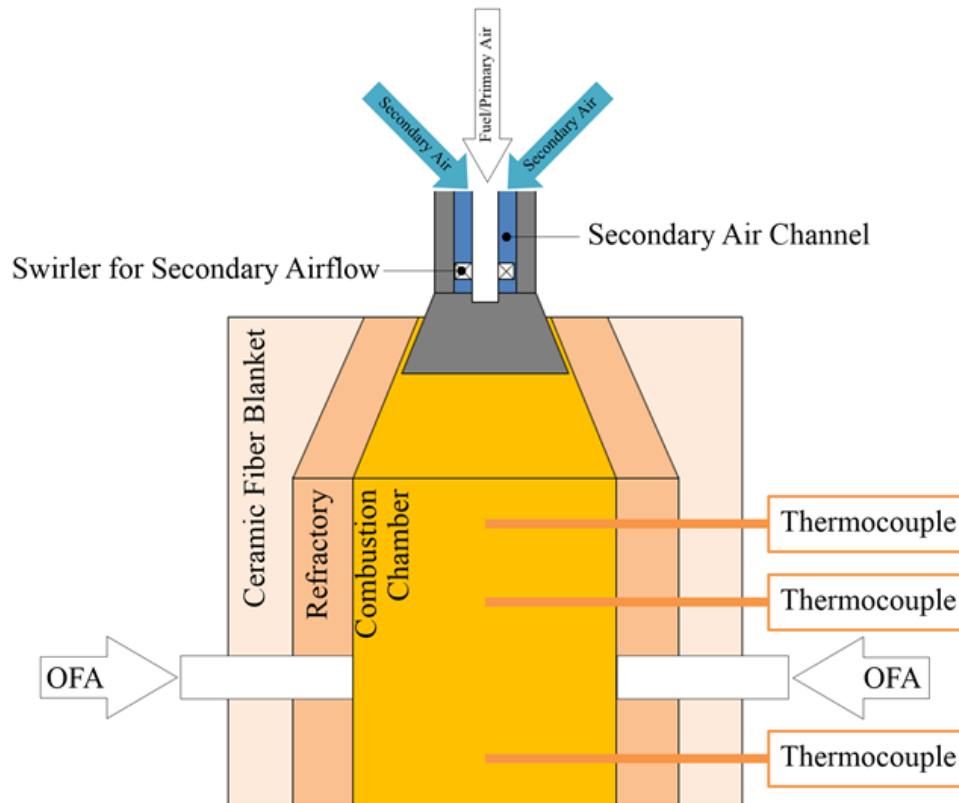
Additionally, the flow velocity is increased when the fuel/primary air passes through the coal spreaders because the effective flow area is reduced. For instance, from Table 11, when the effective flow area is decreased from 188.69 mm<sup>2</sup> to 158.69 mm<sup>2</sup> (decreased by 15.9%), the axial flow velocity is increased from 8.83 m/s to 10.50 m/s (increased by 18.9%). The summary of modification included the velocity components before and after fuel/primary air passes the coal spreader is given in Table 11.

**Table 11 – Summary of coal spreader parameters before and after modification**

Description	Symbol	Unit	Before Modification	After Modification
<b>Burner Components</b>				
<u>Coal spreader</u>				
- Type	-	-	Fin	V-Shaped
- Base width	-	mm	1	3
- Half angle	$\theta_{cs}$	Degree	0	45
<u>Fuel/primary air nozzle</u>				
- Inner radius	$r_{pa,i}$	mm	7.75	8.25
- Flow area				
• Before the coal spreader	-	mm <sup>2</sup>	188.69	213.82
• After the coal spreader	-	mm <sup>2</sup>	158.69	123.82
<b>Velocity Components</b>				
<u>Before the coal spreader</u>				
- Axial velocity	$v_{ax}$	m/s	8.83	7.79
- Tangential velocity	$v_{tan}$	m/s	0	0
<u>After the coal spreader</u>				
- Axial velocity	$v_{ax}$	m/s	10.50	9.52
- Tangential velocity	$v_{tan}$	m/s	0	9.52

### *6.3.3 OFA System Modification*

The air staging system was modified based on the NRF simulations at 300 K and 1,500 K given in Appendix J. The modified main burner and OFA setup is illustrated in Figure 33. The location of the OFA outlet nozzles is kept same as before. The nominal diameter of OFA nozzles was increased from 9.525 mm (0.375 inch) to 12.7 mm (0.5 inch) in order to decrease the exit velocity of the OFA from the outlet nozzles. The simulation results given in Appendix J show that a fraction of OFA goes up toward the recirculation zone (RZ) and the other goes down joining the products from main burner. This phenomenon could result in reducing the residence time of the primary combustion zone because the OFA could mix with the incomplete combustion products from the main burner; it also reduces the residence time for combustion. Thus, reducing the OFA velocity leads to decrease of lateral flow momentum at fixed mass flow rate. Hence, the enlarged diameter is anticipated to decrease the effect of this phenomenon. In other words, this will reduce the amount of upward flow.



**Figure 33 – Main burner and OFA setup after modification**

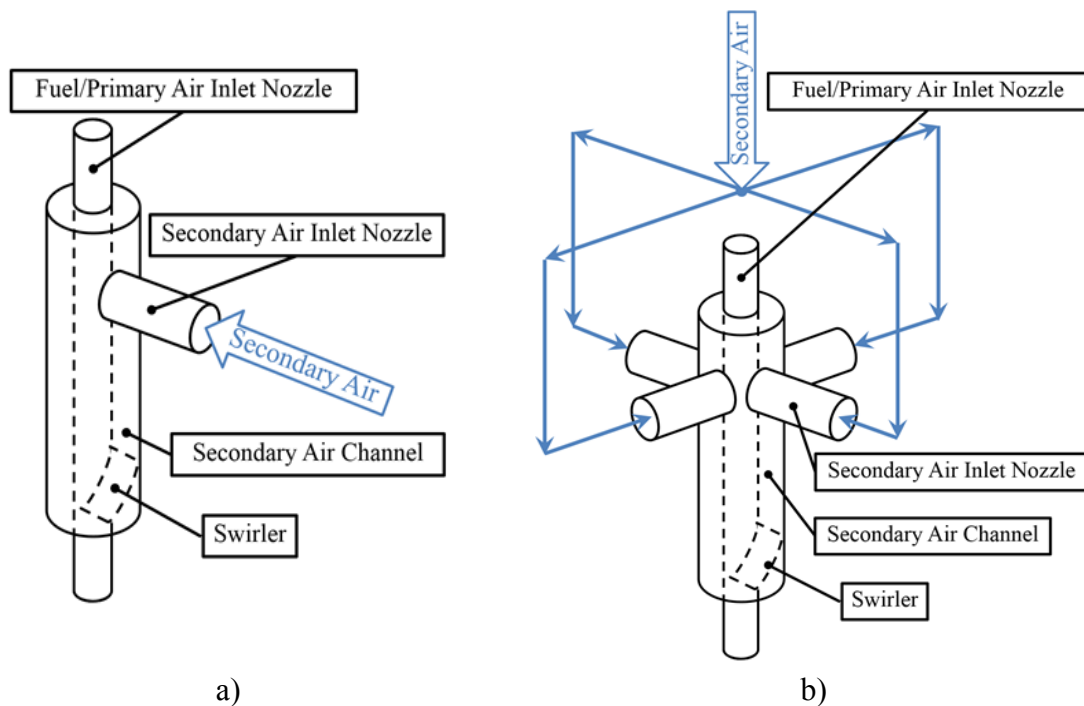
#### *6.3.4 Piping System Modification*

The piping system was modified in order to assure that the secondary air and OFA were uniformly distributed into the secondary channel and the combustion chamber respectively. The details of piping modification are as follows.

#### **Secondary air piping system**

Primarily, the secondary air system had only one inlet nozzle as illustrated in Figure 34-a. However, the simulation results given in Appendix F show that the secondary airflow could not fully develop along the pipe length and lead to the asymmetric recirculation zone problem. In addition, the pipe length cannot be extended

because of the height limitation of the furnace inside the laboratory. Therefore, the number of the secondary air inlet nozzles was increased from one to four regarding the simulation results. The setup of the secondary air system for the present setup is illustrated in Figure 34-b. This setup would evenly distribute the secondary air into each pipeline. Then, the modified secondary air piping system was attached to the main burner as shown in Figure 35.



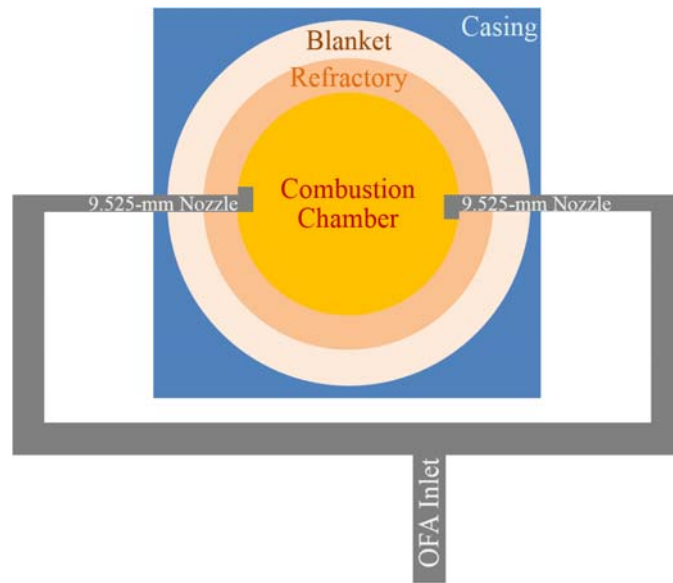
**Figure 34 – Piping diagrams of secondary air system: a) Lawrence’s setup, and b) present setup**



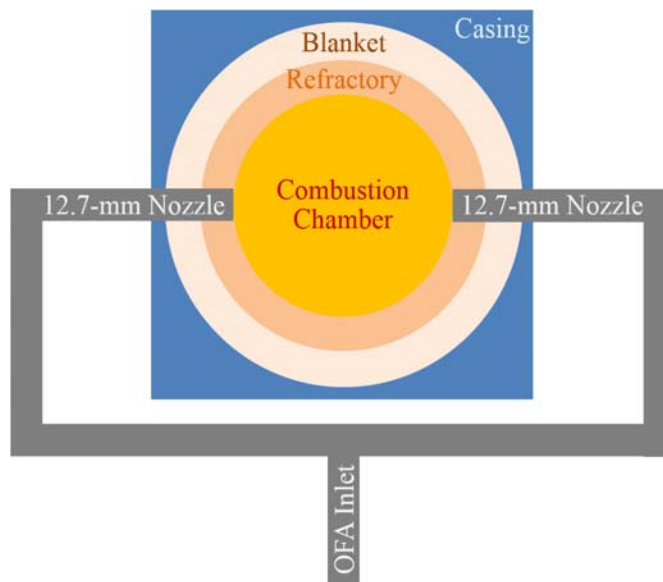
**Figure 35 – The modified secondary air piping system attached to the main burner**

### **OFA piping system**

The previous tertiary air inlet was not symmetrically located. It was offset to the right side of the system as shown in Figure 36-a. Thus, air distribution is non-symmetric in the two branches. So, the OFA inlet was relocated to the center of the main pipe as shown in Figure 36-b in order to assure that the tertiary airflow was evenly distributed to the left and right branches while the furnace was being operated. Figure 37 shows the real piping system of the tertiary air after modification.



a)



b)

**Figure 36 – Top view of the piping diagram for the OFA system: a) previous system, and b) present system**



**Figure 37 – Current piping system of the air staging in the LNB**



## 7. RESULTS AND DISCUSSION

This section mainly shows the results and discussion on fuel analyses, NRF characteristics and flue gas analysis. All of the results will be used to explain what the characteristics of fuels are, why co-firing PRB and DB can decrease  $\text{NO}_x$ , what is the optimum particle size, and what are the operating conditions that can pass EPA limit.

### 7.1 Fuel Analyses

The properties of PRB and DB were obtained by using proximate and ultimate analyses. The results from proximate and ultimate analyses could be used in developing the empirical formulae of fuels as detailed in Appendix A. Furthermore, the results could also be used to estimate the stoichiometric air-to-fuel ratio (A/F) as detailed in Appendix C. Also, TGA and DTG analyses of PRB and DB were conducted in order to determine the temperature at start of pyrolysis and to find the kinetic constants.

#### 7.1.1 Results from Proximate Analysis

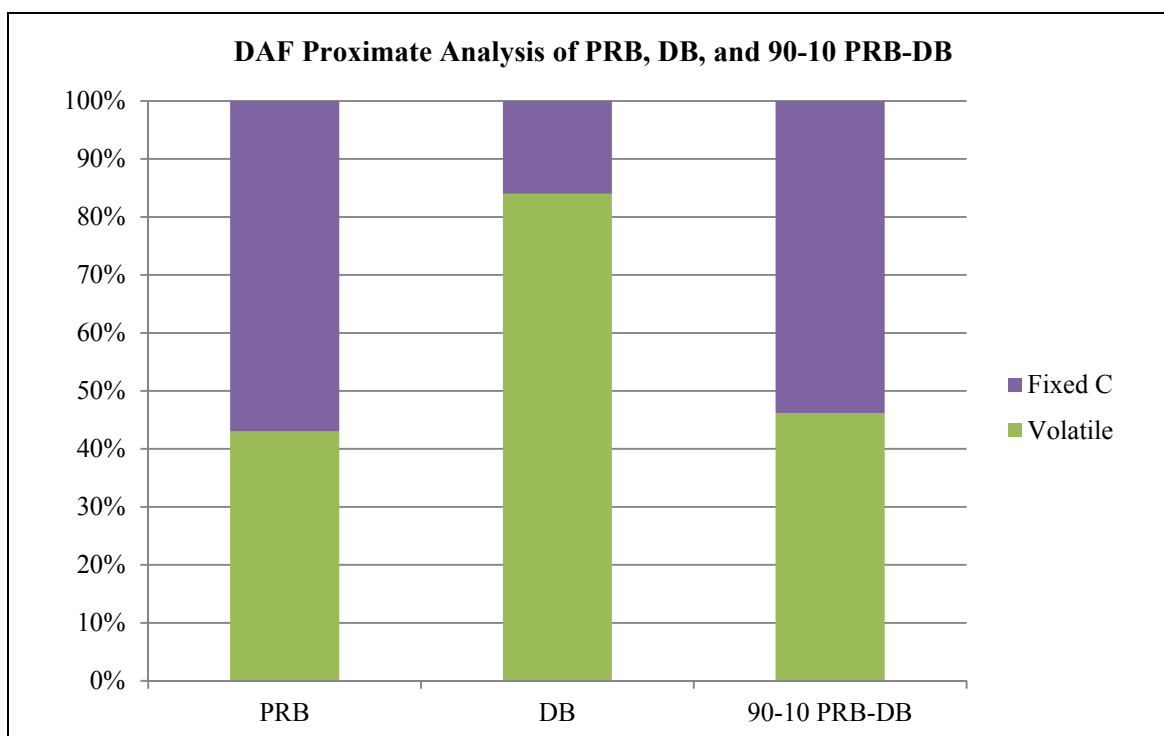
The results of the proximate analysis for PRB and DB on as-received, dry, and dry and ash-free (DAF) bases are shown in Table 12. Please note that the values shown in Table 12 for the fuel blends between PRB and DB with the PRB-to-DB ratio of 90 to 10 on a mass basis (90-10 PRB-DB) are computed by using the weighted average method. The moisture content in PRB is 2.48 times of that in DB, but the ash content in PRB is approximately 0.16 times of the ash content in DB. As a result, the moisture content in the 90-10 PRB-DB blend decreases by 1.22% and the ash content increases by

3.02% relative to PRB. This might result in higher rate of ash accumulation inside the reactor during co-firing 90-10 PRB-DB blend compared to firing pure PRB. More ash number density affects radiator heat transfer.

**Table 12 – Proximate analysis of PRB, DB, and 90-10 PRB-DB blend**

Weight % of	PRB	DB	90-10 PRB-DB
<u>As-Received Basis</u>			
Moisture	20.46	8.25	19.24
VM	31.79	46.97	33.31
FC	42.17	8.95	38.85
Ash	5.58	35.83	8.60
<u>Dry Basis</u>			
VM	39.97	51.19	41.25
FC	53.01	9.76	48.10
Ash	7.02	39.05	10.65
<u>DAF Basis</u>			
VM	42.99	83.99	46.16
FC	57.01	16.01	53.84

Figure 38 shows that the VM content in DB on DAF basis is much higher than the VM content in PRB on DAF basis. The increase in VM will result in decreasing the local O<sub>2</sub> concentration in the primary combustion zone because VM of DB releases much faster than VM of PRB. Consequently, NO<sub>x</sub> emissions could be mitigated. The results from TGA and DTG of PRB and DB will be used to explain the decrease of local O<sub>2</sub> concentration when DB is co-fired with PRB.



**Figure 38 – Proximate analysis of PRB, DB, and 90-10 PRB-DB blend on DAF basis**

### 7.1.2 Results from Ultimate Analysis

The results from the ultimate analysis as shown in Table 13 indicate that PRB contains higher C content than DB. Moreover, the atomic H/C and the atomic O/C of PRB are about a half lower than those of DB as shown in Table 14. This implies that the HHV of PRB is higher than the HHV of DB. Thus, mixing PRB with DB leads to increasing H/C and O/C of the fuel blends and decreasing the HHV of the fuel blends as compared to pure PRB. The as-received HHV of PRB, DB, and the weighted average HHV of 90-10 PRB-DB blend are given in next subsection. The empirical formulae of PRB, DB, and 90-10 PRB-DB blend are developed and given in Table 15 (Appendix A).

**Table 13 – Ultimate analysis of PRB, DB, and 90-10 PRB-DB blend**

Weight % of	PRB	DB	90-10 PRB-DB
<u>As-Received Basis</u>			
Moisture	20.46	8.25	19.24
C	54.78	28.64	52.17
H	2.98	3.26	3.01
N	0.87	2.15	1.00
S	0.27	0.54	0.30
Ash	5.58	35.83	8.61
O	15.06	21.33	15.69
<u>Dry Basis</u>			
C	68.87	31.22	64.60
H	3.75	3.55	3.73
N	1.09	2.34	1.24
S	0.34	0.59	0.37
Ash	7.02	39.05	10.66
O	18.93	23.25	19.43
<u>DAF Basis</u>			
C	74.07	51.22	72.31
H	4.03	5.83	4.17
N	1.18	3.84	1.39
S	0.37	0.97	0.42
O	20.36	38.14	21.75

**Table 14 – Atomic H/C and O/C of PRB, DB, and 90-10 PRB-DB blend**

Atomic Ratio	PRB	DB	90-10 PRB-DB
H/C	0.6488	1.3550	0.6871
O/C	0.2063	0.5591	0.2257

**Table 15 – Empirical formulae of PRB, DB, and 90-10 PRB-DB blend**

Fuel	Empirical Formula Normalized by C Atoms
PRB	C H <sub>0.6488</sub> O <sub>0.2063</sub> N <sub>0.0136</sub> S <sub>0.0018</sub>
DB	C H <sub>1.3550</sub> O <sub>0.5591</sub> N <sub>0.0643</sub> S <sub>0.0071</sub>
90-10 PRB-DB	C H <sub>0.6871</sub> O <sub>0.2257</sub> N <sub>0.0164</sub> S <sub>0.0021</sub>

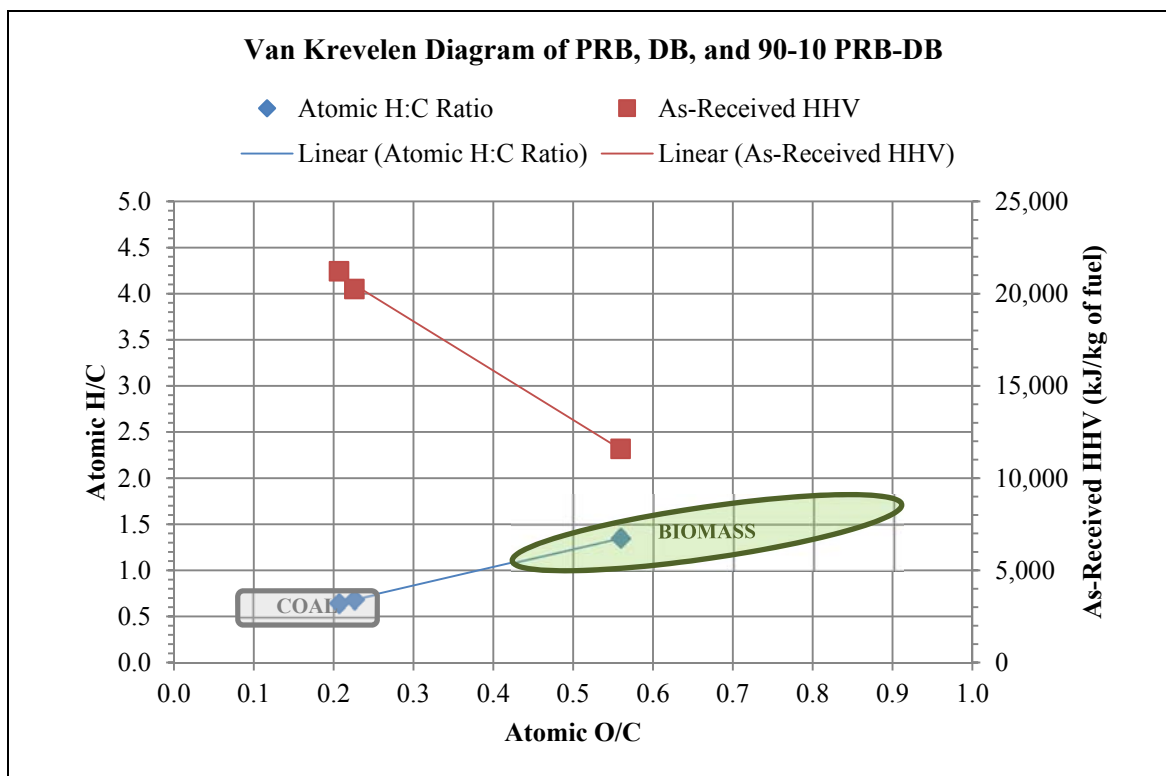
### 7.1.3 Results of HV Analysis

The heating values obtained from Hazen Research Inc., are given in Appendix B. The as-received HV of PRB and DB could be converted into HV on DAF basis in case we have the results from proximate analysis. Moreover, the predicted HHV on DAF basis are compared with the measured values. Finally, the HHV based on the stoichiometric air ( $HHV_{air}$ ) and  $O_2$  ( $HHV_{O_2}$ ) of each fuel type was computed and presented in Table 16. This table shows that the HHV predicted by using Boie equation are very close to the measured values. In Appendix B, it is shown that Boie equation could give the predicted HHV with less than 2% deviation. Moreover, the  $HHV_{O_2}$  are almost constant from fuel to fuel; therefore, in case we know only the amount of  $O_2$  required for the stoichiometric combustion we can estimate the HHV of that fuel by using the average  $HHV_{O_2}$ .

**Table 16 – HHV of PRB, DB, and 90-10 PRB-DB blend on various bases**

HHV (kJ/kg) Based on	PRB	DB	90-10 PRB-DB
As-Received Basis	21,218	11,586	20,255
Dry Basis	26,675	12,628	25,080
DAF Basis	28,687	20,720	28,071
Boie Equation (DAF Basis)	28,584	20,891	27,983
Stoichiometric Air	3,193	3,318	3,200
Stoichiometric O <sub>2</sub>	13,698	14,234	13,728

The HHV on as-received basis of PRB, DB, and 90-10 PRB-DB blend are compared on Van Krevelen diagram altogether with H/C and O/C as shown in Figure 39. This diagram indicates that lower O/C and H/C give the higher HHV which agree with other literatures (Literature Review section).



**Figure 39 – Van Krevelen diagram of PRB, DB, and 90-10 PRB-DB**

Finally, the N, S, and ash loadings of each fuel type in kg/GJ can be determined by using the results from proximate, ultimate, and HV analyses as shown in Table 17. The N, S, and ash loadings of 90-10 PRB-DB blend are all increased because DB has higher N, S, and ash contents.

**Table 17 – N, S, and ash loadings of PRB, DB, and 90-10 PRB-DB blend**

Description	PRB	DB	90-10 PRB-DB
N Loading (kg/GJ)	0.41	1.86	0.49
S Loading (kg/GJ)	0.13	0.47	0.15
Ash Loading (kg/GJ)	2.63	30.93	4.25

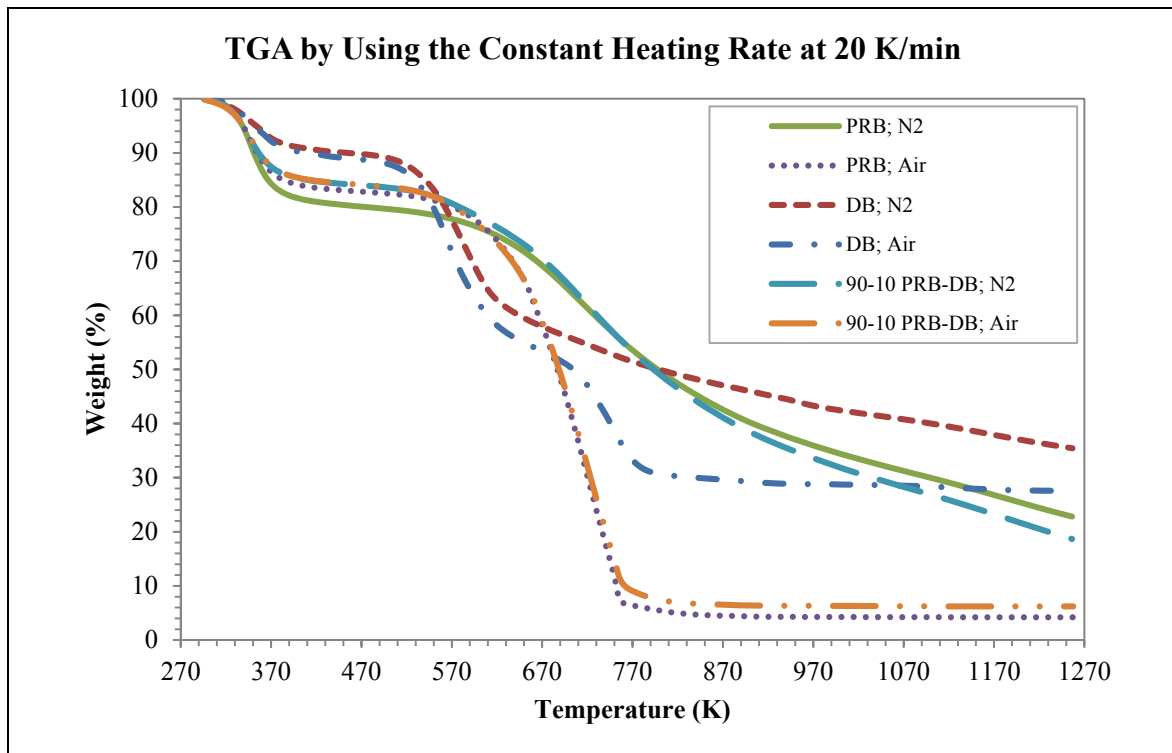
#### *7.1.4 Results of TGA and DTG*

TGA and DTG were used to obtain the experimental thermal decomposition data of PRB, DB, and 90-10 PRB-DB blend. An array of data was used in plotting weight-versus-temperature (W vs T) and derivative-weight-versus-temperature (dW/dT vs T) diagrams. The results from TGA in both inert and oxidizing gases of PRB, DB, and 90-10 PRB-DB blend are shown in Figure 40. It is seen that DB has less moisture content but higher ash content than PRB and 90-10 PRB-DB blend which agree with the results obtained from the proximate analysis. The TGA results can be used to roughly estimate the contents of moisture, ash, VM and FC as shown in Table 18. For instance, Table 18 shows that the procedure used in the current research could give the numbers in the same fashion as the proximate analysis does. However, it is suitable for rough approximation. For example, the ash contents estimated by TGA are lower than 20% with respect to ones obtained from the proximate analysis. Hence, the procedure should be developed in order to improve the accuracy of TGA.



**Table 18 – Comparison of data between proximate analysis and TGA**

Composition	PRB	DB	90-10 PRB-DB
Data from Proximate Analysis			
Moisture	20.46	8.25	19.24
Ash	5.58	35.83	8.61
VM and FC (By Difference)	73.96	55.92	72.15
Data from TGA			
Moisture	19.92	9.75	15.89
	(-0.54)	(+1.50)	(-3.35)
Ash	4.24	27.59	6.27
	(-1.34)	(-8.25)	(-2.34)
VM and FC (By Difference)	75.84	62.66	77.84
	(+1.88)	(+6.74)	(+5.69)



**Figure 40 – TGA curves of PRB, DB, and 90-10 PRB-DB**

Nonetheless, TGA together with DTG can be used to explain the kinetics of solid fuels. For example, the results of DTG in inert gas (nitrogen gas) as shown in Figure 41 clearly show that PRB and 90-10 PRB-DB blend start releasing VM almost at the same temperature but pure DB releases VM at lower temperature. Furthermore, the point where DB releases the maximum amount of the VM is approximately 100 K lower than PRB and fuel blends. Therefore, DB will release its VM in lower temperature compared to PRB. The VM of DB rapidly consumes O<sub>2</sub> and turns into CO<sub>2</sub>, etc. Consequently, the local O<sub>2</sub> concentration will decrease rapidly before PRB releases its VM. As a result, NO<sub>x</sub> formation is reduced because of lowered O<sub>2</sub> concentration.

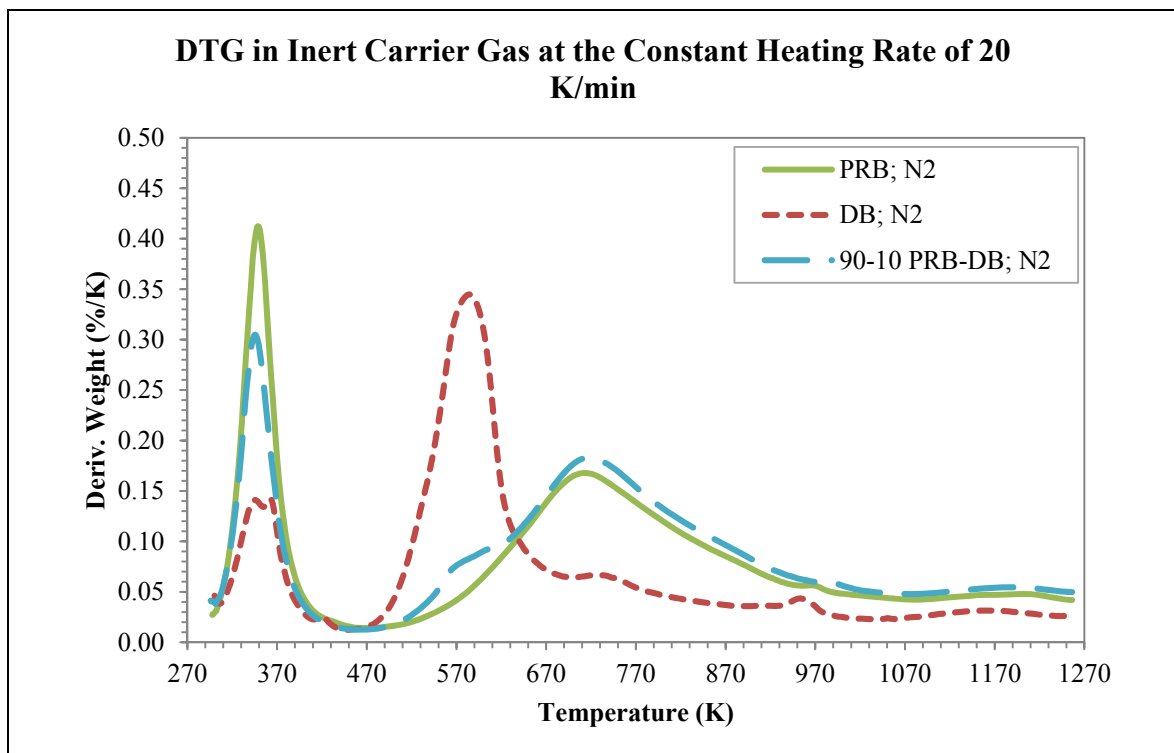


Figure 41 – DTG curves of PRB, DB, and 90-10 PRB-DB in inert carrier gas

By using the results from TGA, DTG, and proximate analysis, the start and end temperatures of pyrolysis,  $T_{ign}$ , and the temperature at the peak of VM release could be determined. Table 19 shows the summary of significant temperatures in pyrolysis process of PRB, DB, and 90-10 PRB-DB blend. The ignition temperature of DB is lower than  $T_{ign}$  of PRB about 100 K which means that DB oxidizes faster than PRB. The details of determining  $T_{ign}$  are described in Appendix D. Furthermore, the pyrolysis data of fuel can be used to determine the kinetic constants of PRB and DB. Table 20 shows that  $B$  and  $E_a$  of DB are higher than PRB which mean DB takes shorter time to react.

**Table 19 – Significant temperatures in pyrolysis of PRB, DB, and 90-10 PRB-DB**

Temperature (K) at	PRB	DB	90-10 PRB-DB
Start of Pyrolysis	472	451	465
5% of Volatile Release	576	519	559
Ignition Point			
- Method I (Tognotti, et al. 1985)	625	529	600
- Method II (Li, et al. 2012)	620	537	608
Peak of Volatile Release	713	585	717
95% of Volatile Release	1,061	870	976
End of Pyrolysis	1,123	933	1,024

**Table 20 – Summary of kinetics constants of PRB, DB, and 90-10 PRB-DB blend**

Kinetic Constants	PRB	DB	90-10 PRB-DB
<u>n = 1</u>			
B (1/min)	12.60	$4.319 \times 10^3$	24.53
E <sub>a</sub> (kJ/kmol)	27,250	46,356	30,638
<u>n = n</u>			
n	2.918	2.340	2.029
B (1/min)	$2.329 \times 10^4$	$1.186 \times 10^8$	$1.939 \times 10^3$
E <sub>a</sub> (kJ/kmol)	68,218	93,691	54,408

## 7.2 Results of Particle Size Analysis

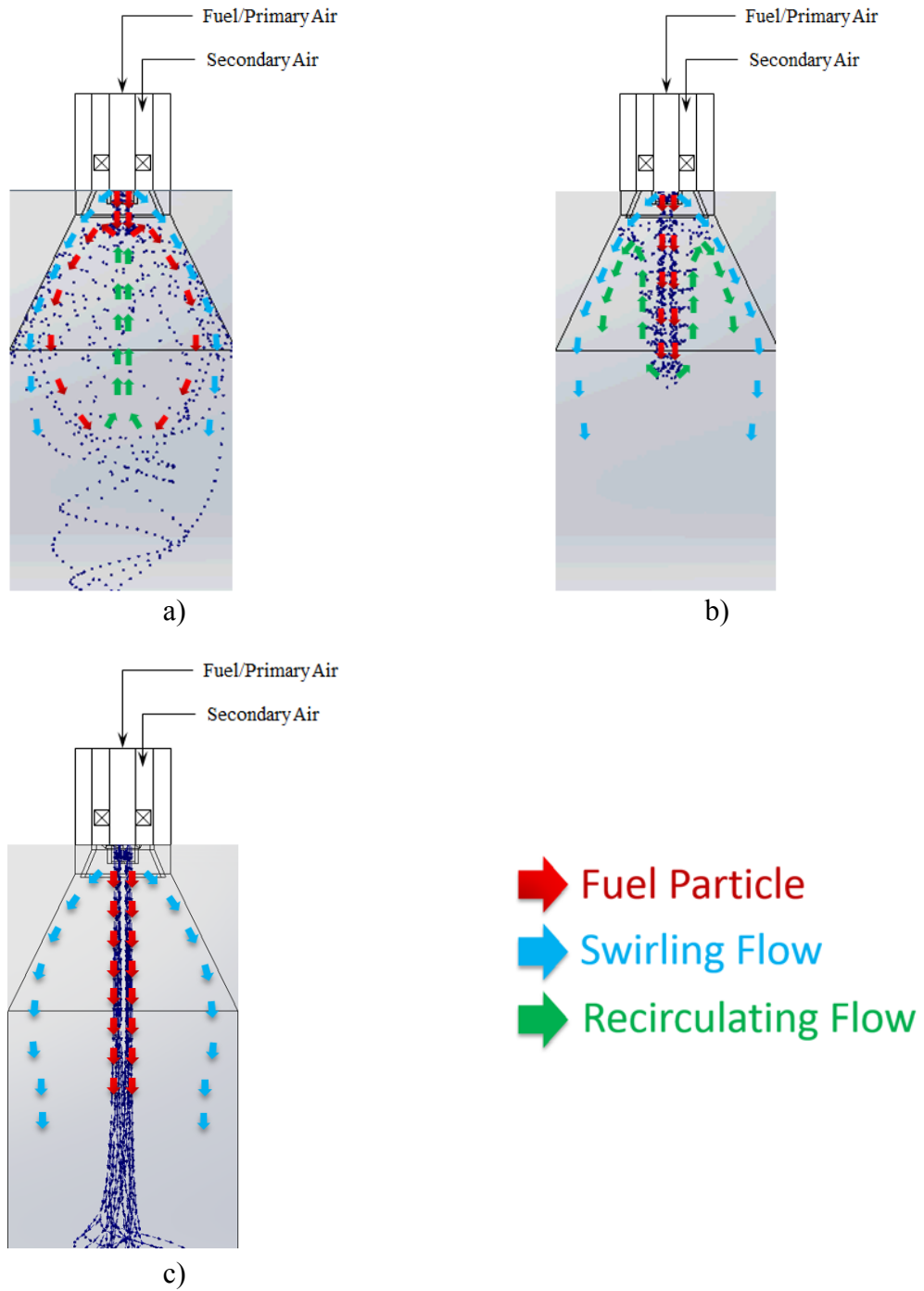
Particle size analysis was conducted in order to obtain the Rosin Rammler distribution parameters ( $\alpha_{dstr}$  and  $\beta$ ) and  $d_{ps, char}$  of PRB and DB. The results of particle size analysis shown that  $d_{ps, char}$  of PRB and DB are 118  $\mu\text{m}$  and 172  $\mu\text{m}$  respectively (Appendix E). This means the on-hand PRB was finer than the on-hand DB.

The recommended fineness of sub-bituminous coal particle is 70% of fuel particle should be smaller than 75  $\mu\text{m}$  (Tomeczek 1994). By assuming this criterion is used to imply that the 75- $\mu\text{m}$  sub-bituminous coal particle can follow the airflow beyond the burner exit, the results from Appendix E show that only 51.07% of PRB will follow the flow (48.93% of PRB  $\geq 75 \mu\text{m}$ ). Nonetheless, the results of particle study obtained from SolidWorks program by varying the particle size from 25  $\mu\text{m}$  to 200  $\mu\text{m}$  with the increment of 25  $\mu\text{m}$  and assuming that densities of PRB and DB are equal to 1,300  $\text{kg/m}^3$  and 500  $\text{kg/m}^3$  respectively (Demirbas 2004) show that the particle flow characteristics could be separated into three models as shown in Figure 42.

First, when particle size of PRB ( $d_{ps,PRB}$ ) is 25  $\mu\text{m}$ , particle will follow the swirling flow, and a portion of the swirled particle flow will follow the recirculating flow as shown in Figure 42-a. Second, when between  $50 \mu\text{m} \leq d_{ps,PRB} \leq 150 \mu\text{m}$ , the particle will penetrate into the RZ first. Then, when the particle velocity decreases to some specific degree, the particle will start following the recirculating flow as shown in Figure 42-b. Please note that the depth that the particle penetrates into the RZ until it is recirculated depends on the particle size and density of the particle. Third, when  $d_{ps,PRB}$  is greater than or equal to 175  $\mu\text{m}$ , the particle does not follow neither swirling flow nor recirculating flow below the burner exit as shown in Figure 42-c. These results agree with the particle trajectory path proposed by Abbas, Costen and Lockwood (1992).

For the DB particle, the results show that when the particle size of DB ( $d_{ps,DB}$ ) is less than or equal to 50  $\mu\text{m}$ , the particle flow characteristics are the same as Figure 42-a. In addition, when  $d_{ps,DB}$  is in between 75  $\mu\text{m}$  and 200  $\mu\text{m}$ , the particle flow characteristics are the same as Figure 42-b.

Hence, most of the on-hand PRB and DB are able to follow either swirling flow or recirculating flow because 84.83% of PRB has  $d_{ps,PRB}$  less than 150  $\mu\text{m}$ , and 60.15% of DB has  $d_{ps,DB}$  less than 150  $\mu\text{m}$ . Additionally, mixing PRB with DB will increase the portion that particle can follow the airflow. In other words, more fuel particle will be recirculated inside the RZ when blend is fired.



**Figure 42 – Particle flow characteristics of PRB when: a)  $d_{ps,PRB} = \{25 \mu\text{m}\}$ , b)  $d_{ps,PRB} = \{50 \mu\text{m}, 75 \mu\text{m}, 100 \mu\text{m}, 125 \mu\text{m}, 150 \mu\text{m}\}$ , and c)  $d_{ps,PRB} = \{175 \mu\text{m}, 200 \mu\text{m}\}$**

### 7.3 Experimental Results

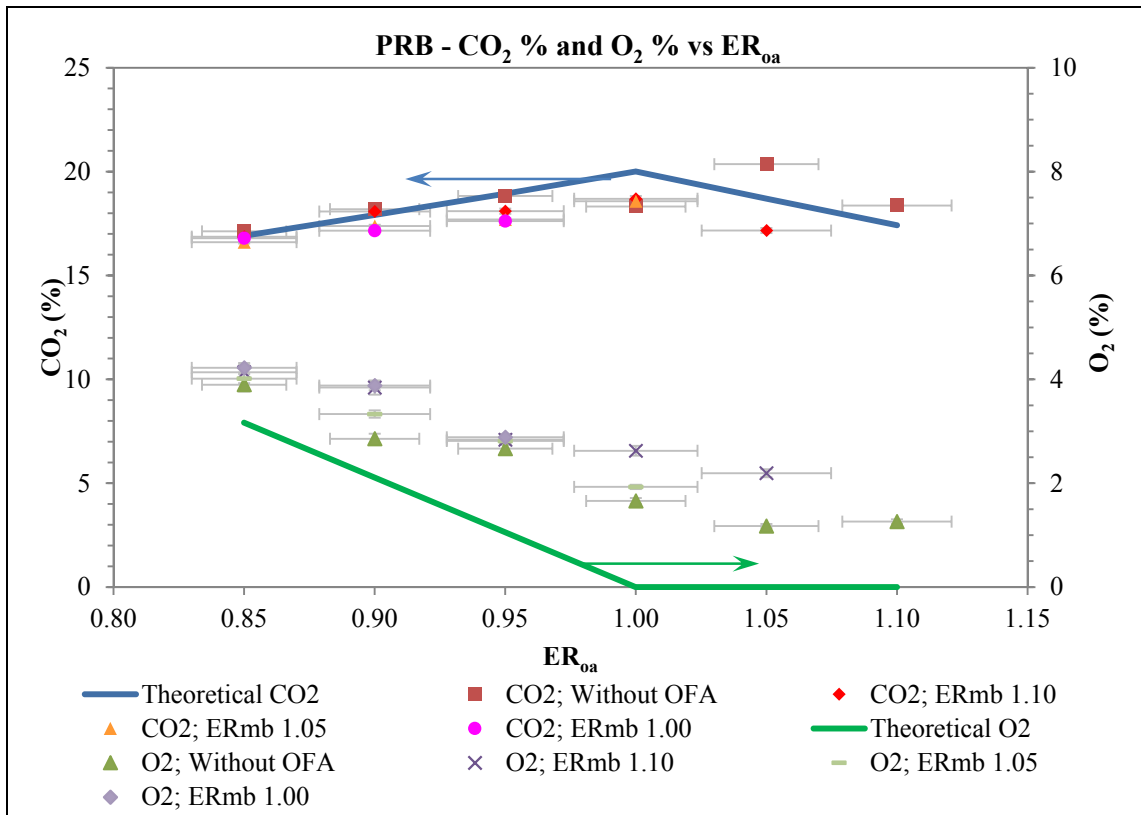
This subsection shows the experimental results such as flue gas composition and temperature along the vertical section of the combustion chamber from firing PRB and co-firing 90-10 PRB-DB blend, and also discussion on experimental results. Flue gas is analyzed and presented in various aspects such as burnt fraction (BF), fuel N conversion efficiency ( $N_{\text{conv}}$ ), and respiratory quotient (RQ). Please note that the values in rich region and stoichiometric condition are also presented and compared as seen though they are of limited practical utility. They are simply presented to improve the understanding of the effects of OFA. Main focus and conclusions will be for lean region where furnaces and boilers are normally being operated. Typically, most coal-fired power plants operate with 3% excess  $O_2$  in dry flue gas (excess air  $\approx 17\%$  and  $ER_{\text{oa}} \approx 0.85$ ).

#### 7.3.1 $O_2$ and $CO_2$ in Flue Gas

The operating conditions of reactors are monitored by measuring the  $CO_2\%$  and  $O_2\%$  in flue gas. To be more specific, these two values could be used to assess whether the reactors are being operated under the design conditions. For example, if a reactor is being operated at the design 3%  $O_2$  in flue gas, then, the measured  $O_2$  in flue gas must be 3%, and the  $CO_2\%$  in flue gas will be comparable to the theoretical  $CO_2$ .

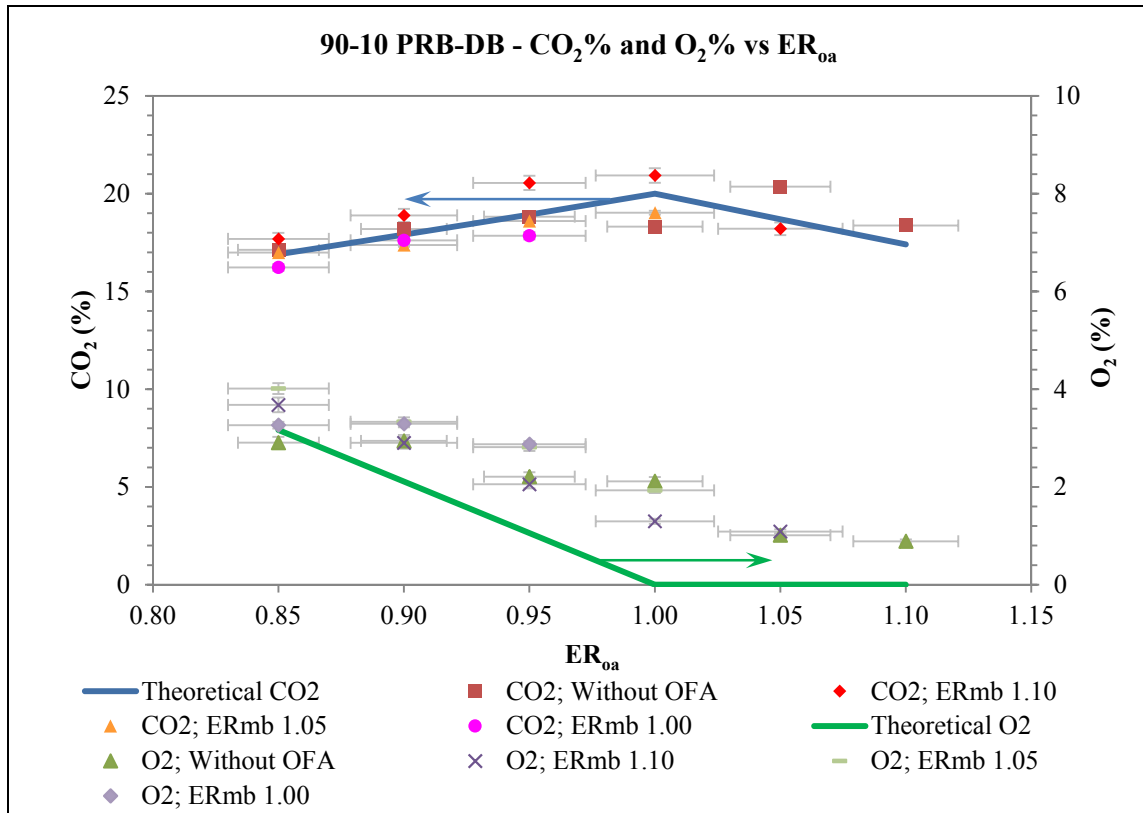
The percentages of measured  $O_2$  and  $CO_2$  compared to the theoretical  $O_2$  and  $CO_2$  are presented in Figure 43 and Figure 44. The values obtained from burning PRB and 90-10 PRB-DB blend show that the measured values of  $CO_2$  emission agree with the theoretical  $CO_2$  emission line. On the other hand, the predicted  $O_2$  values are lower than the measured ones and the differences increase when ER increases.

The simple model presumes that all the carbon in fuel is burnt to a mixture of CO and CO<sub>2</sub> where measured O<sub>2</sub> % indicated that fuel carbon may be left over without any oxidation. As a result, O<sub>2</sub> that is not consumed due to unburnt carbon could present in the product gas.



**Figure 43 – CO<sub>2</sub> and O<sub>2</sub> in flue gas from firing PRB at various ER<sub>0a</sub>**





**Figure 44 – CO<sub>2</sub> and O<sub>2</sub> in flue gas from co-firing 90-10 PRB-DB at various ER<sub>0a</sub>**

### 7.3.2 Effects of OFA and Co-Firing 90-10 PRB-DB Blend on NO<sub>x</sub> Emissions

As mentioned in Literature Review section, NO<sub>x</sub> formation depends on O<sub>2</sub> concentration, residence time and temperature; hence, varying one of these parameters could affect the amount of NO<sub>x</sub> emissions. Figure 45 shows the overview of the measured NO<sub>x</sub> versus ER<sub>0a</sub>. Typically, increasing ER means less air is supplied into the system. In other words, as the O<sub>2</sub> concentration inside the combustion chamber is lowered, fuel N has less probability of colliding and reacting with O<sub>2</sub>. According to the experimental results, the amount of NO<sub>x</sub> emissions from firing PRB at ER<sub>0a</sub> of 0.85

without OFA is 330 g/GJ whilst the amount of NO<sub>x</sub> emissions from firing PRB at ER<sub>oa</sub> of 1.10 without OFA is 91 g/GJ.

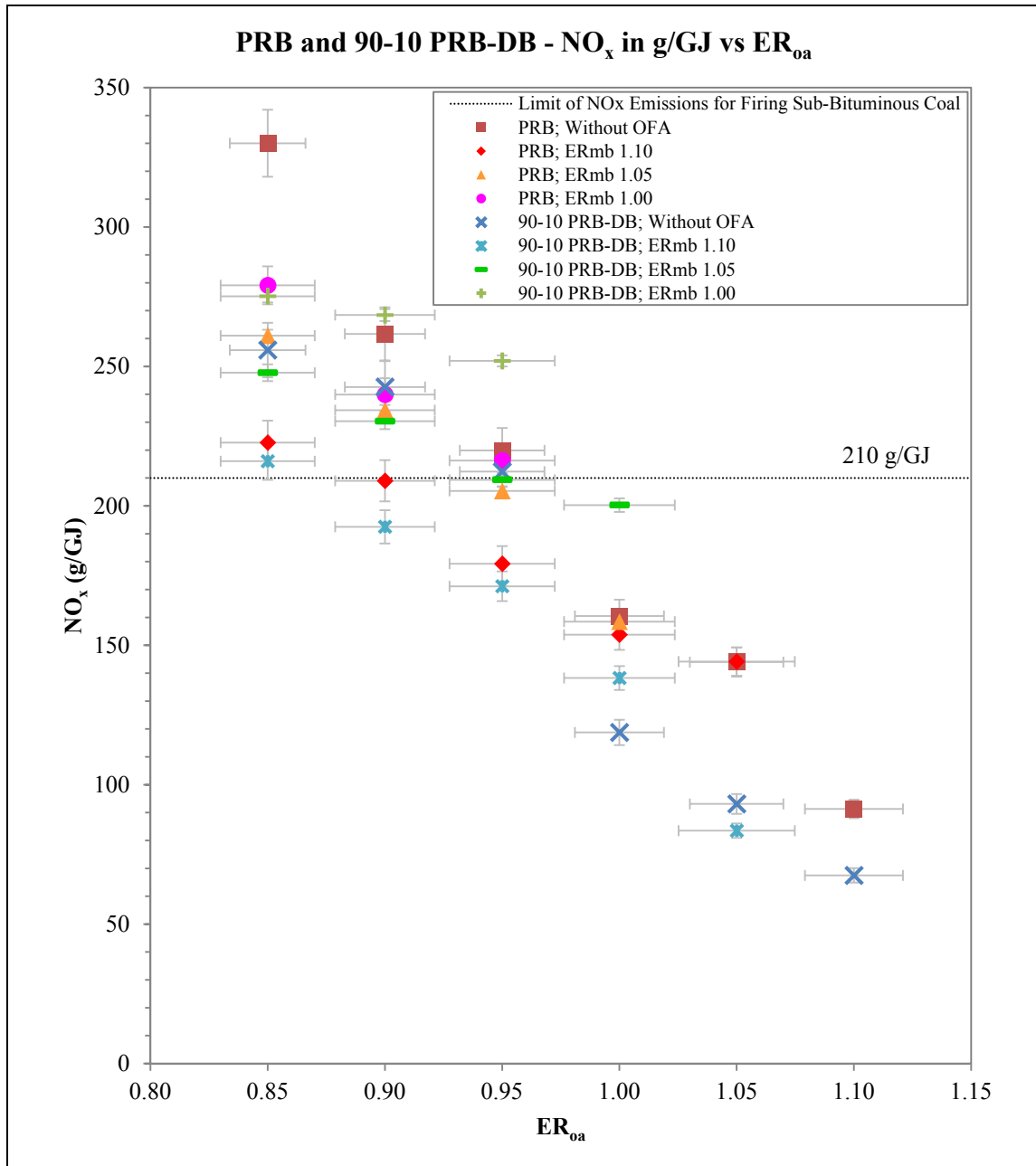
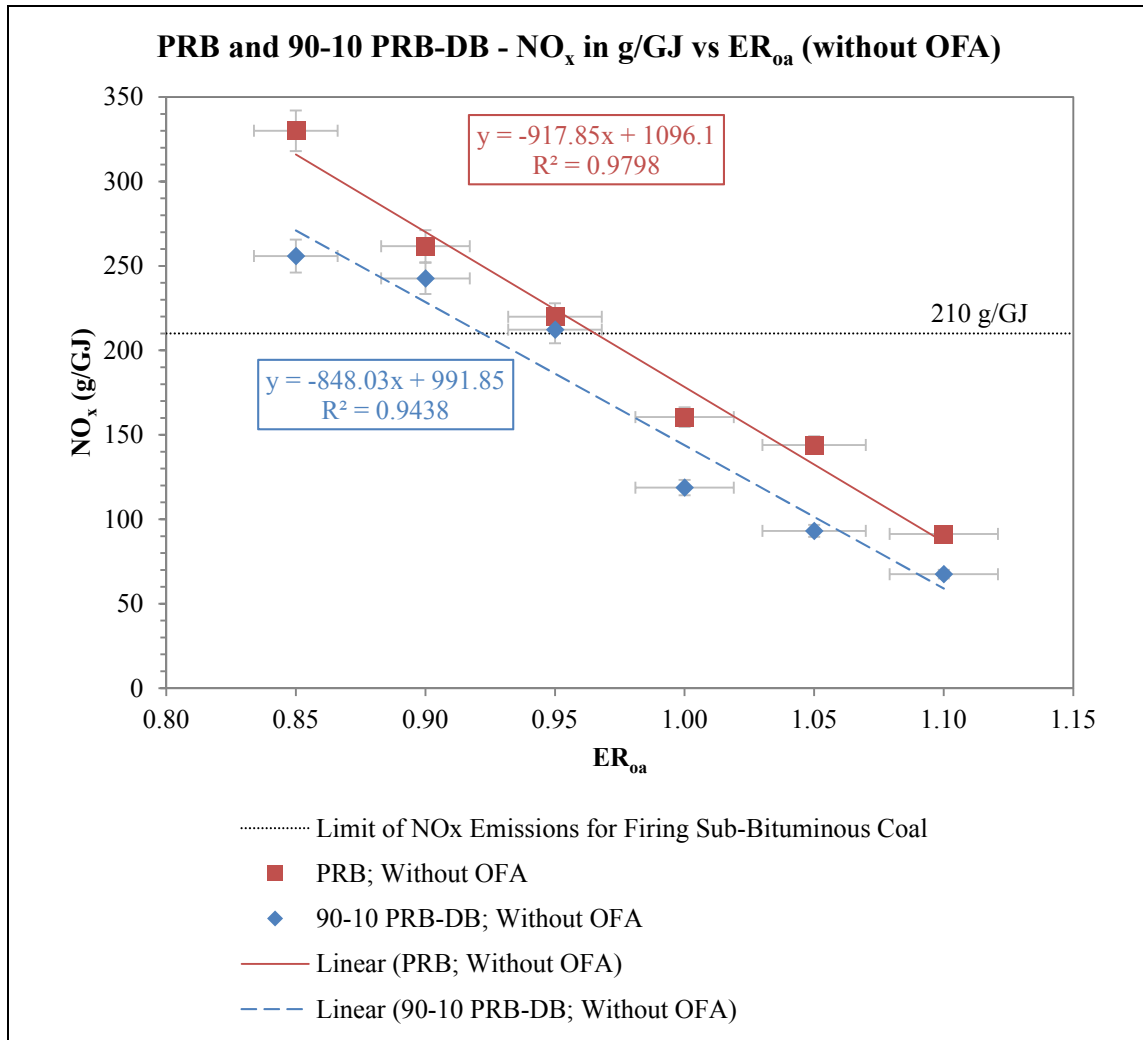


Figure 45 – NO<sub>x</sub> in g/GJ from firing PRB and 90-10 PRB-DB at various ER<sub>oa</sub>

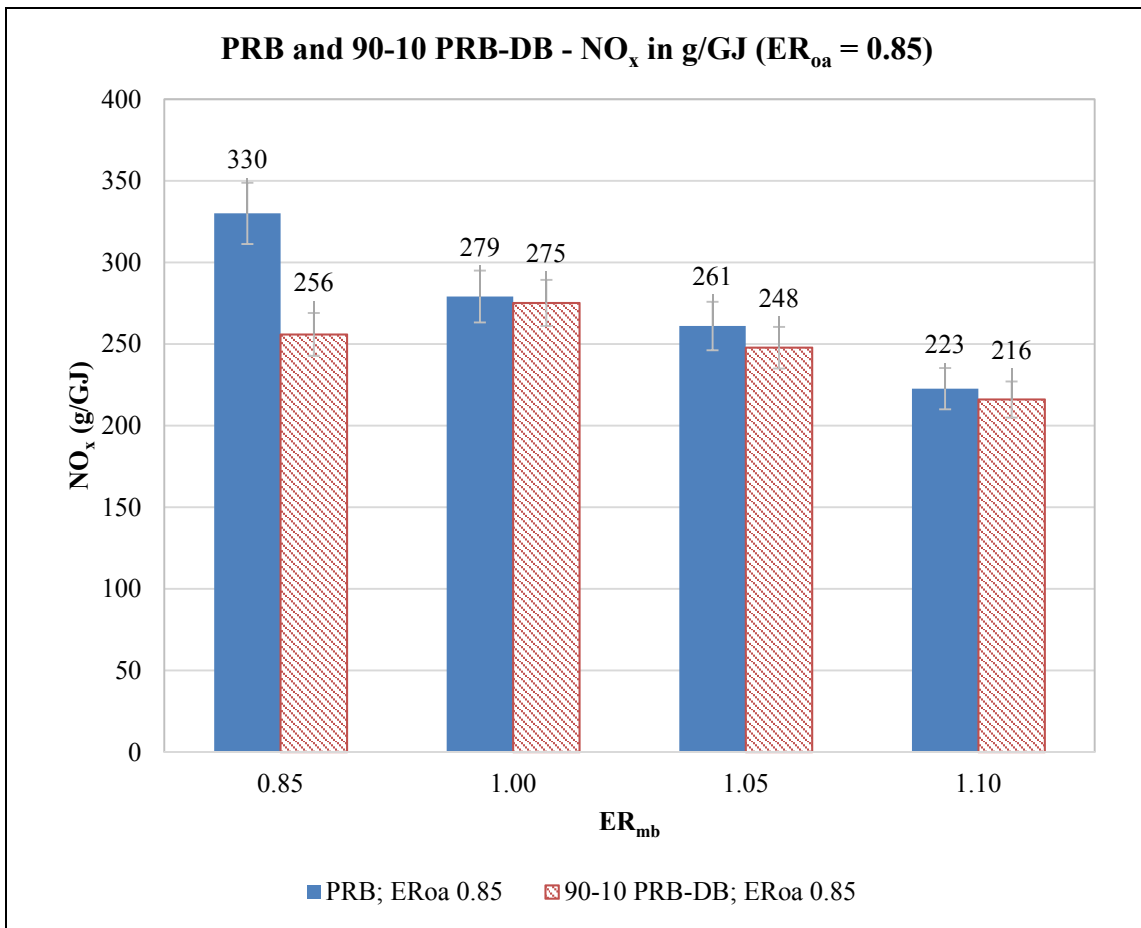
First, co-firing fuel blends of PRB and DB could help in  $\text{NO}_x$  reduction under some specific conditions. First, PRB and 90-10 PRB-DB blend were burned at various  $\text{ER}_{\text{oa}}$  without OFA. In other words, the fuels consumed only primary air and secondary air. The results for  $\text{NO}_x$  versus  $\text{ER}_{\text{oa}}$  in Figure 46 indicate that 90-10 PRB-DB blend emits  $\text{NO}_x$  lesser than PRB. For example, when  $\text{ER}_{\text{oa}}$  was set at 0.85, the amount of  $\text{NO}_x$  produced by PRB was 330 g/GJ whereas the amount of  $\text{NO}_x$  generated by 90-10 PRB-DB blend was 256 g/GJ at the same  $\text{ER}_{\text{oa}}$  which is 22.5% of  $\text{NO}_x$  reduction. The average percentage of  $\text{NO}_x$  reduction by using co-firing technique alone (without OFA injection) was approximately 20.11%. This reduction could be explained by referring to the results from proximate, TGA and DTG analyses. Figure 38, Figure 40 and Figure 41 clearly show that DB has much higher VM content and could release more amount of VM at lower temperature compared to PRB. Consequently, VM released from DB at lower temperature consumes local  $\text{O}_2$  rapidly which is comparable to rich combustion. Hence, local  $\text{NO}_x$  formation is inhibited due to lower local  $\text{O}_2$  concentration.



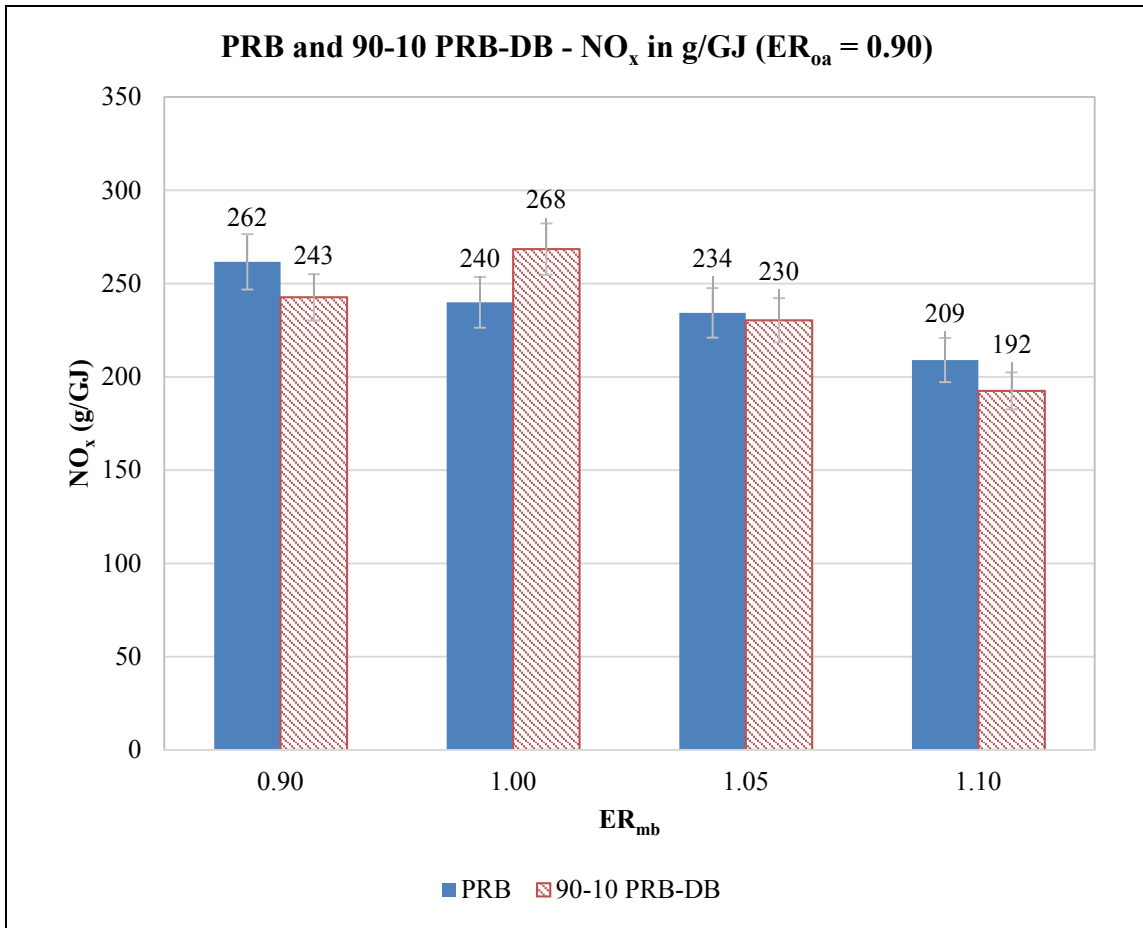
**Figure 46 – NO<sub>x</sub> from firing PRB and co-firing 90-10 PRB-DB blend at various ER without OFA**

Second, the effects of OFA on NO<sub>x</sub> reduction are different between firing PRB and co-firing 90-10 PRB-DB blend. To begin with firing PRB, by decreasing ER<sub>mb</sub> from 1.10 to 1.00 and maintaining ER<sub>0a</sub> in lean region, the amount of NO<sub>x</sub> are increased as shown in Figure 47 through Figure 49 where ER<sub>0a</sub> is maintained. This stems from the increase of O<sub>2</sub> concentration in the primary combustion zone. For instance, from Figure

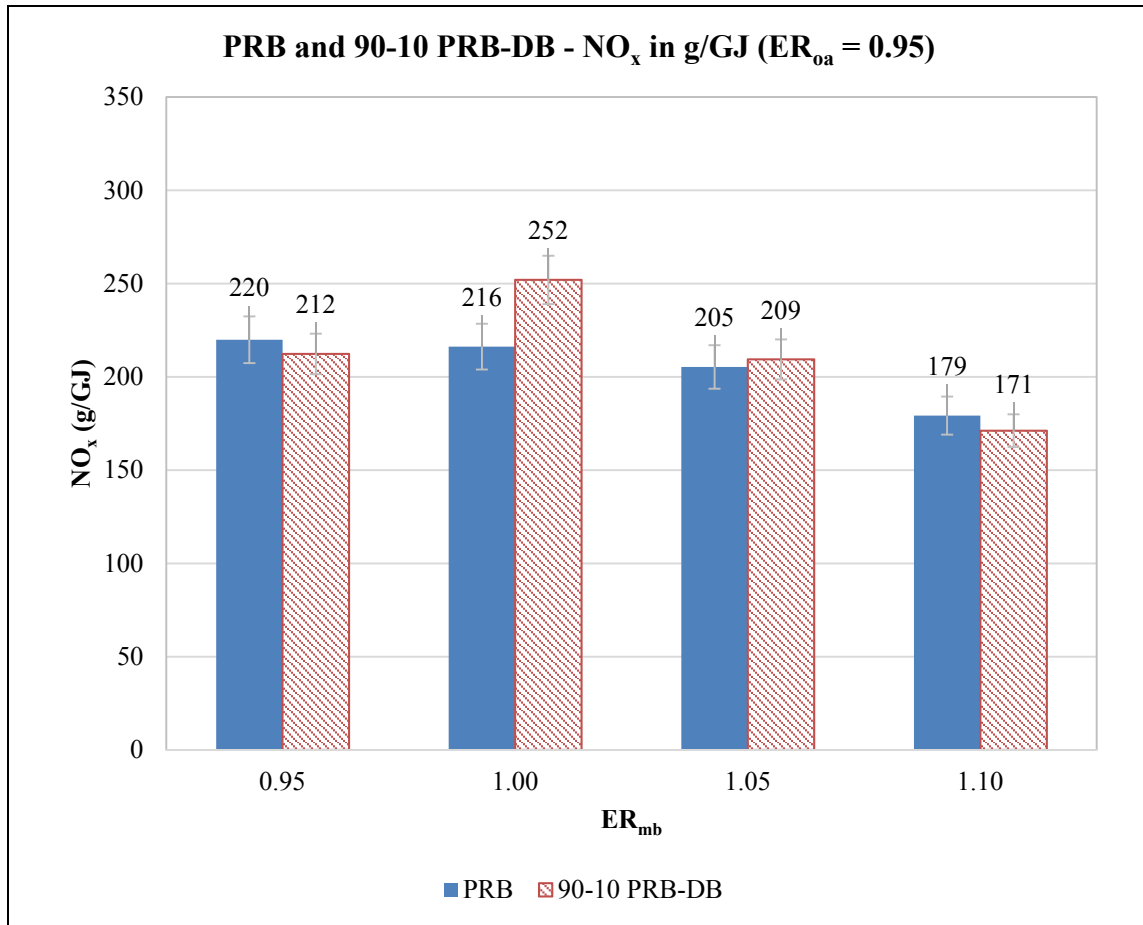
49, the amount of NO<sub>x</sub> is 179 g/GJ when ER<sub>mb</sub> is 1.10 and ER<sub>oa</sub> is 0.95; however, the amount of NO<sub>x</sub> is 220 g/GJ when both ER<sub>mb</sub> and ER<sub>oa</sub> are 0.95 (i.e. without OFA). NO<sub>x</sub> could also be increased by decreasing ER<sub>oa</sub> from 0.95 to 0.85 and keeping ER<sub>mb</sub> at some specific values. For example, from Figure 47 and Figure 49, by setting ER<sub>mb</sub> at 1.10, the amount of NO<sub>x</sub> increases from 179 g/GJ to 223 g/GJ which is approximately 24.6% increase when ER<sub>oa</sub> decreases from 0.95 to 0.85.



**Figure 47 – NO<sub>x</sub> emissions in g/GJ from firing PRB and co-firing 90-10 PRB-DB blend by setting ER<sub>oa</sub> at 0.85 and varying ER<sub>mb</sub>**



**Figure 48 – NO<sub>x</sub> emissions in g/GJ from firing PRB and co-firing 90-10 PRB-DB blend by setting ER<sub>0a</sub> at 0.90 and varying ER<sub>mb</sub>**



**Figure 49 – NO<sub>x</sub> emissions in g/GJ from firing PRB and co-firing 90-10 PRB-DB blend by setting ER<sub>0a</sub> at 0.95 and varying ER<sub>mb</sub>**

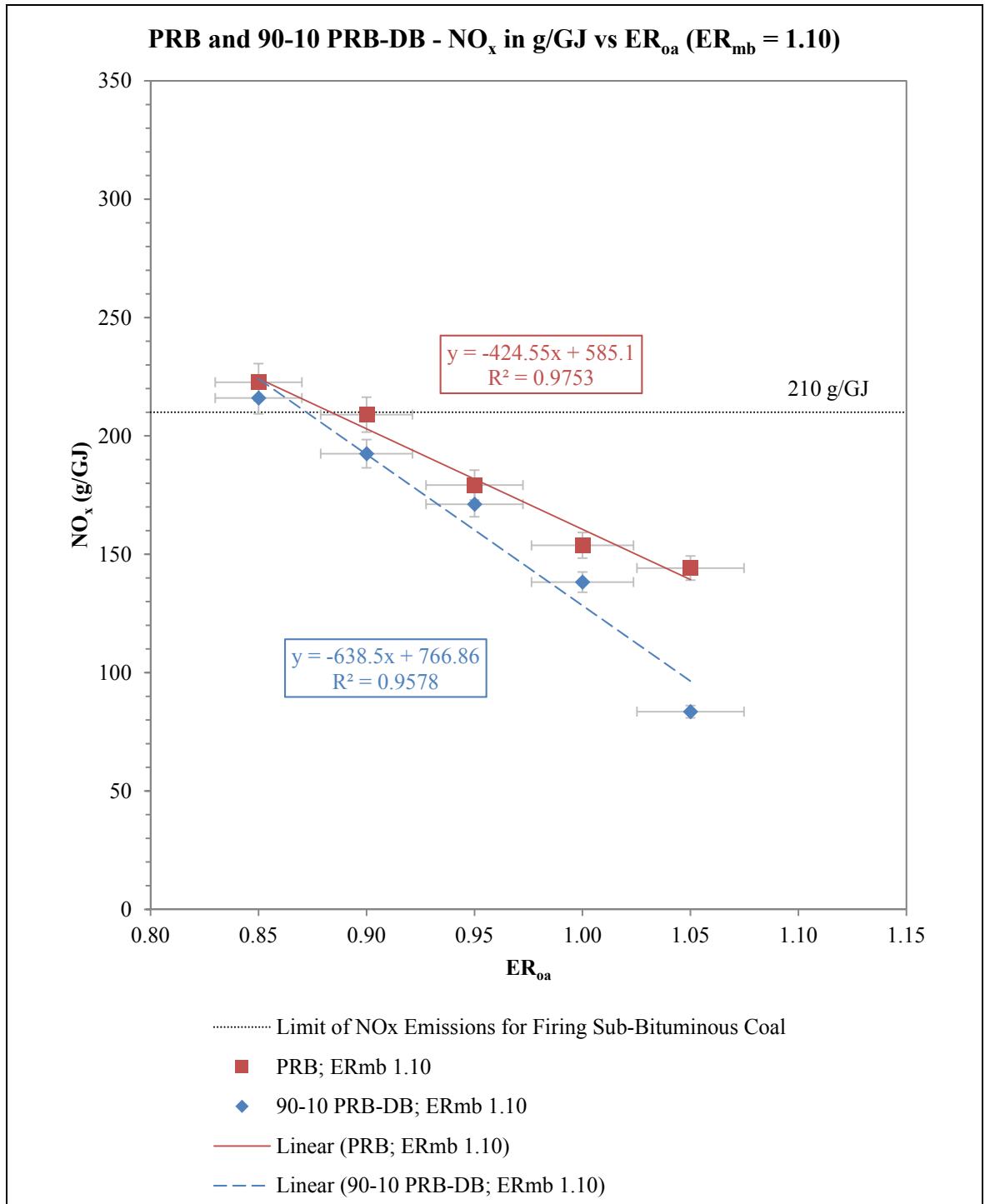
Besides, the results of operating primary combustion zone in the rich regime or stoichiometric condition and injecting OFA into the downstream of the product gases from burning 90-10 PRB-DB blend are not the same as firing PRB. When ER<sub>mb</sub> decreases from 1.10 to 1.00 as shown from Figure 50 to Figure 52 respectively, the amount of NO<sub>x</sub> emissions gradually increases due to increase of O<sub>2</sub> concentration in the primary combustion zone. However, when ER<sub>0a</sub> is varied in the lean region and ER<sub>mb</sub> is

set at 1.00, the values of NO<sub>x</sub> emissions are higher than the values of NO<sub>x</sub> produced by setting ER<sub>mb</sub> in the lean regime and without OFA. This might be explained as follows.

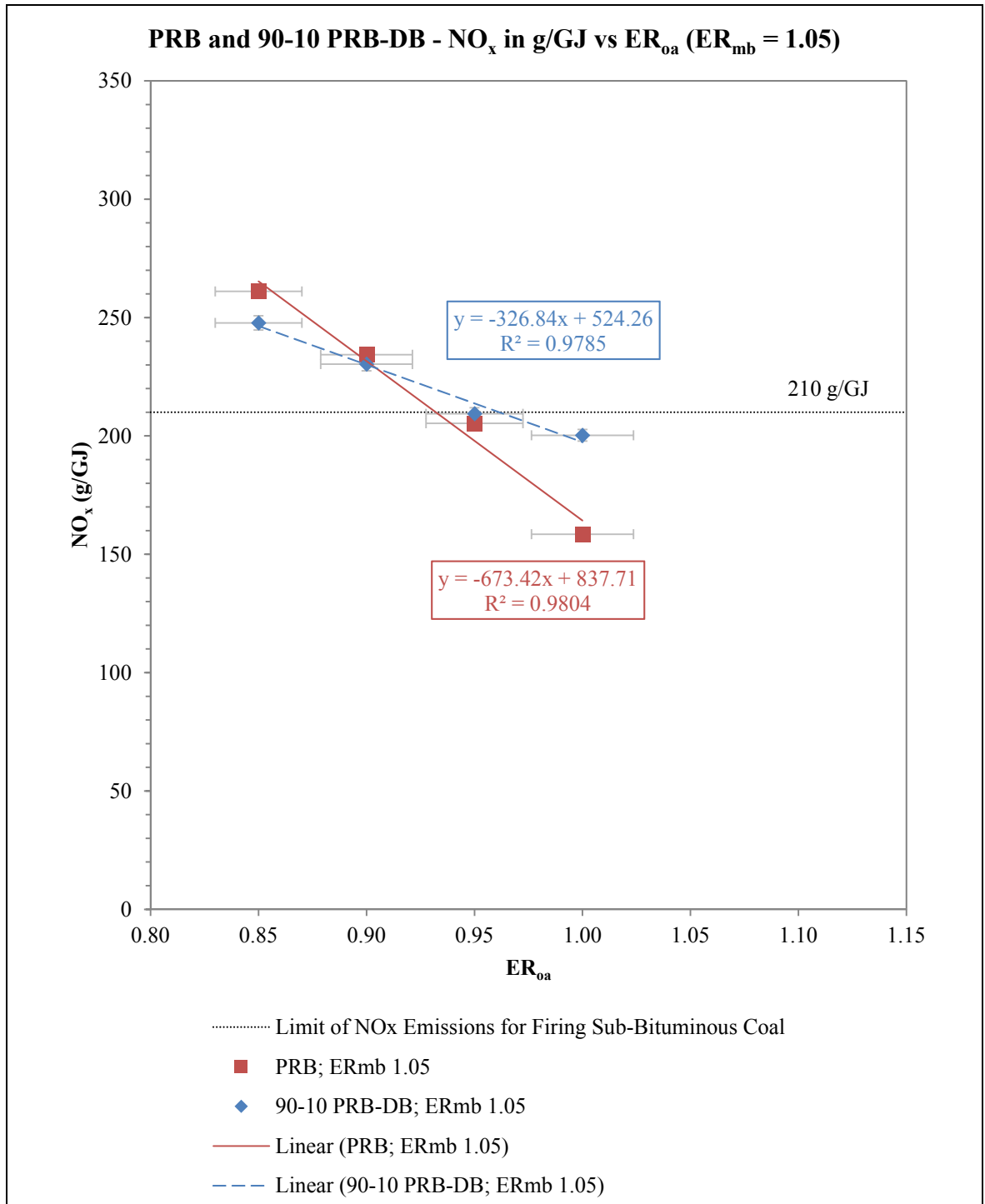
Consider the particle flow characteristic presented in Figure 42-b. By using this model, the 90-10 PRB-DB blend particle of firing with ER<sub>mb</sub> less than one (ER<sub>mb</sub> < 1; higher air flow rate; i.e. more axial flow rate) could penetrate into the RZ deeper than the 90-10 PRB-DB particle of firing with ER<sub>mb</sub> equal to 1 (ER<sub>mb</sub> = 1; lower air flow rate). This results in more residence time of DB particle in the primary combustion zone. Consequently, NO<sub>x</sub> produced when ER<sub>mb</sub> is less than one will be lower than NO<sub>x</sub> generated when ER<sub>mb</sub> is equal to one. On the other hand, although 90-10 PRB-DB particle when ER<sub>mb</sub> is greater than one (ER<sub>mb</sub> > 1) could not penetrate into the RZ as deep as 90-10 PRB-DB particle when ER<sub>mb</sub> is equal to one, NO<sub>x</sub> emissions are lower due to much lower O<sub>2</sub> concentration inside the primary combustion zone. Hence, the residence time of fuel in the primary combustion zone is the key factor when ER<sub>mb</sub> is less than one, and the O<sub>2</sub> concentration is the key factor when ER<sub>mb</sub> is greater than one.

To sum up the effects of co-firing and OFA injection on NO<sub>x</sub> emissions, NO<sub>x</sub> could be decreased by approximately 48.2% when ER<sub>mb</sub> is set at 1.10 and ER<sub>oa</sub> is set at 0.95 compared to the base case (ER<sub>mb</sub> of 0.85 without OFA). Moreover, co-firing 90-10 PRB-DB blend will negatively impact NO<sub>x</sub> emissions in case ER<sub>mb</sub> is set to 1.00 because NO<sub>x</sub> emissions will be more than firing pure PRB.

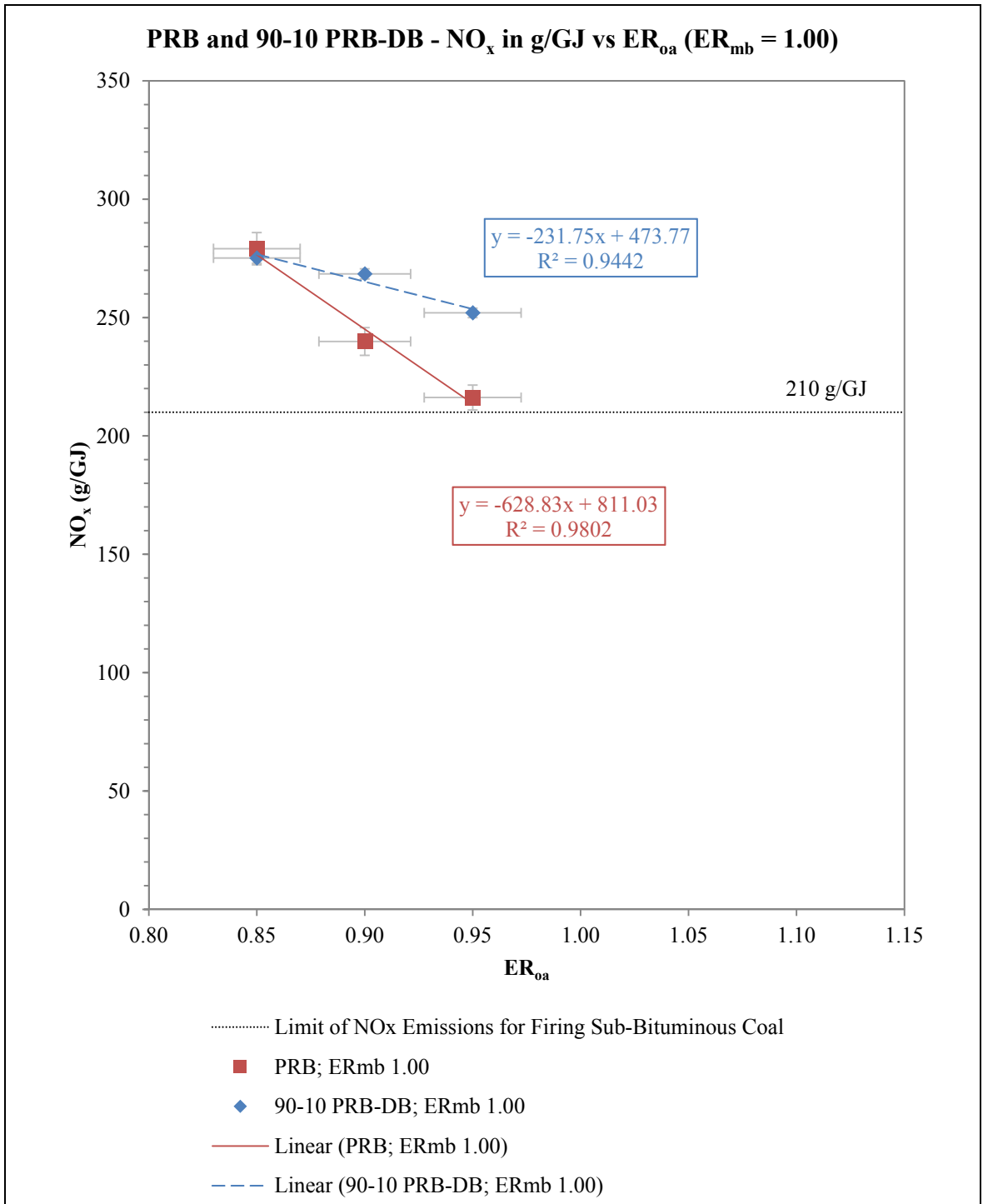




**Figure 50 – NO<sub>x</sub> emissions in g/GJ from firing PRB and co-firing 90-10 PRB-DB blend at various ER<sub>oa</sub> with fixed ER<sub>mb</sub> of 1.10**



**Figure 51 – NO<sub>x</sub> emissions in g/GJ from firing PRB and co-firing 90-10 PRB-DB blend at various ER<sub>oa</sub> with fixed ER<sub>mb</sub> of 1.05**



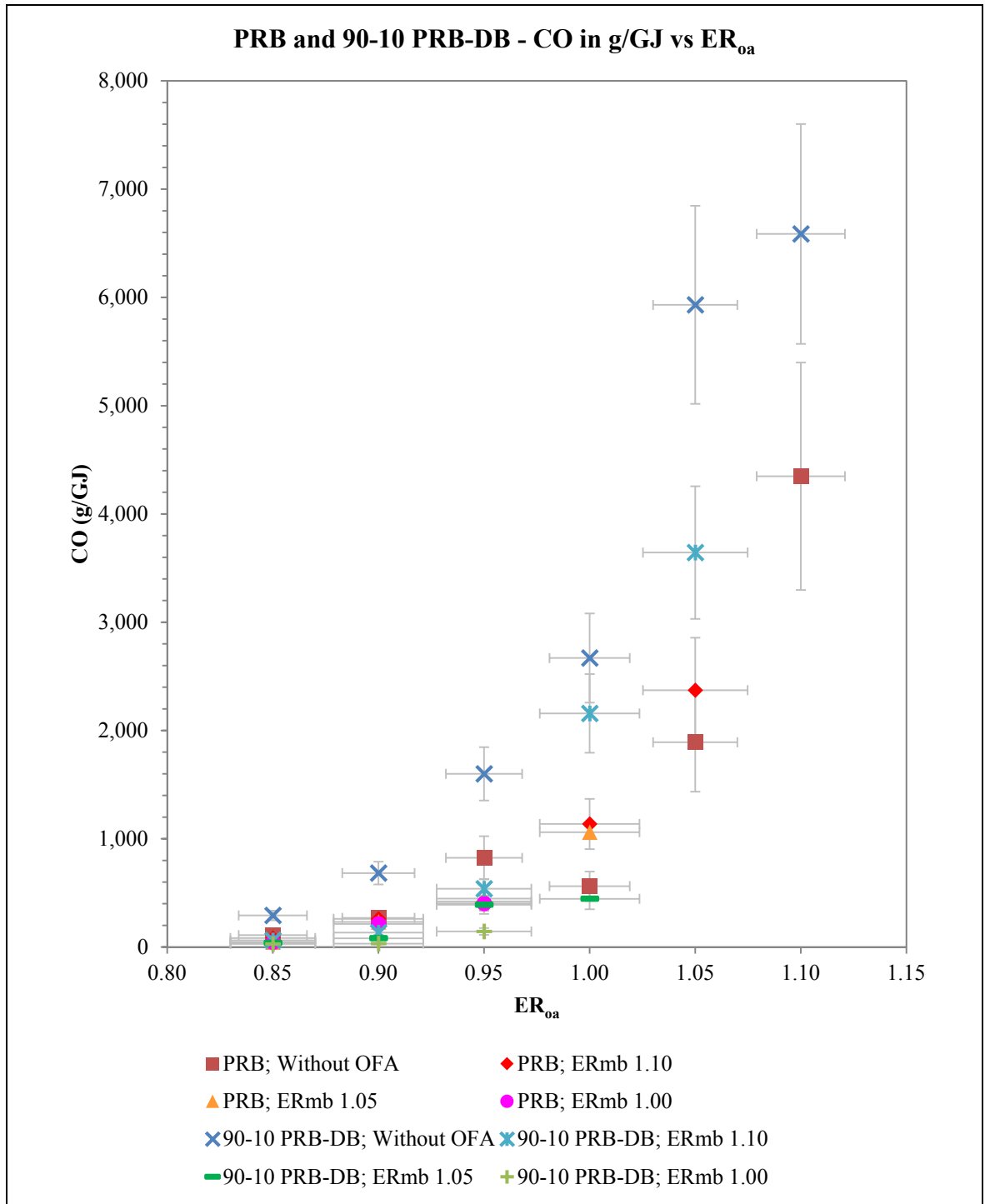
**Figure 52 – NO<sub>x</sub> emissions in g/GJ from firing PRB and co-firing 90-10 PRB-DB blend at various ER<sub>oa</sub> with fixed ER<sub>mb</sub> of 1.00**

### 7.3.3 Effects of OFA and Co-Firing 90-10 PRB-DB on CO Emission

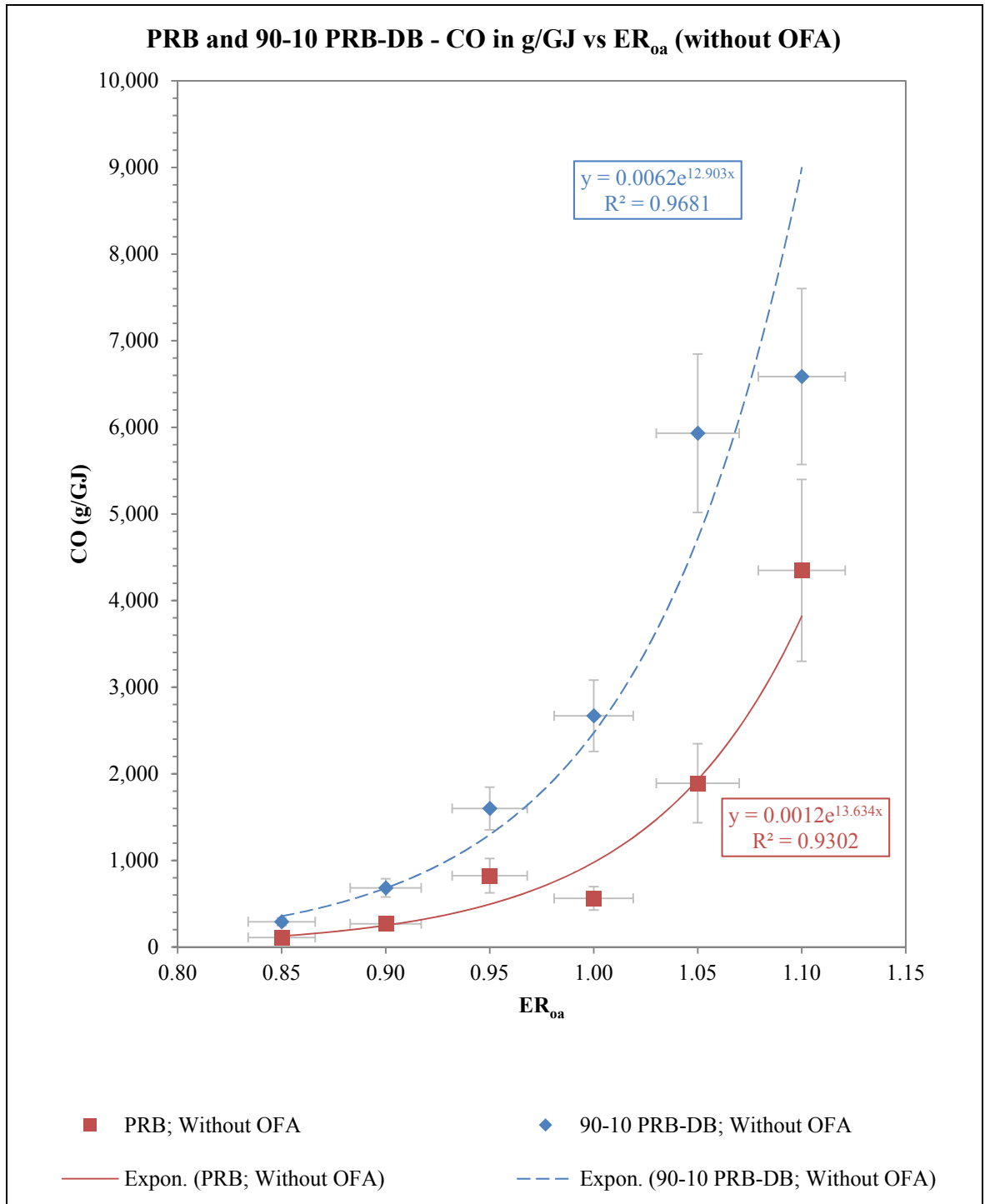
Next, from Figure 53 to Figure 57, CO rapidly increases when  $ER_{oa}$  increases and more so in rich regime due to incomplete combustion. The consequences of using OFA and co-firing 90-10 PRB-DB blend on CO emission are described as follows.

In general, the OFA introduced into the system could substantially decrease the amount of CO emission relative to the case without using OFA. Increasing  $ER_{mb}$  from 1.00 to 1.10 with the increment of 0.05 for firing pure PRB could result in the average percentages of CO reduction over the considering lean region ( $0.85 \leq ER_{oa} \leq 0.95$ ) at 35.3 %, 39.6 % and 25.4 % respectively. On the other hand, the results from co-firing 90-10 PRB-DB blend show that the average percentages of CO reduction are 86.9 %, 83.6 %, and 75.2 % respectively compared to the case without using OFA. By considering only  $ER_{oa}$  in the lean regime, blending PRB with DB will benefit in CO reduction especially when  $ER_{mb}$  is close to 1 ( $ER_{mb} \approx 1$ ).

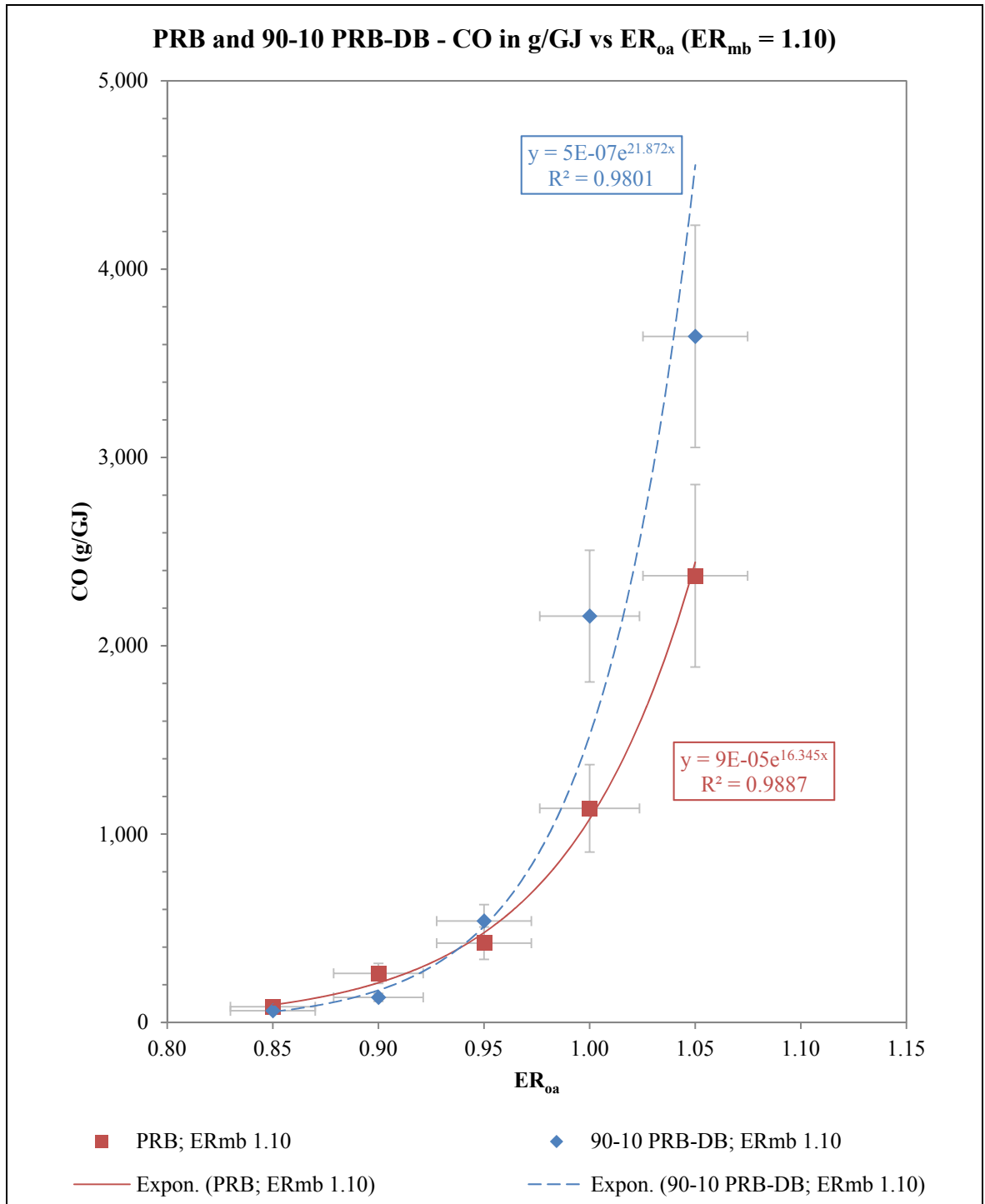
Moreover, by applying the proposed  $ER_{mb}$  and  $ER_{oa}$ , the excess  $O_2$  could be decreased from 3% to 1.1%, and the excess air could be reduced from 17.65% to 5.3%. Minimizing excess air will result in enhancing combustion and boiler efficiency and reducing energy consumption at the induced draft fan (IDF) of the reactor.



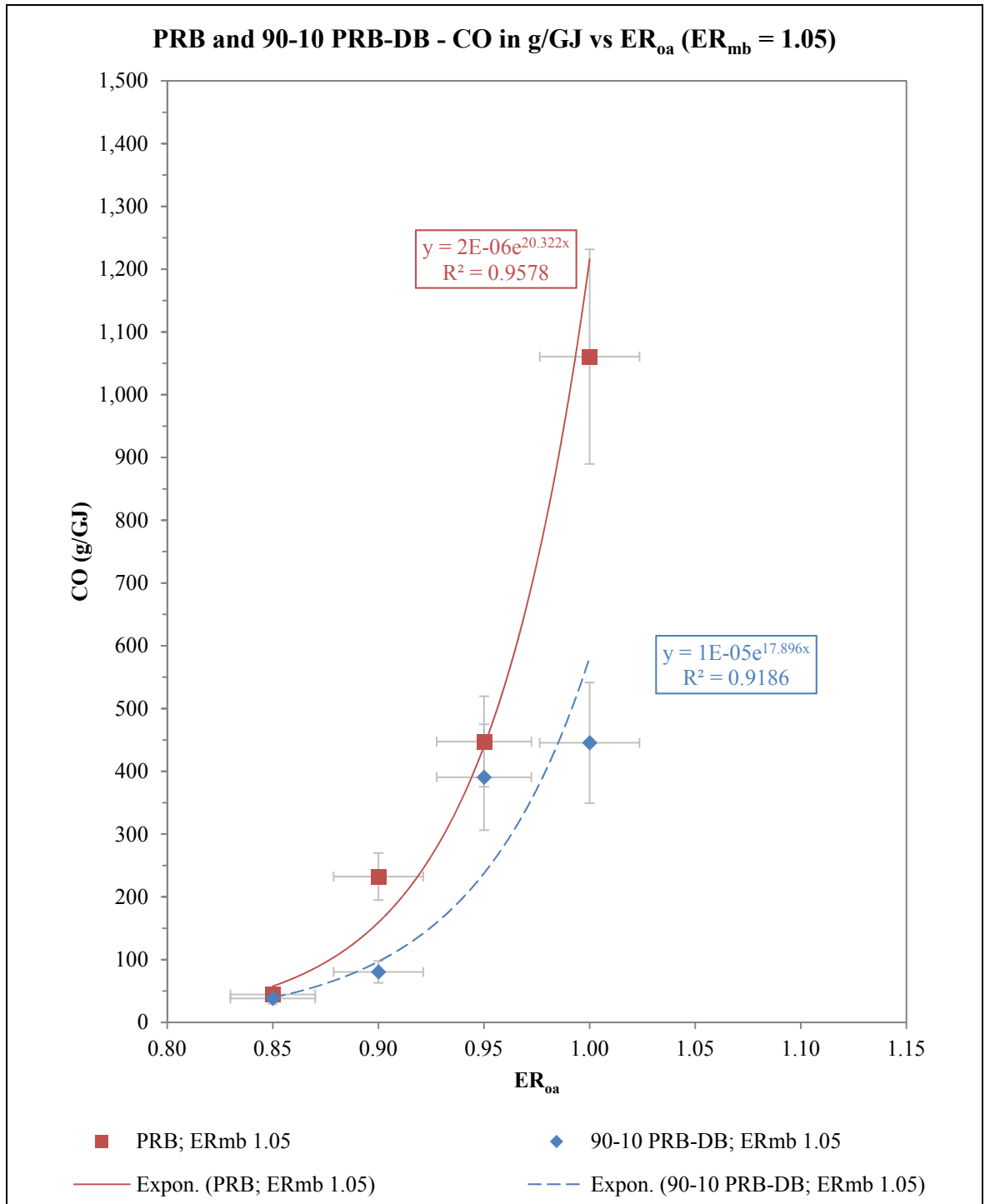
**Figure 53 – CO emission in g/GJ from firing PRB and co-firing 90-10 PRB-DB blend at various ER<sub>oa</sub>**



**Figure 54 – CO emission in g/GJ from firing PRB and co-firing 90-10 PRB-DB blend at various ER<sub>oa</sub> without OFA**

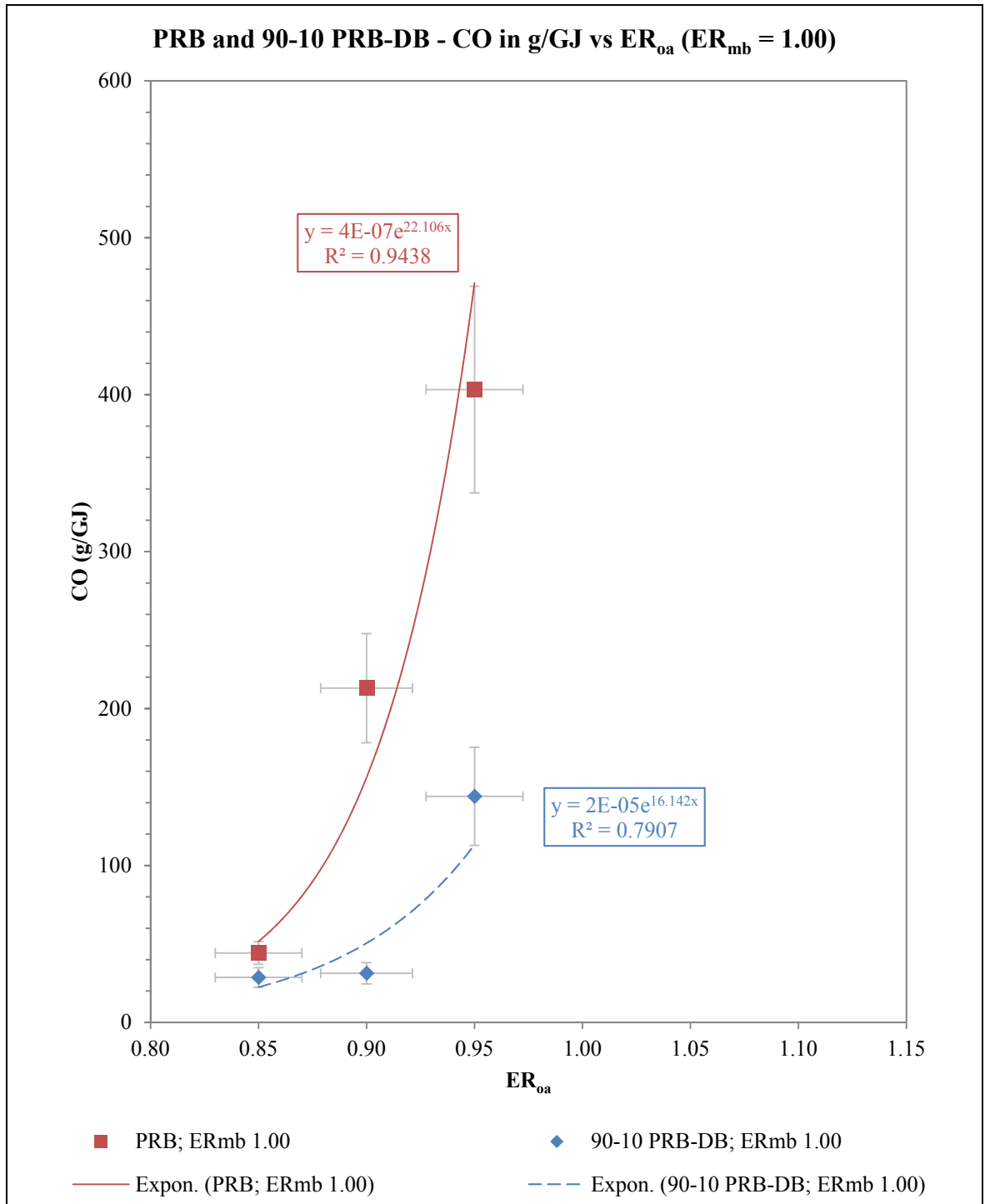


**Figure 55 – CO emission in g/GJ from firing PRB and co-firing 90-10 PRB-DB blend at various ER<sub>oa</sub> with ER<sub>mb</sub> of 1.10**



**Figure 56 – CO emission in g/GJ from firing PRB and co-firing 90-10 PRB-DB blend at various ER<sub>oa</sub> with ER<sub>mb</sub> of 1.05**

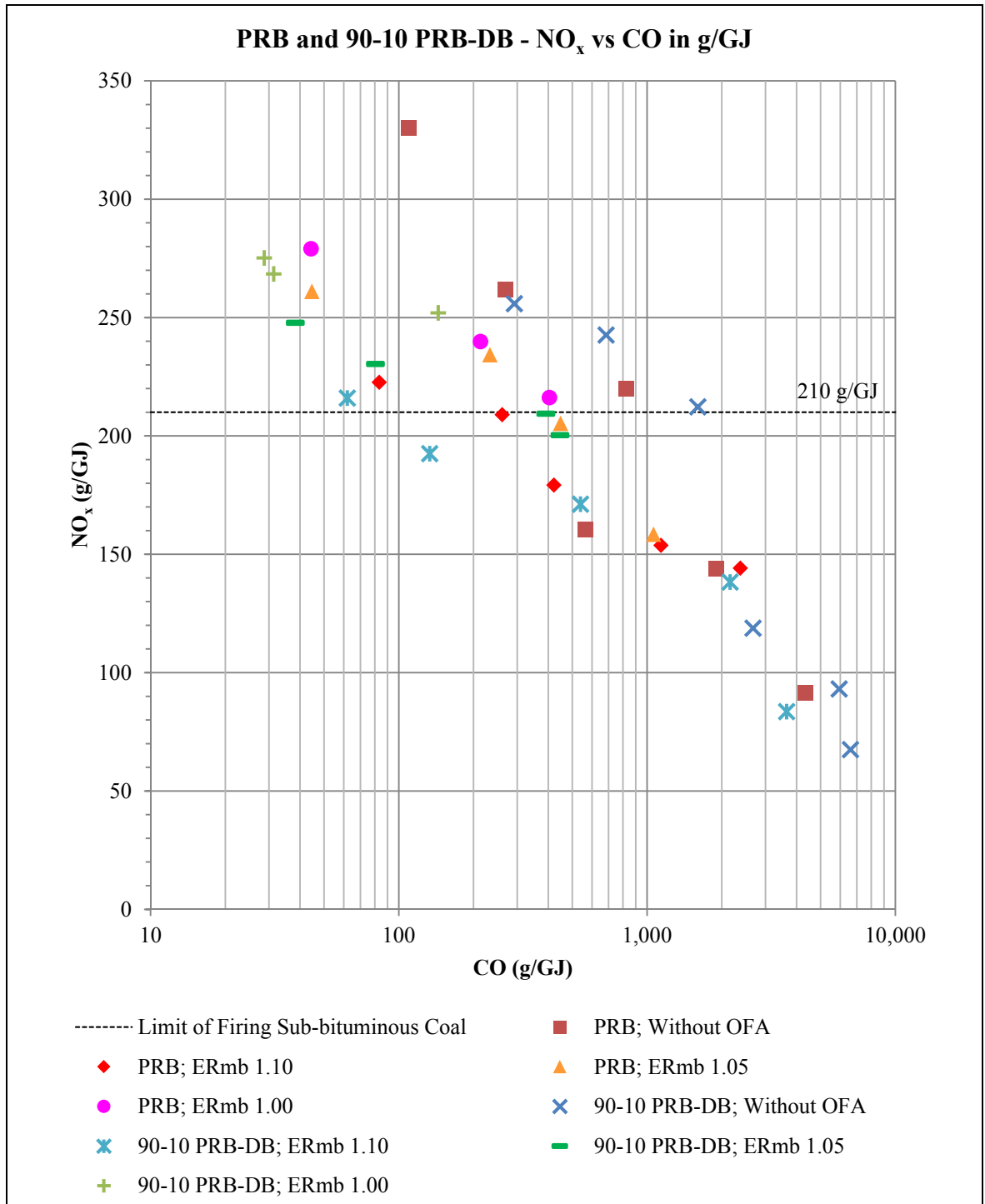




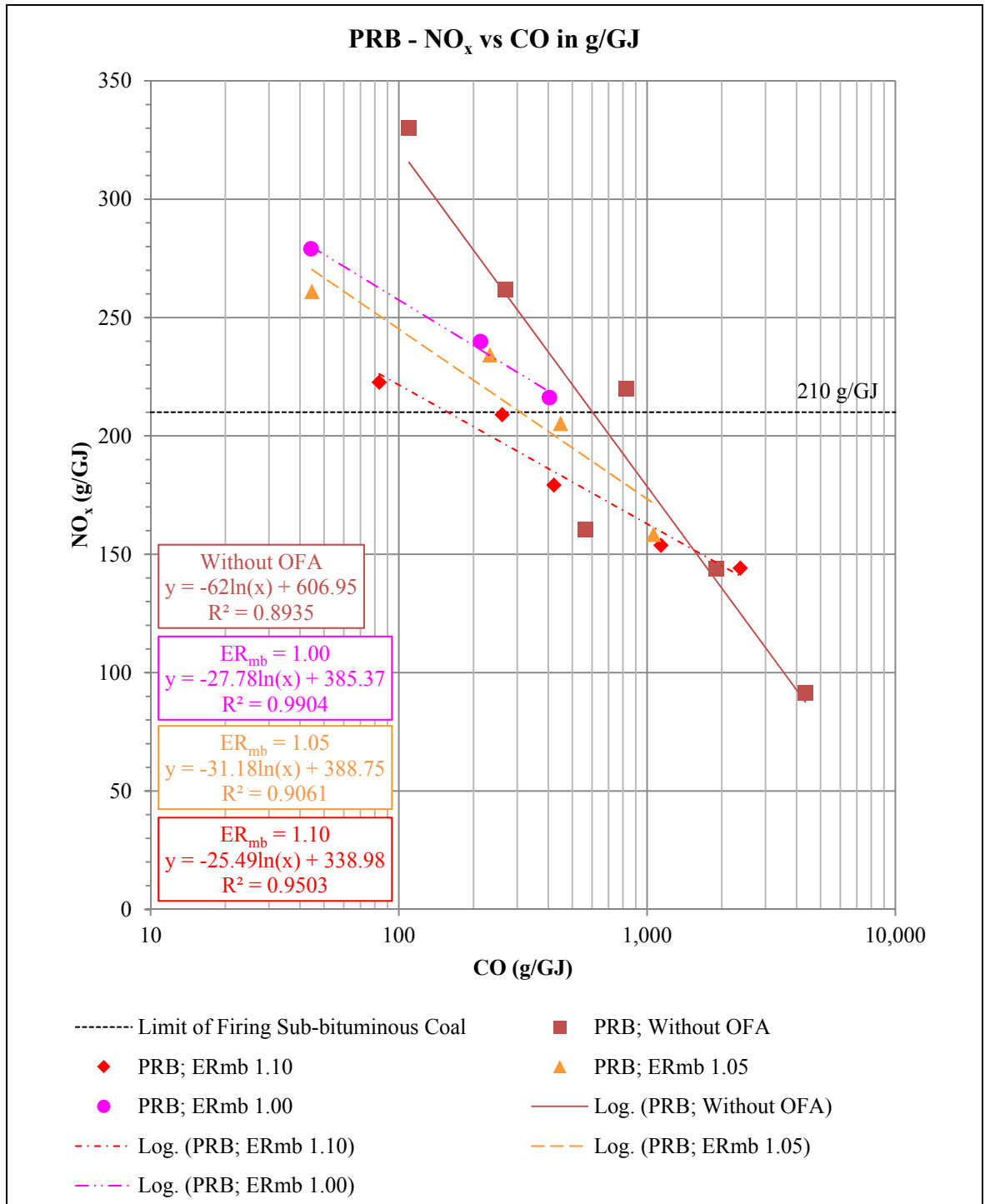
**Figure 57 – CO emission in g/GJ from firing PRB and co-firing 90-10 PRB-DB blend at various ER<sub>oa</sub> with ER<sub>mb</sub> of 1.00**

#### 7.3.4 Relations between $NO_x$ and CO

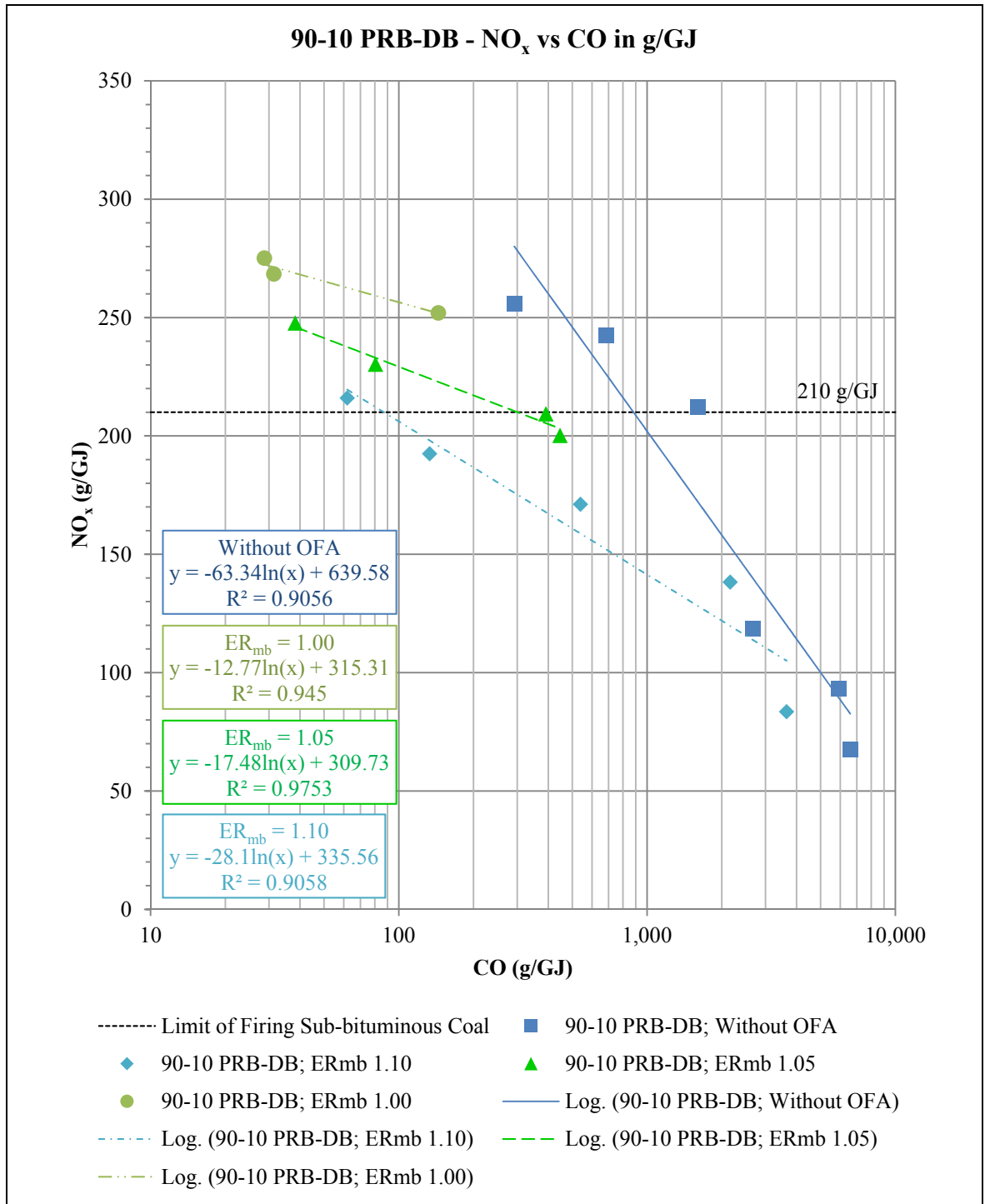
$NO_x$  and CO have an inverse relation as shown in Figure 58. When CO increases due to  $O_2$  deficiency,  $NO_x$  decreases because of lower  $O_2$  concentration. The plots, trend lines on logarithmic scale were drawn based on the experimental results as shown from Figure 59 to Figure 60. These plots indicate that when CO is fixed, increasing  $ER_{mb}$  will decrease the amount of  $NO_x$  emissions because  $O_2$  in the main burner zone decreases. For example, when CO from firing PRB is 200 g/GJ,  $NO_x$  from firing PRB at  $ER_{mb}$  of 1.10 and 1.00 will be approximately 210 and 260 g/GJ according to the trend lines shown in Figure 59. Equations for predicting the amount of  $NO_x$  or CO under various conditions are presented in Table 21. These equations can be used to estimate the amount of  $NO_x$  or CO in g/GJ when only one of the two values is known.



**Figure 58 – NO<sub>x</sub> versus CO in g/GJ from firing PRB and co-firing 90-10 PRB-DB blend at various ER<sub>oa</sub>**



**Figure 59 – NO<sub>x</sub> versus CO emissions from firing PRB in g/GJ at various ER<sub>oa</sub>**



**Figure 60 – NO<sub>x</sub> versus CO emissions from co-firing 90-10 PRB-DB blend in g/GJ**

**Table 21 – Equations for predicting the amount of NO<sub>x</sub> or CO**

Fuel/Condition	Equation of the Trend Line (y = NO <sub>x</sub> in g/GJ and x = CO in g/GJ)	R <sup>2</sup>
<u>PRB</u>		
- Without OFA	$y = -62 \ln(x) + 606.95$	0.8935
- ER <sub>mb</sub> 1.10	$y = -25.49 \ln(x) + 338.98$	0.9503
- ER <sub>mb</sub> 1.05	$y = -31.18 \ln(x) + 388.75$	0.9061
- ER <sub>mb</sub> 1.00	$y = -27.78 \ln(x) + 385.37$	0.9904
<u>90-10 PRB-DB</u>		
- Without OFA	$y = -63.34 \ln(x) + 639.58$	0.9056
- ER <sub>mb</sub> 1.10	$y = -28.1 \ln(x) + 335.56$	0.9058
- ER <sub>mb</sub> 1.05	$y = -17.48 \ln(x) + 309.73$	0.9753
- ER <sub>mb</sub> 1.00	$y = -12.77 \ln(x) + 315.31$	0.945

### 7.3.5 Burnt Fraction (BF)

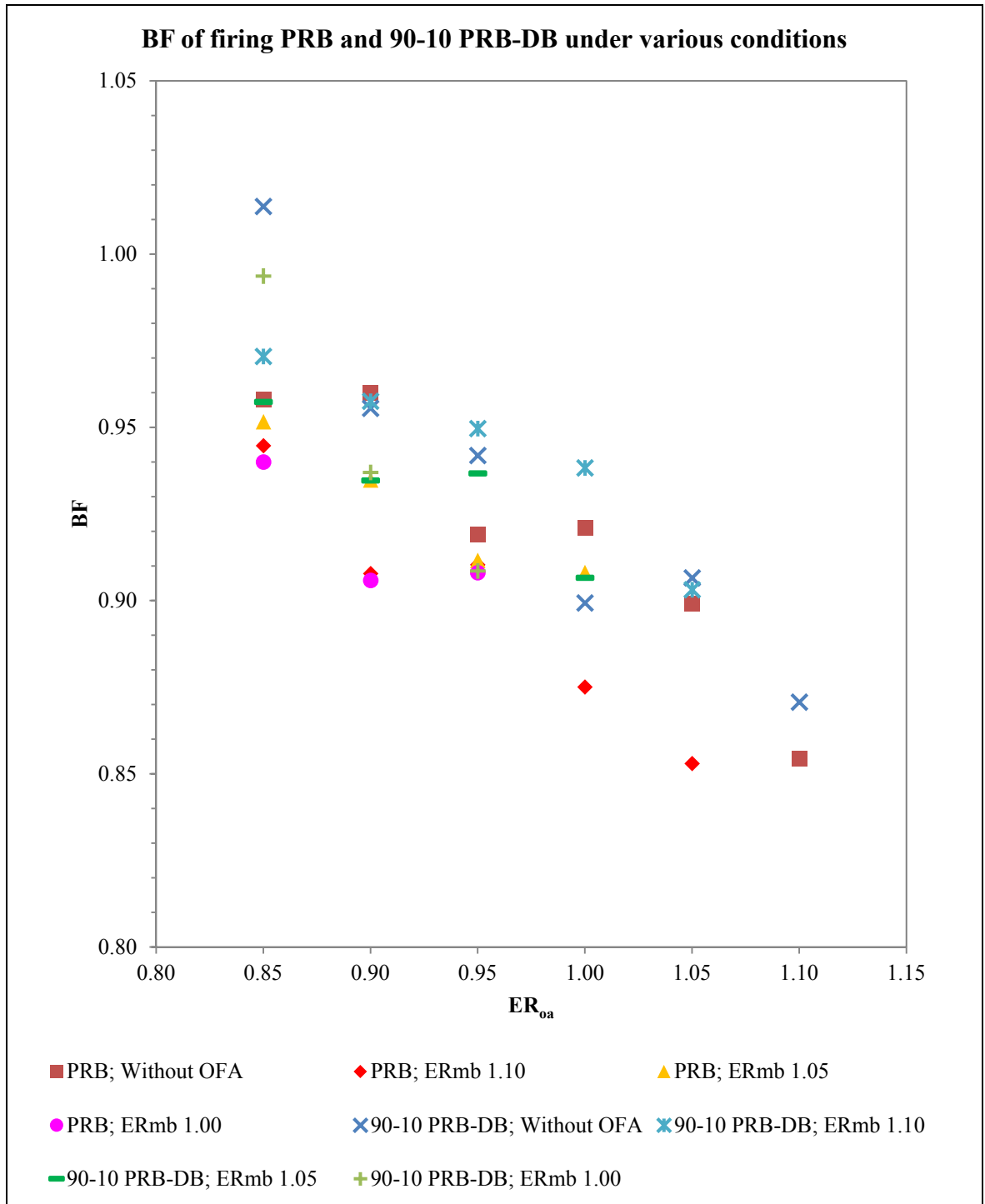
The BF can be estimated by using gas analyzer. The details and formula of BF calculation are given in Appendix L. First, Figure 61 shows that BF decreases when ER<sub>oa</sub> increases. In other words, when air is deficient (rich region), the combustion is incomplete. Therefore, there is fuel leftover in the process. This effect could be used to answer the question why there is excess O<sub>2</sub> even when the combustion occurs in the rich region as discussed earlier.

The results from BF calculation show that OFA does not substantially affect BF of each fuel type. In other words, OFA does not significantly change BF when  $ER_{oa}$  is maintained the same. For example, BF is 0.96 when both  $ER_{mb}$  and ER are 0.85 whilst BF is 0.94 when  $ER_{mb}$  is 1.00 and ER is 0.85. In addition, BF is 0.94 when  $ER_{mb}$  is 1.10 and ER is maintained at 0.85. This trend also occurs when  $ER_{oa}$  are 0.90 and 0.95.

Lastly, 90-10 PRB-DB blends seem to have higher BF. Table 22 shows the average BF of firing PRB and 90-10 PRB-DB in the lean regime when  $ER_{oa}$  is changed from 0.85 to 0.95. The values shown in Table 22 indicate that BF of co-firing 90-10 PRB-DB blend is slightly higher than BF of firing PRB.

**Table 22 – Average BF of firing PRB and 90-10 PRB-DB in lean region ( $ER_{oa}$  ranged from 0.85 to 0.95)**

Condition	PRB	90-10 PRB-DB	% Difference
Without OFA	0.95	0.97	+2.11
$ER_{mb}$ 1.10	0.92	0.96	+4.35
$ER_{mb}$ 1.05	0.93	0.94	+1.08
$ER_{mb}$ 1.00	0.92	0.95	+3.26



**Figure 61 – BF of firing PRB and co-firing 90-10 PRB-DB blend under various conditions**

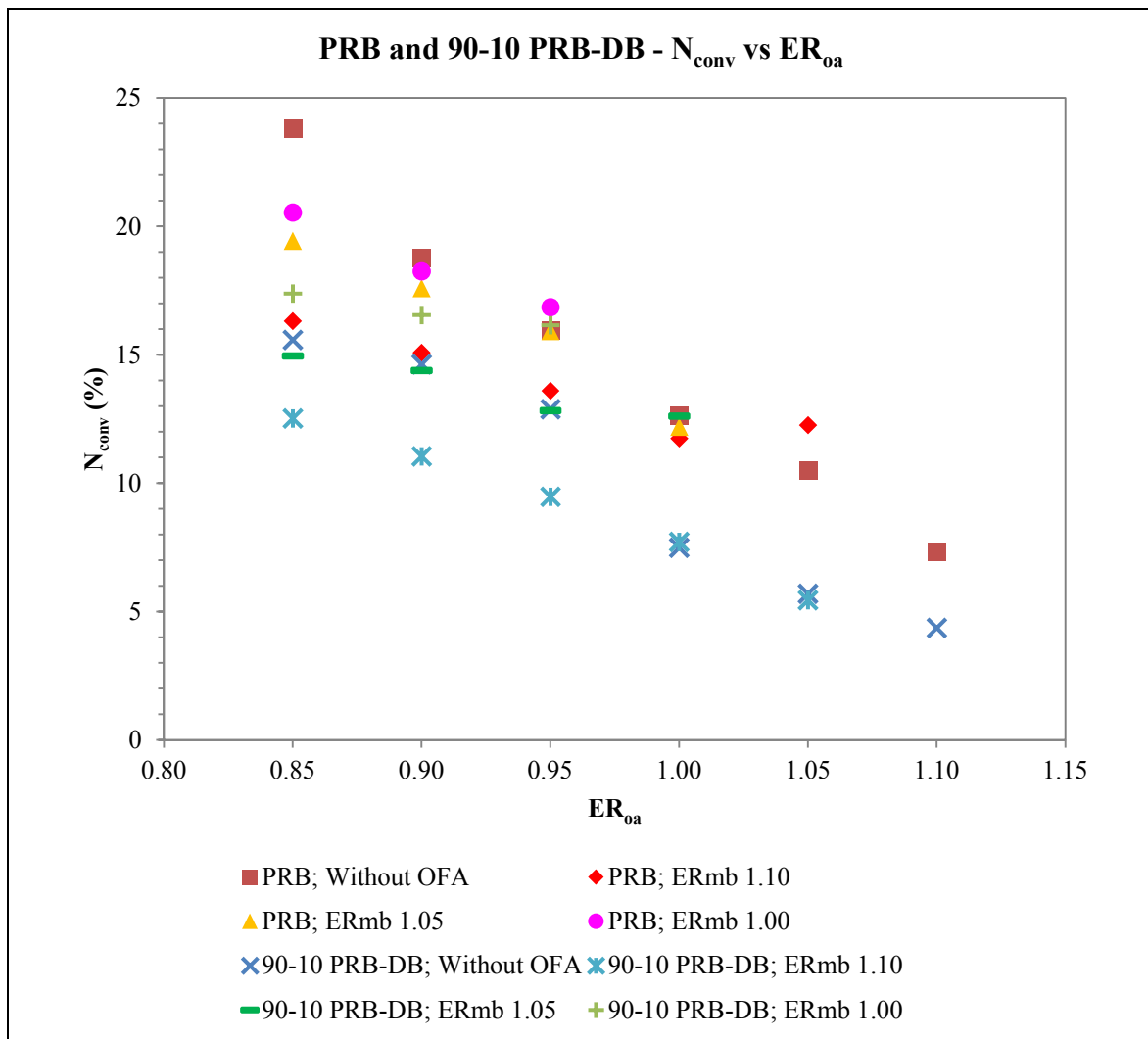


### 7.3.6 Fuel Nitrogen Conversion Efficiency ( $N_{conv}$ )

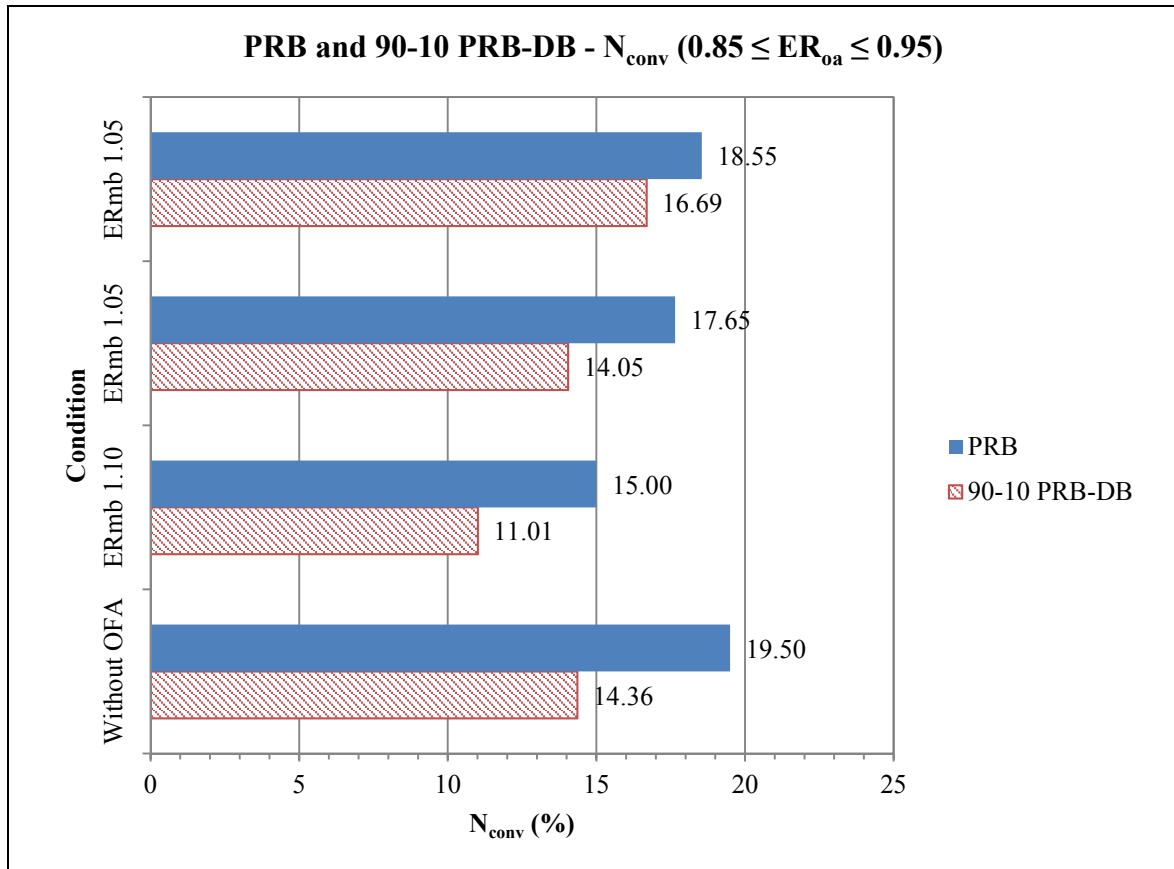
The fuel  $N_{conv}$  is used to estimate how much fuel N could be converted into  $NO_x$ . In other words, this value could be used to imply how much  $NO_x$  are formed by the fuel-bound mechanism. The equation used for  $N_{conv}$  calculation and the results of calculation are given in Appendix M. Typically, the  $NO_x$  emitted in coal combustion causes of fuel, thermal and prompt  $NO_x$ . Thermal  $NO_x$  mechanism is assumed to follow Zeldovich model, the amount of thermal  $NO_x$  will be insignificant when the temperature is below 1,800 K. As a result, the amount of thermal  $NO_x$  measured is negligible since temperature is less than 1,800 K. Typically, prompt  $NO_x$  even for natural gas is small. Hence, it is assumed that all  $NO_x$  originated from fuel N in estimating  $N_{conv}$ . Also, there is likelihood of prompt  $NO_x$  when occurs in rich regime where HC fragments are produced. Thus, when main burner is operated under rich condition, there is likelihood of formation of prompt  $NO_x$ .

From Figure 62, the plot shows that  $N_{conv}$  decreases when  $ER_{oa}$  increases. That means the effect of fuel-bound  $NO_x$  formation is lowered when  $O_2$  concentration is reduced. The reason that DB could decrease  $NO_x$  formation despite the fact that DB contains higher N content (higher N loading) than PRB (refer to Table 13 and Table 17) is VM released by DB at lower temperature could interrupt fuel-bound mechanism. However,  $N_{conv}$  of 90-10 PRB-DB blend increases when  $ER_{mb}$  decreases due to more residence time in the high  $O_2$  concentration environment as discussed earlier. For example, when  $ER_{mb}$  of co-firing 90-10 PRB-DB blend decreases from 1.10 to 1.00 with  $ER_{oa}$  of 0.95,  $N_{conv}$  increases from 9.47% to 16.15%.

In conclusion, refer to Figure 63, firing PRB with OFA could decrease  $N_{conv}$  when the primary combustion zone is operated in the rich region. However, co-firing 90-10 PRB-DB blend should be done only when  $ER_{mb}$  is 1.10; otherwise, blending DB into PRB will increase  $N_{conv}$  instead.



**Figure 62 – Fuel N conversion efficiency of firing PRB and co-firing 90-10 PRB-DB blend under various conditions**



**Figure 63 – Average fuel N conversion efficiency of lean combustion under various conditions ( $ER_{oa}$  ranged from 0.85 to 0.95)**

### 7.3.7 Respiratory Quotient (RQ)

RQ can be used to estimate the  $CO_2$  loading per GJ of heat input. If RQ is high, it means that  $CO_2$  is produced more with the same amount of  $O_2$  consumed (same heat input). Therefore, any modification in combustion system should also concern how to maintain or lower RQ. The formulae for calculating RQ are given in Appendix N.

From Table 23, RQ of PRB and DB calculated by fuel composition are constant at 0.94. Additionally, RQ of PRB and DB computed by using theoretical flue gas composition are 0.94 and 0.93 respectively. Therefore, blending PRB and DB together will not theoretically impact the RQ.

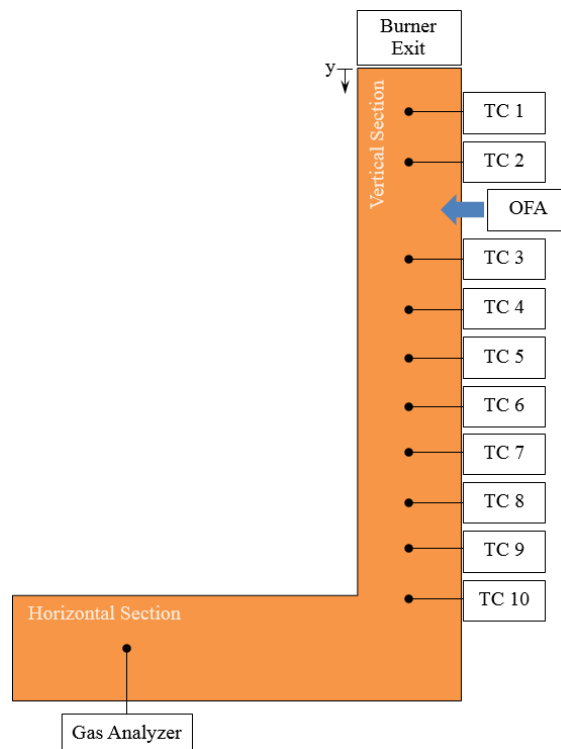
However, by using flue gas composition obtained from the experiments, RQ increases when  $ER_{mb}$  is in the rich region and OFA is introduced into the system. RQ also increases when fuel blends are burned. CO formation increases  $O_2$  in flue gas which results in decrease of RQ. RQ formulae presume that fuel is burnt completely to  $CO_2$  and  $H_2O$ ; thus, the formation of CO results in more  $O_2$  in exhaust. The stoichiometric  $O_2$  in RQ analysis is computed by difference between  $O_2$  supplied and  $O_2$  in flue gas; thus, increased  $O_2$  due to CO results in underestimation of stoichiometric  $O_2$  and RQ increase.

**Table 23 – RQ of PRB, DB and 90-10 PRB-DB blend**

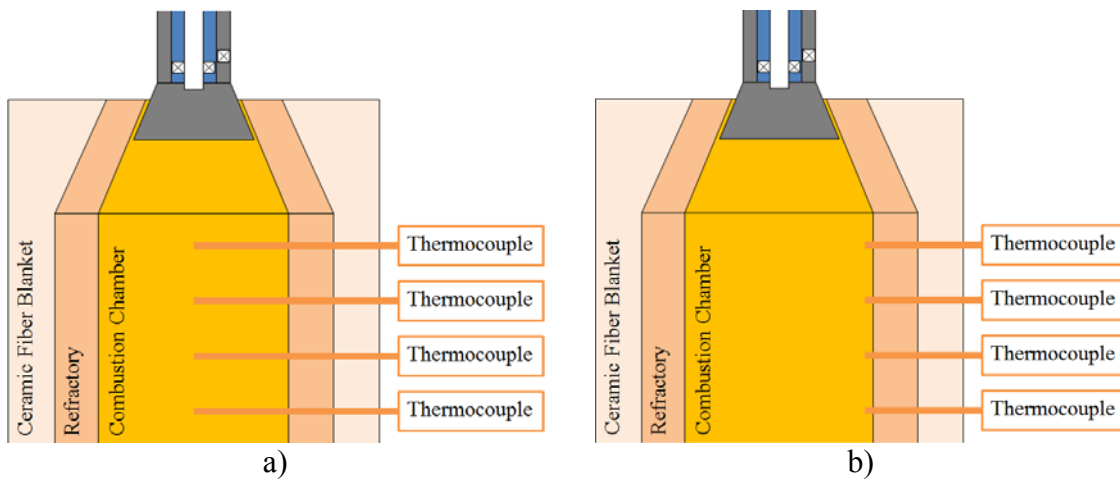
RQ by	PRB	DB	90-10 PRB-DB
Fuel Composition	0.94	0.94	0.94
Theoretical flue gas	0.94	0.93	0.94
Experimental results			
- Without OFA	0.94	N/A	0.97
- $ER_{mb}$ 1.05	0.97	N/A	1.00
- $ER_{mb}$ 1.10	1.03	N/A	1.09

### 7.3.8 Effects of OFA and Co-Firing 90-10 PRB-DB on Temperature Profiles

Temperature along the vertical section of the furnace was measured by type-K thermocouples at ten different levels as shown as “TC” in Figure 64. Each thermocouple measured temperature at the center of the flow ( $T_c$ ) and temperature of the flow near the wall of the combustion chamber ( $T_w$ ) on the same horizontal plane as illustrated in Figure 65-a and Figure 65-b respectively. Note that TC 1 was used to measure  $T_w$  only. The reason is measuring  $T_c$  at TC 1 level can interrupt the recirculating flow because TC 1 is 179 mm below the burner exit whilst the length of RZ ( $L_{rz}$ ) obtained from NRF simulation is approximately 200 – 220 mm (see Appendix F).



**Figure 64 – Illustration of thermocouples arrangement**

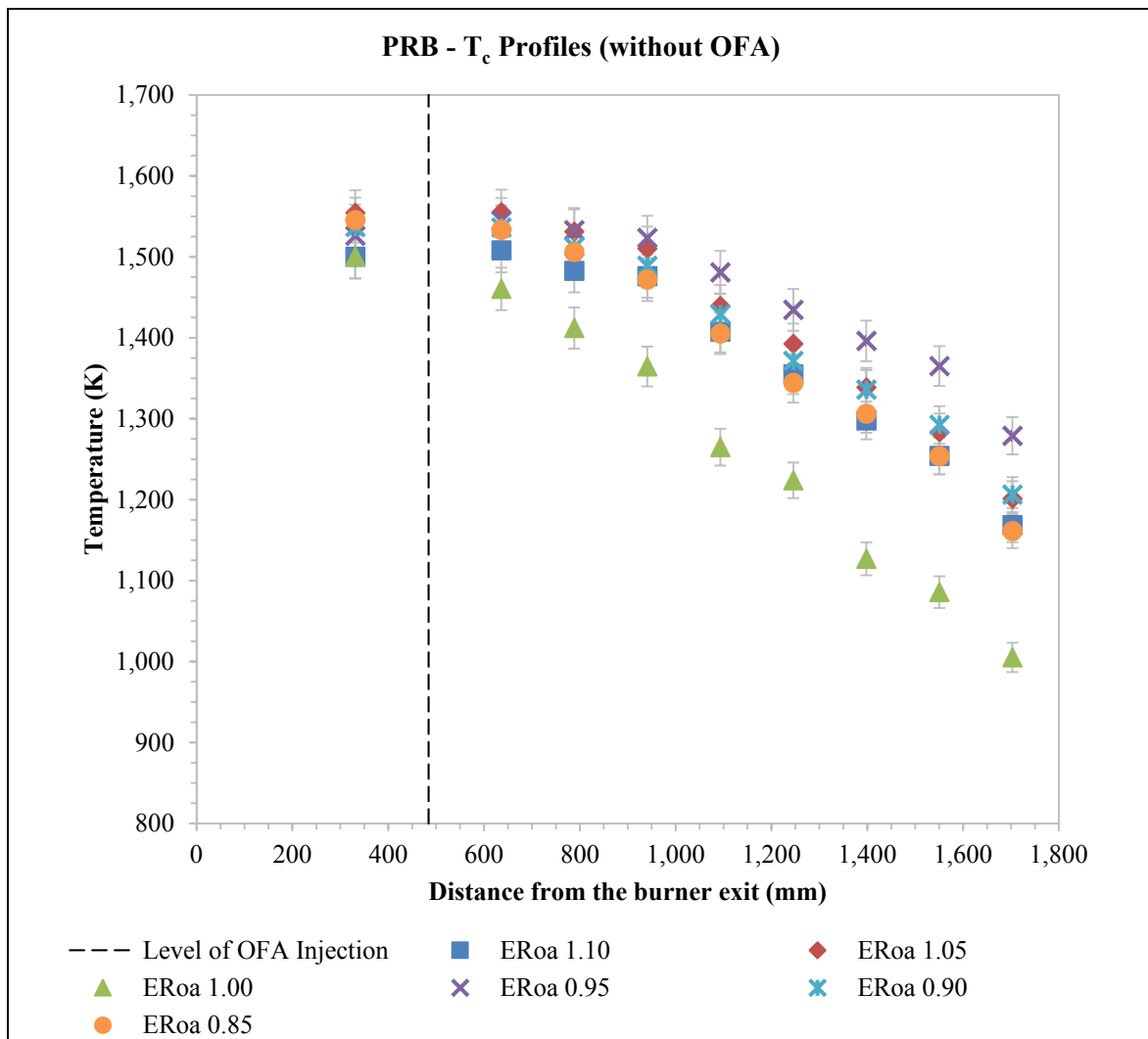


**Figure 65 – Location of thermocouples for measuring: a)  $T_c$  and b)  $T_w$**

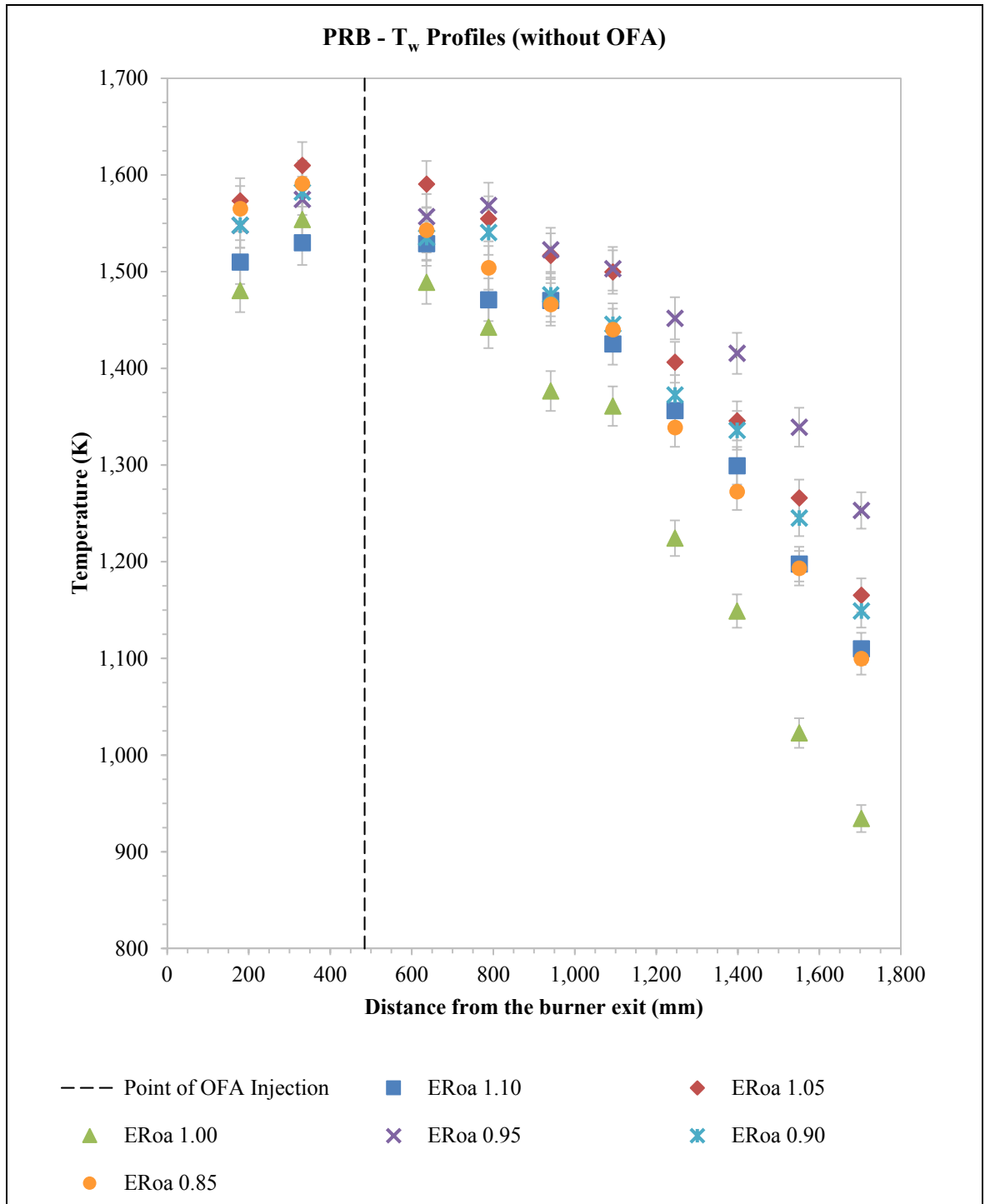
The results of firing PRB and co-firing 90-10 PRB-DB blend without OFA injection as shown from Figure 66 to Figure 69 indicate that the values of  $T_w$  measured from TC 1 to TC 8 are higher than  $T_c$ , but  $T_w$  measured from TC 9 and TC 10 are lower than  $T_c$ . On the average,  $T_w$  is higher than  $T_c$  by approximately 30 K if calculated by using the peak temperature data (Appendix K). In addition, consider the combustion in the lean regime ( $0.85 \leq ER_{oa} \leq 0.95$ ). The average  $T_w$  ( $T_{w,avg}$ ) of firing PRB are and co-firing 90-10 PRB-DB blend are higher than the average  $T_c$  ( $T_{c,avg}$ ) calculated by the integration method as detailed in Appendix K. To be more specific,  $T_{w,avg}$  is 65.7 K higher than  $T_{c,avg}$  when PRB is burned without OFA, and  $T_{w,avg}$  is slightly higher than  $T_{c,avg}$  when 90-10 PRB-DB blend is burned.

It is due to the swirling flow from the main burner which creates RZ below the main burner and forces the product gases (i.e. hot gases) to adhere to the wall of combustion chamber. However, even though the reactor is insulated, heat loss still

occurs due to higher surface-to-volume ratio (S/V) in a small reactor. The temperature gradient ( $T_c - T_w$ ) is created. At the same time, swirl also creates pressure gradient at the center of the chamber and induces a portion of hot gases from the far field into the near field of burner. Thus,  $T_c$  and  $T_w$  are not too much different.

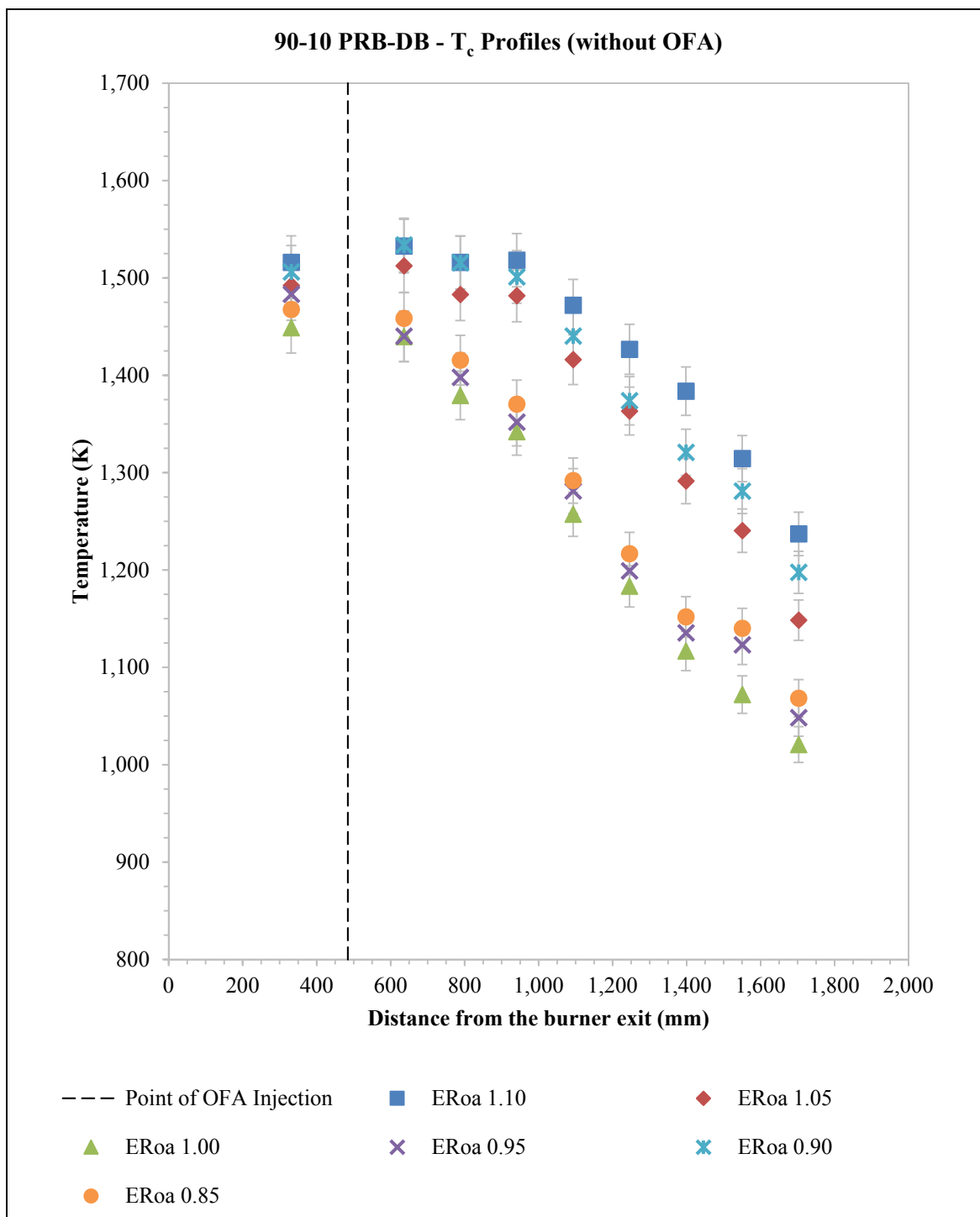


**Figure 66 –  $T_c$  profile of firing PRB without OFA at various  $ER_{oa}$**

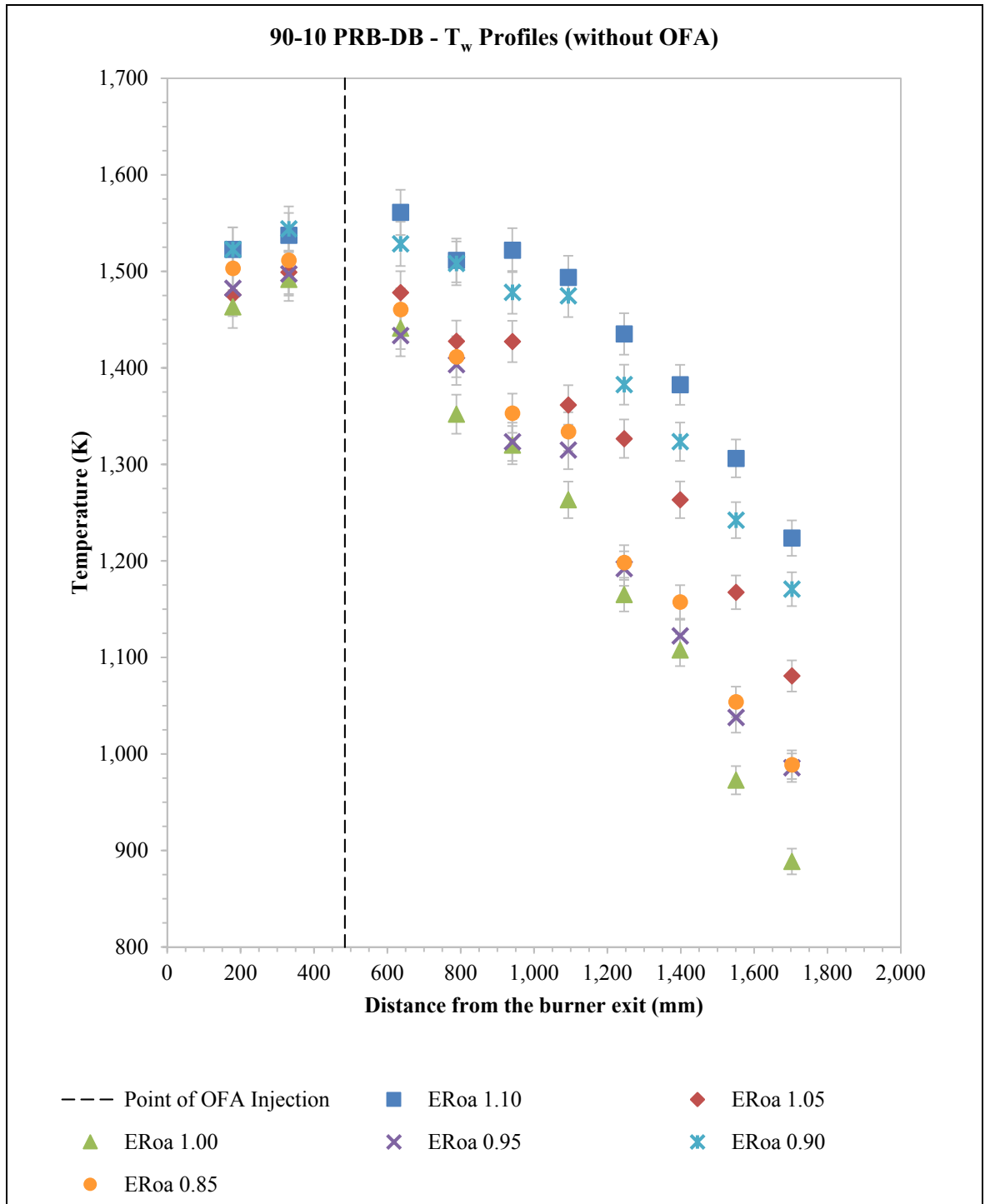


**Figure 67 –  $T_w$  profile of firing PRB without OFA at various  $ER_{oa}$**





**Figure 68 –  $T_c$  profile of co-firing 90-10 PRB-DB blend without OFA at various  $ER_{oa}$**



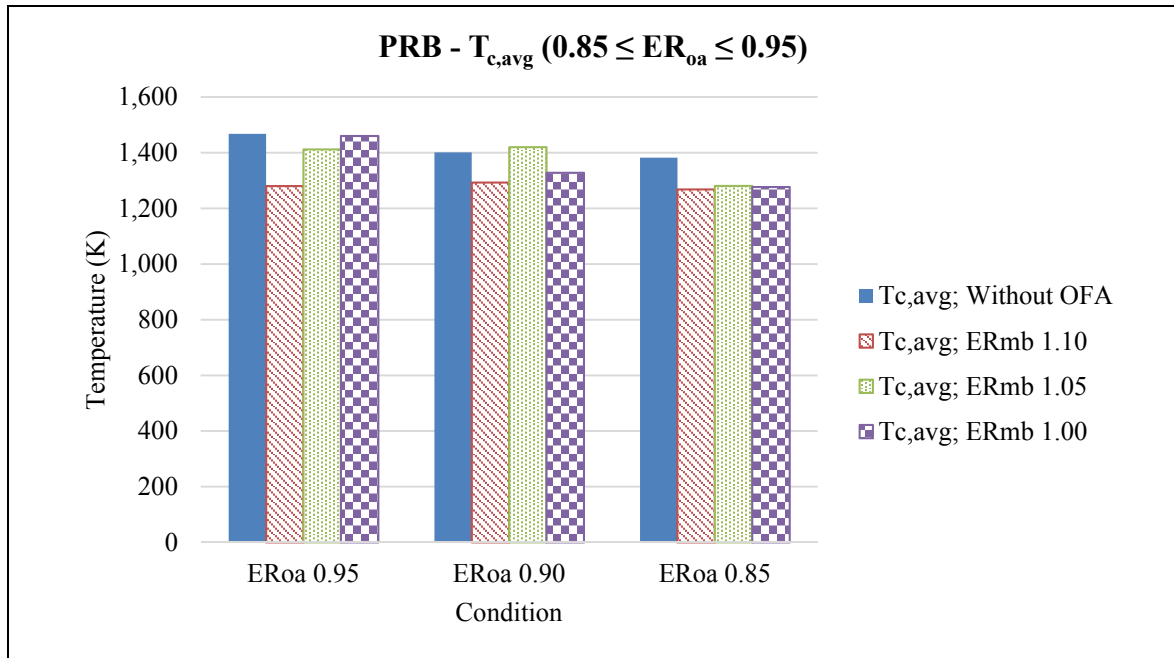
**Figure 69 –  $T_w$  profile of co-firing 90-10 PRB-DB blend without OFA at various  $ER_{oa}$**

The effects of OFA injection on temperature profile could be investigated by keeping  $ER_{oa}$  constant and varying  $ER_{mb}$ . In other words, more OFA is injected into the combustion chamber when the amount of secondary air is decreased in order to maintain the  $ER_{oa}$  at the same value. For example, from Appendix C, in case  $ER_{mb}$  is initially set at 1.00, the mass flow rate of OFA will be 5.97 kg/hr in order to make  $ER_{oa}$  equal to 0.85. However, when  $ER_{mb}$  is increased to 1.10, the mass flow rate of OFA will be adjusted to 9.04 kg/hr in order to keep  $ER_{oa}$  at 0.85 or overall mass flow rate of air at 39.79 kg/hr. Percentages of the mass flow rate of OFA to the mass flow rate of the main airflow ( $\dot{m}_{OFA}/(\dot{m}_{PA} + \dot{m}_{SA})$ ) are given in Table 24.

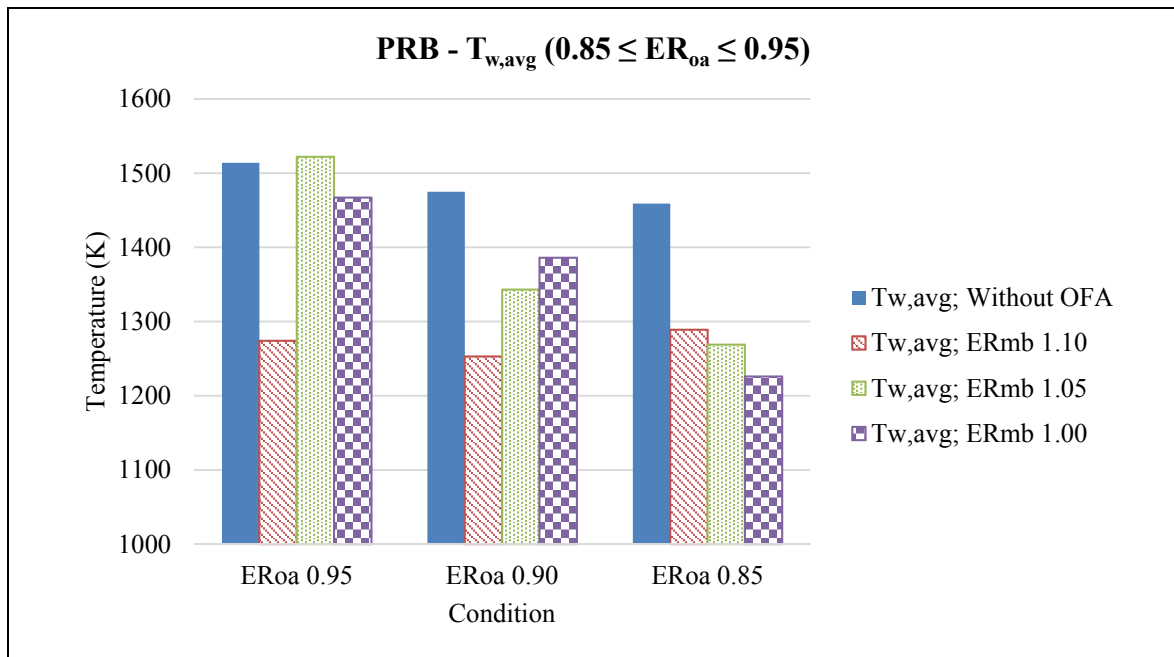
**Table 24 – Percentages of the mass flow rates of OFA to the main airflow**

$ER_{mb}$	Percentages of the mass flow rates of OFA to the main airflow at $ER_{oa}$					
	1.10	1.05	1.00	0.95	0.90	0.85
1.10	0	4.76	10	15.79	22.22	29.41
1.05	-	0	5	10.53	16.67	23.53
1.00	-	-	0	5.26	11.11	17.65

$T_{c,avg}$  and  $T_{w,avg}$  from firing PRB with OFA in lean regimes ( $0.85 \leq ER_{oa} \leq 0.95$ ) are shown from Figure 70 to Figure 71. When  $ER_{oa}$  was set at 0.95 and  $ER_{mb}$  was increased from 1.00 to 1.10, i.e. decreased the volume flow rate of secondary air and increased the volume flow rate of OFA,  $T_{c,avg}$  significantly dropped from 1,460 K to 1,280 K because hot gases were mixed with cold gas (air at ambient temperature). It can be deduced that injecting OFA into coal combustion system will decrease the average flow temperature.



**Figure 70 – Average  $T_c$  of firing PRB in lean regime by varying  $ER_{mb}$**



**Figure 71 – Average  $T_w$  of firing PRB in lean regime by varying  $ER_{mb}$**

For 90-10 PRB-DB blend, the values of  $T_{c,avg}$  and  $T_{w,avg}$  as shown in Figure 72 and Figure 73 are very fluctuating and it is very difficult to assess the effect of OFA injection on temperature profile. Nonetheless, by setting  $ER_{mb}$  at 1.05 and  $ER_{oa}$  at 0.85 or 0.95,  $T_{c,avg}$  and  $T_{w,avg}$  are higher than co-firing 90-10 PRB-DB blend without OFA.

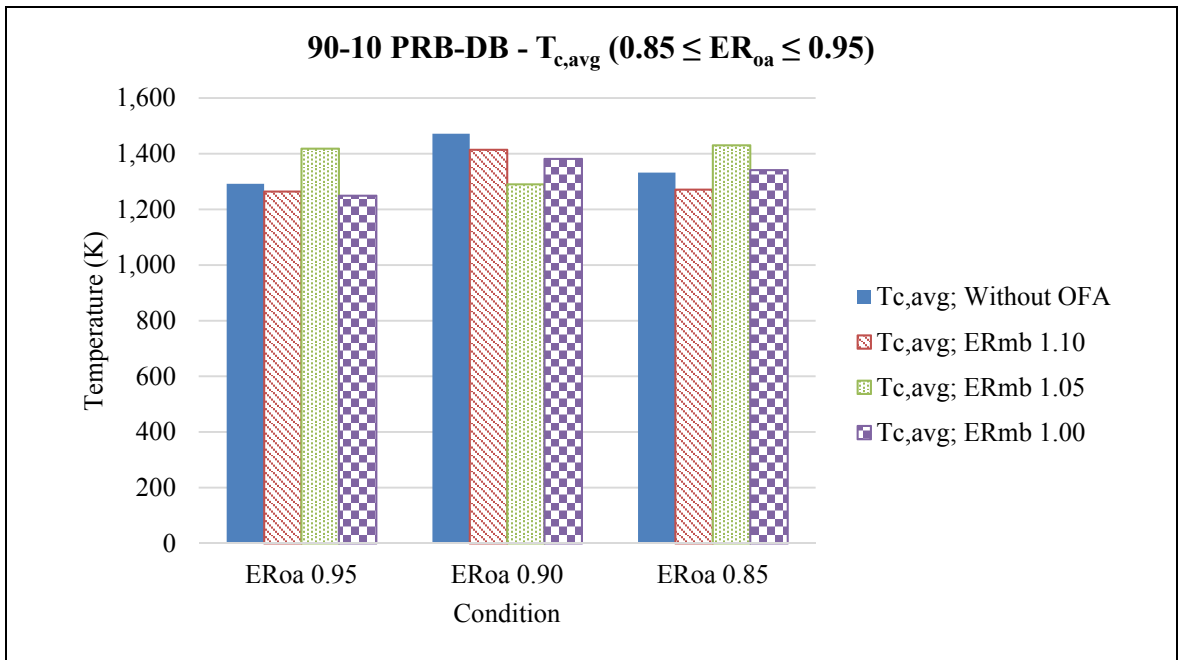
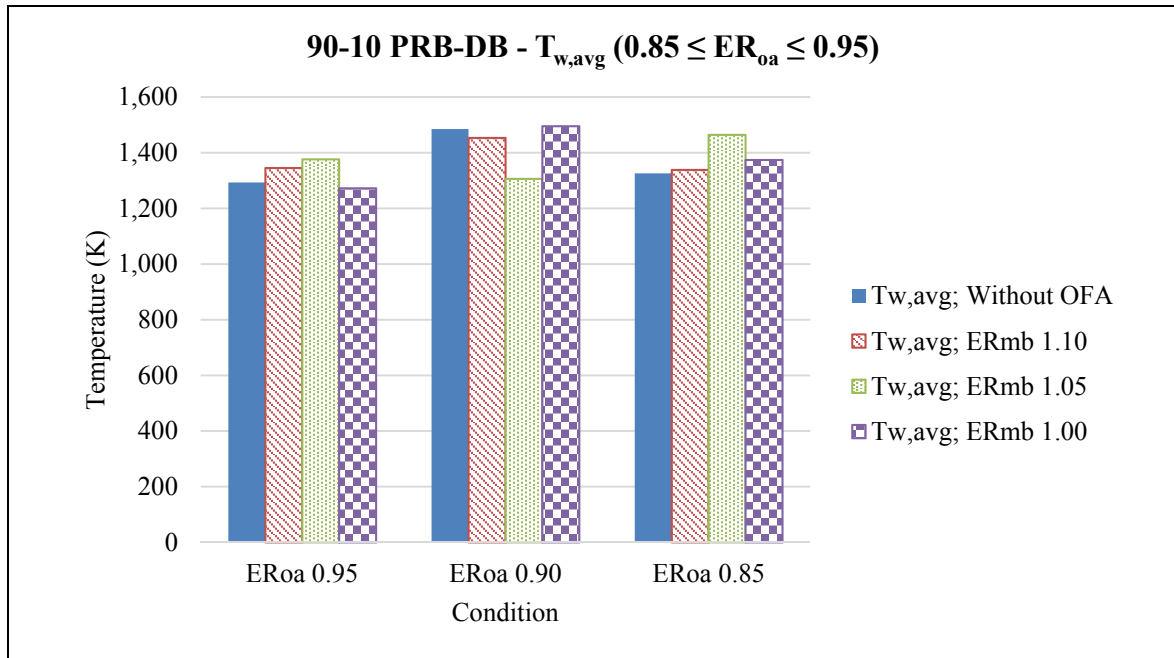
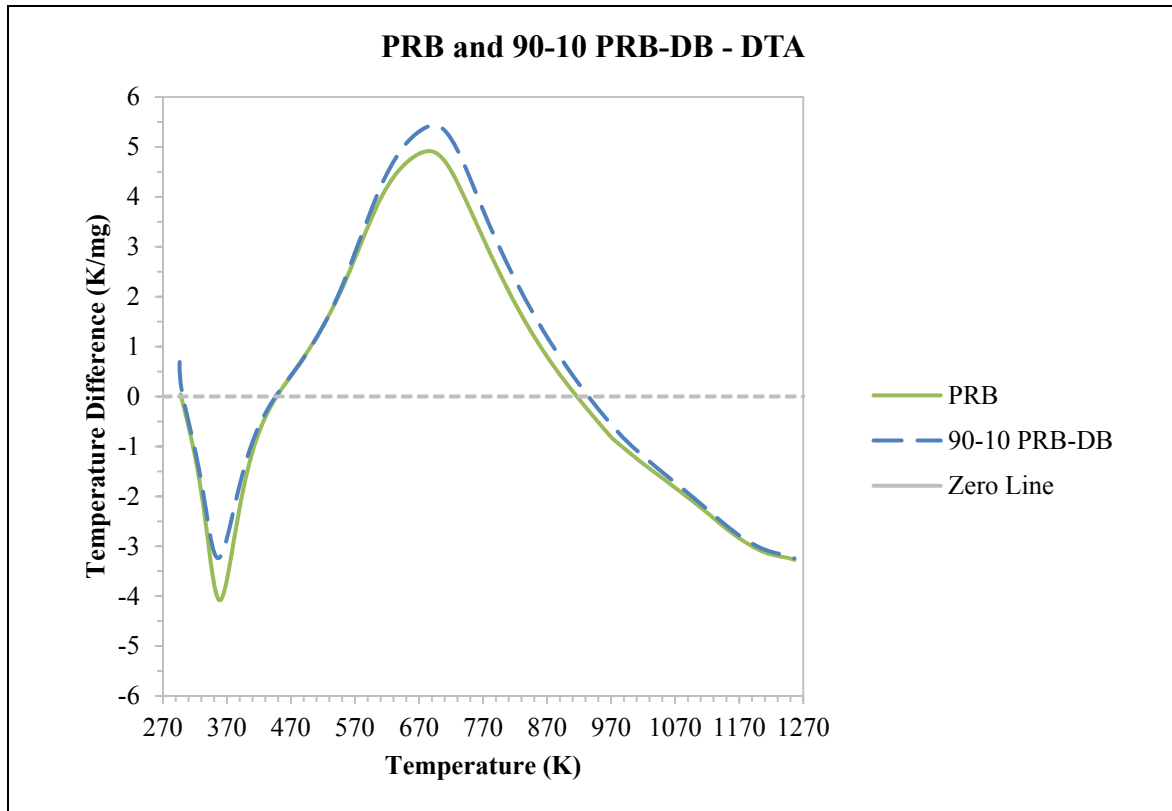


Figure 72 – Average  $T_c$  of co-firing 90-10 PRB-DB in lean regime by varying  $ER_{mb}$



**Figure 73 – Average  $T_w$  of co-firing 90-10 PRB-DB in lean regime by varying  $ER_{mb}$**

For PRB, the peak  $T_c$  (1,559 K) occurred at  $x = 636$  mm (TC 3) when  $ER_{mb}$  and  $ER_{oa}$  were set at 1.05 and 0.95 respectively; meanwhile, the peak  $T_w$  (1,610 K) occurred at  $x = 331$  mm (TC 2) when  $ER_{mb}$  was 1.05 without OFA. For 90-10 PRB-DB, both peak  $T_c$  (1,544 K) and peak  $T_w$  (1,577 K) occurred at  $x = 636$  mm (TC 3) when  $ER_{mb}$  and  $ER_{oa}$  were set at 1.05 and 1.00 respectively. The overall average of peak  $T_c$  and  $T_w$  from firing PRB and co-firing 90-10 PRB-DB blend indicates that firing 90-10 PRB-DB decreases  $T_c$  and  $T_w$  about 17 K and 14 K respectively. Note that the results from differential thermal analysis (DTA) (Figure 74) indicate that 90-10 PRB-DB releases volatiles at the faster rate compared to PRB. Even though DB has more VM, its HV is lower than that of VM from PRB (Appendix B); the 90-10 PRB-DB blend is on mass basis but it is approximately 94:6 on heat basis since DB has lower HHV.



**Figure 74 – Results of DTA in inert gas of PRB and 90-10 PRB-DB blend**

However, the solidified ash was found on the surface of the thermocouples that were used after running all of the proposed experimental conditions for 90-10 PRB-DB blend. It is speculated that this solidified ash might act like insulation and block heat transfer from the hot gases to the metal surface of the thermocouples; hence,  $T_c$  and  $T_w$  from co-firing 90-10 PRB-DB blend might be lower because of this.

To sum up, the operating condition proposed in the earlier subsection (co-firing 90-10 PRB-DB with  $ER_{mb}$  of 1.10 and  $ER_{oa}$  of 0.95) shows that peak  $T_c$  and peak  $T_w$  decrease by 76 K and 77 K respectively compared to the base case (firing PRB with  $ER_{oa}$  of 0.85 without OFA) due to addition of low quality (low HV) biomass fuels.

### 7.3.9 Uncertainty Analysis of Flue Gas Measurement

Lastly, the uncertainty analysis was conducted in order to check whether the data obtained from the experiments were reliable particularly the flue gas composition which is the main part of the current research. Table 25 and Table 26 show that the overall uncertainties of O<sub>2</sub>, CO<sub>2</sub> and NO<sub>x</sub> are lower than 5% which are generally within the acceptable range. However, the uncertainty of CO is higher than 15% due to the fact that E-8500 gas analyzer has to usually purge the CO line in order to prevent the line from clogging. Therefore, in the future, specific CO detector should be used instead of E-8500 gas analyzer in order to obtain more accurate results.

**Table 25 – Overall uncertainties of flue gas measurement from firing PRB under various conditions**

Condition	O <sub>2</sub> (%)	CO (%)	CO <sub>2</sub> (%)	NO <sub>x</sub> (%)
Without OFA	3.37	24.15	0.62	3.64
ER <sub>mb</sub> 1.10	3.57	20.43	0.71	3.53
ER <sub>mb</sub> 1.05	2.14	16.12	0.36	0.80
ER <sub>mb</sub> 1.00	2.26	16.33	0.37	2.44

**Table 26 – Overall uncertainties of flue gas measurement from co-firing 90-10 PRB-DB blend under various conditions**

Condition	O <sub>2</sub> (%)	CO (%)	CO <sub>2</sub> (%)	NO <sub>x</sub> (%)
Without OFA	4.65	15.42	0.49	3.82
ER <sub>mb</sub> 1.10	4.11	16.82	1.77	3.10
ER <sub>mb</sub> 1.05	2.78	21.57	0.52	1.22
ER <sub>mb</sub> 1.00	2.13	21.71	1.05	0.80



## 8. CONCLUSIONS

This section summarizes all the work done in this current research as well as the significant results. The conclusions are as follows:

1. The LNB was modified by changing the swirler vane profile from helix vane to straight vane, adjusting  $\alpha_v$  from 33 degrees to 59 degrees, decreasing  $L_{sr}$  from 24 mm to 10.5 mm, and increasing number of secondary air inlet nozzle from one to four. These modifications result in symmetric RZ and stronger swirling flow.
2. The coal spreader was changed from the fin type to v-shaped type.
3. The OFA system was modified by relocating the OFA inlet nozzle in order to evenly distribute OFA into the piping system. In addition, the diameter of OFA outlet nozzle was increased from 9.525 mm to 12.7 mm in order to enhance mixing between OFA and product gases from the main burner.
4. Co-firing 90-10 PRB-DB blend without OFA can decrease  $NO_x$  by approximately 20.1% on the average ( $0.85 \leq ER_{oa} \leq 1.10$ ) because DB mixed in the fuel blend releases VM at lower temperature compared to PRB.
5. OFA injection can decrease  $NO_x$  of firing pure PRB whenever  $ER_{mb}$  is set in the rich regime and  $ER_{oa}$  is set in the lean regime. On the average, injecting OFA into pure PRB combustion system whilst  $ER_{mb}$  is set at 1.10 and  $ER_{oa}$  is ranged from 0.85 to 0.95 can reduce  $NO_x$  by 23.8%.
6. Consider  $ER_{oa}$  in the lean regime ( $0.85 \leq ER_{oa} \leq 0.95$ ). The amount of  $NO_x$  emissions from co-firing 90-10 PRB-DB blend with OFA injection is indifferent

from co-firing without OFA when  $ER_{mb}$  is set at 1.05, and is higher by 11.2% on the average when  $ER_{mb}$  is set at 1.00.

7. Co-firing 90-10 PRB-DB blend with OFA will work only when  $ER_{mb}$  is set at 1.10. The average percentage of  $NO_x$  reduction when  $ER_{oa}$  is ranged from 0.85 to 0.95 is approximately 18.7%.
8. Co-firing 90-10 PRB-DB blend at  $ER_{mb}$  of 1.10 and  $ER_{oa}$  of 0.95 should be applied to coal-fired power plants because this operating condition can decrease  $NO_x$  by 159 g/GJ compared to the base case ( $ER_{oa}$  at 0.85 without OFA) which is 48.2% reduction. Moreover, this operating condition can decrease excess  $O_2$  in dry flue gas from 3% to 1.1%, and also the excess air could be reduced from 17.65% to 5.3%. Reducing excess air will result in enhancing combustion efficiency.

## 9. FUTURE WORK

This section suggests future work that should be further performed in order to broaden the horizon in emissions control technology as follows:

1. Examine emissions from burning natural gas during the preheating process. This could provide a basic understanding of gas combustion in strong swirl.
2. Change the type of CO detector to get more accurate results (less standard error).
3. Investigate the effects of preheating secondary air and OFA at various temperatures on NO<sub>x</sub> emissions and temperature profiles. The results would be used to indicate what temperature the air should be preheated to.
4. Investigate the effects of injecting OFA into the combustion chamber through flat spray nozzles on NO<sub>x</sub> and CO emissions. Flat spray nozzles are supposed to enhance mixing between OFA and the product gas from the main burner. Thus, injecting OFA through flat spray nozzles is expected to decrease NO<sub>x</sub> emissions.
5. Investigate emissions from firing pure DB in lean and rich regimes by using SN'<sub>sa</sub> at 1.42, i.e. strong swirl. The results could provide a deeper understanding of the effects of firing DB in the strong swirl region on emissions.
6. Investigate emissions from co-firing 90-10 PRB-DB blend with a characteristic particle size of 75 μm or less ( $d_{ps,char}$  of 90-10 PRB-DB blend in the current research was 125 μm). The results of this investigation could be used to indicate the optimum fuel particle size.

7. Measure mercury emission from firing pure PRB, pure DB, 90-10 PRB-DB blend. EPA is going to control mercury emission from coal-fired power plants. Hence, the results of this study will provide information of how DB affects the mercury emission.
8. Develop particle flow model by using various burner geometries, fuel types and particle sizes. Also, particle flow characteristic of char should be developed. Data obtained from this study could provide the approximate residence time of fuel particle inside the recirculation zone, and the estimated residence time could be used in NO<sub>x</sub> modeling.
9. Study the burner-to-burner interaction by creating a furnace model with two main burners. The interaction between burners is important to flame stability since the large-scale furnace could consist of more than one burner.
10. Perform feasibility study of using ash from firing PRB and co-firing fuel blends in refractory production in order to avoid landfill.

## REFERENCES

- Abbas, T., P. Costen, and F. C. Lockwood. 1992. "The Influence of Near Burner Region Aerodynamics on the Formation and Emission of Nitrogen Oxides in a Pulverized Coal-Fired Furnace." *Combustion and Flame* 91 (3-4): 346-363.
- AK Steel Corporation. 2013. *316/316L Stainless Steel*. Product Data Bulletin, West Chester, OH: AK Steel Corporation. Accessed March 10, 2014.  
[http://www.aksteel.com/pdf/markets\\_products/stainless/austenitic/316\\_316l\\_data\\_bulletin.pdf](http://www.aksteel.com/pdf/markets_products/stainless/austenitic/316_316l_data_bulletin.pdf).
- Annamalai, K., J. M. Sweeten, and S. C. Ramalingam. 1987. "Estimation of Gross Heating Values of Biomass Fuels." *Transactions of the ASAE* 30 (4): 1205-1208.
- Annamalai, Kalyan, and Ishwar K. Puri. 2007. *Combustion Science and Engineering*. Boca Raton, FL: CRC Press.
- Apte, S. V., K. Mahesh, P. Moin, and J. C. Oefelein. 2003. "Large-Eddy Simulation of Swirling Particle-Laden Flows in a Coaxial-Jet Combustor." *International Journal of Multiphase Flow* 29 (8): 1311-1331.
- Arumugam, Senthilvasan. 2004. *Nitrogen Oxides Emission Control Through Reburning with Biomass in Coal-Fired Power Plants*. Master Thesis, College Station, TX: Texas A&M University.

- Baukal, Charles E. 2013. *Introduction*. Vol. 1, chap. 1 in *The John Zink Hamworthy Combustion Handbook*, edited by Charles E. Baukal, 1-30. Boca Raton, FL: CRC Press.
- Baukal, Charles. 2005. "Everything You Need to Know About NO<sub>x</sub>." *Metal Finishing* 103 (11): 18-24.
- Beér, J. M., and N. A. Chigier. 1983. *Combustion Aerodynamics*. Malabar, FL: Robert E. Krieger Publishing Company, Inc.
- Bhimani, Shreyas, Jorge L. Alvarado, Kalyan Annamalai, and Charles Marsh. 2013. "Emission Characteristics of Methanol-in-Canola Oil Emulsions in a Combustion Chamber." *Fuel* 113: 97-106.
- Biagini, E., C. Fantozzi, and L. Tognotti. 2004. "Characterization of Devolatilization of Secondary Fuels in Different Conditions." *Combustion Science and Technology* 176 (5-6): 685-703.
- Boie, W. 1952/53. "Beiträge Zum Feuerungstechnischen Rechnen." *Wissenschaftliche Zeitschrift der Technischen Hochschule Dresden* 2: 688-718.
- Cathles III, Lawrence M., Larry Brown, Milton Taam, and Andrew Hunter. 2012. "A Commentary on "The Greenhouse-Gas Footprint of Natural Gas in Shale Formations" by R.W. Howarth, R. Santoro, and Anthony Ingraffea." *Climatic Change* 113 (2): 525-535.

- Chang, Liping, Zhihua Feng, and Kechang Xie. 2005. "Effect of Coal Properties on HCN and NH<sub>3</sub> Release During Coal Pyrolysis." *Energy Sources* 27 (15): 1399-1407.
- Cheng, Robert K., and Howard Levinsky. 2008. "Lean Premixed Burners." Chap. 6 in *Lean Combustion Technology and Control*, edited by Derek Dunn-Rankin, 161-177. Amsterdam, Boston: Academic Press.
- Demirbas, Ayhan. 2004. "Combustion Characteristics of Different Biomass Fuels." *Progress in Energy and Combustion Science* 30 (2): 219-230.
- Fan, Weidong, Zhengchun Lin, Jinguo Kuang, and Youyi Li. 2010. "Impact of Air Staging Along Furnace Height on NO<sub>x</sub> Emissions from Pulverized Coal Combustion." *Fuel Processing Technology* 91 (6): 625-634.
- Fenimore, C. P. 1971. "Formation of Nitric Oxide in Premixed Hydrocarbon Flames." *Symposium (International) on Combustion* 13 (1): 373-380.
- Gomez, Patsky Oridel. 2009. *Development of a Low NO<sub>x</sub> Burner System for Coal Fired Power Plants Using Coal and Biomass Blends*. Master Thesis, College Station, TX: Texas A&M University.
- Goughnour, Paul Gordon. 2006. *NO<sub>x</sub> Reduction with the Use of Feedlot Biomass as a Reburn Fuel*. Master Thesis, College Station, TX: Texas A&M University.
- Koch, Wendy. 2014. *EPA Seeks 30% Cut in Power Plant Carbon Emissions by 2030*. June 3. Accessed June 11, 2014.

<http://www.usatoday.com/story/money/business/2014/06/02/epa-proposes-sharp-cuts-power-plant-emissions/9859913/>.

Lam, Ka-Leung, Adetoyese O. Oyedun, Kwok-Yuen Cheung, King-Lung Lee, and Chi-Wai Hui. 2011. "Modelling Pyrolysis with Dynamic Heating." *Chemical Engineering Science* 66 (24): 6505-6514.

Lawn, C. J. 1987. *Principles of Combustion Engineering for Boilers*. Orlando, FL: Academic Press.

Lawrence, Ben, Kalyan Annamalai, John M. Sweeten, and Kevin Heflin. 2009. "Cofiring Coal and Dairy Biomass in a 29 kWt Furnace." *Applied Energy* 86 (11): 2359-2372.

Lawrence, Benjamin Daniel. 2013. *Investigation of Synergistic NO<sub>x</sub> Reduction from Cofiring and Air Staged Combustion of Coal and Low Ash Dairy Biomass in a 30 Kilowatt Low NO<sub>x</sub> Furnace*. PhD Diss., College Station, TX: Texas A&M University.

Li, Pei-Sheng, Qin Wang, Qiao Xu, Wan Yu, Ya-Nan Yue, Zhe Liang, Xing-Chen Dong, and Song Hu. 2012. "Combustion Reaction Mechanism of Four Typical Chinese Biomass by TG and DTG." *Asia-Pacific Journal of Chemical Engineering* 7 (2): S209-S215.

Li, Songgeng, Andy Wu, Shuang Deng, and Wei-ping Pan. 2008. "Effect of Co-Combustion of Chicken Litter and Coal on Emissions in a Laboratory-Scale Fluidized Bed Combustor." *Fuel Processing Technology* 89 (1): 7-12.



- Martin, Brandon Ray. 2006. *Pyrolysis and Ignition Behavior of Coal, Cattle Biomass, and Coal/Cattle Biomass Blends*. Master Thesis, College Station, TX: Texas A&M University.
- Mayoral, M. C., M. T. Izquierdo, J. M. Andrés, and B. Rubio. 2001. "Different Approaches to Proximate Analysis by Thermogravimetry Analysis." *Thermochimica Acta* 370 (1-2): 91-97.
- McAdams, Jason D., Scott D. Reed, and Daniel C. Itse. 2001. "Minimize NO<sub>x</sub> Emissions Cost-Effectively." *Hydrocarbon Processing*, June: 51-58.
- Mesroghli, Sh., E. Jorjani, and S. Chehreh Chelgani. 2009. "Estimation of Gross Calorific Value Based on Coal Analysis Using Regression and Artificial Neural Networks." *International Journal of Coal Geology* 79 (1-2): 49-54.
- Oh, Hyuk Jin. 2008. *Reburning Renewable Biomass for Emissions Control and Ash Deposition Effects in Power Generation*. PhD Diss., College Station, TX: Texas A&M University.
- OnlineMetals.com. n.d. *Melting Points of Various Metals*. Accessed March 10, 2014. [www.onlinemetals.com/meltpt.cfm](http://www.onlinemetals.com/meltpt.cfm).
- Orbay, R. C., K. J. Nogenmyr, J. Klingmann, and X. S. Bai. 2013. "Swirling Turbulent Flows in a Combustion Chamber with and without Heat Release." *Fuel* 104: 133-146.

- Ribeirete, A., and M. Costa. 2009. "Impact of the Air Staging on the Performance of a Pulverized Coal Fired Furnace." *Proceedings of the Combustion Institute* 32 (2): 2667-2673. doi:10.1016/j.proci.2008.06.061.
- Sami, M., K. Annamalai, and M. Wooldridge. 2001. "Co-Firing of Coal and Biomass Fuel Blends." *Progress in Energy and Combustion Science* 27 (2): 171-214.
- Sami, Muhammad. 2000. *Numerical Modeling of Coal-Feedlot Biomass Blend Combustion and NOx Emissions in Swirl Burner*. PhD Diss., College Station, TX: Texas A&M University.
- Seebold, James G. 2013. "Plant-Wide NOx Reduction Projects." *Industrial Combustion Journal of the International Flame Research Foundation*. January. Accessed March 10, 2014.  
[http://www.industrial.combustion.ifrf.net/paper\\_download.html?paperId=99](http://www.industrial.combustion.ifrf.net/paper_download.html?paperId=99).
- Syred, N., and J. M. Beér. 1974. "Combustion in Swirling Flows: A Review." *Combustion and Flame* 23 (2): 143-201.
- Thien, Ben Filibert. 2002. *Cofiring with Coal-Feedlot Biomass Blends*. PhD Diss., College Station, TX: Texas A&M University.
- Tognotti, Leonardo, Andrea Malotti, Luigi Petarca, and Severino Zanelli. 1985. "Measurement of Ignition Temperature of Coal Particles Using a Thermogravimetric Technique." *Combustion Science and Technology* 44 (1-2): 15-28.
- Tomeczek, Jerzy. 1994. *Coal Combustion*. Malabar, FL: Krieger Publishing Company.

- U.S. EIA. 2014. *Coal*. May 27. Accessed May 28, 2014.  
[http://www.eia.gov/energyexplained/index.cfm?page=coal\\_home#tab1](http://www.eia.gov/energyexplained/index.cfm?page=coal_home#tab1).
- . 2012. *Emissions Allowance Prices for SO<sub>2</sub> and NO<sub>x</sub> Remained Low in 2011*.  
February 2. Accessed May 22, 2014.  
<http://www.eia.gov/todayinenergy/detail.cfm?id=4830>.
- . 2014. *Planned Coal-Fired Power Plant Retirements Continue to Increase*. March 20.  
Accessed April 18, 2014.  
<http://www.eia.gov/todayinenergy/detail.cfm?id=15491>.
- U.S. EPA. 2012. "Rules and Regulations." *Federal Register* 77 (32): 9304-9513.  
Accessed March 27, 2014. <http://www.gpo.gov/fdsys/pkg/FR-2012-02-16/pdf/2012-806.pdf>.
- Van Loo, Sjaak, and Jaap Koppejan. 2007. *The Handbook of Biomass Combustion and Co-firing*. London: Earthscan.
- Vanormelingen, J., and E. Van Den Bulck. 1999. "Optimization of Overfire Air Systems of Cylindrical Combustion Chambers." *Environmental Engineering Science* 16 (5): 353-373.
- Yaverbaum, Lee H. 1979. *Nitrogen Oxides Control and Removal: Recent Developments*. Park Ridge, NJ: Noyes Data Corp.

## APPENDIX A

### EMPIRICAL FORMULAE

The empirical formulae of PRB, DB, and 90-10 PRB-DB were computed by using the values of C, H, N, S and O from Table 13 on DAF basis. As a result, the empirical formulae and the empirical formulae normalized by the number of C atoms of the aforementioned fuels are respectively shown in Table 27 and Table 28. These formulae were used in finding the air-to-fuel ratio for stoichiometric, lean, and rich combustions at various ER as described in Appendix C.

**Table 27 – Empirical formulae of PRB, DB, and 90-10 PRB-DB on DAF basis**

Fuel	Empirical Formulae	M <sub>fuel</sub> (kg/kmol)
PRB	C <sub>6.1670</sub> H <sub>4.0014</sub> O <sub>1.2725</sub> N <sub>0.0837</sub> S <sub>0.0114</sub>	16.22
DB	C <sub>4.2647</sub> H <sub>5.7786</sub> O <sub>2.3842</sub> N <sub>0.2741</sub> S <sub>0.0302</sub>	23.45
90-10 PRB-DB	C <sub>6.0193</sub> H <sub>4.1359</sub> O <sub>1.3588</sub> N <sub>0.0987</sub> S <sub>0.0128</sub>	16.64

**Table 28 – Normalized empirical formulae of PRB, DB, and 90-10 PRB-DB**

Fuel	Empirical Formulae Normalized by C Atoms	M <sub>fuel</sub> (kg/kmol)
PRB	C H <sub>0.6488</sub> O <sub>0.2063</sub> N <sub>0.0136</sub> S <sub>0.0018</sub>	16.22
DB	C H <sub>1.3550</sub> O <sub>0.5591</sub> N <sub>0.0643</sub> S <sub>0.0071</sub>	23.45
90-10 PRB-DB	C H <sub>0.6871</sub> O <sub>0.2257</sub> N <sub>0.0164</sub> S <sub>0.0021</sub>	16.64

## APPENDIX B

### HEATING VALUES CALCULATION

The HV of PRB and DB were obtained from Hazen Research Inc., and the HV of 90-10 PRB-DB was estimated by using the weighted average method. The HV of the aforementioned fuels are given in Table 29. This table shows that the HHV of 90-10 PRB-DB is 4.54% less than the HHV of PRB. Hence, the mass flow rate of 90-10 PRB-DB must be higher than the mass flow rate of PRB in order to meet the same heat input.

**Table 29 – Heating Values of PRB, DB, and 90-10 PRB-DB**

Heating Value	PRB	DB	90-10 PRB-DB
HHV (kJ/kg of fuel)			
As-Received Basis	21,218	11,586	20,255
Dry Basis	26,675	12,628	25,080
DAF Basis	28,687	20,720	28,071
LHV (kJ/kg of fuel)			
As-Received Basis	20,085	10,686	19,145
Dry Basis	25,867	11,863	23,706
DAF Basis	27,157	19,109	26,533

Moreover, HHV of fuels could be predicted by applying the results from proximate and ultimate analyses. Boie (1952/53) developed the formula for predicting HHV of solid fuels based on DAF basis as expressed in equation (B.1) (Annamalai, Sweeten and Ramalingam 1987) where C, H, O, N, and S represent the mass percentages of elements with respect to the total mass.

$$HHV_{Boie} = 351.60(C\%) + 1162.25(H\%) - 110.90(O\%) + 62.80(N\%) + 104.65(S\%) \quad (B.1)$$

Thus, the HHV of solid fuels on any basis could be predicted by plugging the values of C, H, O, N, and S from the ultimate analysis on that basis into equation (B.1). In other words, if C, H, N, O, and S are reported on an as-received basis,  $HHV_{Boie}$  will be on the as-received basis. The predicted HHV of PRB, DB, and 90-10 PRB-DB by using equation (B.1) and the values from Table 13 are shown in Table 30. The percentage of difference between  $HHV_{Boie}$  and HHV ( $\Delta HHV$ ) of each fuel type can be calculated by equation (B.2) where  $HHV_{pred}$  and  $HHV_{meas}$  are the predicted HHV and the measured HHV. The results show that the percentage of deviation for each fuel type is less than 2%. Annamalai, Sweeten and Ramalingam (1987) also showed that Boie equation has good agreement between the predicted HHV and the measured HHV.

$$\Delta HHV = \frac{(HHV_{pred} - HHV_{meas})}{HHV_{meas}} \times 100\% \quad (B.2)$$

**Table 30 – Comparison between the  $HHV_{meas}$  and the  $HHV_{pred}$  using Boie equation**

Heating Value	PRB	DB	90-10 PRB-DB
<u>As-Received Basis</u>			
HHV (kJ/kg of fuel)	21,218	11,586	20,255
HHV <sub>Boie</sub> (kJ/kg of fuel)	21,141	11,682	20,192
$\Delta$ HHV (%)	-0.363	+0.829	-0.311
<u>DAF Basis</u>			
HHV <sub>DAF</sub> (kJ/kg of fuel)	28,687	20,720	28,071
HHV <sub>Boie</sub> (kJ/kg of fuel)	28,584	20,891	27,983
$\Delta$ HHV (%)	-0.359	+0.825	-0.313

Furthermore, Mesroghli, Jorjani and Chelgani (2009) proposed a correlation for predicting HHV of coal in kJ/kg from the proximate and ultimate analyses on the as-received basis provided in equation (B.3). All of the variables in equation (B.3) are expressed in the mass percentages on the as-received basis. They examined their models over 4,540 samples of U.S. coals, compared the results among measured HHV, HHV predicted by multiple linear regression method, and HHV predicted by artificial neural networks. They finally found that their correlation in equation (B.3) gave the most accurate results with the  $R^2$  of 0.995. However,  $HHV_{Mesroghli}$  of PRB, DB and 90-10 PRB-DB as shown in Table 31 shows that the predicted values of PRB and 90-10 PRB-DB are much lower than the measured values, but the predicted value of DB is 6.45% deviated from the measured one. This might stem from the fact that there were only 33 samples of Texas coals out of 4,540 samples of all U.S. coals. This implies that the geology might affect the HHV of coals. Hence, HHV predicted by using Boie equation

is more accurate for predicting the HHV in case the results of the proximate and ultimate analyses are known.

$$HHV_{Mesroghli} = 6,971 + 269(C\%) + 195(N\%) - 61(Ash\%) - 251(O\%) + 1080(H\%) - 210(Moisture\%) \quad (B.3)$$

**Table 31 – Comparison between HHV on as-received basis using and the predicted HHV by Mesroghli, Jorjani, Chelgani’s correlation**

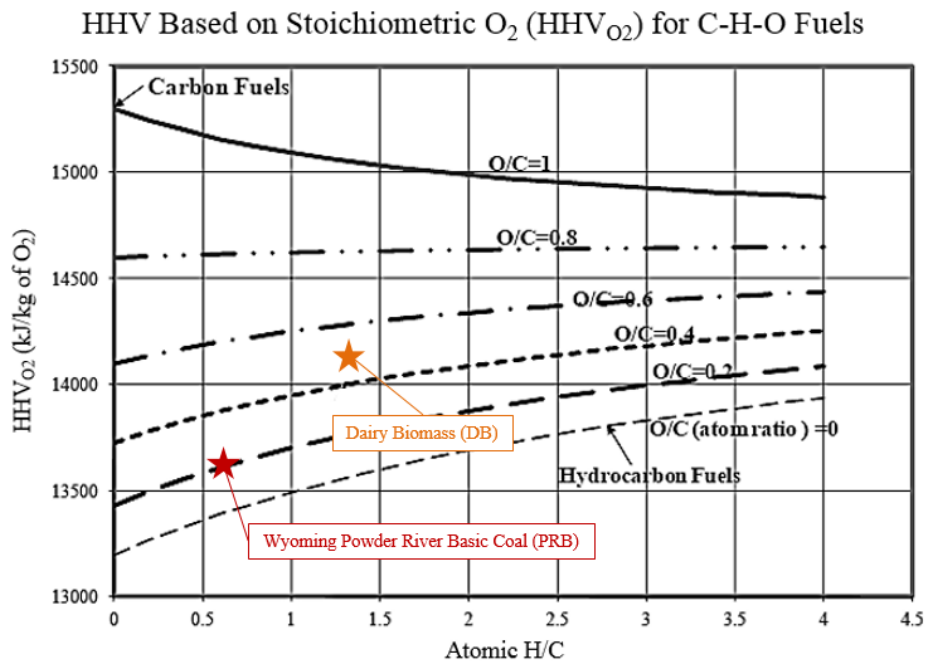
Heating Value	PRB	DB	90-10 PRB-DB
HHV <sub>As-Received</sub> (kJ/kg of fuel)	21,218	11,586	20,255
HHV <sub>Mesroghli</sub> (kJ/kg of fuel)	16,678	10,839	15,944
ΔHHV (%)	-21.40	-6.45	-21.28

Annamalai and Puri (2007) mentioned that, for hydrocarbon fuels, the HHV based on the stoichiometric air (HHV<sub>air</sub>) or O<sub>2</sub> (HHV<sub>O2</sub>) is almost the same. Hence, the HHV<sub>air</sub> or HHV<sub>O2</sub> of PRB, DB, and 90-10 PRB-DB can be calculated by using the HHV on the as-received basis from Table 29 and the amount of the stoichiometric air or oxygen from Appendix C. The HHV<sub>air</sub> and HHV<sub>O2</sub> in Table 32 agree with the above statement. Moreover, the HHV<sub>O2</sub> of PRB and DB plotted on HHV<sub>O2</sub> versus atomic H/C diagram as shown in Figure 75 show that their HHV<sub>O2</sub> agree with the theoretical HHV<sub>O2</sub> of other types of C-H-O fuels.



**Table 32 – HHV based on stoichiometric air and O<sub>2</sub>**

Heating Value	PRB	DB	90-10 PRB-DB
<u>HHV based on stoichiometric air</u>			
HHV <sub>air</sub> (kJ/kg of air)	3,193	3,318	3,200
HHV' <sub>air</sub> (kJ/m <sup>3</sup> of air at SATP)	3,708	3,854	3,716
HHV <sub>Boie, air</sub> (kJ/kg of air)	3,182	3,346	3,190
HHV' <sub>Boie, air</sub> (kJ/m <sup>3</sup> of air at SATP)	3,695	3,886	3,705
ΔHHV (%)	-0.362	0.834	-0.305
<u>HHV based on stoichiometric O<sub>2</sub></u>			
HHV <sub>O2</sub> (kJ/kg of O <sub>2</sub> )	13,698	14,234	13,728
HHV' <sub>O2</sub> (kJ/m <sup>3</sup> of O <sub>2</sub> at SATP)	17,930	18,631	17,969
HHV <sub>Boie, O2</sub> (kJ/kg of O <sub>2</sub> )	13,649	14,353	13,686
HHV' <sub>Boie, O2</sub> (kJ/m <sup>3</sup> of O <sub>2</sub> at SATP)	17,865	18,787	17,914
ΔHHV (%)	-0.362	+0.834	-0.305



**Figure 75 – HHV based on stoichiometric O<sub>2</sub> of PRB, DB and other types of C-H-O fuels compared to the atomic H/C and O/C (adapted from B. D. Lawrence 2013)**

Lastly, the  $HV_{vm}$  of PRB and DB could be estimated by using the data from proximate analysis and equation (5.1) where HV of FC is assumed to equal to HV of char or 32,500 kJ/kg (Sami, Annamalai and Wooldridge 2001). As shown in Table 33 the  $HV_{vm}$  of DB is lower than  $HV_{vm}$  of PRB. This can explain why the increased amount of VM in fuel blend decreases the temperature of combustion.

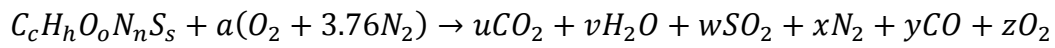
**Table 33 –  $HV_{vm}$  of PRB and DB**

Description	PRB	DB
$HV_{vm}$ (kJ/kg)	23,278	18,424

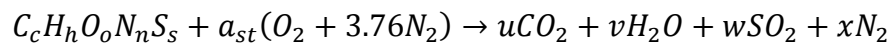
## APPENDIX C

### AIR-TO-FUEL RATIOS

Stoichiometric air-to-fuel ratio ( $A/F_{\text{stoich}}$ ) of each fuel is typically different because every fuel has its own chemical formula. Especially, many solid fuels such as coal and biomass do not have specific chemical formulae. Thus, the empirical formulae are necessary for calculating the A/F ratios. Generally, the combustion process could be categorized into stoichiometric combustion, fuel-lean or oxidizer-rich combustion, and fuel-rich or oxidizers-lean combustion. Overall chemical expression and its stoichiometric coefficients for solid fuel combustion are given below.



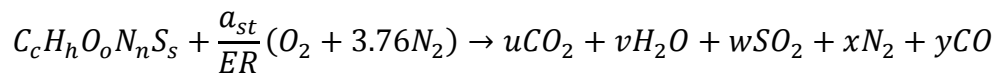
The empirical formula of the solid fuel in the above expression assumes to compose of C, H, O, N, and S, and it is developed by using the result from the ultimate analysis on DAF basis. Thus, c, h, o, n, and s are known values. Theoretical air used as the oxidizer has the O<sub>2</sub>-to-N<sub>2</sub> ratio of 1 to 3.76 on a mole basis, and its molecular weight is 28.84 kg/kmol. The products are assumed to be only CO<sub>2</sub>, H<sub>2</sub>O, SO<sub>2</sub>, N<sub>2</sub>, CO, and O<sub>2</sub> in this consideration. The stoichiometric combustion is defined when the reactants are completely consumed, and the reaction produces only CO<sub>2</sub>, H<sub>2</sub>O, SO<sub>2</sub>, and N<sub>2</sub>.



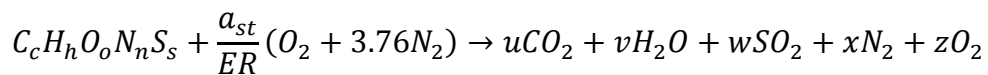
Number of O<sub>2</sub> moles in the stoichiometric combustion process is represented by  $a_{st}$ . Furthermore, other stoichiometric coefficients could be determined by balancing numbers of C, H, O, N, and S atoms on both sides of the expression. As a result, the stoichiometric coefficient of air for stoichiometric combustion could be determined by equation (C.1).

$$a_{st} = c + \frac{h}{4} + s - \frac{o}{2} \quad (C.1)$$

Rich combustion is the process that the amount of fuel exceeds the stoichiometric amount of fuel. It is also generally known as incomplete combustion process. Because of the insufficient amount of oxidizer, C does not only turn into CO<sub>2</sub> but also CO. In this case, the equivalence ratio (ER) is greater than one (ER > 1) or the stoichiometric ratio (SR) is less than one (SR < 1). The general expression of rich combustion is:



In contrast, lean combustion consumes the amount of oxidizer more than the stoichiometric combustion. In other words, the amount of oxidizer could not be completely consumed, so there is excess oxidizer left in the products. In this case, ER is less than one (ER < 1), or SR is greater than one (SR > 1). The reaction of lean combustion could be expressed as shown below.



The results of atom balances for stoichiometric, rich and lean combustion processes are shown in Table 34. The A/F on mass basis ( $A/F_{mass}$ ) could be determined by using equation (C.2). By using the results shown in Table 34 and molecular weight of fuel ( $M_{fuel}$ ) given in Appendix A, the general equation for calculating  $A/F_{mass}$  could be expressed in equation (C.3).

$$A: F_{mass} = \frac{a \times 4.76 \times M_{air}}{1 \times M_{fuel}} \quad (C.2)$$

$$A: F_{mass} = \frac{4.76}{ER} \left( c + \frac{h}{4} + s - \frac{o}{2} \right) \left( \frac{28.84}{M_{fuel}} \right) \quad (C.3)$$

Therefore,  $A/F_{mass}$  of PRB and DB on mass basis computed by using equation (C.3) and the results in Appendix A and by varying ER from 0.85 to 1.10 with the increment of 0.05 are given in Table 35 on both DAF and as-received bases. Furthermore,  $A/F_{mass}$  of 90-10 PRB-DB blend on as-received basis with the same range of ER are given in Table 36. Then, the values from Table 35 and Table 36 are converted into mass and volume flow rates at 300 K as shown in Table 37 and Table 38. Lastly, the fuel loading is defined as the ratio of mass flow rate of fuel to mass flow rate of primary air as shown in equation (C.4). The values of fuel loading are given in Table 39.

$$Fuel\ Loading = \frac{Mass\ flow\ rate\ of\ fuel\ in\ kg/hr}{Mass\ flow\ rate\ of\ primary\ air\ in\ kg/hr} \quad (C.4)$$

**Table 34 – Stoichiometric coefficients for stoichiometric, rich, and lean combustion processes**

Coefficient	Stoichiometric Combustion	Rich Combustion	Lean Combustion
a	$c + \frac{h}{4} + s - \frac{o}{2}$	$\frac{1}{ER} \left( c + \frac{h}{4} + s - \frac{o}{2} \right)$	$\frac{1}{ER} \left( c + \frac{h}{4} + s - \frac{o}{2} \right)$
u	$c$	$2 \left( \frac{1}{ER} - 1 \right) \left( c + \frac{h}{4} + s - \frac{o}{2} \right) + c$	$c$
v	$\frac{h}{2}$	$\frac{h}{2}$	$\frac{h}{2}$
w	$s$	$s$	$s$
x	$3.76 \left( c + \frac{h}{4} + s - \frac{o}{2} \right) + \frac{n}{2}$	$\frac{3.76}{ER} \left( c + \frac{h}{4} + s - \frac{o}{2} \right) + \frac{n}{2}$	$\frac{3.76}{ER} \left( c + \frac{h}{4} + s - \frac{o}{2} \right) + \frac{n}{2}$
y	-	$2 \left( 1 - \frac{1}{ER} \right) \left( c + \frac{h}{4} + s - \frac{o}{2} \right)$	-
z	-	-	$\left( \frac{1}{ER} - 1 \right) \left( c + \frac{h}{4} + s - \frac{o}{2} \right)$

**Table 35 – A/F<sub>mass</sub> on DAF and as-received bases of PRB and DB at various ER**

ER	A:F <sub>mass</sub> on DAF Basis		A:F <sub>mass</sub> on As-Received Basis	
	PRB	DB	PRB	DB
0.85	10.57	7.35	7.82	4.11
0.90	9.98	6.94	7.38	3.88
0.95	9.46	6.57	6.99	3.68
1.00	8.98	6.24	6.64	3.49
1.05	8.56	5.95	6.33	3.33
1.10	8.17	5.68	6.04	3.17

**Table 36 – A/F<sub>mass</sub> on as-received basis of 90-10 PRB-DB blend at various ER**

ER	A:F <sub>mass</sub> on As-Received Basis
0.85	5.75
0.90	6.03
0.95	6.33
1.00	6.66
1.05	7.03
1.10	7.45

**Table 37 – Required mass flow rates for firing PRB and co-firing 90-10 PRB-DB blend at various ER**

ER	Required Air Mass Flow Rate (kg/hr)	
	PRB	90-10 PRB-DB
0.85	39.79	39.71
0.90	37.58	37.50
0.95	35.60	35.53
1.00	33.82	33.75
1.05	32.21	32.14
1.10	30.75	30.68

**Table 38 – Required volume flow rates for firing PRB and co-firing 90-10 PRB-DB blend at various ER**

ER	Required Air Volume Flow Rate (LPM)	
	PRB	90-10 PRB-DB
0.85	571.03	569.80
0.90	539.30	538.14
0.95	510.92	509.82
1.00	485.37	484.33
1.05	462.26	461.27
1.10	441.25	440.30

**Table 39 – Fuel loadings of PRB and 90-10 PRB-DB blend**

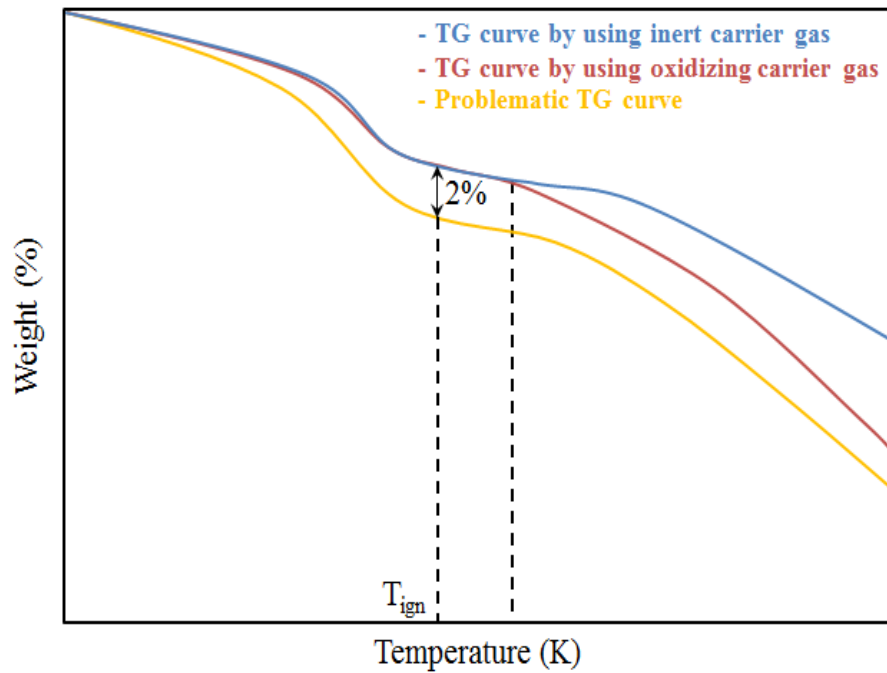
Description	PRB	90-10 PRB-DB
Mass Flow Rate (kg/hr) of		
- Fuel	5.09	5.33
- Primary Air	6.97	6.97
Fuel Loading	0.73	0.76



## APPENDIX D

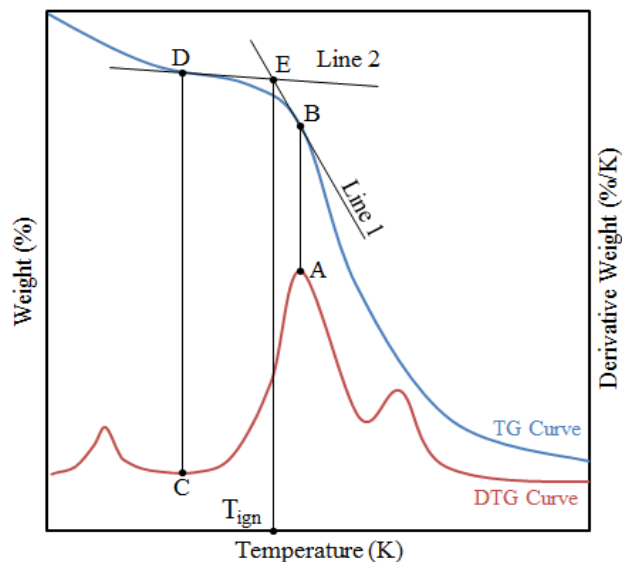
### TGA AND DTG IN DETERMINING IGNITION TEMPERATURES

In the current research, the ignition temperatures ( $T_{\text{ign}}$ ) of PRB, DB, and 90-10 PRB-DB were determined by using the methods from Tognotti, et al. (1985) and Li, et al. (2012) that are mentioned earlier in Literature Review section. Tognotti, et al., (1985) mentioned that  $T_{\text{ign}}$  of a solid fuel could be determined when the TGA curve in an oxidizing carrier gas starts to separate from the TGA curve in an inert carrier gas as shown in Figure 76. However, this method has a problem when one curve has separated from the other curve since the beginning of an experiment as illustrated by the orange line in Figure 76. Thus, in the current research,  $T_{\text{ign}}$  is determined when the TGA curve of oxidizing carrier gas separates from the TGA curve of inert carrier gas about 2%. This method is named as Method I in the current research.



**Figure 76 – Determination of  $T_{ign}$  using Method I**

On the other hand, as described in the Literature Review section, Li, et al. (2012) used TGA-DTG method in determining  $T_{ign}$ . However, in the current research, line 2 is tangent to the TGA curve at point D which is the projection from point C on DTG curve where the solid fuel totally releases the moisture from its structure. The point where line 2 crosses line 1 is named as point E, and the temperature at this point is defined as  $T_{ign}$  (Figure 77). This method is called Method II. The current research also compares the results of Method II by using both oxidizing carrier gas and inert carrier gas.



**Figure 77 – Determination of  $T_{ign}$  by using Method II**

The results from Method I are shown from Figure 78 to Figure 80, the results from Method II by using an oxidizing carrier gas are shown from Figure 81 to Figure 83, and the results from Method II in an inert carrier gas are shown from Figure 84 to Figure 86. The summary in Table 40 shows that the values obtained from the Method II by using the inert gas are more close to the values obtained from Method I. To be more specific, the values from Method II by using the inert gas are within the range of  $\pm 2\%$  compared to the values from Method I. However, the results from Method II by using the oxidizing carrier gas with PRB and 90-10 PRB-DB have more deviation compared to using the inert carrier gas. The reason is there is a spike during the volatile release that might be part of fixed carbon is burning. Therefore, running TGA-DTG analyses only in the inert carrier gas could give us the ignition temperature as well.

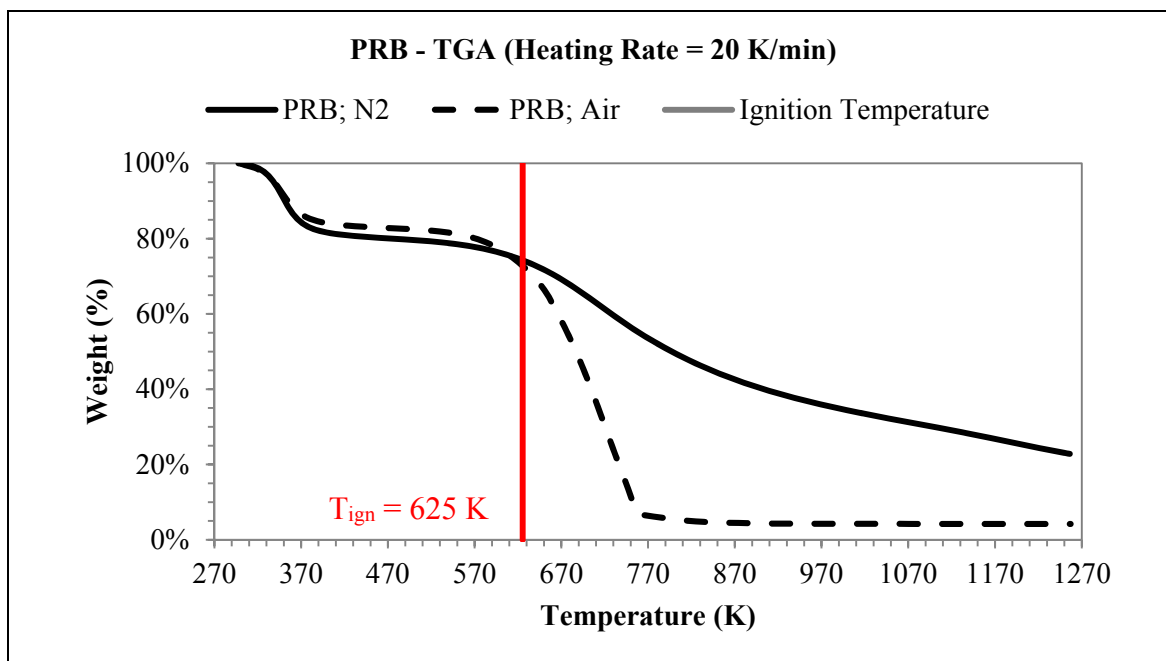


Figure 78 – T<sub>ign</sub> of PRB determined by Method I

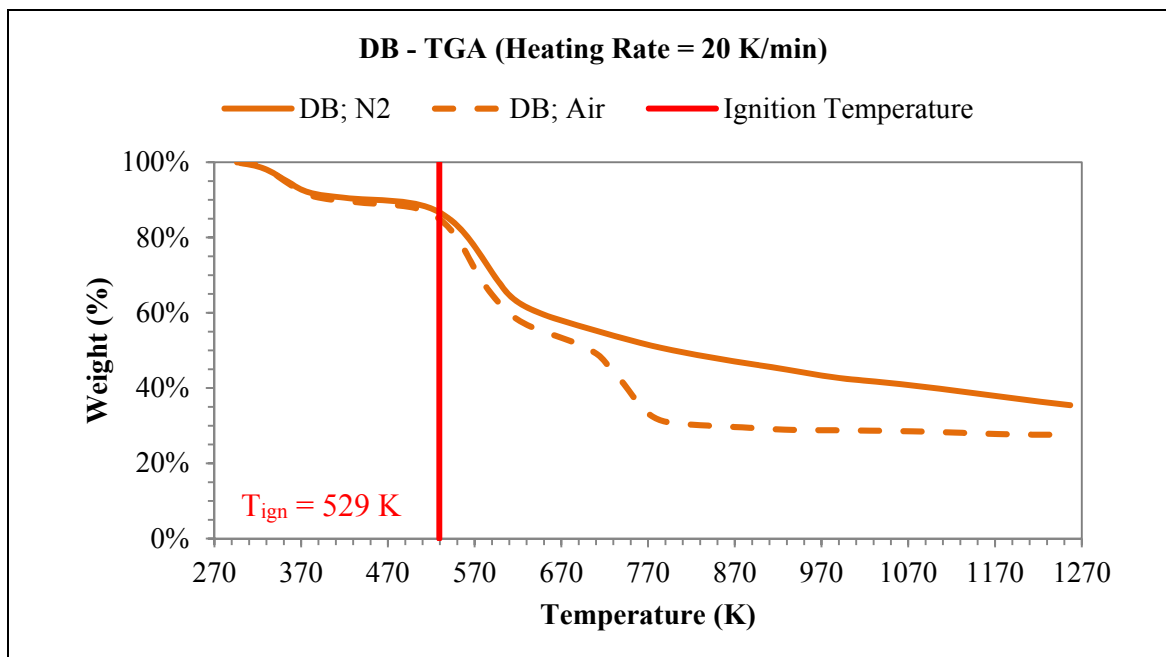
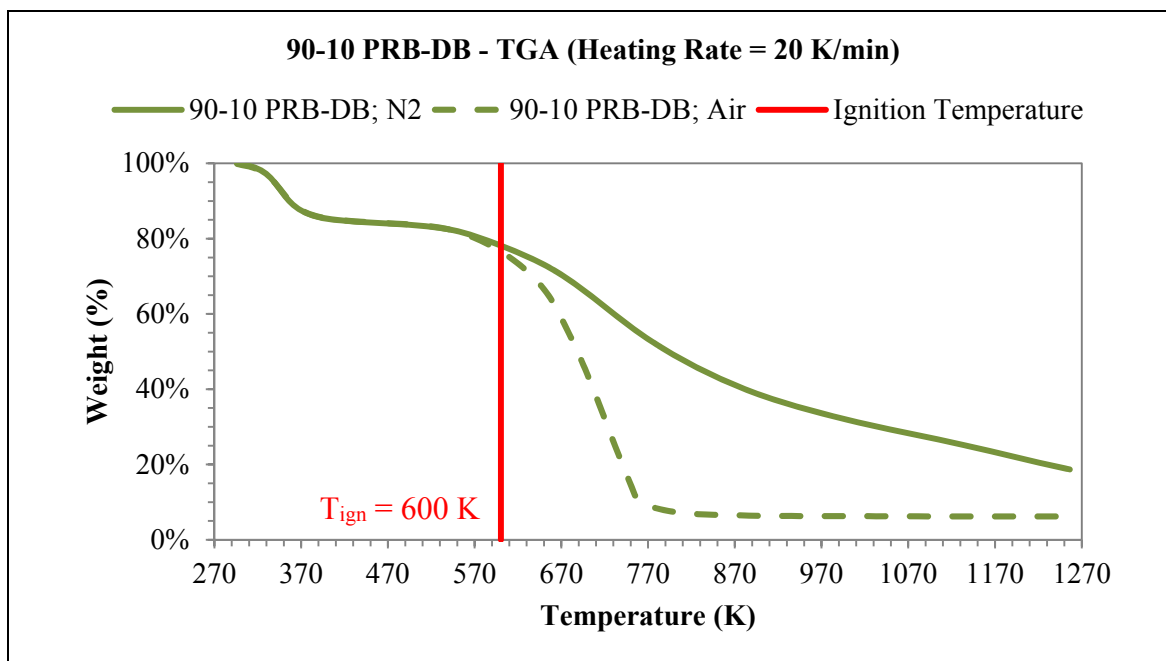
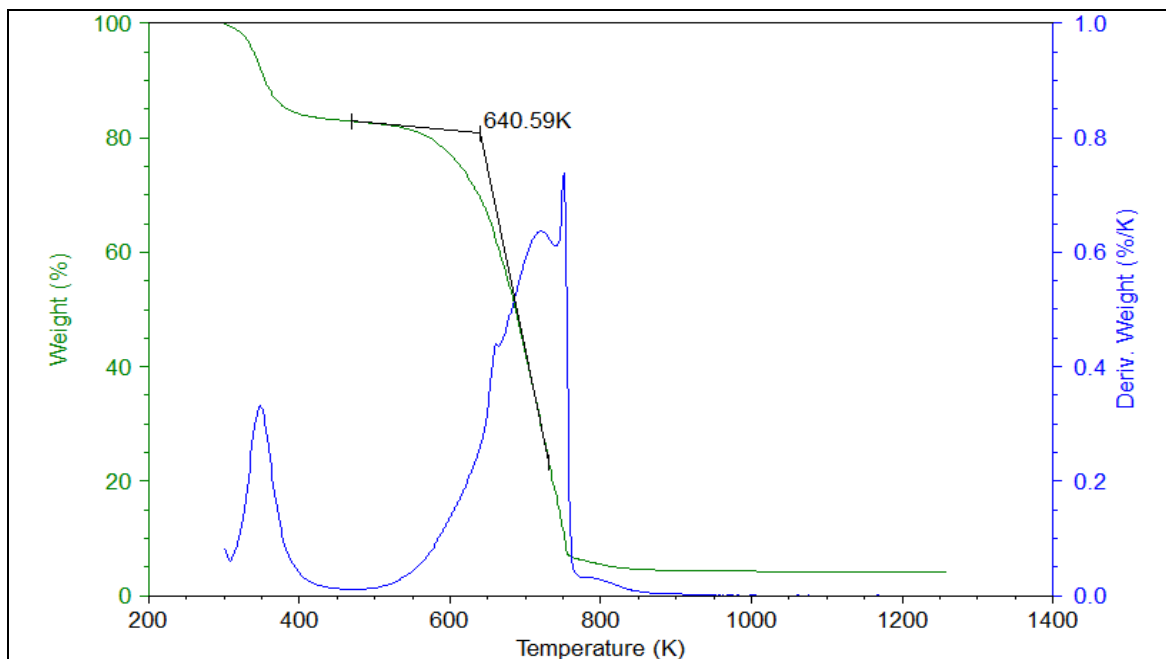


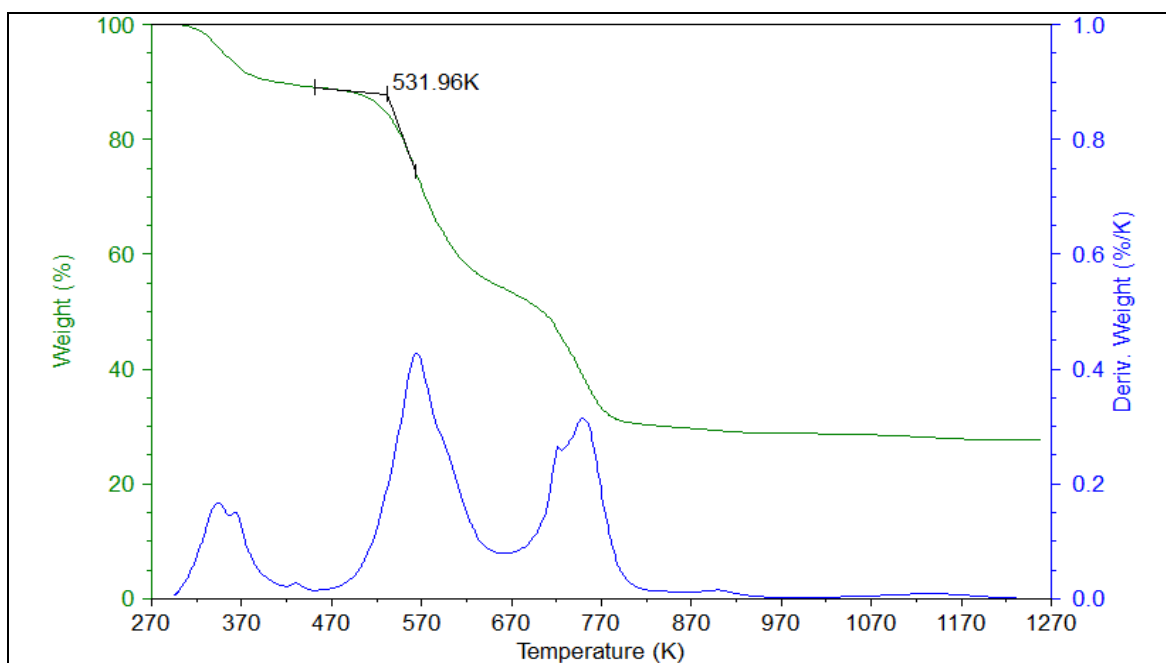
Figure 79 – T<sub>ign</sub> of DB determined by Method I



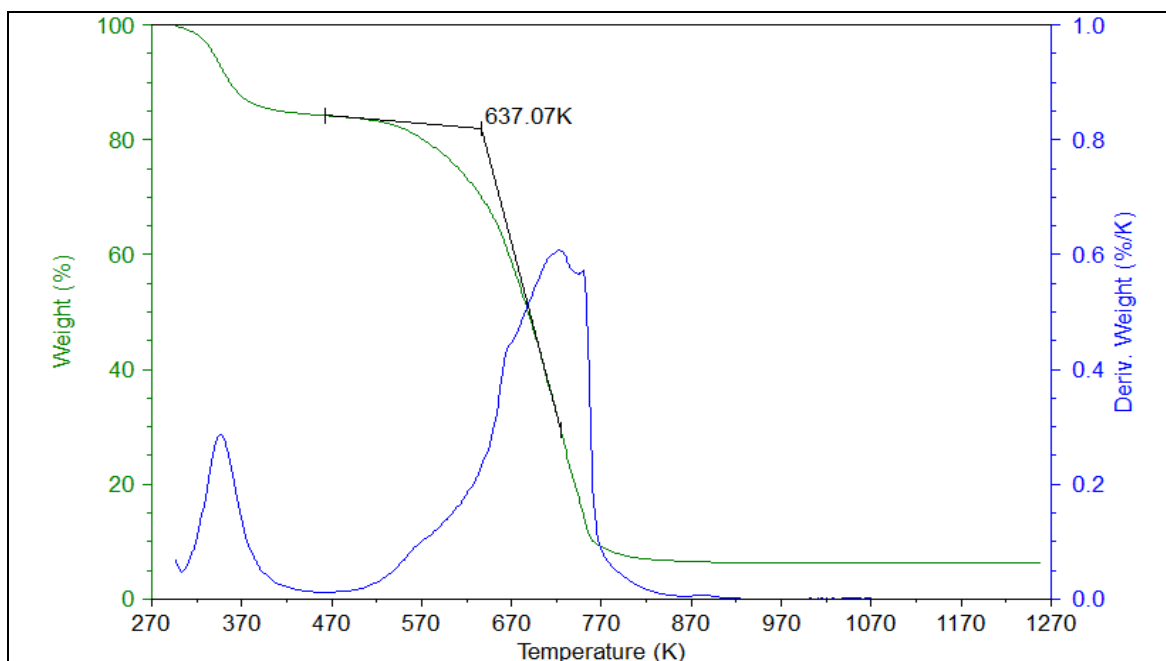
**Figure 80 – T<sub>ign</sub> of 90-10 PRB-DB blend determined by Method I**



**Figure 81 – T<sub>ign</sub> of PRB determined by Method II with the oxidizing gas**



**Figure 82 –  $T_{ign}$  of DB determined by Method II with the oxidizing gas**



**Figure 83 –  $T_{ign}$  of 90-10 PRB-DB determined by Method II with the oxidizing gas**

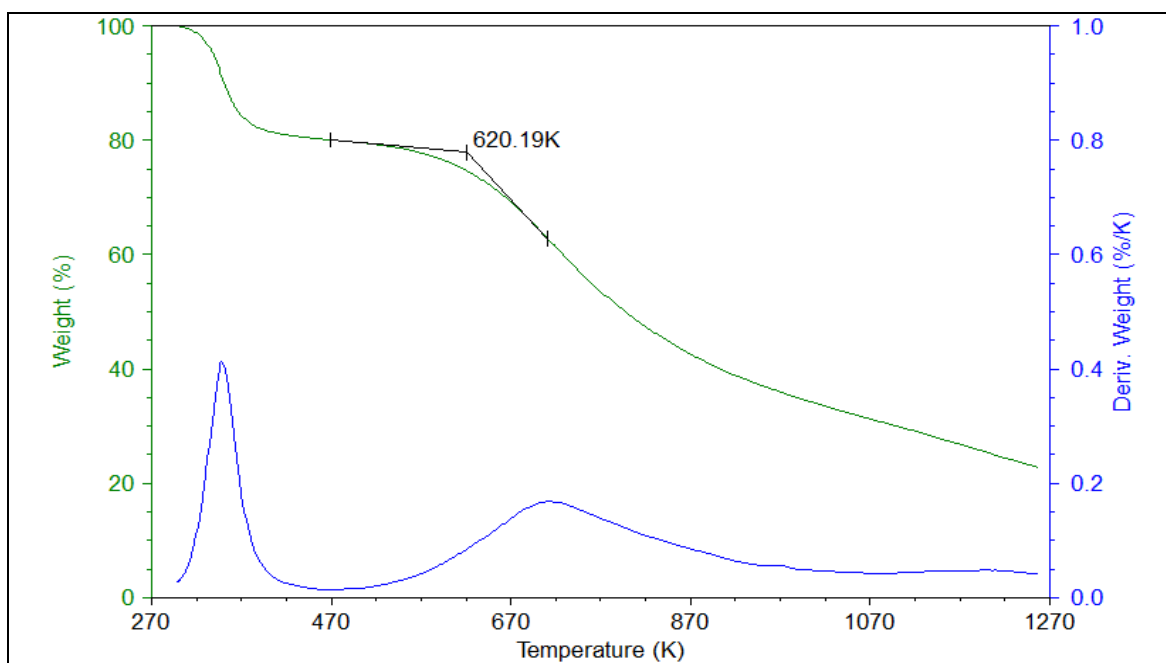


Figure 84 –  $T_{ign}$  of PRB determined by Method II with the inert gas

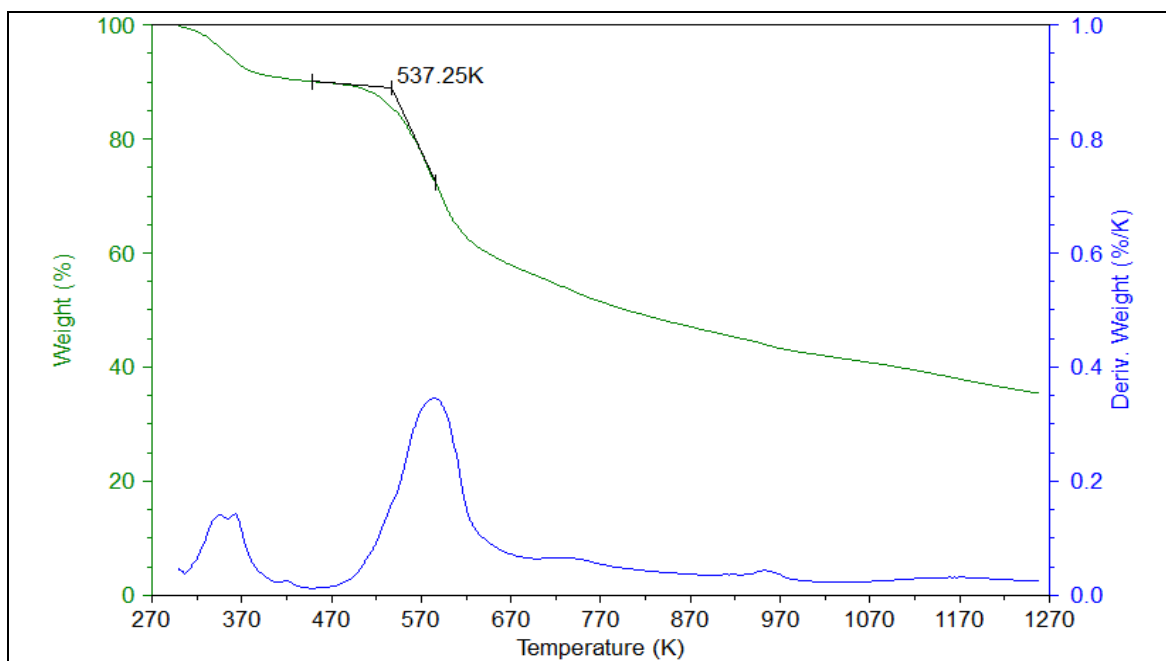
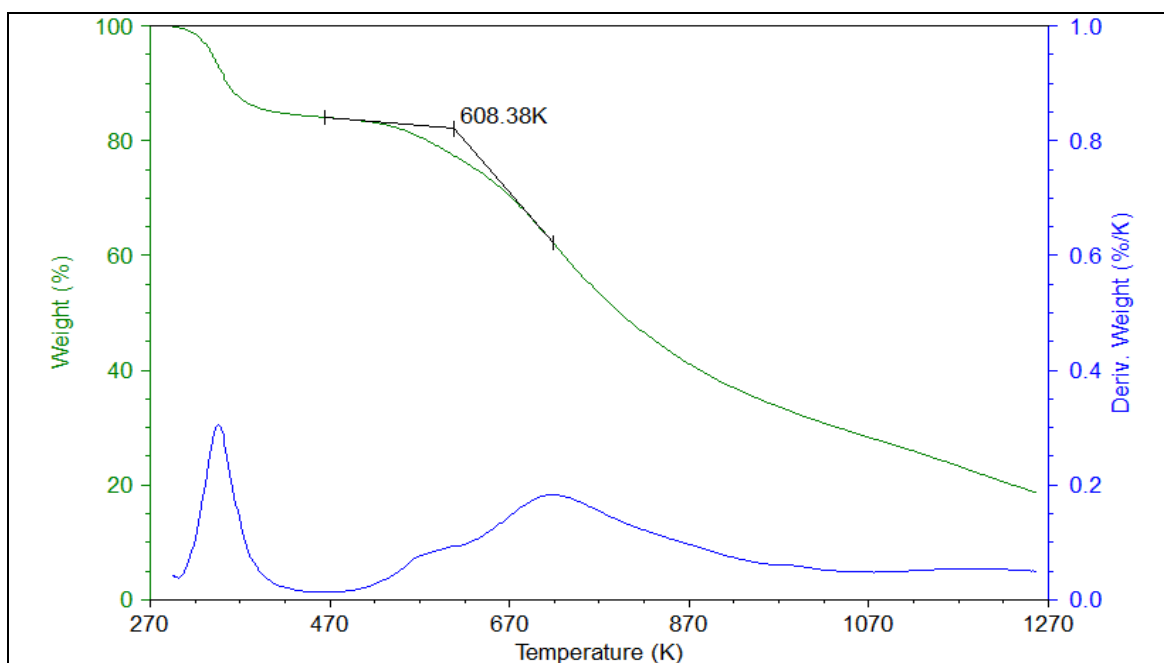


Figure 85 –  $T_{ign}$  of DB determined by Method II with the inert gas



**Figure 86 –  $T_{ign}$  of 90-10 PRB-DB determined by Method II with the inert gas**

**Table 40 –  $T_{ign}$  of PRB, DB, and 90-10 PRB-DB estimated by various methods**

Ignition Temperature (K)	PRB	DB	90-10 PRB-DB
Method I	625 (Reference)	529 (Reference)	600 (Reference)
Method II			
- with the oxidizing gas	642 (+2.72%)	532 (+0.567%)	637 (+6.17%)
- with the inert gas	620 (-0.8%)	537 (+1.51%)	608 (+1.33%)

The impact of particle size on  $T_{ign}$  was examined by using Method II in inert gas. The samples were obtained from layer 6 ( $d_{ps} < 53 \mu\text{m}$ ), layer 7 ( $53 \mu\text{m} \leq d_{ps} < 75 \mu\text{m}$ ) and layer 8 ( $75 \mu\text{m} \leq d_{ps} < 150 \mu\text{m}$ ) from the particle size analysis by sieving (Appendix E). Consider the as-received sample, i.e. the sample that was not sieved, as the reference.



The results in Table 41 show that the particle size does not substantially affect the ignition temperature of fuels. To be more specific, ignition temperature of each particle size is within  $\pm 2\%$  relative to the reference value.

**Table 41 –  $T_{ign}$  of PRB and DB with various particle sizes**

Fuel Type	$T_{ign}$ at $d_{ps, avg}$ of			
	As-Received	Less than 53 $\mu\text{m}$	53 $\mu\text{m}$ – 75 $\mu\text{m}$	75 $\mu\text{m}$ – 150 $\mu\text{m}$
PRB	620	624	627	627
DB	537	531	534	540

## APPENDIX E

### PARTICLE SIZE ANALYSIS BY SIEVING

The recommended fineness of pulverized sub-bituminous coal is, at least, 70% of its total weight has the particle size ( $d_{ps}$ ) smaller than 75  $\mu\text{m}$ , and less than 2% of its total weight has  $d_{ps}$  bigger than 300  $\mu\text{m}$  (Tomeczek 1994). Particle size analysis (PSA) by sieving is the method used for generating particle size distribution (PSD) of a sample. The procedure of PSA by sieving is given in section 4. Result from PSA by sieving could identify whether the sample reaches the recommended fineness.

Rosin-Rammler distribution (RRD) which is generalized from Weibull distribution is generally used in PSA of coal and biomass because it is suitable for highly skewed distribution. This type of distribution function is accepted by American Society for Testing and Materials (ASTM) C136-06: Standard Test Method for Sieve Analysis of Fine and Coarse Aggregates. Rosin-Rammler density function,  $r$ , is defined in equation (E.1) where  $\alpha_{dstr}$  is the distribution constant and  $\beta$  is the size constant. The result of integrating equation (E.1) by setting the lower and upper limits as  $d_{ps}$  and infinity ( $\infty$ ) respectively defines RRD function,  $R$ , as shown in equation (E.2). Furthermore, by using Cumulative Weight Fraction (CWF) defined in equation (E.3), equation (E.2) could be simplified to equation (E.4) (Annamalai and Puri 2007).

The characteristic particle size ( $d_{ps, char}$ ) of RRD means 63.2% of the sample is smaller than  $d_{ps, char}$ . In other words, this is not the weighted average  $d_{ps}$ , but it is  $d_{ps}$  where  $R$  is equal to  $1/e$  as shown in equation (E.5). As a result,  $d_{ps, char}$  and  $\beta$  could be

determined by equation (E.6) and (E.7) respectively, and equation (E.4) could be rewritten by using  $d_{ps, char}$  instead of  $\beta$  as shown in equation (E.8).

$$r(x) = \alpha\beta x^{\alpha-1} \exp(-\beta x^\alpha) \quad (E.1)$$

$$\int_{d_{ps}}^{\infty} r(x) dx = R \quad (E.2)$$

$$CWF = \int_0^{d_{ps}} r(x) dx = 1 - \exp(-\beta d_{ps}^\alpha) \quad (E.3)$$

$$R = \int_{d_{ps}}^{\infty} r(x) dx = 1 - \int_0^{d_{ps}} r(x) dx = 1 - CWF = \exp(-\beta d_{ps}^\alpha) \quad (E.4)$$

$$R = \exp(-1) = \exp(-\beta d_{ps, char}^\alpha) \quad (E.5)$$

$$d_{ps, char} = \beta^{-\frac{1}{\alpha}} \quad (E.6)$$

$$\beta = d_{ps, char}^{-\alpha} \quad (E.7)$$

$$R = \exp \left[ - \left( \frac{d_{ps}}{d_{ps, char}} \right)^\alpha \right] \quad (E.8)$$

RRD function could be written in a linear form by taking two-step logarithm.

The first step is taking natural logarithm of equation (E.8) which results in equation (E.9). The second step is multiplying minus one (-1) throughout equation (E.9) and taking logarithm with base 10 which result in equation (E.10). Next, by using logarithm rules, equation (E.10) could be simplified to equation (E.11). This equation could be compared to the general expression of the linear equation as shown in equation (E.12).

$$\ln R = \ln \left\{ \exp \left[ - \left( \frac{d_{PS}}{d_{PS,char}} \right)^\alpha \right] \right\} = - \left( \frac{d_{PS}}{d_{PS,char}} \right)^\alpha \quad (E.9)$$

$$\log_{10}(-\ln R) = \log_{10} \left[ \left( \frac{d_{PS}}{d_{PS,char}} \right)^\alpha \right] \quad (E.10)$$

$$\log_{10} \left( \ln \frac{1}{R} \right) = \alpha \log_{10}(d_{PS}) - \alpha \log_{10}(d_{PS,char}) \quad (E.11)$$

$$y = mx + c \quad (E.12)$$

Plot of  $(\log_{10}(d_{ps}), \log_{10}[\ln(1/R)])$  on  $(x, y)$  coordinate can be used to find the values of  $\alpha_{dstr}$ ,  $\beta$ , and  $d_{ps, char}$  by comparing equation of the linear trend line with equation (E.11). However, size of sieve aperture ( $d_s$ ) is normally used in place of  $d_{ps}$  in order to make it simple. Therefore, the values of  $\log_{10}(d_s)$  will be plotted instead of  $\log_{10}(d_{ps})$ . The sizes of sieve aperture used in the current research are given in Table 42.

**Table 42 – Size of sieve aperture of each mesh number**

Layer	Mesh	Range of $d_{ps}$ ( $\mu\text{m}$ )	$d_s$ ( $\mu\text{m}$ )
1	10	$\geq 2000$	2000
2	20	840 – 2000	840
3	30	590 – 840	590
4	50	300 – 590	300
5	100	150 – 300	150
6	200	75 – 150	75
7	270	53 – 75	53
8	Pan	$\leq 53$	0

The results of comparison between equations (E.11) and (E.12) are shown from equation (E.13) to (E.17). Furthermore, in the current research, sample remained on each sieve layer after shaking is weighted and recorded as W. Then, the weight fraction (WF) of each layer is calculated by using equation (E.18). Moreover, from the definition, R can be found by using equation (E.19).

$$x = \log_{10}(d_{PS}) \quad (\text{E.13})$$

$$y = \log_{10}\left(\ln \frac{1}{R}\right) \quad (\text{E.14})$$

$$\alpha = m \quad (\text{E.15})$$

$$-\alpha \log_{10}(d_{PS, char}) = c \quad (\text{E.16})$$

$$d_{PS, char} = 10^{-\left(\frac{c}{\alpha}\right)} \quad (\text{E.17})$$

$$WF_n = \frac{W_n}{\sum_1^8 W_i} \quad (\text{E.18})$$

$$R_n = \sum_1^n WF_i \quad (\text{E.19})$$

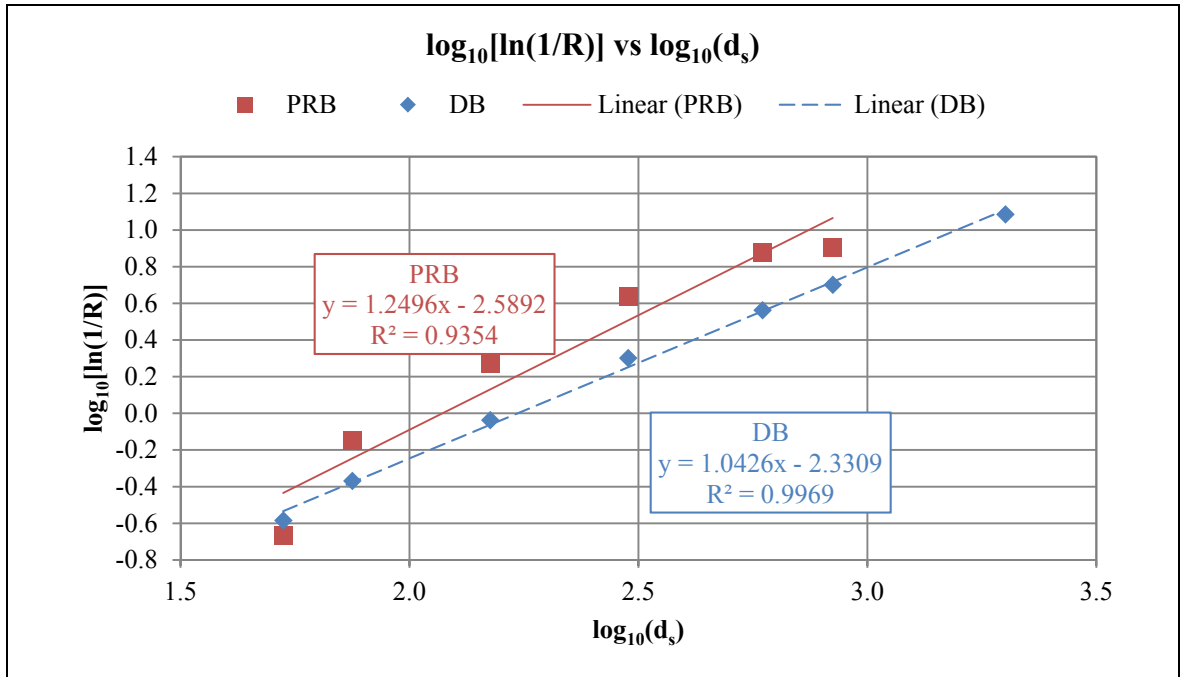
The results from PSA by sieving on 400-gram samples of PRB and DB are presented in Table 43 and Table 44 respectively. Then, the values of  $\log_{10}(d_s)$  and  $\log_{10}[\ln(1/R)]$  are plotted on (x, y) coordinate as shown in Figure 87. By using equations (E.13) to (E.19), the values of  $\alpha_{dstr}$ ,  $d_{ps, char}$ ,  $\beta$ ,  $CWF_6$  (CWF where  $d_{ps}$  is less than 75  $\mu\text{m}$ ), and  $R_4$  (R where  $d_{ps}$  is greater than or equal to 300  $\mu\text{m}$ ) can be obtained. The summary of the aforementioned values are given in Table 45.

**Table 43 – Result from PSA by sieving on PRB**

Layer	Mesh	$d_s$ ( $\mu\text{m}$ )	$\log_{10}(d_s)$	W (g)	WF	R	CWF	$\ln(1/R)$	$\log_{10}[\ln(1/R)]$
1	10	2000	3.30	0	0	0	1	N/A	N/A
2	20	840	2.92	0.120	0.0003	0.0003	0.9997	8.095	0.908
3	30	590	2.77	0.079	0.0002	0.0005	0.9995	7.589	0.880
4	50	300	2.48	4.863	0.0124	0.0129	0.9871	4.353	0.639
5	100	150	2.18	54.604	0.1388	0.1517	0.8483	1.886	0.275
6	200	75	1.88	132.755	0.3376	0.4893	0.5107	0.715	-0.146
7	270	53	1.72	124.130	0.3156	0.8049	0.1951	0.217	-0.663
8	Pan	0	N/A	76.737	0.1951	1	0	0	N/A

**Table 44 – Result from PSA by sieving on DB**

Layer	Mesh	$d_s$ ( $\mu\text{m}$ )	$\log_{10}(d_s)$	W (g)	WF	R	CWF	$\ln(1/R)$	$\log_{10}[\ln(1/R)]$
1	10	2000	3.30	0	0	0	1	12.199	1.086
2	20	840	2.92	0.0065	0.0065	0.0065	0.9935	5.036	0.702
3	30	590	2.77	0.0192	0.0257	0.0257	0.9743	3.661	0.564
4	50	300	2.48	0.1088	0.1345	0.1345	0.8655	2.006	0.302
5	100	150	2.18	0.2640	0.3985	0.3985	0.6015	0.920	-0.036
6	200	75	1.88	0.2529	0.6514	0.6514	0.3486	0.429	-0.368
7	270	53	1.72	0.1191	0.7705	0.7705	0.2295	0.261	-0.584
8	Pan	0	N/A	0.2295	1	1	0	0	N/A



**Figure 87 – Plots of PSA by sieving on PRB and DB**

Table 45 shows that CWF<sub>6</sub> of PRB and DB are 51.07% and 34.86% respectively which are not as high as the recommended value of 70%. Thus, fuels should be ground into the finer size in order to improve the quality of the future research.

**Table 45 – Summary of PSA by sieving on PRB and DB**

Parameter	PRB	DB
$\alpha_{dstr}$	1.2496	1.0426
$d_{ps, char}$ ( $\mu\text{m}$ )	118	172
$\beta$	$2.5751 \times 10^{-3}$	$4.6677 \times 10^{-3}$
CWF <sub>6</sub> × 100% ( $d_{ps} < 75\mu\text{m}$ )	51.07	34.86
R <sub>4</sub> × 100% ( $d_{ps} \geq 300\mu\text{m}$ )	1.29	13.45

## APPENDIX F

### NON-REACTING FLOW (NRF) CHARACTERISTICS

This appendix shows some significant results from NRF simulation in various aspects such as velocity profile, mass fraction profile (or mass distribution profile), particle flow characteristics, and values obtained from NRF simulation.

#### F.1 Secondary Air Distribution System

Secondary air distribution system was investigated by using the NRF simulation in order to know the effects of number of the secondary air inlet nozzles on the shape of the recirculation zone generated by the secondary airflow. The simulation was run by setting the temperature of the secondary airflow at 300 K i.e. room temperature. Moreover, the volume flow rate of the secondary air in each case was varied from 100 LPM to 500 LPM with the increment of 100 LPM, and neither primary air nor OFA was involved in this study. The details of pipe sizes and flow areas used in NRF simulation of secondary distribution system are given in Table 46.

**Table 46 – Details of pipe sizes and flow areas for various numbers of secondary air inlet nozzles**

No. of Inlet Nozzles	Nominal Pipe Size	Pipe Schedule	Outside Diameter (mm)	Inside Diameter (mm)	Flow Area (mm <sup>2</sup> )
1	1"	40s	33.4	26.64	557.389
2	3/4"	80s	26.7	18.86	279.366
4	1/2"	80s	21.3	13.82	150.005



First, the streamlines and velocity profiles of the pre-existing secondary air distribution system was simulated in order to obtain the information of the base case. The results presented in Table 47 show that injecting secondary air through one inlet nozzle could not generate a symmetric recirculation zone below the burner exit. This problem was stemmed from non-uniform secondary air distribution inside the secondary air channel; to be more specific, the secondary airflow could not fully develop along the set length of the secondary air channel. Consequently, the mass flux of the secondary airflow was not uniform over the cross-sectional area prior to entering the swirler zone. Therefore, the uniform mass flux over the cross-sectional area of the secondary air channel is required in order to generate the symmetric recirculation zone below the burner exit.

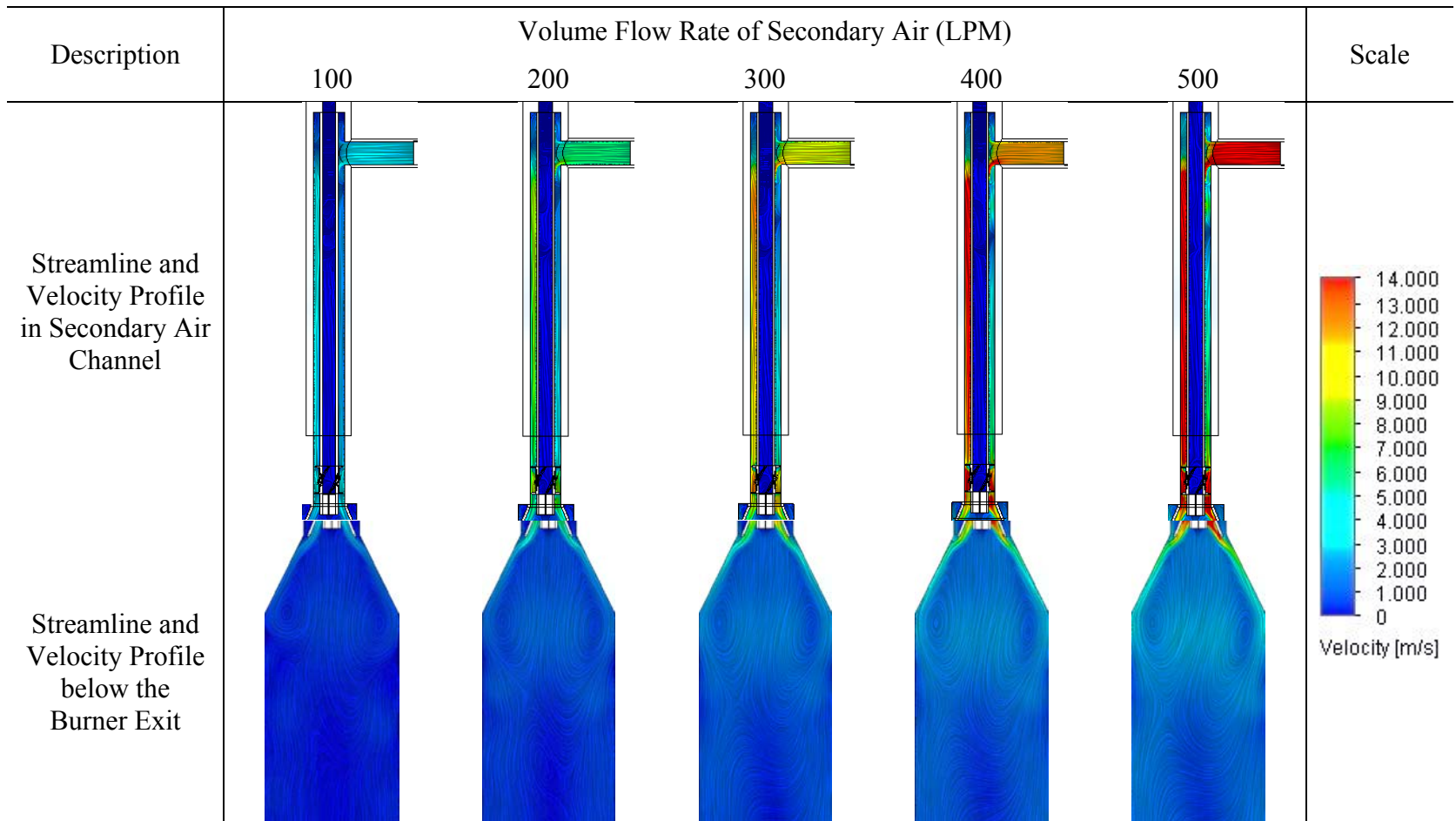
The first attempt was adding another one secondary air inlet nozzle at the opposite side of the old one but decreased the flow area in order to maintain the velocity of the airflow. The results of using two secondary air inlet nozzles showed that the symmetric recirculation zone could be formed only when the volume flow rate of the secondary air is high. As shown in Table 48, the symmetric recirculation zone could be generated only at 500 LPM. When the volume flow rates are less than or equal to 400 LPM, the generated recirculation zone are asymmetric.

The second attempt was increasing the number of the secondary air inlet nozzles from two to four. Each nozzle was located 90 degree apart and aligned on the same planar. The results as shown in Table 49 indicate that, by injecting the secondary air

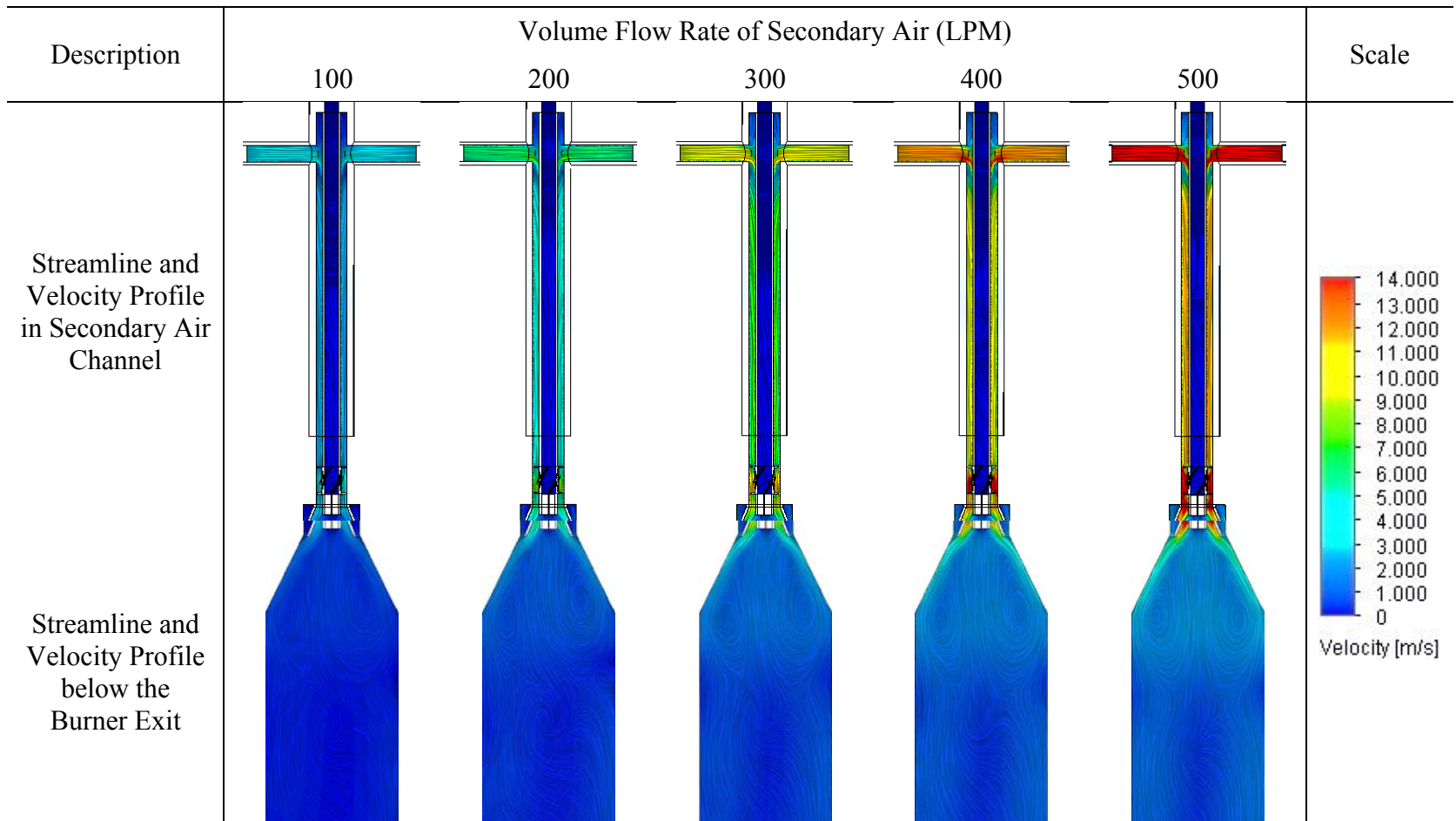
through four inlet nozzles, the symmetric recirculation zone could be formed even at low secondary air volume flow rate i.e. 100 LPM.

To sum up, the number of secondary air inlet nozzles was increased from one to four in order to be able to generate the symmetric recirculation zone by using wide range of secondary air volume flow rates.

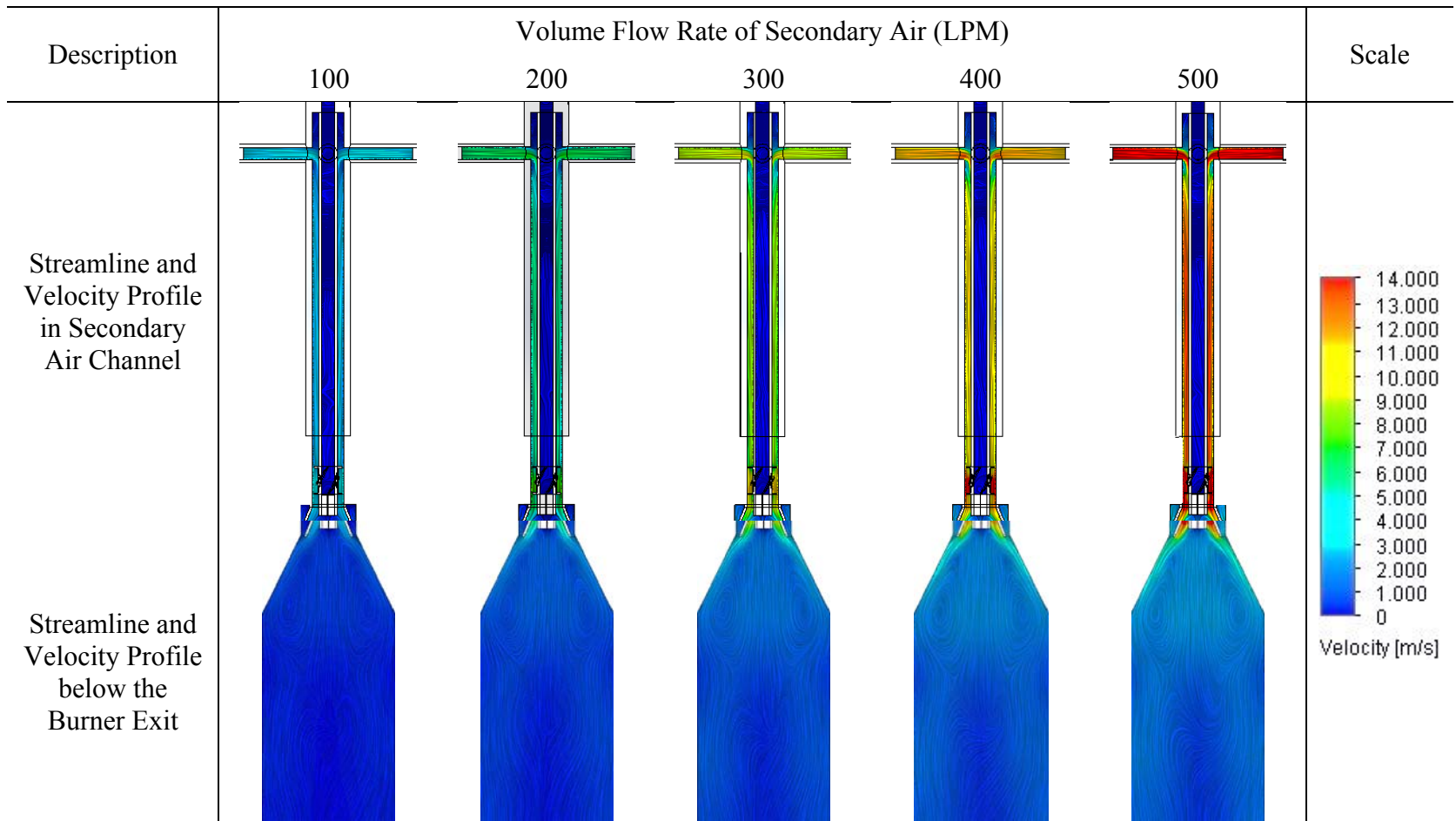
**Table 47 – Streamlines and velocity profiles of secondary airflow through one secondary air inlet nozzle at various secondary air volume flow rates**



**Table 48 – Streamlines and velocity profiles of secondary airflow through two secondary air inlet nozzles at various secondary air volume flow rates**



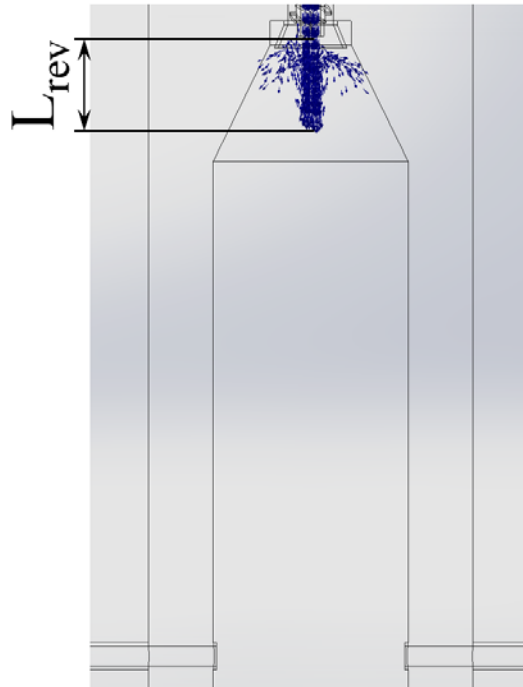
**Table 49 – Streamlines and velocity profiles of secondary airflow through four secondary air inlet nozzles at various volume flow rates**



## F.2 Coal Spreader

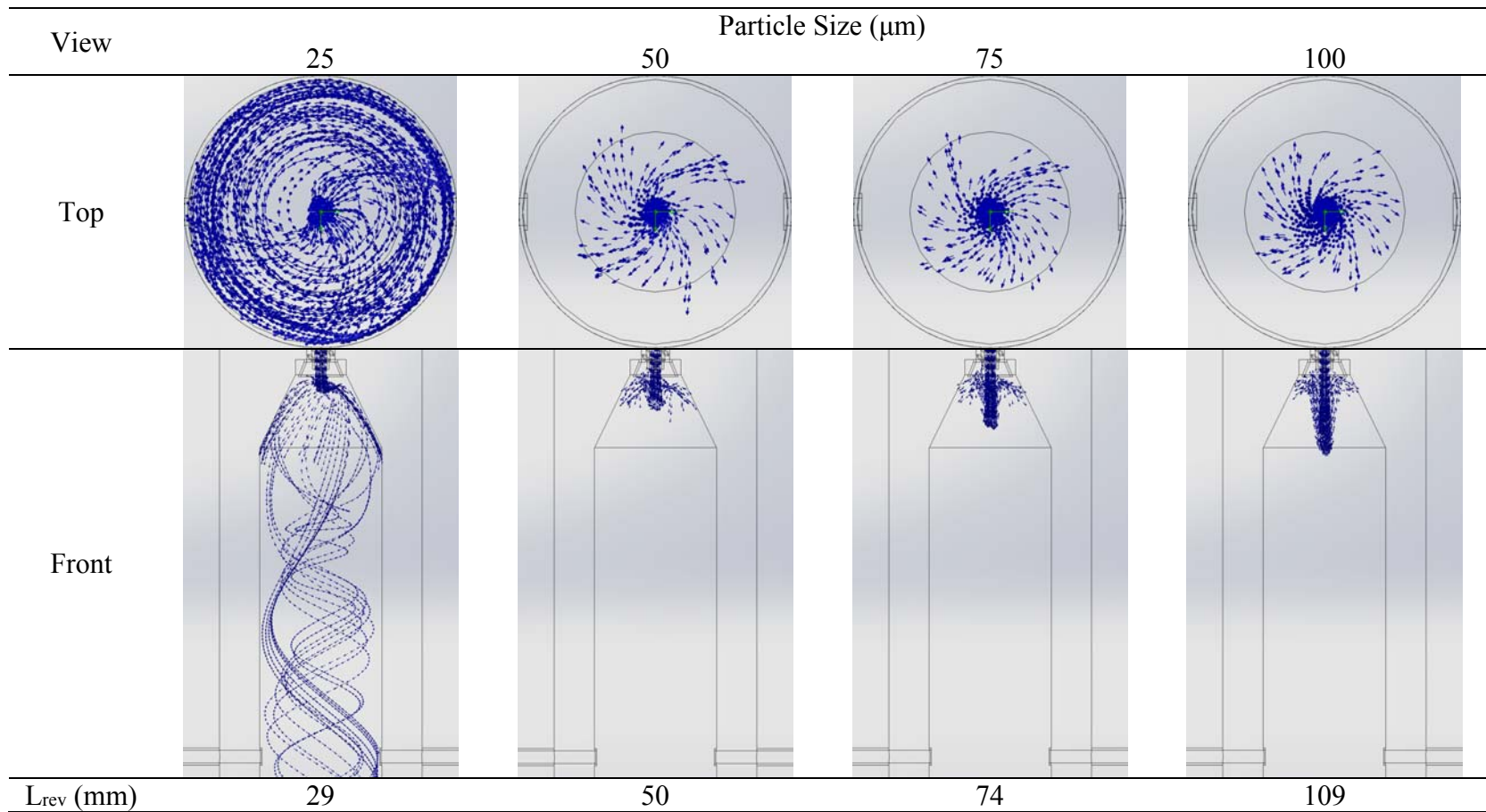
There were two types of coal spreader used in the NRF simulation. The first one was the fin-type coal spreader that installed two thin plates at the center of the fuel/primary air nozzle. The other one was the v-shaped coal spreader which installed the two v-shaped plates at the center of the fuel/primary air nozzle. The differences between these two types are described in LNB Modifications section. This Appendix shows only the particle flow simulation results of injecting PRB particle at various particle sizes; also, the distance between the burner exit and the point where the path of particle flow is reversed by the recirculating flow ( $L_{rev}$ , Figure 88) of each case is included in Table 50 thru Table 52. Please note that  $L_{rev}$  could not be measured if the particle size is too large because the recirculating flow is not strong enough to overcome the particle flow. The following conditions are set on Flow Simulation program for this study:

1. Flow temperature : 300 K.
2.  $ER_{oa}$  : 1.00
3. Mass flow rate of PRB : 5.09 kg/hr
4. Mass flow rate of primary air : 6.97 kg/hr
5. Fuel loading (Ratio of mass flow rate of PRB to primary air) : 0.73
6. OFA injection : No
7. Swirl angle of swirler : 60 degrees



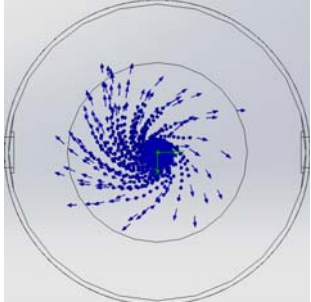
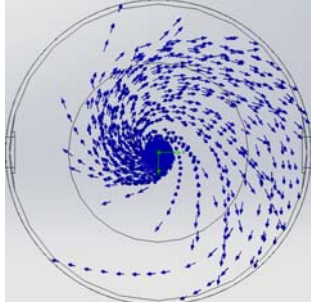
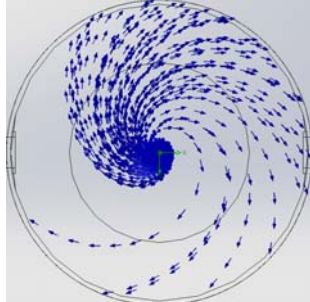
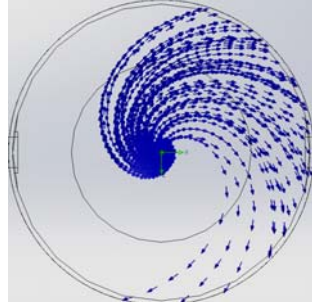
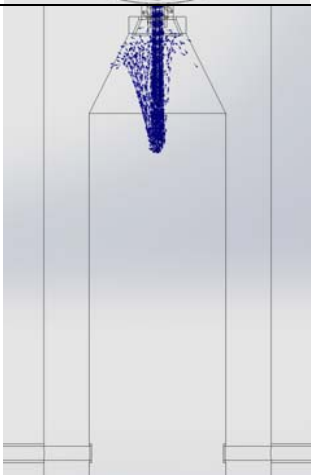
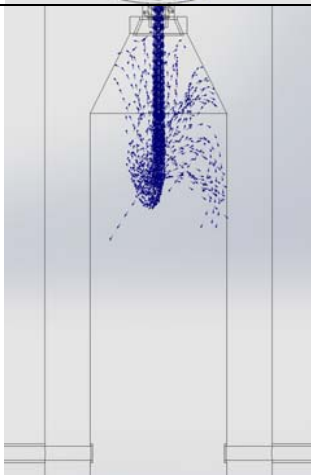
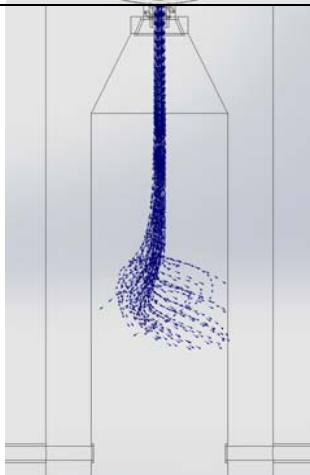
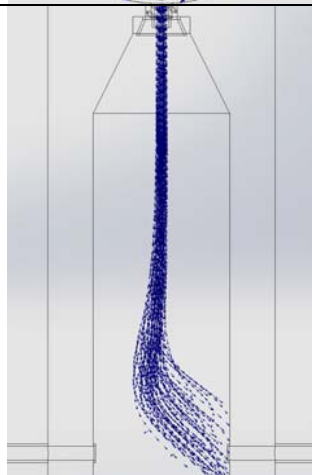
**Figure 88 – Method of  $L_{rev}$  determination**

**Table 50 – Particle flow characteristics of injecting PRB particle through fin-type coal spreader with 1-mm base width at various particle sizes**

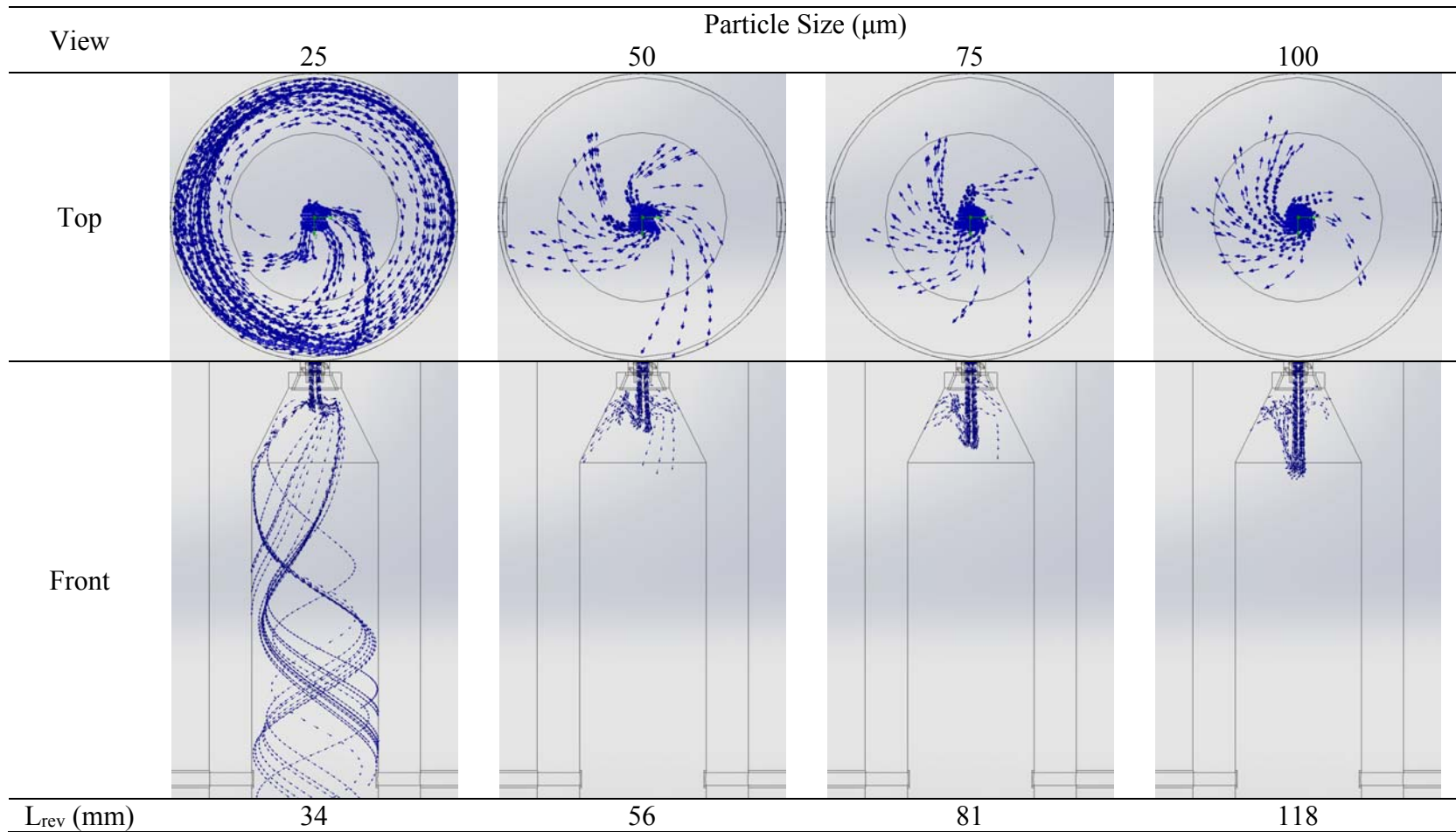




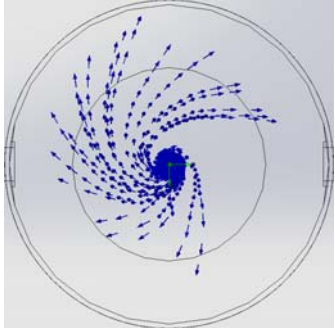
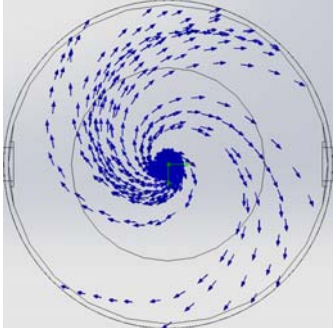
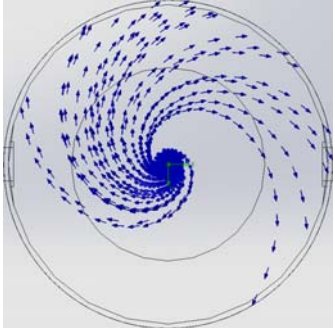
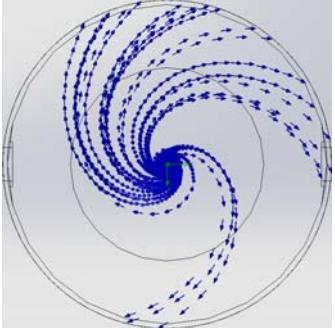
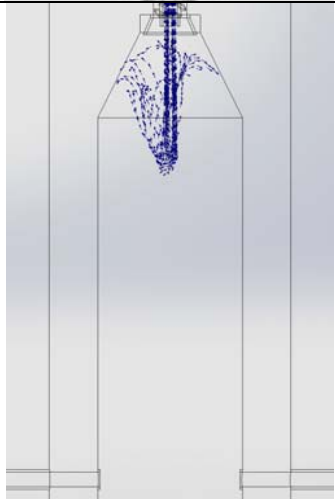
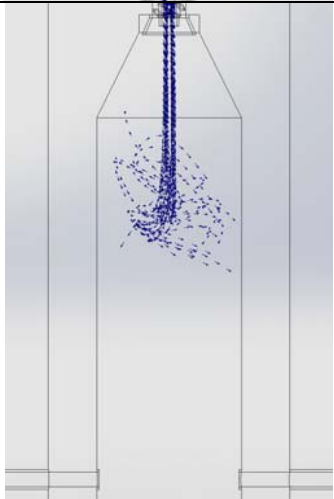
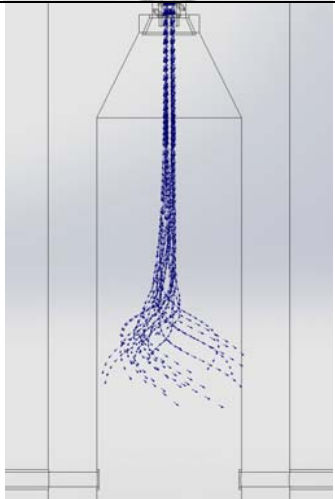
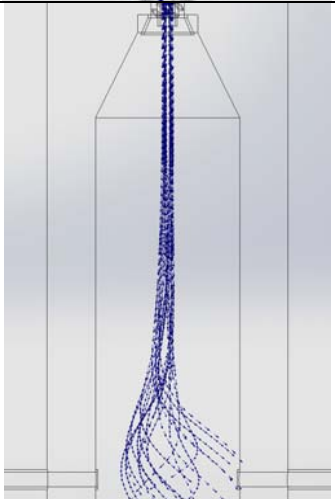
**Table 50 Continued**

View	Particle Size ( $\mu\text{m}$ )			
	125	150	175	200
Top				
Front				
$L_{\text{rev}}$ (mm)	142	204	N/A	N/A

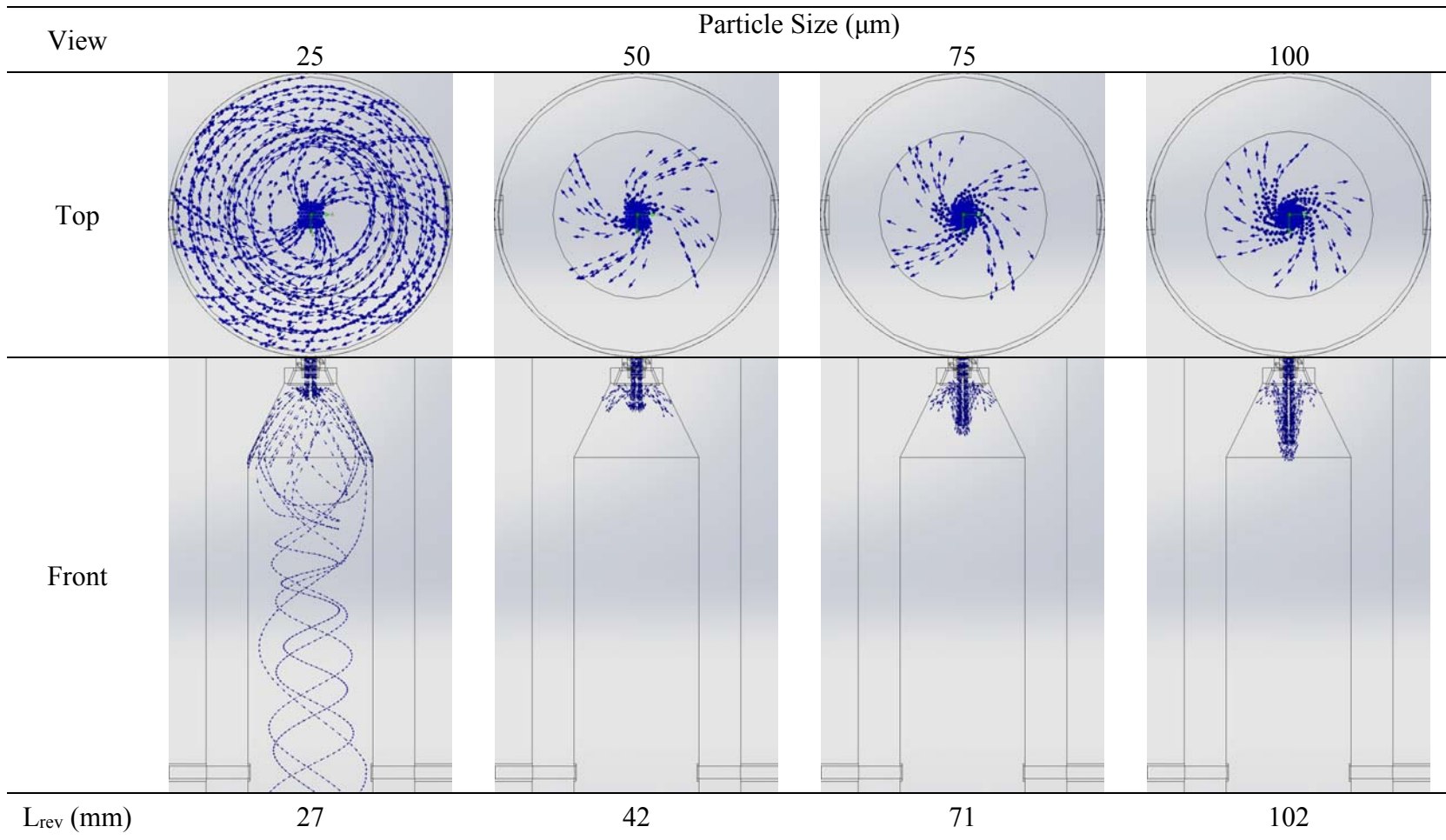
**Table 51 – Particle flow characteristics of injecting PRB particle through fin-type coal spreader with 3-mm base width at various particle sizes**



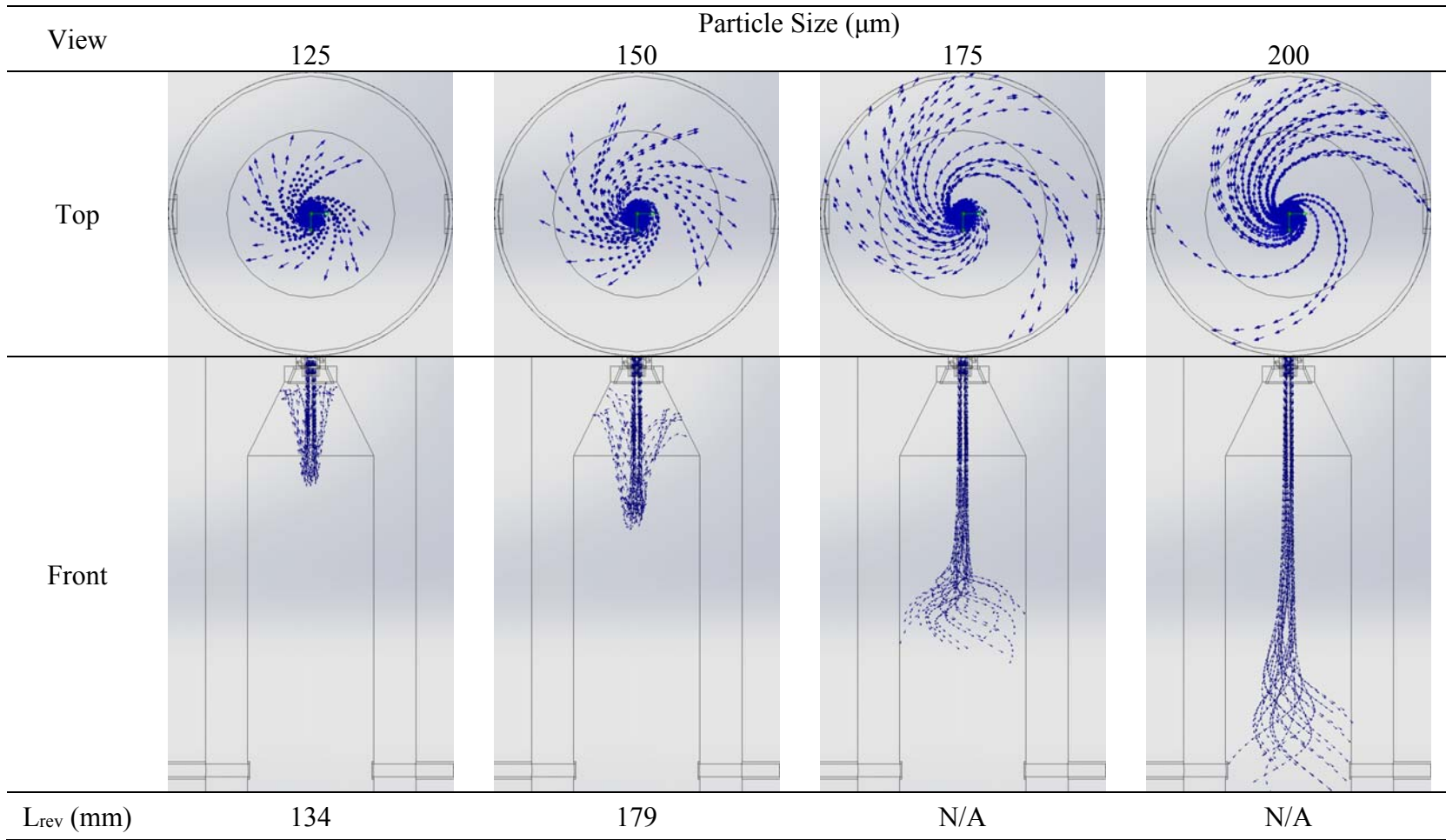
**Table 51 Continued**

View	Particle Size ( $\mu\text{m}$ )			
	125	150	175	200
Top				
Front				
$L_{rev}$ (mm)	158	N/A	N/A	N/A

**Table 52 – Particle flow characteristics of injecting PRB particle through v-shaped coal spreader with 3-mm base width at various particle sizes**



**Table 52 Continued**



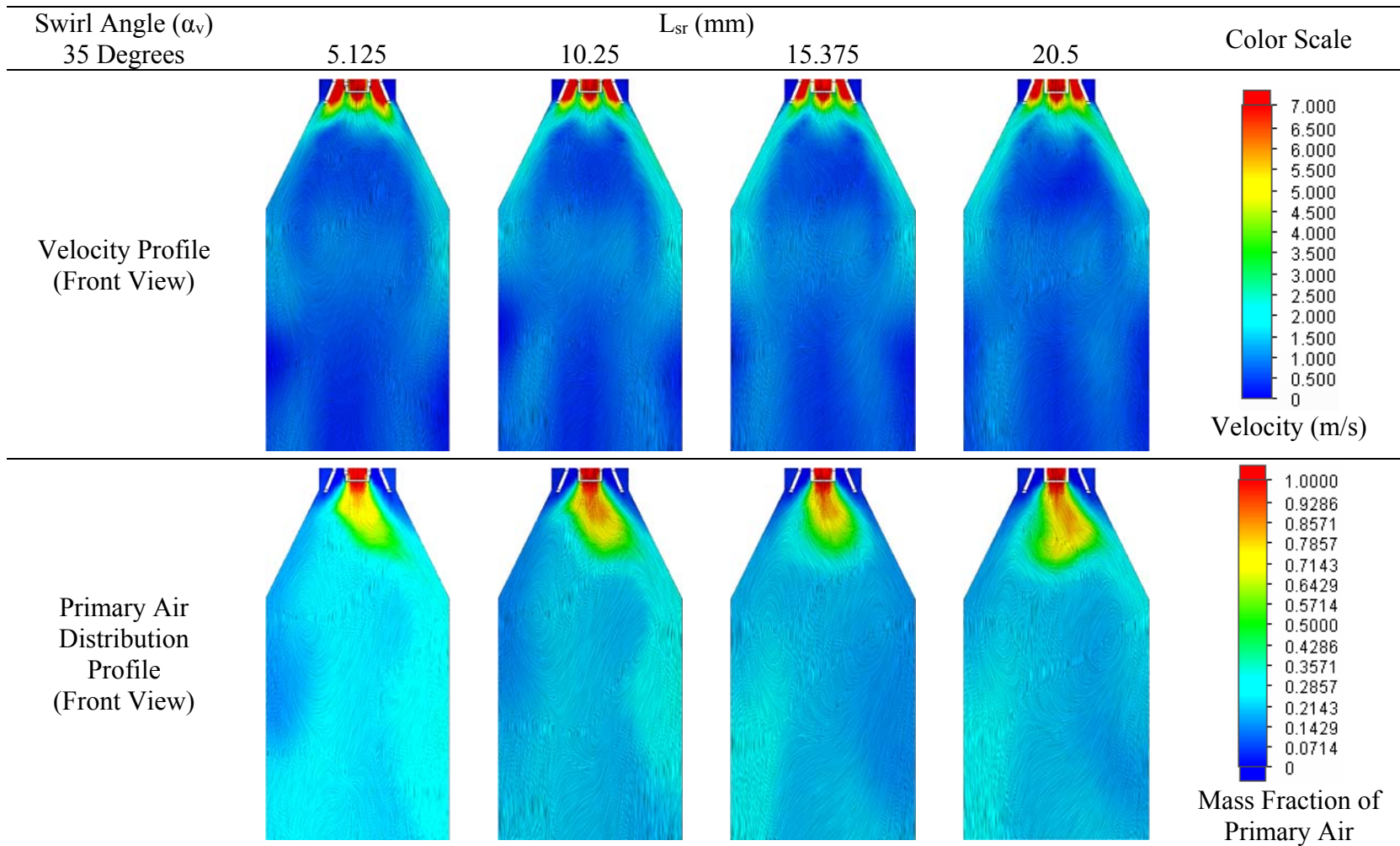
### F.3 Swirler

Refer to Syred and Beér (1974), although straight-vane swirlers have less efficiency compared to profile swirlers due to pressure drop across the swirler, the straight-vane swirlers are easier to fabricate. Therefore, the current research focuses on redesigning the straight-vane swirler with the aid of CFD and CAD programs.

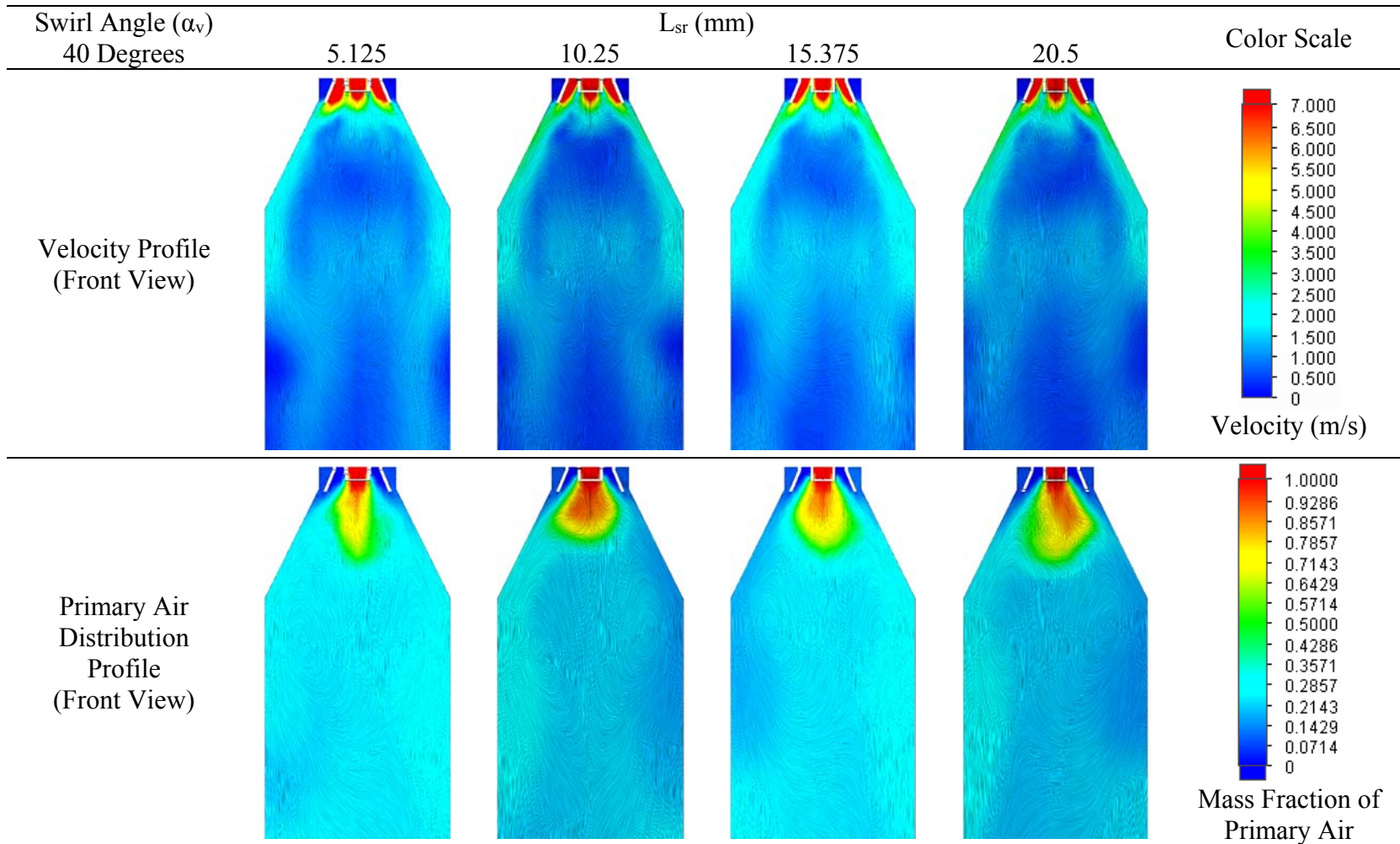
The temperature was set at 300 K. Swirl angle was varied from 35 degrees to 60 degrees with the increment of 5 degrees, and swirl recess length was varied from 5.125 mm to 20.5 mm with the increment of 5.125 mm. The mass flow rates of primary air and secondary air at  $ER_{mb}$  of 1.10 were applied. The mass flow rates of secondary air at  $ER_{mb}$  of 1.10 can prove whether the redesigned swirler can generate symmetric RZ. When the recirculating flow encounters the primary air, the axial momentum of primary air can lessen the effect of swirling flow on RZ formation. Thus, if the mass flow rate of secondary air at  $ER_{mb}$  of 1.10 can create symmetric RZ, the mass flow rate of secondary air at lesser  $ER_{mb}$  will be able to generate symmetric RZ as well. The results from NRF simulation as shown from Table 53 to Table 58 indicate that the swirler with  $\alpha_v$  of 60 degrees and  $L_{sr}$  of 10.25 mm can generate symmetric RZ.



**Table 53 – Velocity and primary air distribution profiles by setting swirl angle at 35 degrees and varying  $L_{sr}$**

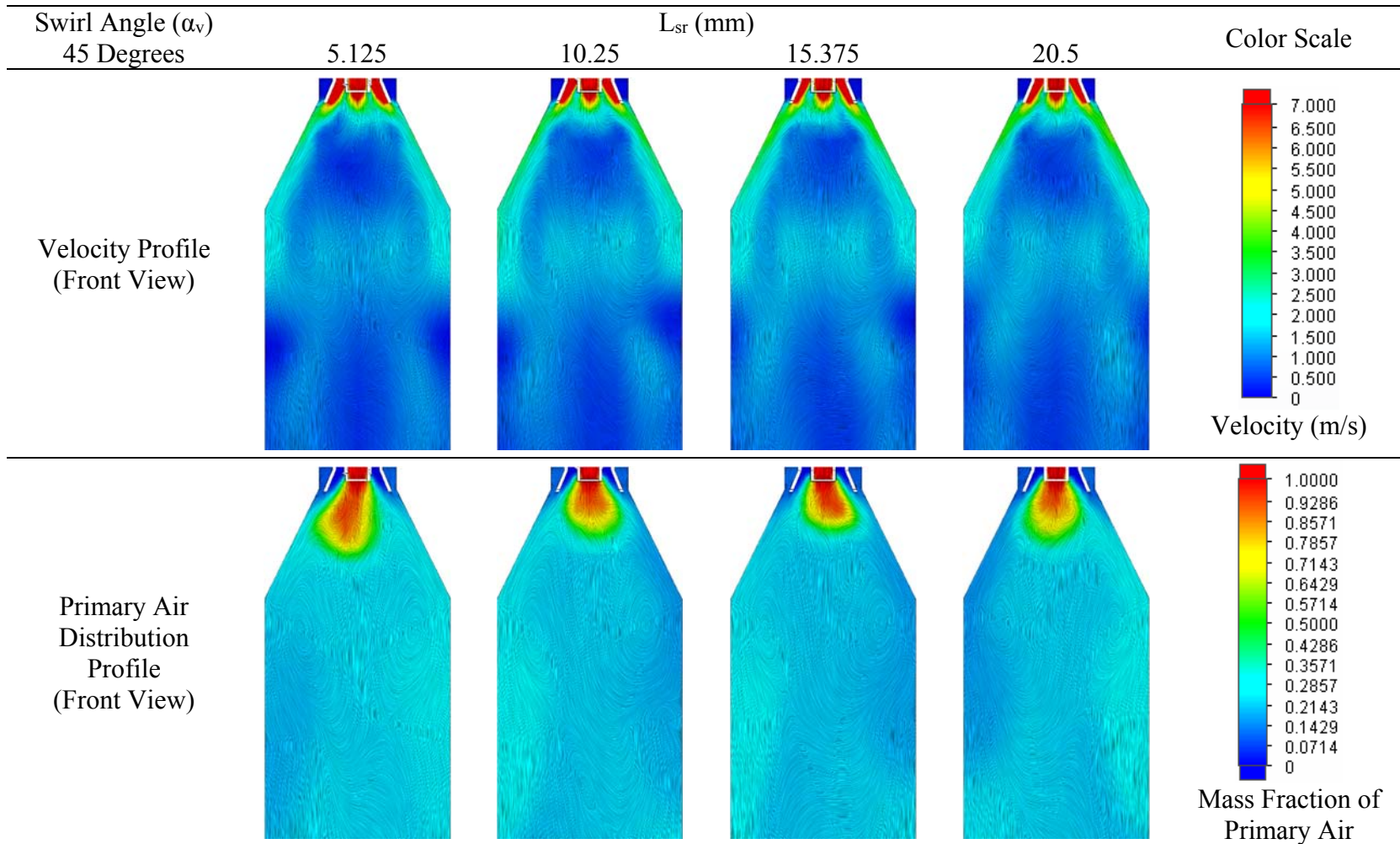


**Table 54 – Velocity and primary air distribution profiles by setting swirl angle at 40 degrees and varying  $L_{sr}$**

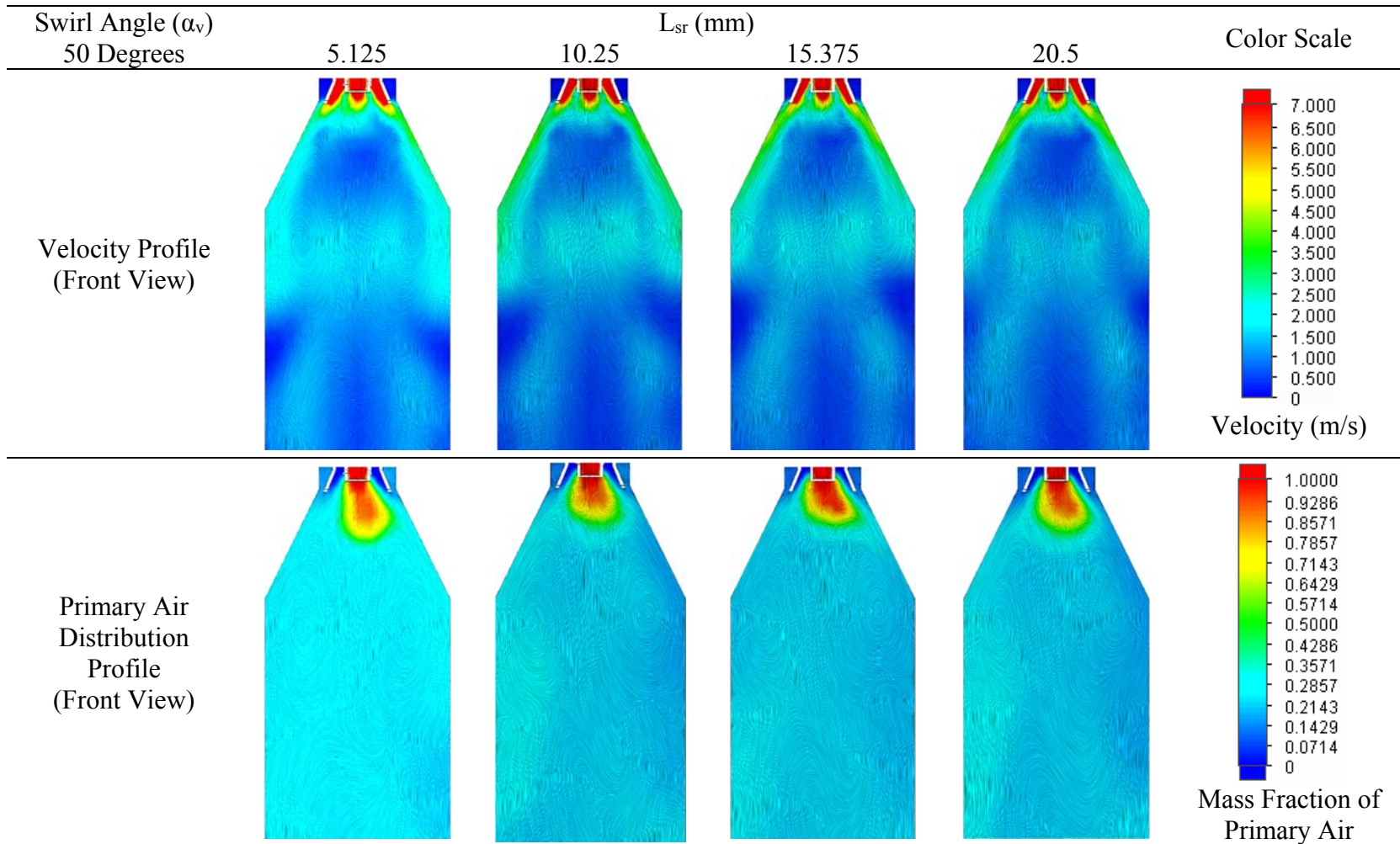




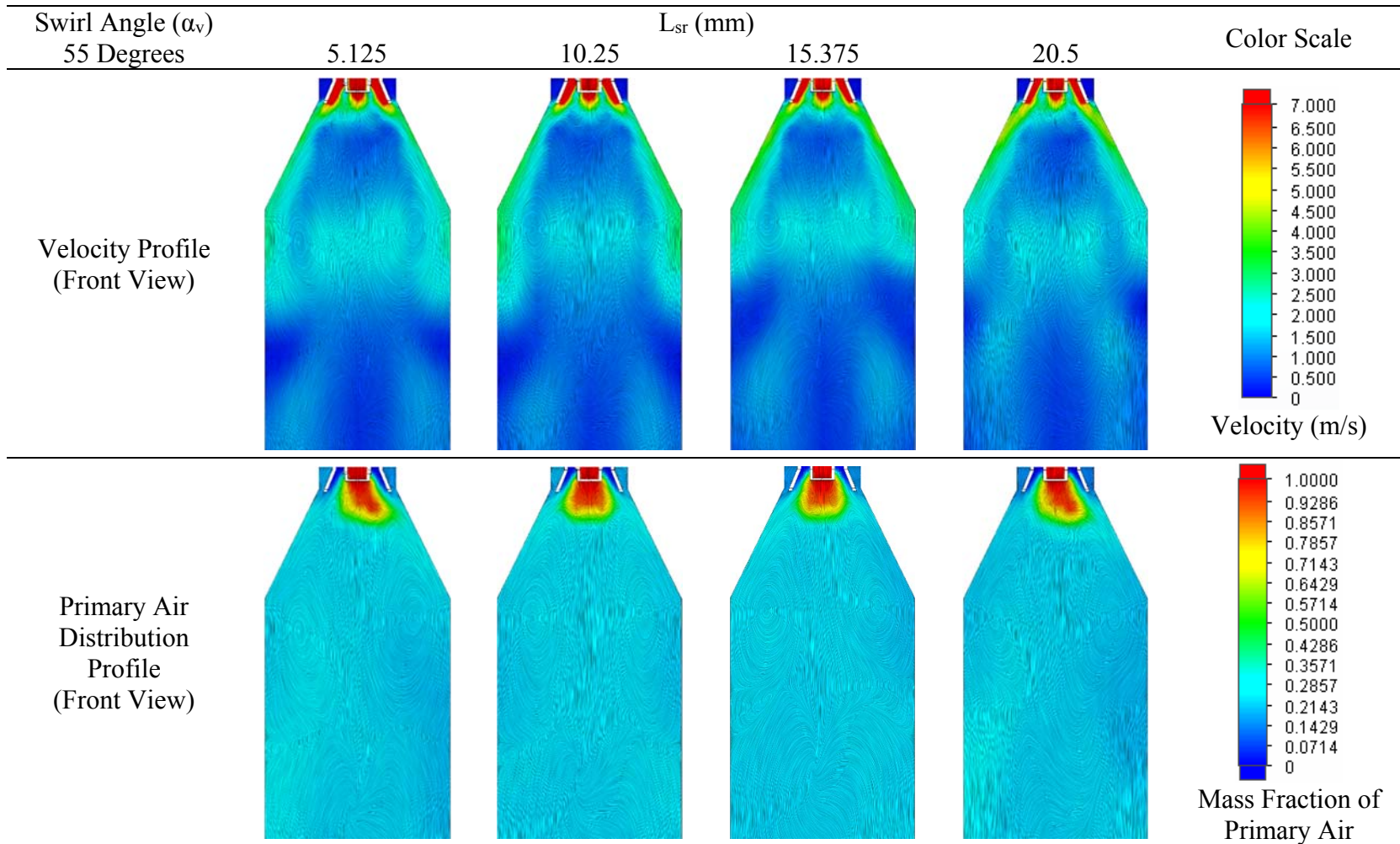
**Table 55 – Velocity and primary air distribution profiles by setting swirl angle at 45 degrees and varying  $L_{sr}$**



**Table 56 – Velocity and primary air distribution profiles by setting swirl angle at 50 degrees and varying  $L_{sr}$**

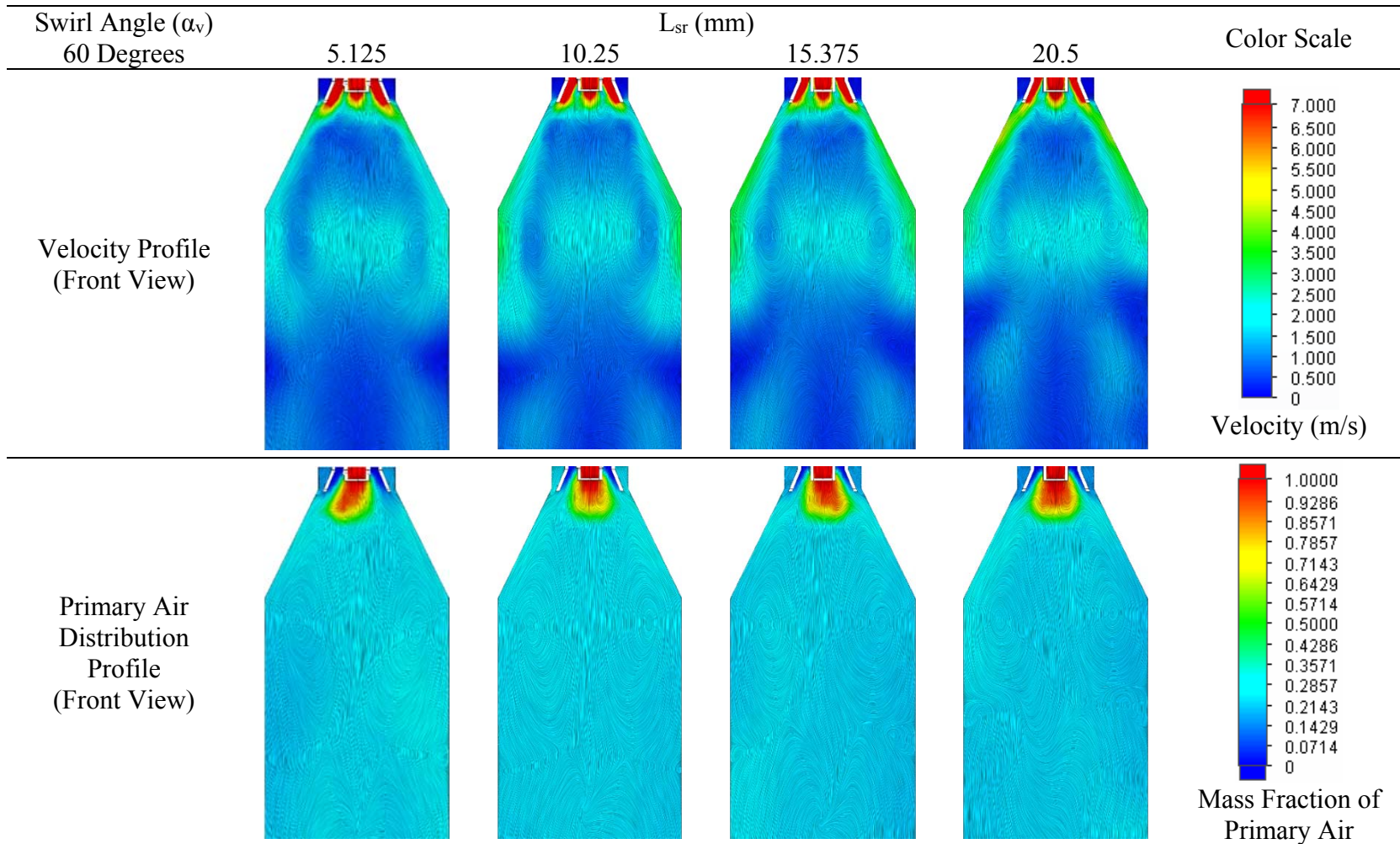


**Table 57 – Velocity and primary air distribution profiles by setting swirl angle at 55 degrees and varying  $L_{sr}$**





**Table 58 – Velocity and primary air distribution profiles by setting swirl angle at 60 degrees and varying  $L_{sr}$**



#### **F.4 Burner Diffuser**

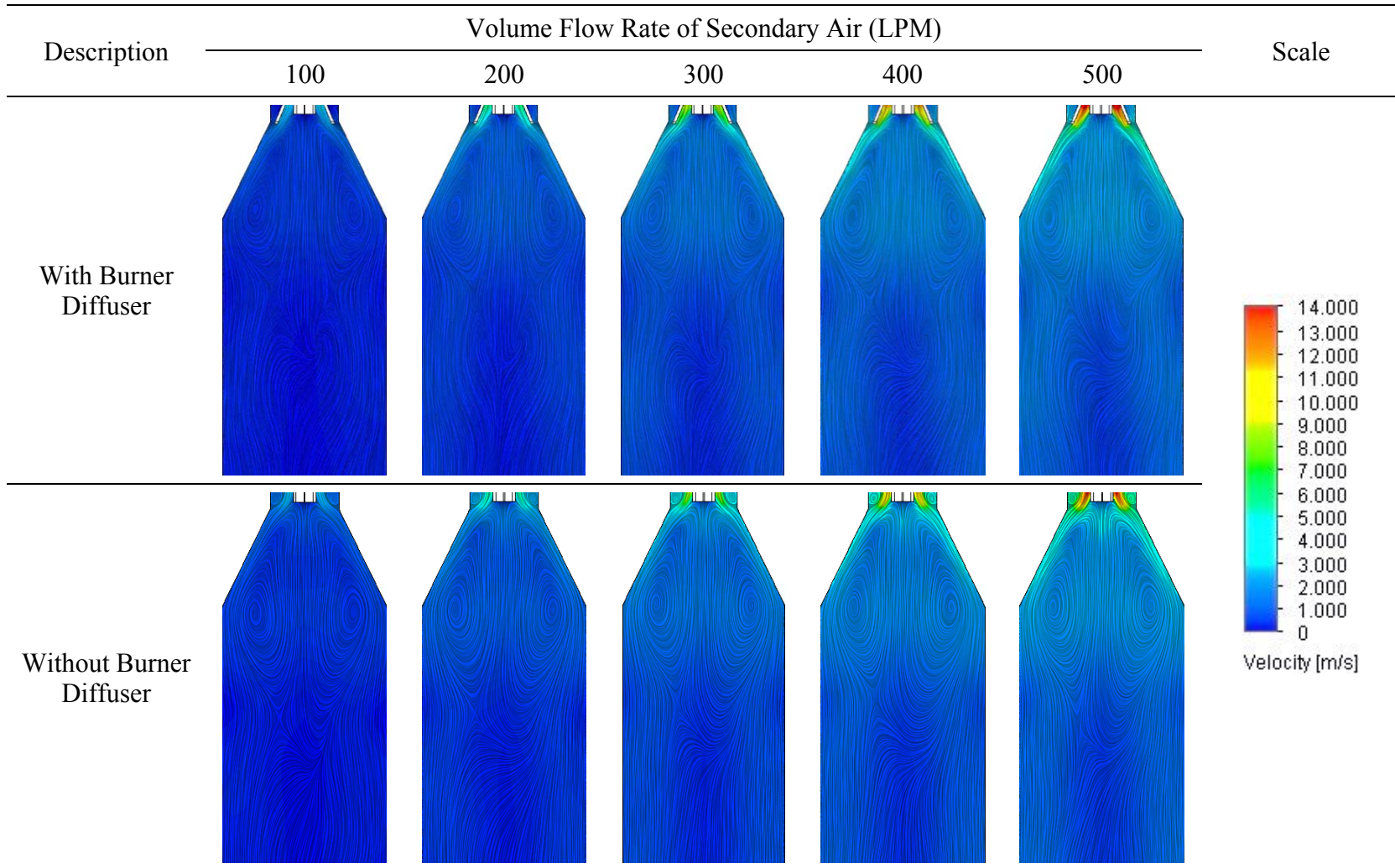
A burner diffuser was used in the current research in addition to quarl because the results from the NRF simulation indicated that, with the diffuser, the central recirculation zone (CRZ) could be generated more uniformly than without the diffuser. In Table 59, the streamlines of the CRZ with the diffuser installed at the burner exit are more symmetric than the streamlines of the CRZ without the diffuser.

Moreover, without the burner, the external recirculation zone (ERZ) would be formed in the gap between the fuel/primary air nozzle and the quarl. If ash accumulates in this gap and is solidified by high temperature after long-term operation, it will be problematic for maintenance work. Figure 89 shows the ash solidified in the quarl zone. This solidified ash is difficult to be removed. Thus, if the diffuser had not been installed, the burner would not have been able to be removed because of solidified ash.



**Figure 89 – Ash solidified in the quarl zone**

**Table 59 – Effects of burner diffuser on NRF characteristics at various volume flow rates**



## **F.5 Over-Fire Air (OFA) Injection**

The effects of injecting OFA into the combustion chamber on NRF characteristics were investigated by using conditions given in Table 60. The values of parameters in Condition 1 are from the pre-existing LNB system. Meanwhile, Condition 2 to 4 adopt the selected design of swirler from Appendix F.3 and vary the direction of OFA injection. The results are shown from Table 61 to Table 63.

Under condition 1, injecting OFA in tangential direction creates the clockwise (CW) OFA swirl below the main burner, and the OFA swirl has the direction of rotation as same as swirling flow from the main burner. Primarily, this method was supposed to enhance mixing between OFA and the product gases from the main burner. However, the results show that the OFA cannot penetrate into the center of the combustion chamber. In addition, a portion of OFA swirl rises up to the main burner. This will increase the O<sub>2</sub> concentration inside the primary combustion zone. As a result, NO<sub>x</sub> will increase due to higher O<sub>2</sub> concentration in the primary combustion zone. The same trend also occurs in condition 2 where the swirl angle is 59 degrees and number of secondary air inlet nozzles is four. In contrast to condition 1 and 2, the OFA swirl in condition 3 rotates in the counter clockwise (CCW) direction. However, the OFA still cannot penetrate into the center of the combustion chamber.

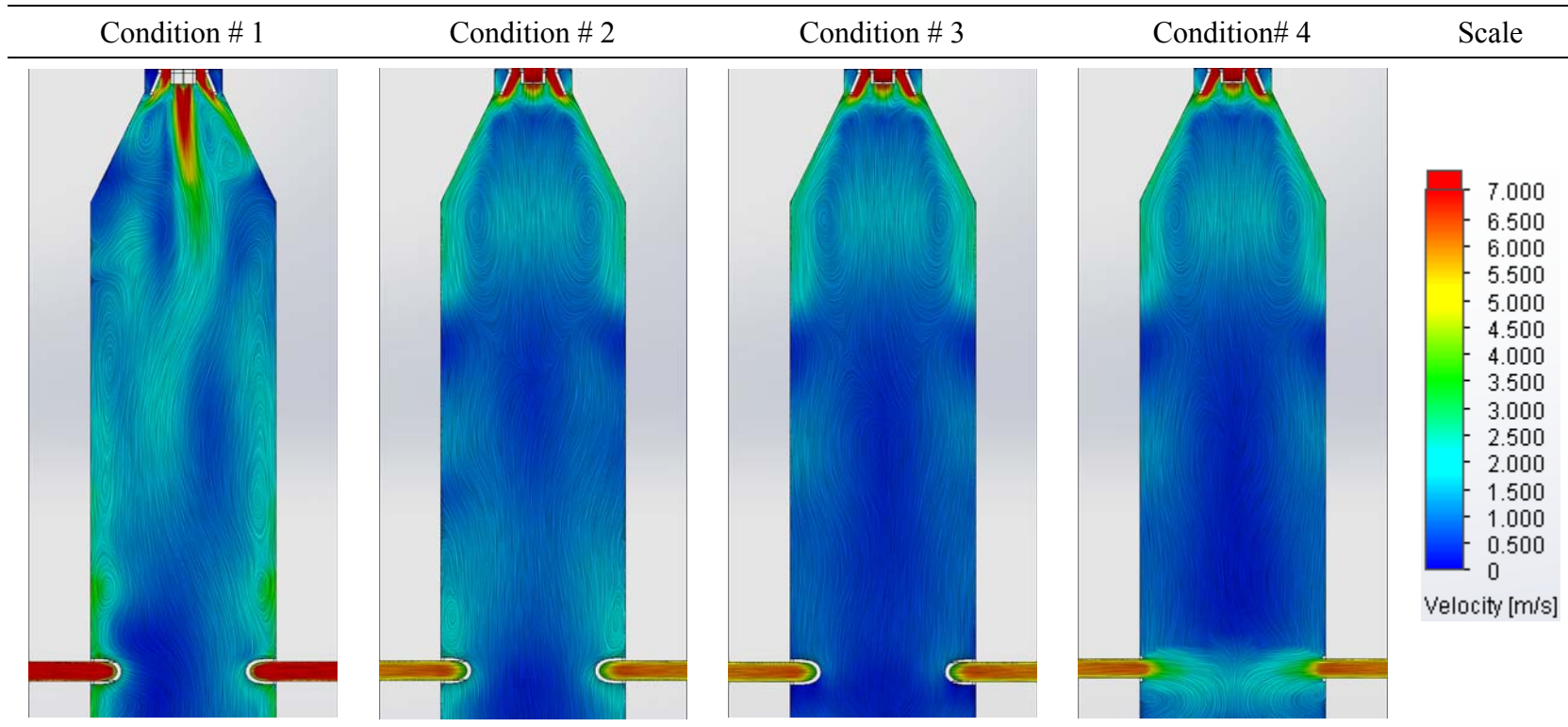
Lastly, the OFA injected in the radial direction (condition 4) can penetrate into the center of the swirling flow from the main burner, and only a small portion of OFA rises up above the level of OFA outlet nozzles. Hence, injecting OFA in radial direction is better than tangential direction.

**Table 60 – Conditions for investigating the effects of OFA on NRF characteristics**

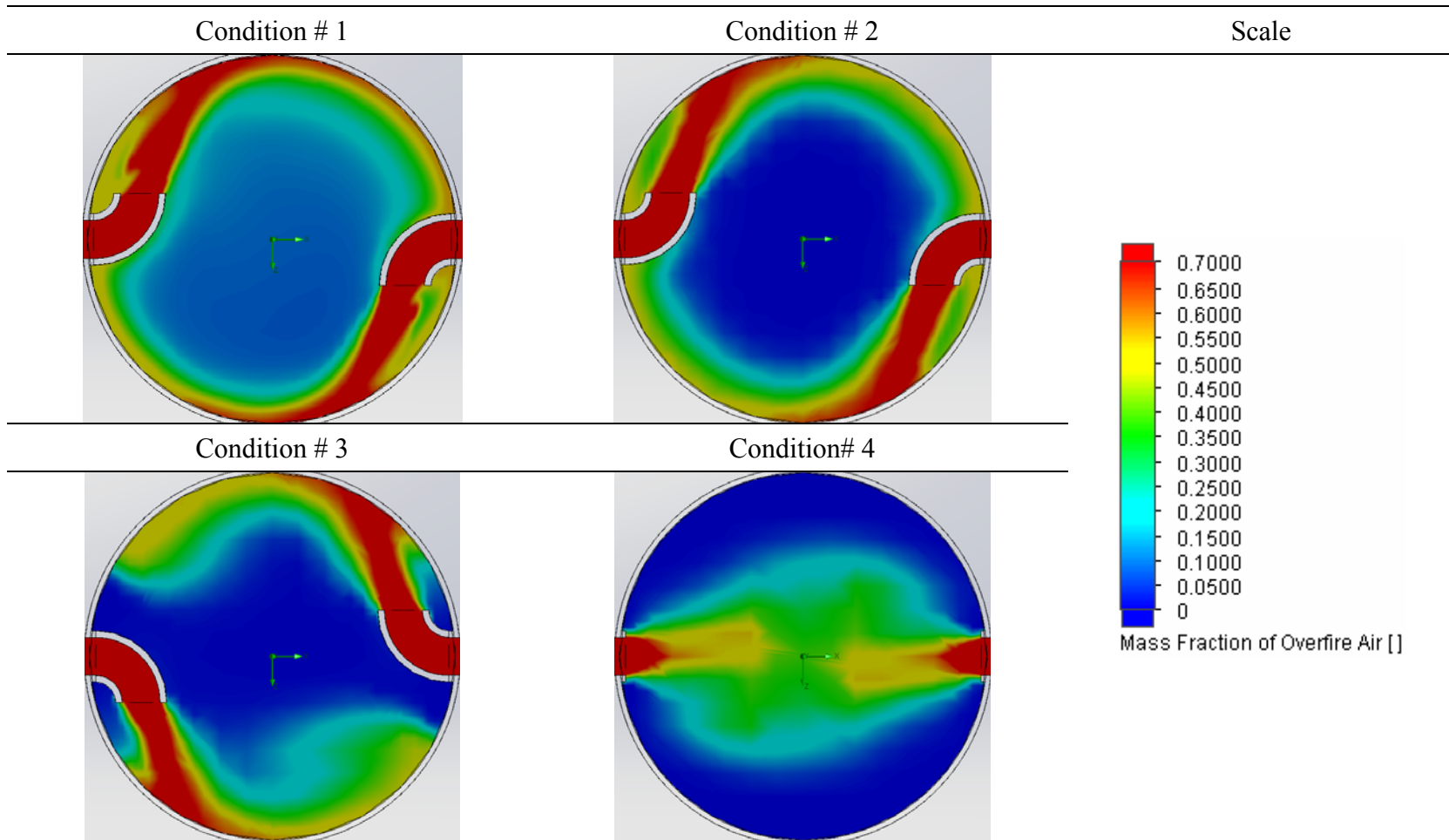
Parameter	Condition			
	1	2	3	4
ER <sub>oa</sub>	0.85	0.85	0.85	0.85
ER <sub>mb</sub>	1.10	1.10	1.10	1.10
Temperature (K)	300	300	300	300
Secondary Air				
- Number of secondary air inlet nozzles	1	4	4	4
- $\alpha_v$	33	59	59	59
- SN <sup>2</sup> <sub>sa</sub>	0.54	1.42	1.42	1.42
- Rotation of Swirl	CW	CW	CW	CW
OFA				
- Direction of Injection	Tangential	Tangential	Tangential	Radial
- Rotation of Swirl	CW	CW	CCW	-



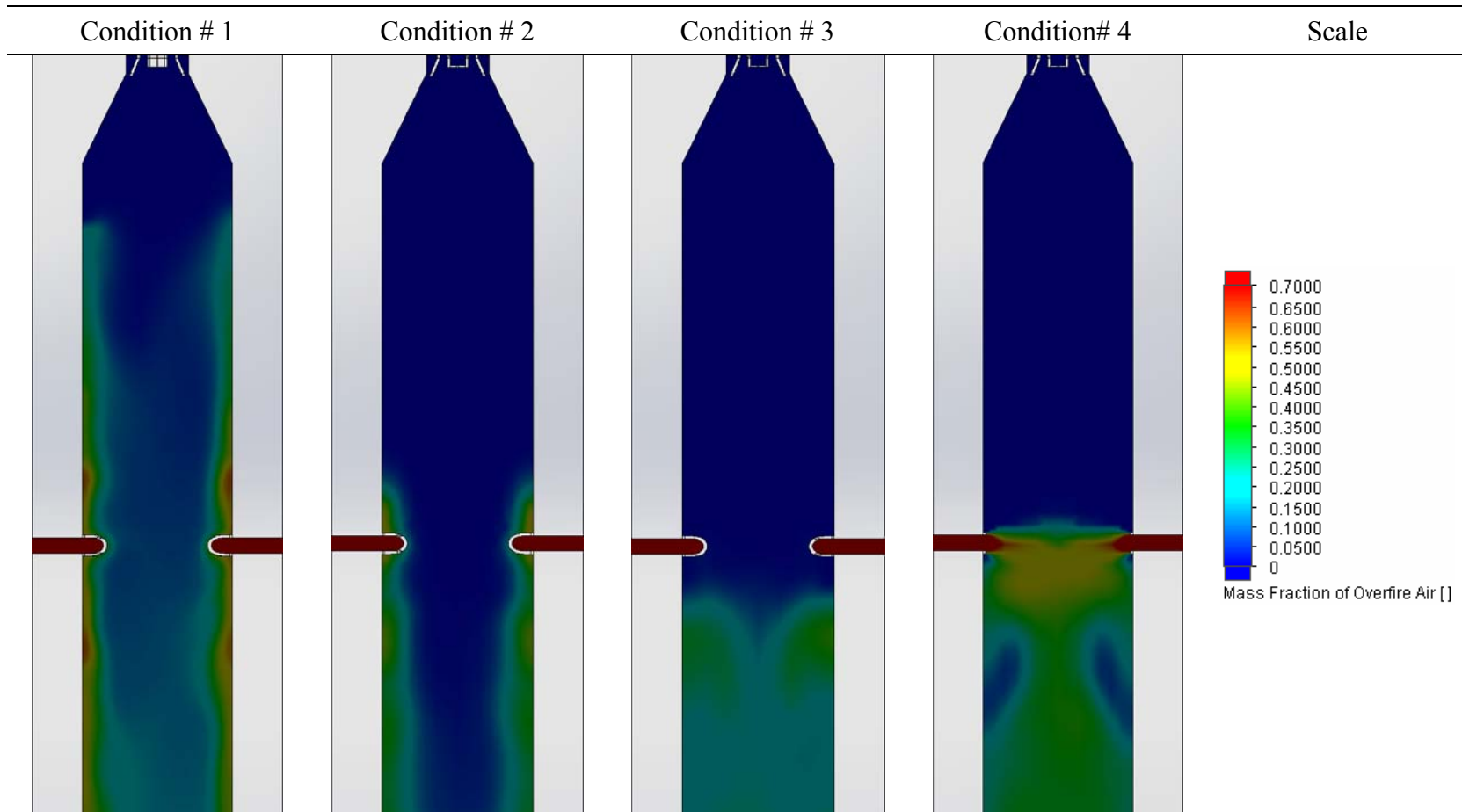
**Table 61 – Front view of velocity profiles of airflows under various conditions**



**Table 62 – Top view of mass fraction profiles of OFA under various conditions**



**Table 63 – Front view of mass fraction profiles of OFA under various conditions**



## F.6 Length of Recirculation Zone ( $L_{rz}$ )

The  $L_{rz}$  is defined as the length from the burner exit to the end of the RZ.  $L_{rz}$  of each operating condition at 300 K and 1,500 K could be determined by applying the method shown in Figure 90 to the velocity profile obtained from SolidWorks program. The values of  $L_{rz}$  are shown in Table 64.

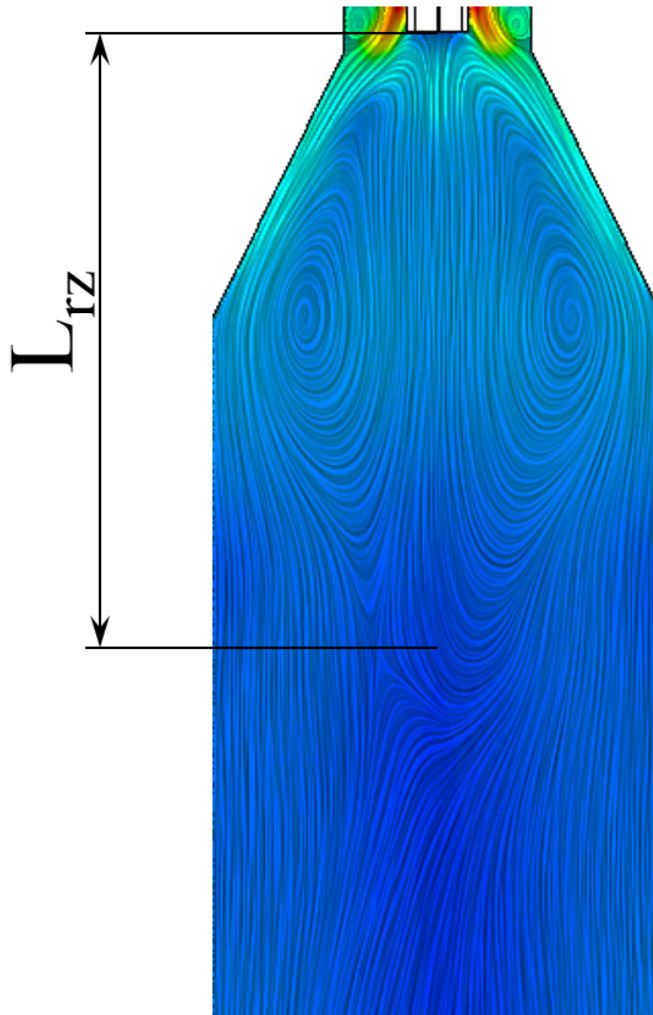


Figure 90 – Method of  $L_{rz}$  determination

**Table 64 –  $L_{rz}$  at 300 K and 1,500 K under various conditions**

$ER_{mb}$	$ER_{oa}$	$L_{rz}$ (mm)	
		Cold Flow (300 K)	Hot Flow (1,500 K)
Without OFA			
1.10	1.10	219	196
1.05	1.05	215	204
1.00	1.00	216	203
0.95	0.95	211	205
0.90	0.90	208	205
0.85	0.85	212	210
With OFA			
1.10	1.05	217	194
	1.00	219	194
	0.95	221	197
	0.90	224	197
	0.85	217	198
1.05	1.00	211	203
	0.95	216	200
	0.90	210	201
	0.85	211	204
1.00	0.95	215	204
	0.90	211	202
	0.85	210	200

APPENDIX G  
SWIRL NUMBERS (SN)

Swirl number (SN) is a dimensionless number which is defined as the ratio of the axial flux of angular momentum ( $G_{ang}$ ) to the product of the axial flux of axial momentum ( $G_{ax}$ ) and the radius of the swirler vane ( $r_v$ ) i.e. equation (G.1) (Beér and Chigier 1983). Inserting definitions of  $G_{ang}$  and  $G_{ax}$  in equation (G.1) yields equation (G.2) where  $\rho$  is the density of the fluid,  $v_{ax}$  and  $v_{tan}$  are respectively axial and tangential flow velocities at the burner exit,  $r$  is the radius at the considering point,  $r_o$  and  $r_i$  are outer and inner radii respectively, and  $P_{stat}$  is the static pressure (Lawn 1987).

$$SN = \frac{G_{ang}}{G_{ax}r_v} \quad (G.1)$$

$$SN = \frac{\int_{r_i}^{r_o} 2\pi\rho v_{ax}v_{tan}r^2 dr}{r_v \int_{r_i}^{r_o} 2\pi(P_{stat} + \rho v_{ax}^2)dr} \quad (G.2)$$

However, it is difficult to measure  $P_{stat}$  at the burner exit in reality. So, SN is simplified by neglecting  $P_{stat}$  which results in equation (G.3) and symbolized as SN' (Lawn 1987). Equation (G.3) allows SN' to be derived by using the burner geometry. The following assumptions are necessary for simplifying the swirl number by using burner geometry:

1. Primary and secondary airflows have flat and uniform flow distribution over the cross-sectional area prior to meeting with the coal spreader and the swirler respectively.

2. Density of primary air is equal to density of secondary air.
3. Coal particle attaches to the airflows.
4. Radial velocity of non-swirling flow is negligible.
5. Swirl angle is constant and does not depend on the vane profile.

$$SN' = \frac{\int_{r_i}^{r_o} \rho v_{ax} v_{tan} r^2 dr}{r_v \int_{r_i}^{r_o} \rho v_{ax}^2 r dr} \quad (G.3)$$

### G.1 SN of Secondary Airflow

The first derivation will consider only the swirled secondary airflow after it exits from the swirler zone. Therefore,  $r_o$  and  $r_i$  in equation (G.3) will be replaced by  $r_v$  and the hub radius ( $r_h$ ) respectively where  $r_h$  in the current research is equal to the outer radius of the fuel/primary air nozzle. Moreover, according to the assumptions made earlier, flow velocity at the burner exit ( $v$ ) could be estimated by using equation (G.4) where  $\dot{V}_{2nd}$  and  $A_{eff, 2nd}$  are the secondary air volume flow rate and the effective flow area of the secondary airflow respectively. The effective flow area ( $A_{eff}$ ) is the actual cross-sectional area that fluid passes the swirler as defined in equation (G.5) where the thickness of the swirler vane ( $t_v$ ) must be known. In addition, the calculations of  $v_{ax}$  and  $v_{tan}$  as shown in equation (G.6) and (G.7) require the swirl angle of the swirler vane ( $\alpha_v$ ).

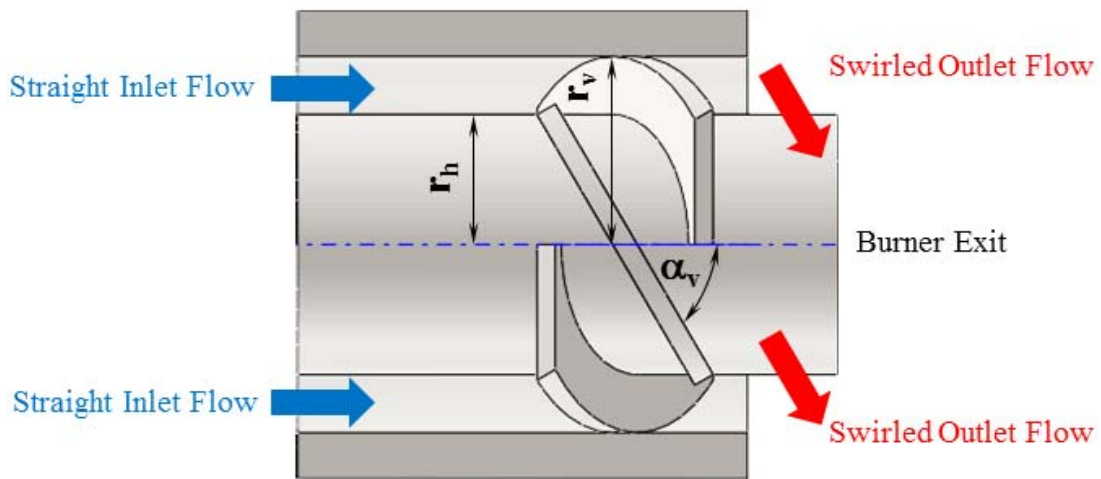
$$v = \frac{\dot{V}_{2nd}}{A_{eff, 2nd}} \quad (G.4)$$

$$A_{eff, 2nd} = \pi(r_v^2 - r_h^2) - 4[(r_v - r_h) \times t_v] \quad (G.5)$$

$$v_{ax} = v \cos(\alpha_v) \quad (G.6)$$

$$v_{tan} = v \sin(\alpha_v) \quad (G.7)$$

The geometry used in deriving swirl number of secondary airflow ( $SN'_{sa}$ ) is shown in Figure 91. The secondary airflow prior to entering the swirler zone is the straight flow. When the straight inlet flow meets the swirler, its direction is diverted by the swirler with the angle of  $\alpha_v$ . The outlet flow is so-called the swirled outlet flow. By using this geometry and the steps shown below,  $SN'_{sa}$  can be derived as shown in equation (G.8). This equation also presents in Beér and Chigier (1983) and Lawn (1987). By applying this equation with the measured values of  $r_h$  and  $r_v$  and varying  $\alpha_v$ , the plot of  $SN'_{sa}$  versus  $\alpha_v$  could be obtained as shown in Figure 92. Thus, for the current research where  $\alpha_v$  is 59 degrees,  $SN'_{sa}$  is equal to 1.42.



**Figure 91 – Geometry of burner for deriving  $SN'_{sa}$**



$$SN'_{sa} = \frac{\int_{r_h}^{r_v} \rho(v \cos \alpha_v)(v \sin \alpha_v)r^2 dr}{r_v \int_{r_h}^{r_v} \rho(v \cos \alpha_v)^2 r dr}$$

$$SN'_{sa} = (\tan \alpha_v) \frac{\frac{1}{3}r_v^3 - \frac{1}{3}r_h^3}{r_v \left( \frac{1}{2}r_v^2 - \frac{1}{2}r_h^2 \right)}$$

$$SN'_{sa} = \frac{2}{3} (\tan \alpha_v) \frac{1 - (r_h/r_v)^3}{1 - (r_h/r_v)^2} \quad (G.8)$$

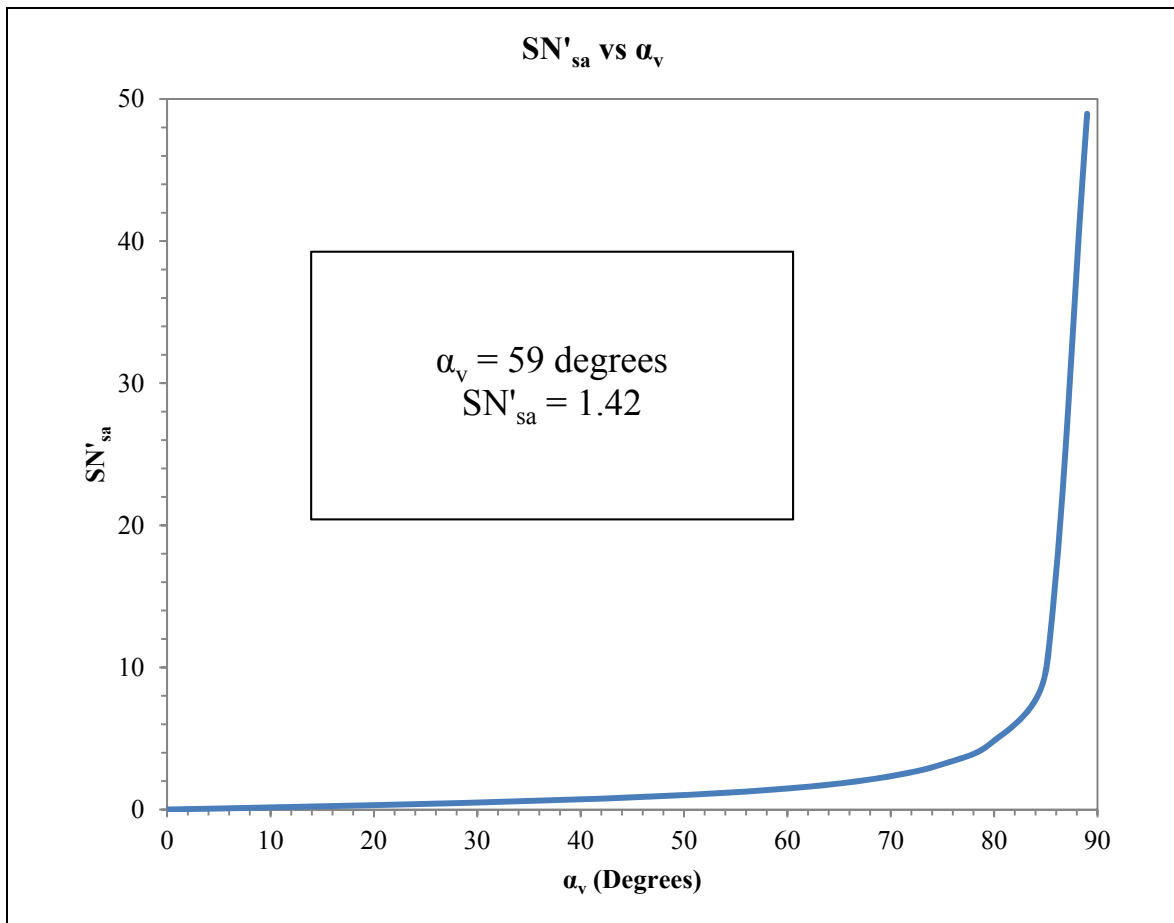
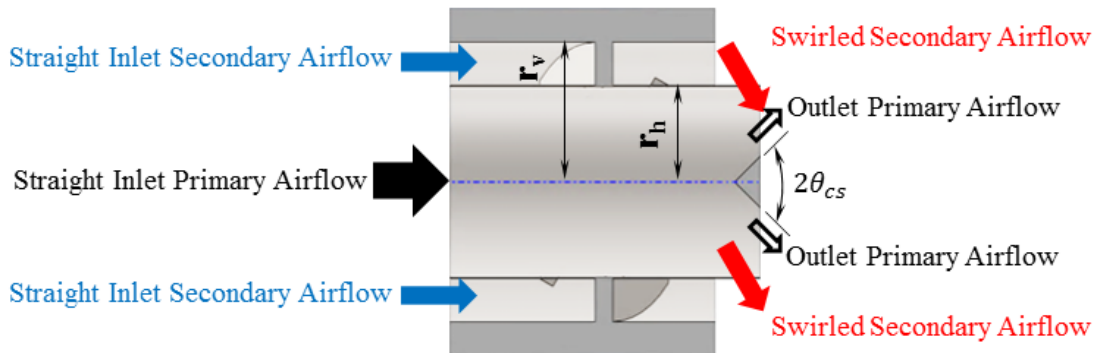


Figure 92 – Plot of SN'\_{sa} versus \alpha\_v

## G.2 SN of Very Thin-Walled Fuel/Primary Air Nozzle with V-Shaped Coal

### Spreader

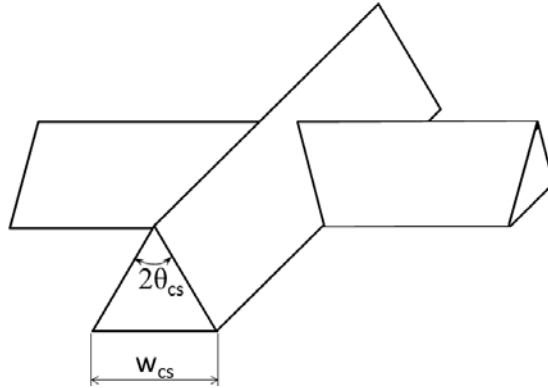
The geometry of very thin-walled fuel/primary air nozzle with v-shaped coal spreader installed at the center of the nozzle is illustrated in Figure 93. By using this geometry, the integration terms in equation (G.3) could be separated into two parts. The first part considers the unswirled flow exits from the fuel/primary air nozzle which takes the effect of v-shaped coal spreader on the unswirled flow velocity ( $v_{us}$ ) into account. The other part considers the swirled flow exits from the swirler. The swirled flow velocity ( $v_s$ ) at the burner exit is identical to  $v$  in the earlier case.



**Figure 93 – Burner geometry with very thin-walled fuel/primary air nozzle and v-shaped coal spreader**

Since the very-thin walled fuel/primary air nozzle is being considered, both inner and outer radii of the nozzle could be assumed to be equal to  $r_h$ . The equations used to find  $v_{us}$  and  $v_s$  are given in equations (G.9) and (G.10) where  $\dot{V}_{1st}$  represents the volume flow rate of the primary air, and  $A_{eff, 1st}$  as defined in equation (G.11) is the effective

flow area of the fuel/primary air nozzle at the exit which takes the base width of the coal spreader,  $w_{cs}$ , as illustrated in Figure 94 into account.



**Figure 94 – Illustration of the base width and the half angle of the v-shaped coal spreader**

$$v_{us} = \frac{\dot{V}_{1st}}{A_{eff,1st}} \quad (G.9)$$

$$v_s = \frac{\dot{V}_{2nd}}{A_{eff,2nd}} \quad (G.10)$$

$$A_{eff,1st} = \pi r_h^2 - [2(2r_h \times w_{cs}) - w_{cs}^2] \quad (G.11)$$

Then, the equations for calculating the axial and tangential unswirled flow velocities ( $v_{us, ax}$  and  $v_{us, tan}$ ) are given in equation (G.12) and (G.13) where the half angle of the v-shaped coal spreader ( $\theta_{cs}$ ) as shown in Figure 94 is included in consideration. Furthermore, the axial and tangential swirled flow velocities are given in equations (G.14) and (G.15) which are identical to equations (G.6) and (G.7).

$$v_{us,ax} = v_{us} \cos \theta_{cs} \quad (G.12)$$

$$v_{us,tan} = v_{us} \sin \theta_{cs} \quad (G.13)$$

$$v_{s,ax} = v_s \cos \alpha_v \quad (G.14)$$

$$v_{s,tan} = v_s \sin \alpha_v \quad (G.15)$$

The overall swirl number for the flows pass through the very thin-walled fuel/primary air nozzle with v-shaped coal spreader and the swirler is symbolized as  $SN'_{oa,v}$ . Conditions and equations described earlier are applied into equation (G.3). The following steps show how  $SN'_{oa,v}$  as given in equation (G.16) could be derived.

$$\begin{aligned}
 SN'_{oa,v} &= \frac{\int_0^{r_h} \rho(v_{us} \cos \theta_{cs})(v_{us} \sin \theta_{cs})r^2 dr + \int_{r_h}^{r_v} \rho(v_s \cos \alpha_v)(v_s \sin \alpha_v)r^2 dr}{r_v \left( \int_0^{r_h} \rho(v_{us} \cos \theta_{cs})^2 r dr + \int_{r_h}^{r_v} \rho(v_s \cos \alpha_v)^2 r dr \right)} \\
 SN'_{oa,v} &= \frac{\int_0^{r_h} (v_{us} \cos \theta_{cs})(v_{us} \sin \theta_{cs})r^2 dr + \int_{r_h}^{r_v} (v_s \cos \alpha_v)(v_s \sin \alpha_v)r^2 dr}{r_v \left( \int_0^{r_h} (v_{us} \cos \theta_{cs})^2 r dr + \int_{r_h}^{r_v} (v_s \cos \alpha_v)^2 r dr \right)} \\
 SN'_{oa,v} &= \frac{\frac{1}{3} v_{us}^2 \sin \theta_{cs} \cos \theta_{cs} (r_h^3) + \frac{1}{3} v_s^2 \sin \alpha_v \cos \alpha_v (r_v^3 - r_h^3)}{r_v \left( \frac{1}{2} (v_{us} \cos \theta_{cs})^2 r_h^2 + \frac{1}{2} (v_s \cos \alpha_v)^2 (r_v^2 - r_h^2) \right)} \\
 SN'_{oa,v} &= \frac{2 v_{us}^2 \sin \theta_{cs} \cos \theta_{cs} (r_h^3) + v_s^2 \sin \alpha_v \cos \alpha_v (r_v^3 - r_h^3)}{3 r_v \left( (v_{us} \cos \theta_{cs})^2 r_h^2 + (v_s \cos \alpha_v)^2 (r_v^2 - r_h^2) \right)} \quad (G.16)
 \end{aligned}$$

Next, assume that the coal spreader is a fin type instead of a v-shaped one.  $\theta_{cs}$  will be equal to zero. By applying this assumption into equation (G.16) and following steps shown below, the  $SN'_{oa}$  for a very thin-walled fuel/ primary air nozzle with a fin-

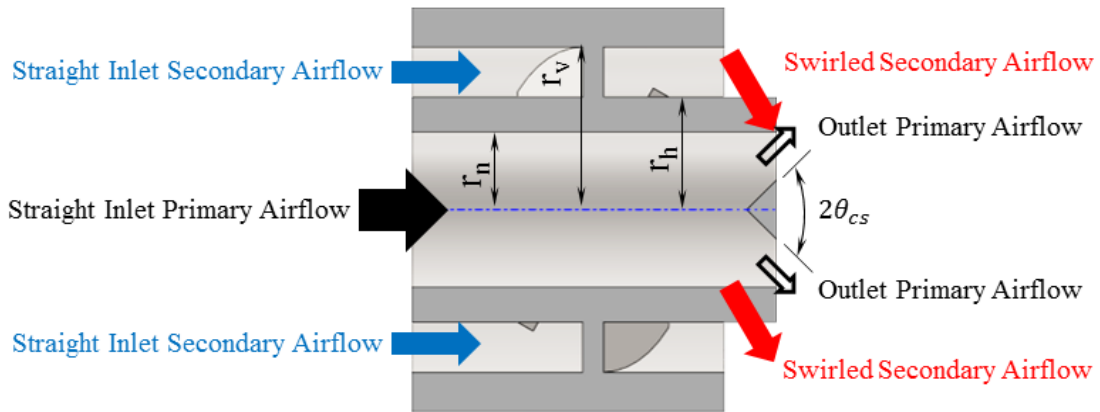
type coal spreader ( $SN'_{oa,fin}$ ) could be derived as shown in equation (G.17). Equation (G.17) is similar to the swirl number mentioned by Cheng and Levinsky (2008).

$$\begin{aligned}
 SN'_{oa,fin} &= \frac{2}{3} \frac{v_s^2 \sin \alpha_v \cos \alpha_v (r_v^3 - r_h^3)}{r_v (v_{us}^2 r_h^2 + (v_s \cos \alpha_v)^2 (r_v^2 - r_h^2))} \\
 SN'_{oa,fin} &= \frac{2}{3} \frac{r_v^3 v_s^2 \sin \alpha_v \cos \alpha_v \left[ 1 - \left( \frac{r_h}{r_v} \right)^3 \right]}{r_v^3 v_s^2 \left\{ \left( \frac{v_{us}}{v_s} \right)^2 \left( \frac{r_h}{r_v} \right)^2 + (\cos \alpha_v)^2 \left[ 1 - \left( \frac{r_h}{r_v} \right)^2 \right] \right\}} \\
 SN'_{oa,fin} &= \frac{2}{3} \frac{r_v^3 v_s^2 \sin \alpha_v \cos \alpha_v \left[ 1 - \left( \frac{r_h}{r_v} \right)^3 \right]}{r_v^3 v_s^2 (\cos \alpha_v)^2 \left\{ \left( \frac{v_{us}}{v_s \cos \alpha_v} \right)^2 \left( \frac{r_h}{r_v} \right)^2 + \left[ 1 - \left( \frac{r_h}{r_v} \right)^2 \right] \right\}} \\
 SN'_{oa,fin} &= \frac{2}{3} \frac{\frac{\sin \alpha_v}{\cos \alpha_v} \left[ 1 - \left( \frac{r_h}{r_v} \right)^3 \right]}{\left[ \left( \frac{v_{us}}{v_s \cos \alpha_v} \right)^2 \left( \frac{r_h}{r_v} \right)^2 + 1 - \left( \frac{r_h}{r_v} \right)^2 \right]} \\
 SN'_{oa,fin} &= \frac{2}{3} \frac{\tan \alpha_v \left( 1 - \left( \frac{r_h}{r_v} \right)^3 \right)}{1 + \left[ \left( \frac{v_{us}}{v_s \cos \alpha_v} \right)^2 - 1 \right] \left( \frac{r_h}{r_v} \right)^2} \tag{G.17}
 \end{aligned}$$

### G.3 SN of Thick-Walled Fuel/Primary Air Nozzle with V-Shaped Coal Spreader

In this case, the wall thickness of the fuel/primary air nozzle which is the difference between  $r_h$  and the inner radius of the nozzle ( $r_n$ ) will be included in the overall swirl number calculation. The burner geometry for this consideration is shown in Figure 95. As a result, the redefined  $A_{eff,1st}$  is given in equation (G.18).

$$A_{eff,1st} = \pi r_n^2 - [2(2r_n \times w_{cs}) - w_{cs}^2] \tag{G.18}$$



**Figure 95 – Burner geometry with thick-walled fuel/primary air nozzle and v-shaped coal spreader**

By applying this geometry and earlier assumptions into equation (G.3) and using equation (G.18), the overall swirl number for the flows pass through the thick-walled fuel/primary air nozzle with v-shaped coal spreader and the swirler which is symbolized as  $SN_{oa,vt}^2$  could be derived by using the steps shown below. Equation (G.20) shows the result of the derivation. However, please note that this equation cannot apply to the condition where  $\theta_{cs}$  is exactly equal to 90 degrees. The reason is  $v_{us}$  term will be cancelled out from the calculation although there actually is the unswirled flow passes through the coal spreader. So, the range of  $\theta_{cs}$  for this equation is:  $0 \leq \theta_{cs} < 90$ . Similarly,  $\alpha_v$  could not be exactly equal to zero and 90 because the swirl cannot be generated by these values. Hence, the range of  $\alpha_v$  for equation (G.20) is:  $0 < \alpha_v < 90$ .

$$\begin{aligned}
SN'_{oa,vt} &= \frac{\int_0^{r_n} \rho(v_{us} \cos \theta_{cs})(v_{us} \sin \theta_{cs})r^2 dr + \int_{r_h}^{r_v} \rho(v_s \cos \alpha_v)(v_s \sin \alpha_v)r^2 dr}{r_v \left( \int_0^{r_n} \rho(v_{us} \cos \theta_{cs})^2 r dr + \int_{r_h}^{r_v} \rho(v_s \cos \alpha_v)^2 r dr \right)} \\
SN'_{oa,vt} &= \frac{\int_0^{r_n} (v_{us} \cos \theta_{cs})(v_{us} \sin \theta_{cs})r^2 dr + \int_{r_h}^{r_v} (v_s \cos \alpha_v)(v_s \sin \alpha_v)r^2 dr}{r_v \left( \int_0^{r_n} (v_{us} \cos \theta_{cs})^2 r dr + \int_{r_h}^{r_v} (v_s \cos \alpha_v)^2 r dr \right)} \\
SN'_{oa,vt} &= \frac{\frac{1}{3} v_{us}^2 \sin \theta_{cs} \cos \theta_{cs} (r_n^3) + \frac{1}{3} v_s^2 \sin \alpha_v \cos \alpha_v (r_v^3 - r_h^3)}{r_v \left( \frac{1}{2} (v_{us} \cos \theta_{cs})^2 r_n^2 + \frac{1}{2} (v_s \cos \alpha_v)^2 (r_v^2 - r_h^2) \right)} \\
SN'_{oa,vt} &= \frac{2 v_{us}^2 \sin \theta_{cs} \cos \theta_{cs} (r_n^3) + v_s^2 \sin \alpha_v \cos \alpha_v (r_v^3 - r_h^3)}{3 r_v \left( (v_{us} \cos \theta_{cs})^2 r_n^2 + (v_s \cos \alpha_v)^2 (r_v^2 - r_h^2) \right)} \quad (G.20)
\end{aligned}$$

In the current research, the angle of the v-shaped coal spreader is set at 90 degrees; in other words,  $\theta_{cs}$  is set at 45 degrees. Equation (G.21) which is mainly used in the current thesis is the result from inserting this value into equation (G.20).

$$SN'_{oa,vt} = \frac{2 v_{us}^2 r_n^3 + 2 v_s^2 \sin \alpha_v \cos \alpha_v (r_v^3 - r_h^3)}{3 r_v \left( v_{us}^2 r_n^2 + (\sqrt{2} v_s \cos \alpha_v)^2 (r_v^2 - r_h^2) \right)} \quad (G.21)$$

The results from Appendix B show that the volume flow rates of air required for firing pure PRB or co-firing blends of PRB and DB with the PRB-to-DB ratio of 90 to 10 on a mass basis could be considered not different. Therefore, only the volume flow rates of pure PRB will be used for the swirl number calculation in the current thesis. The plot of  $SN'_{oa,vt}$  versus  $\alpha_v$  for ER from 0.85 to 1.10 with the increment of 0.05 could be obtained as shown in Figure 96. This shows that, when  $\alpha_v$  is 60 degrees, the values of  $SN'_{oa,vt}$  range from 0.94 to 1.1 which are in the strong swirl region (Tomeczek 1994).

The deviation of  $SN'_{oa, vt}$  caused by the change in volume flow rate is not significant when  $\alpha_v$  is less than 30 degrees. In addition, the values of  $SN'_{oa, vt}$  tend to drop when  $\alpha_v$  is above 70 degrees. This implies that the strength of the swirl could be decreased by the excessive swirl angle.

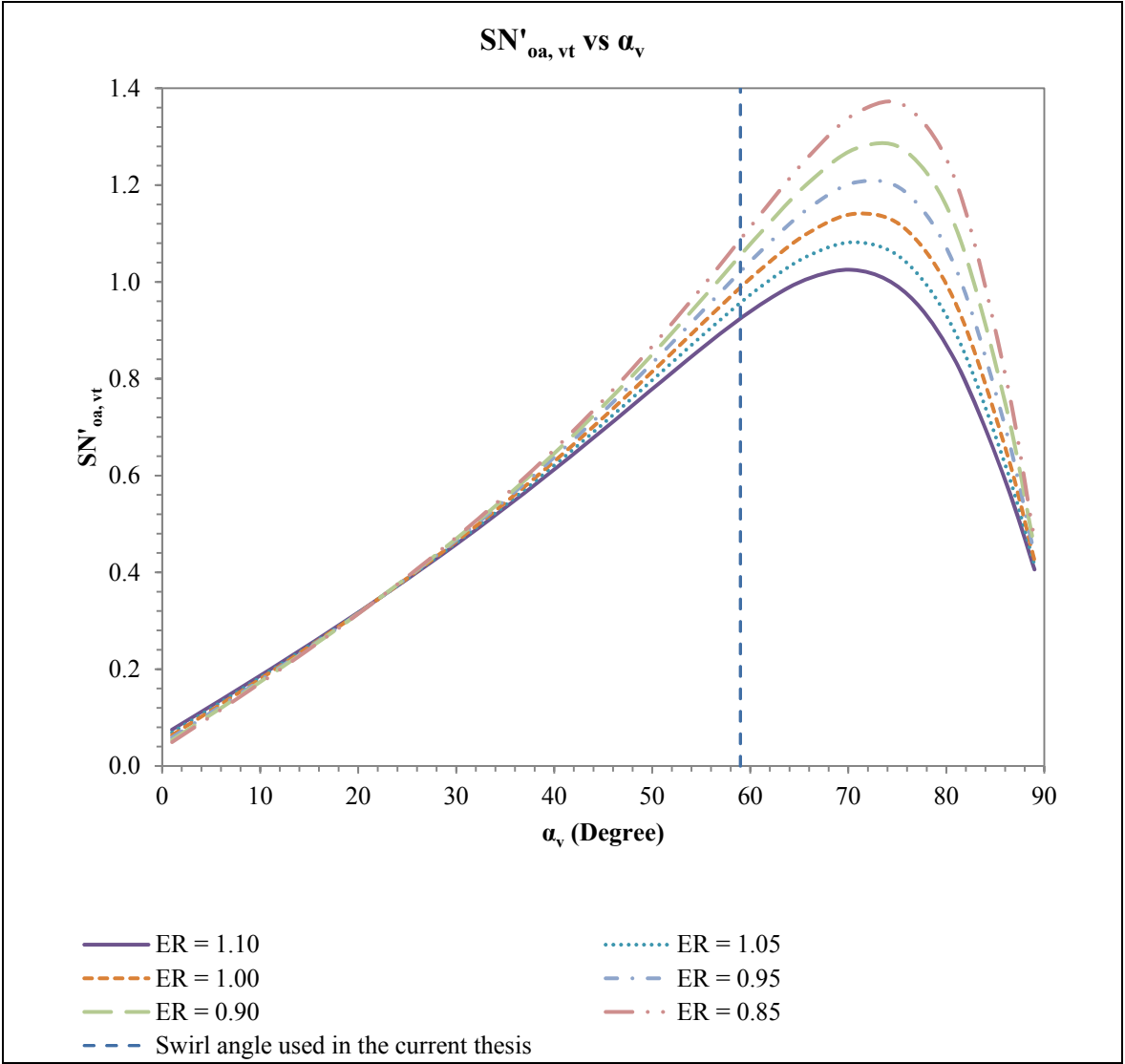


Figure 96 – Plot of  $SN'_{oa, vt}$  versus  $\alpha_v$



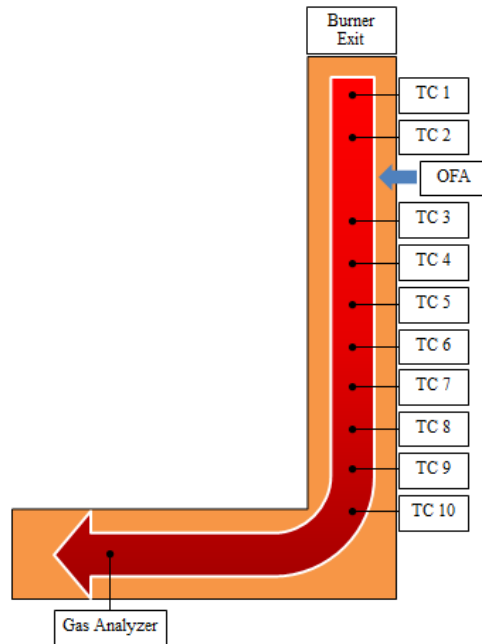
## APPENDIX H

### MEAN RESIDENCE TIME

Mean residence time,  $t_{res}$ , is the approximate time that gas resides in the combustion chamber. Actually, the effects of swirling flow and recirculating flow should be included in the calculation in order to increase the accuracy. However, it is difficult to include all effects in calculation. Therefore, equation (H.1) is used in determining the mean time that gas resides in each section of the combustion chamber as illustrated in Figure 97.

$$t_{res} = \frac{3,600 \times [Volume (m^3)]}{\left(\dot{m}_{air} \text{ in } \frac{kg}{hr}\right) \left(v_{air} \text{ in } \frac{m^3}{kg}\right)} \quad (H.1)$$

Volume in the numerator part of equation (H.1) represents the volume from the burner exit to each section of the chamber. Mass flow rate of air ( $\dot{m}_{air}$ ) is the amount of air supplied into the system, and  $v_{air}$  represents the specific volume of air at the considering temperature. The results of calculation are shown in Table 65.



**Figure 97 – Illustration of gas travelling through sections of combustion chamber**

**Table 65 – Mean residence times at various equivalence ratios**

Location	t <sub>res</sub> (ms) at equivalence ratio of					
	0.85	0.90	0.95	1.00	1.05	1.10
Burner Exit	0	0	0	0	0	0
TC 1	36.931	35.253	33.574	31.895	30.216	28.538
TC 2	112.51	107.39	102.28	97.17	92.05	86.94
OFA	188.09	179.54	170.99	162.44	153.89	145.34
TC 3	263.66	251.68	239.69	227.71	215.72	203.74
TC 4	339.24	323.82	308.40	292.98	277.56	262.14
TC 5	414.82	395.96	377.11	358.25	339.40	320.54
TC 6	490.40	468.11	445.81	423.52	401.23	378.94
TC 7	565.97	540.25	514.52	488.80	463.07	437.34
TC 8	641.55	612.39	583.23	554.07	524.91	495.74
TC 9	717.13	684.53	651.93	619.34	586.74	554.14
TC 10	792.71	756.67	720.64	684.61	648.58	612.55
Gas Analyzer	1,816.8	1,734.2	1,651.6	1,569.1	1,486.5	1,403.9

## APPENDIX I

### PARTICLE STOKES NUMBER AND PARTICLE REYNOLDS NUMBER

Particle Stokes number ( $St_p$ ) is defined as the ratio of particle time scale ( $\tau_p$ ) to mean flow time scale ( $\tau_f$ ). Equation (I.1) is used for calculating  $St_p$  where  $\rho_p$  is the density of the fuel particle,  $D_p$  is the diameter of the fuel particle,  $\mu_g$  is the dynamic viscosity of the gas flow,  $D_{chb}$  is the diameter of the combustion chamber, and  $U_o$  is the mean flow velocity (Apte, et al. 2003). In the current research, the  $St_p$  is used to predict whether the fuel particle can follow the swirling flow as mentioned earlier in the Results and Discussion section. The  $St_p$  of PRB and DB are shown in Table 66 and Table 67.

$$St_p = \frac{\tau_p}{\tau_f} = \frac{(\rho_p D_p^2 / 18\mu_g)}{(D_{chb} / U_o)} \quad (I.1)$$

Then, the particle relaxation time ( $\tau_{pr}$ ), i.e. time constant in the decrease of particle velocity ( $V_p$ ) can be calculated by using particle Reynolds number,  $Re_p$ , obtained from SolidWorks program. The  $Re_p$  is defined in equation (I.2) where  $V_f$  is the velocity of the flow and  $\rho_g$  is the density of the gas flow. Inserting  $Re_p$  into equation (I.3) yields  $\tau_{pr}$  (Apte, et al. 2003). Note that equation (I.3) is appropriate for  $Re_p$  up to 800.

$$Re_p = \frac{\rho_g (|V_p - V_f|) D_p}{\mu_g} \quad (I.2)$$

$$\tau_{pr} = \frac{\rho_p D_p^2}{18\mu_g} (1 + 0.15 Re_p^{0.687})^{-1} \quad (I.3)$$

Since the current research uses coal spreader to divert the particle and the secondary air was also swirled, it is difficult to find  $Re_p$  by hand. However, Flow Simulation on SolidWorks has a function to find  $Re_p$ . All  $Re_p$  exported from Flow Simulation are presented in Table 68 and Table 69. Also, please note that  $Re_p$  presented in Table 68 and Table 69 are the maximum values occurred when particle is centrifuged by the swirling flow. The values of  $\tau_{pr}$  are given in Table 70 and Table 71.

**Table 66 – Particle Stokes numbers of PRB ( $St_{p,PRB}$ ) at various particle sizes and equivalence ratios**

ER	$St_{p,PRB}$								$d_{ps,char}$
	25	50	75	100	125	150	175	200	
1.10	0.006469	0.025874	0.058217	0.103497	0.161714	0.232868	0.31696	0.413988	0.144109
1.05	0.006777	0.027106	0.060989	0.108425	0.169414	0.243956	0.332052	0.4337	0.150971
1.00	0.007115	0.028461	0.064038	0.113846	0.177884	0.256152	0.348652	0.455382	0.158519
0.95	0.00749	0.02996	0.067409	0.119838	0.187248	0.269636	0.367005	0.479354	0.166863
0.90	0.007906	0.031624	0.071153	0.126495	0.197649	0.284614	0.387391	0.50598	0.176132
0.85	0.008371	0.033484	0.07534	0.133937	0.209277	0.301359	0.410183	0.53575	0.186495

**Table 67 – Particle Stokes numbers of DB ( $St_{p,DB}$ ) at various particle sizes and equivalence ratios**

ER	$St_{p,DB}$								$d_{ps,char}$
	25	50	75	100	125	150	175	200	
1.10	0.002394	0.009577	0.021548	0.038308	0.059856	0.086193	0.117319	0.153232	0.113331
1.05	0.002508	0.010033	0.022574	0.040132	0.062707	0.090297	0.122905	0.160529	0.118727
1.00	0.002634	0.010535	0.023703	0.042139	0.065841	0.094812	0.129049	0.168554	0.124663
0.95	0.002772	0.011089	0.02495	0.044356	0.069306	0.099801	0.13584	0.177424	0.131223
0.90	0.002926	0.011705	0.026337	0.046821	0.073157	0.105346	0.143388	0.187282	0.138514
0.85	0.003098	0.012394	0.027886	0.049575	0.077461	0.111543	0.151823	0.198299	0.146662

**Table 68 – Particle Reynolds number from particle study on PRB ( $Re_{p,PRB}$ )**

ER	$Re_{p, PRB}$								$d_{ps,char}$
	25	50	75	100	125	150	175	200	
1.10	6.560	21.238	37.343	53.207	69.045	85.036	101.292	117.663	64.446
1.05	6.817	22.413	39.717	55.878	71.667	88.083	104.164	120.283	67.061
1.00	6.970	23.066	40.498	57.065	73.076	89.725	106.251	122.777	68.372
0.95	7.054	23.181	41.091	57.993	74.366	91.513	108.372	125.034	69.537
0.90	7.144	23.548	41.887	59.013	75.840	93.330	110.587	127.737	70.909
0.85	7.277	27.079	42.673	60.291	77.541	95.454	113.217	130.762	72.467

**Table 69 – Particle Reynolds number from particle study on DB ( $Re_{p,DB}$ )**

ER	$Re_{p, DB}$								$d_{ps,char}$
	25	50	75	100	125	150	175	200	
1.10	4.048	14.938	29.129	44.373	60.258	75.778	91.366	106.852	89.389
1.05	4.103	15.579	30.492	47.082	63.896	80.726	96.745	111.669	94.681
1.00	4.161	15.795	31.125	48.000	65.768	82.512	98.486	114.008	96.725
0.95	4.232	16.014	31.562	48.921	66.674	83.666	100.243	115.902	98.332
0.90	4.298	16.238	32.066	49.936	67.979	85.072	102.036	117.994	100.025
0.85	4.400	16.487	32.763	50.606	69.070	86.913	104.138	120.637	101.879

**Table 70 – Particle relaxation time of PRB ( $\tau_{pr,PRB}$ ) at various particle sizes and equivalence ratios**

ER	$\tau_{p,PRB}$ (ms)								$d_{ps,char}$
	25	50	75	100	125	150	175	200	
1.10	1.5815	4.3977	7.8489	11.854	16.295	21.085	26.159	31.498	15.031
1.05	1.5667	4.3083	7.6364	11.577	15.991	20.700	25.768	31.119	14.735
1.00	1.5581	4.2608	7.5698	11.460	15.833	20.500	25.494	30.769	14.593
0.95	1.5815	4.3977	7.8489	11.854	16.295	21.085	26.159	31.498	15.031
0.90	1.5667	4.3083	7.6364	11.577	15.991	20.700	25.768	31.119	14.735
0.85	1.5581	4.2608	7.5698	11.460	15.833	20.500	25.494	30.769	14.593

**Table 71 – Particle relaxation time of DB ( $\tau_{pr,DB}$ ) at various particle sizes and equivalence ratios**

ER	$\tau_{p,DB}$ (ms)								$d_{ps,char}$
	25	50	75	100	125	150	175	200	
1.10	0.67565	1.9181	3.3577	4.9649	6.7064	8.6080	10.629	12.768	10.387
1.05	0.67388	1.8910	3.2943	4.8304	6.5150	8.3321	10.311	12.466	10.076
1.00	0.67203	1.8821	3.2659	4.7870	6.4220	8.2380	10.214	12.326	9.962
0.95	0.67565	1.9181	3.3577	4.9649	6.7064	8.6080	10.629	12.768	10.387
0.90	0.67388	1.8910	3.2943	4.8304	6.5150	8.3321	10.311	12.466	10.076
0.85	0.67203	1.8821	3.2659	4.7870	6.4220	8.2380	10.214	12.326	9.962

APPENDIX J  
FLUE GAS COMPOSITION

Flue gas composition of firing PRB and co-firing 90-10 PRB-DB blend on dry basis were measured by using E-Instruments E-8500 gas analyzer. Data that were collected while the gas analyzer was purging its lines in order to avoid clogging problem were not included in the report or calculation. Then, the data were averaged and presented in Table 72 and Table 73, and CO and NO<sub>x</sub> were converted into g/GJ as shown in Table 74. Although E-8500 gas analyzer cannot measure N<sub>2</sub>, the percentage of N<sub>2</sub> in dry flue gas can be estimated by assuming that gases that cannot be measured by E-8500 gas analyzer are N<sub>2</sub> (Table 75).



**Table 72 – Experimental results of firing PRB**

ER <sub>mb</sub>	ER <sub>oa</sub>	O <sub>2</sub> (%)	CO (ppm)	CO <sub>2</sub> (%)	NO (ppm)	NO <sub>2</sub> (ppm)	NO <sub>x</sub> (ppm)
<u>Without OFA</u>							
1.10	1.10	1.3	15,522	18.4	198	0	198
1.05	1.05	1.2	6,444	20.4	299	0	299
1.00	1.00	1.7	1,823	18.3	317	0	317
0.95	0.95	2.7	2,540	18.8	413	0	413
0.90	0.90	2.9	786	18.2	464	1	465
0.85	0.85	3.9	303	17.1	550	4	554
<u>With OFA</u>							
1.10	1.05	2.2	8,082	17.2	299	0	299
	1.00	2.6	3,688	18.7	304	0	304
	0.95	2.8	1,298	18.1	336	0	336
	0.90	3.8	761	18.1	371	1	372
	0.85	4.1	230	16.9	373	0	374
1.05	1.00	1.9	3,442	18.6	313	0	313
	0.95	2.8	1,380	17.7	385	0	385
	0.90	3.3	679	17.4	416	1	417
	0.85	4.0	123	16.6	436	2	438
1.00	0.95	2.9	1,243	17.6	406	0	406
	0.90	3.9	622	17.2	427	0	427
	0.85	4.2	122	16.8	468	1	469

**Table 73 – Experimental results of co-firing 90-10 PRB-DB blend**

ER <sub>mb</sub>	ER <sub>oa</sub>	O <sub>2</sub> (%)	CO (ppm)	CO <sub>2</sub> (%)	NO (ppm)	NO <sub>2</sub> (ppm)	NO <sub>x</sub> (ppm)
<u>Without OFA</u>							
1.10	1.10	0.9	23,559	18.2	147	0	147
1.05	1.05	1.0	20,253	18.7	194	0	194
1.00	1.00	2.1	8,681	18.3	235	0	235
0.95	0.95	2.2	4,942	18.4	399	0	399
0.90	0.90	2.9	1,999	17.8	431	1	432
0.85	0.85	2.9	806	16.8	430	1	431
<u>With OFA</u>							
1.10	1.05	1.1	12,440	18.2	174	0	174
	1.00	1.3	7,016	20.9	274	0	274
	0.95	2.1	1,663	20.6	322	0	322
	0.90	2.9	389	18.9	343	0	343
	0.85	3.7	171	17.7	363	0	363
1.05	1.00	2.0	1,449	19.0	396	0	396
	0.95	2.3	1,207	18.6	394	0	394
	0.90	3.3	235	17.4	410	0	410
	0.85	3.9	106	17.0	417	0	417
1.00	0.95	2.9	445	17.8	473	1	474
	0.90	3.3	92	17.6	476	2	478
	0.85	3.3	79	16.2	460	3	463

**Table 74 – NO<sub>x</sub> and CO emissions in g/GJ**

Condition		Pure PRB		90-10 PRB-DB		% Difference	
ER <sub>mb</sub>	ER <sub>o</sub>	CO (g/GJ)	NO <sub>x</sub> (g/GJ)	CO (g/GJ)	NO <sub>x</sub> (g/GJ)	CO	NO <sub>x</sub>
<u>Without OFA</u>							
1.10	1.10	4,349	91	6,586	67	51.5	-26.1
1.05	1.05	1,891	144	5,932	93	214	-35.3
1.00	1.00	562	161	2,670	119	375	-26.0
0.95	0.95	824	220	1,600	212	94.1	-3.46
0.90	0.90	269	262	683	243	154	-7.28
0.85	0.85	110	330	292	256	166	-22.5
<u>With OFA</u>							
1.10	1.05	2,372	144	3,643	84	53.6	-42.1
	1.00	1,137	154	2,158	138	89.8	-10.1
	0.95	421	179	538	171	27.9	-4.51
	0.90	260	209	133	192	-48.9	-7.90
	0.85	83	223	62	216	-25.6	-3.00
1.05	1.00	1,061	158	445	200	-58.0	26.4
	0.95	448	205	391	209	-12.7	1.95
	0.90	232	234	80	230	-65.4	-1.69
	0.85	45	261	38	248	-14.4	-5.10
1.00	0.95	403	216	144	252	-64.3	16.5
	0.90	213	240	31	268	-85.3	11.9
	0.85	44	279	29	275	-35.2	-1.41

**Table 75 – Estimated percentage of N<sub>2</sub> in dry flue gas**

ER <sub>mb</sub>	ER <sub>oa</sub>	N <sub>2</sub> (%) in dry flue gas	
		PRB	90-10 PRB-DB
<u>Without OFA</u>			
1.10	1.10	78.80	78.56
1.05	1.05	77.79	78.24
1.00	1.00	79.81	78.71
0.95	0.95	78.21	78.86
0.90	0.90	78.83	79.01
0.85	0.85	78.89	80.20
<u>With OFA</u>			
1.10	1.05	79.81	79.45
	1.00	78.28	77.05
	0.95	78.90	77.20
	0.90	77.96	78.14
	0.85	78.94	78.58
1.05	1.00	79.12	78.83
	0.95	79.32	78.93
	0.90	79.18	79.23
	0.85	79.33	79.05
1.00	0.95	79.33	79.19
	0.90	78.86	79.04
	0.85	78.92	80.45

For C-H-O fuels in CH<sub>x</sub>O<sub>y</sub>, knowing only y/x, CO<sub>2</sub>% and O<sub>2</sub>% on dry basis can calculate the values of x (H/C ratio) and y (O/C ratio) included ER. However, wet analysis gives a better result for H/C ratio since H is properly accounted for. An example for coal combustion (C-H-O-N-S fuel) shown below assumes complete combustion.

Example: Coal ( $\text{CH}_{0.714}\text{N}_{0.014}\text{O}_{0.18}\text{S}_{0.0014}$ ) is burned with 20% excess air ( $\text{ER} = 0.833$ )

By assuming complete combustion,  $\text{CO}_2\%$ ,  $\text{H}_2\text{O}\%$ ,  $\text{O}_2\%$ ,  $\text{N}_2\%$ , and  $\text{SO}_2\%$  on dry and wet bases can be calculated and shown below.

Flue Gas Composition	% on Dry Basis	% on Wet Basis
$\text{CO}_2$	16.2694	15.3763
$\text{H}_2\text{O}$	0	5.4894
$\text{O}_2$	3.5464	3.3517
$\text{N}_2$	80.1842	75.7826
$\text{SO}_2$	0.0228	0.0215

Back calculation shows that H/C is equal to 0.714007921 and O/C is equal to 0.171400557. H/C results with trace amounts of S and N.

However, in case only y/x,  $\text{CO}_2\%$  and  $\text{O}_2\%$  on dry basis are known and assume S and N in fuel are negligible, the results of calculation by using gas analysis equations (J.1) through (J.3) show that H/C is 0.748, O/C is 0.189, and ER is 0.834.

$$ER = \frac{\frac{10,000}{\text{CO}_2\%} - 476 \left( \frac{\text{O}_2\%}{\text{CO}_2\%} \right) - 100}{\frac{10,000}{\text{CO}_2\%} - 100 \left( \frac{\text{O}_2\%}{\text{CO}_2\%} \right) - 100} \quad (\text{J.1})$$

$$v_{\text{O}_2} = \frac{\frac{100}{\text{CO}_2\%} - 1}{\frac{4.76}{ER} - 1} \quad (\text{J.2})$$

$$x = \frac{v_{\text{O}_2} - 1}{\frac{1}{4} - \frac{y/x}{2}} \quad (\text{J.3})$$

Consider only H/C. The actual H/C is 0.714, but the calculated H/C by assuming coal as a C-H-O fuel is 0.748. There is an error of 4.8%. The reason for this error is described below. Consider  $\text{CH}_{0.714}\text{N}_{0.014}\text{O}_{0.18}\text{S}_{0.0014}$  fuel. Let it burn completely with 20% excess air;  $\text{CO}_2$  % with  $\text{SO}_2$  and additional  $\text{N}_2$  due to fuel N yields  $\text{CO}_2$  % and  $\text{O}_2$  % dry as 16.2694 and 3.5464. Presence of S causes  $\text{O}_2$  to decrease in exhaust. The  $\text{O}_2$  in exhaust is reduced by  $\text{SO}_2$  since it consumes  $\text{O}_2$ ; further  $\text{O}_2$ % must be without  $\text{SO}_2$  being present in dry gases. Thus,  $\text{O}_2$  without  $\text{SO}_2$  can be calculated as shown below where  $N_{\text{dry}}$  is the total moles of dry flue gas.

$$\begin{aligned}
 O_2 \text{ with } SO_2 \text{ present} &= (O_2 \text{ without } SO_2) - (O_2 \text{ used in } SO_2) \\
 O_2 \text{ without } SO_2 &= (O_2 \text{ with } SO_2 \text{ present}) + (O_2 \text{ used in } SO_2) \\
 \frac{O_2 \text{ without } SO_2}{N_{\text{dry}}} &= \frac{(O_2 \text{ with } SO_2 \text{ present})}{N_{\text{dry}}} + \frac{(O_2 \text{ moles used in } SO_2)}{N_{\text{dry}}}
 \end{aligned}$$

Since  $\text{O}_2$  moles used is exactly the same as  $\text{SO}_2$  moles,  $\text{O}_2$ % without  $\text{SO}_2$  can be estimated as follows.

$$\begin{aligned}
 \frac{O_2 \text{ without } SO_2}{N_{\text{dry}}} &= (O_2 \text{ mole fraction in put to gas analysis equation}) \\
 \frac{O_2 \text{ without } SO_2}{N_{\text{dry}}} &= \frac{(O_2 \text{ with } SO_2 \text{ present})}{N_{\text{dry}}} + (SO_2 \text{ in ppm}) \times 10^{-6} \\
 O_2 \% \text{ without } SO_2 &\approx (O_2 \% \text{ with } SO_2) + (SO_2 \% \text{ in exhaust})
 \end{aligned}$$

With  $SO_2 = 0.0228\%$  on dry basis (from complete combustion calculation) and  $O_2\%$  with  $SO_2 = 3.5464$ ,  $O_2\%$  without  $SO_2$  in exhaust is equal to  $3.5464 + 0.0228 = 3.5692$ . Inserting this value into equation (J.1) instead of 3.5464 yields  $H/C = 0.734$  whilst actual  $H/C$  is 0.714. The error is reduced to 3.6%. In addition, the error can be minimized if one account for change in moles due to fuel N and  $SO_2$ , i.e. ignoring N, one may account for change in dry moles due to  $SO_2$  as follows. If  $SO_2$  is not included in the dry analysis, then  $CO_2\%$  and  $O_2\%$  will become 16.2731% and 3.5472% respectively. In order to get the actual values of  $H/C$  and  $O/C$ ,  $CO_2\%$  and  $O_2\%$  must be increased since only C-H-O products are considered in exhaust.

$$\frac{CO_2\% \text{ without } SO_2 \text{ (input to Gas Analysis)}}{CO_2\% \text{ with } SO_2} = \frac{N_{dry} \text{ with } SO_2}{N_{dry} \text{ without } SO_2}$$

$$\frac{CO_2\% \text{ without } SO_2 \text{ (input to Gas Analysis)}}{CO_2\% \text{ with } SO_2} = \frac{N_{dry} \text{ without } SO_2 + SO_2 \text{ moles}}{N_{dry} \text{ without } SO_2}$$

$$\frac{CO_2\% \text{ without } SO_2 \text{ (input to Gas Analysis)}}{CO_2\% \text{ with } SO_2} = 1 + \frac{SO_2 \text{ moles}}{N_{dry} \text{ without } SO_2}$$

$$\frac{CO_2\% \text{ without } SO_2 \text{ (input to Gas Analysis)}}{CO_2\% \text{ with } SO_2} \approx 1 + (SO_2 \text{ in ppm}) \times 10^{-6}$$

However the later correction is small; it is change in  $O_2$  moles in exhaust which may be significant. One concludes that error in  $H/C$  estimation for fuels with N and S is less than 5% for typical coal fuels and will be less for biomass fuels since they have almost no sulfur.

## APPENDIX K

### TEMPERATURE DATA AND ANALYSIS

Table 76 through Table 79 show the average measured temperature data obtained from each thermocouple under various conditions. The maximum  $T_c$  and  $T_w$  of each operating condition are shown in Table 80. These temperature profiles can be used to find the overall heat transfer coefficient ( $U_{oa}$ ) of the system.

The thermal-electrical network analogy is applied to the vertical section of the combustion chamber as shown in Figure 98 and Figure 99. Assume thermal conductivity of refractory ( $k_{ref}$ ), thermal conductivity of insulation ( $k_{ins}$ ), heat transfer coefficient of hot gas inside the combustion chamber ( $h_{hg}$ ), and heat transfer coefficient of cold gas outside the combustion chamber ( $h_{cg}$ ) are unknown.  $U_{oa}$  can be estimated by using equation (K.1) where  $T_{\infty,hg}$  and  $T_{w,hg}$  can be calculated by equation (K.2) and (K.3) respectively,  $T_{\infty,cg}$  is 298.15 K,  $y_1$  and  $y_2$  are 331 mm and 1,703 mm (TC 2 and TC 10) respectively, and  $T(y)$  is the equation of trend line of  $T_c$  profile obtained from measurement. The results of  $T_{\infty,hg}$  and  $U_{oa}$  are shown in Table 81 thru Table 84.

$$U_{oa} = \frac{\dot{m}_f \times HHV_f}{(\pi D_{chb} L)(T_{\infty,hg} - T_{\infty,cg})} \quad (K.1)$$

$$T_{\infty,hg} = \frac{\int_{y_1}^{y_2} T(y) dy}{y_2 - y_1} \quad (K.2)$$

$$T_{w,hg} = \frac{\int_{y_1}^{y_2} T(y) dy}{y_2 - y_1} \quad (K.3)$$



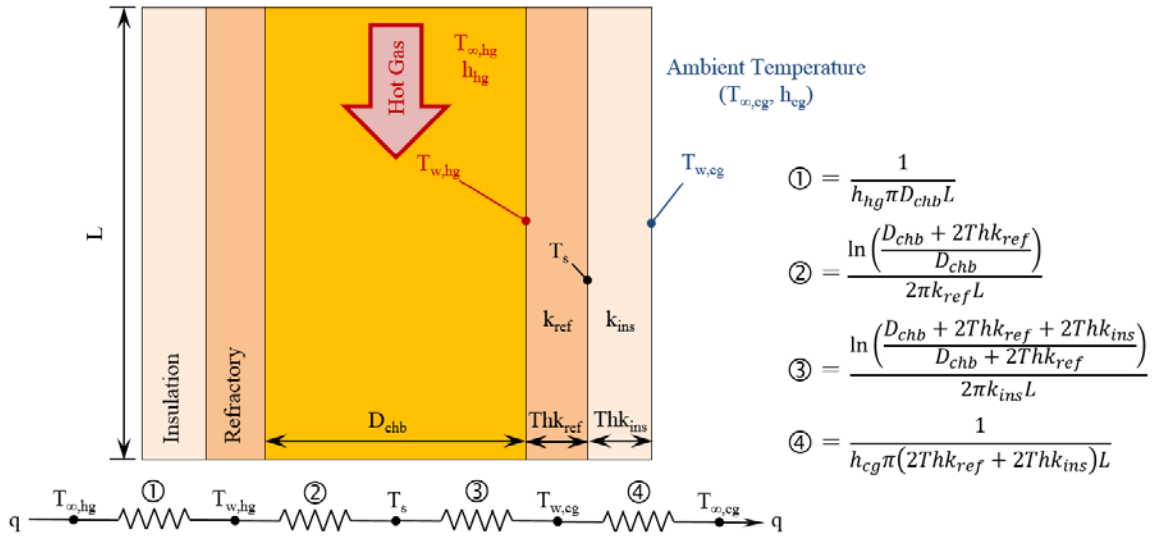


Figure 98 – The system for  $U_{oa}$  consideration

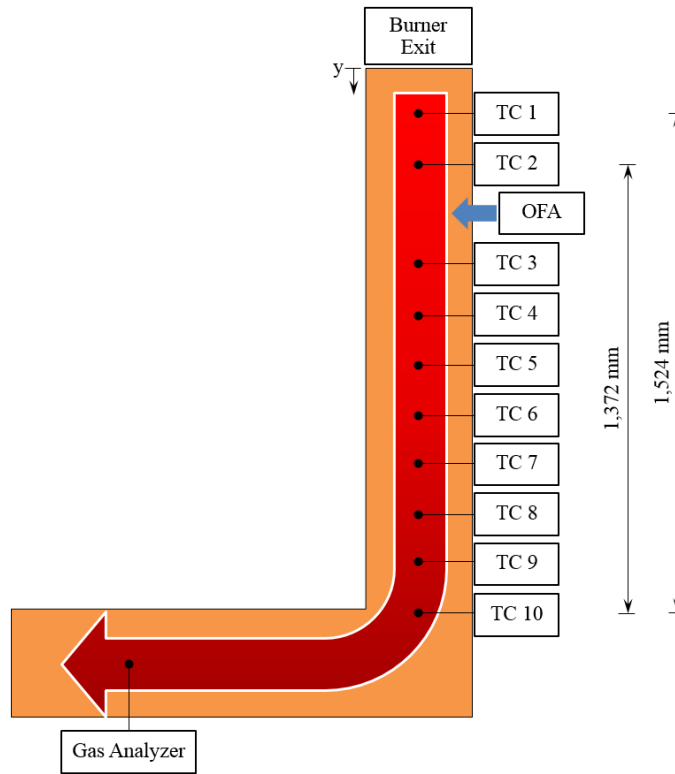


Figure 99 – Coordinate for  $T_{\infty, hg}$  calculation

**Table 76 – T<sub>c</sub> profiles of firing PRB**

ER <sub>mb</sub>	ER <sub>oa</sub>	Thermocouple Number (Distance from the burner exit in mm)									
		TC 1 (179)	TC 2 (331)	TC 3 (636)	TC 4 (788)	TC 5 (941)	TC 6 (1,093)	TC 7 (1,246)	TC 8 (1,398)	TC 9 (1,550)	TC 10 (1,703)
<u>Without OFA</u>											
1.10	1.10	N/A	1,500	1,508	1,483	1,476	1,407	1,355	1,298	1,254	1,169
1.05	1.05	N/A	1,554	1,555	1,531	1,510	1,439	1,392	1,339	1,283	1,201
1.00	1.00	N/A	1,500	1,460	1,412	1,365	1,265	1,224	1,127	1,086	1,005
0.95	0.95	N/A	1,526	1,545	1,533	1,523	1,481	1,434	1,396	1,365	1,279
0.90	0.90	N/A	1,537	1,536	1,512	1,489	1,429	1,371	1,336	1,292	1,206
0.85	0.85	N/A	1,545	1,533	1,506	1,472	1,405	1,344	1,306	1,254	1,161
<u>With OFA</u>											
1.10	1.05	N/A	1,535	1,554	1,539	1,527	1,480	1,435	1,400	1,349	1,270
	1.00	N/A	1,515	1,523	1,500	1,475	1,408	1,357	1,308	1,259	1,189
	0.95	N/A	1,467	1,421	1,378	1,329	1,262	1,204	1,137	1,110	1,046
	0.90	N/A	1,463	1,438	1,386	1,336	1,261	1,208	1,183	1,130	1,053
	0.85	N/A	1,473	1,420	1,367	1,314	1,239	1,177	1,146	1,102	1,000
1.05	1.00	N/A	1,448	1,446	1,385	1,352	1,275	1,219	1,165	1,134	1,061
	0.95	N/A	1,511	1,559	1,545	1,533	1,484	1,440	1,396	1,348	1,268
	0.90	N/A	1,486	1,516	1,490	1,466	1,395	1,341	1,299	1,252	1,166
	0.85	N/A	1,447	1,417	1,365	1,323	1,250	1,194	1,164	1,125	1,031
1.00	0.95	N/A	1,515	1,546	1,530	1,513	1,470	1,417	1,390	1,341	1,274
	0.90	N/A	1,489	1,492	1,464	1,430	1,377	1,328	1,275	1,247	1,169
	0.85	N/A	1,448	1,410	1,367	1,320	1,256	1,191	1,141	1,128	1,049

**Table 77 – T<sub>w</sub> profiles of firing PRB**

ER <sub>mb</sub>	ER <sub>oa</sub>	Thermocouple Number (Distance from the burner exit in mm)									
		TC 1 (179)	TC 2 (331)	TC 3 (636)	TC 4 (788)	TC 5 (941)	TC 6 (1,093)	TC 7 (1,246)	TC 8 (1,398)	TC 9 (1,550)	TC 10 (1,703)
<u>Without OFA</u>											
1.10	1.10	1,510	1,530	1,529	1,471	1,470	1,425	1,356	1,299	1,198	1,110
1.05	1.05	1,573	1,610	1,591	1,555	1,517	1,500	1,406	1,346	1,266	1,165
1.00	1.00	1,480	1,554	1,489	1,442	1,377	1,361	1,224	1,149	1,023	934
0.95	0.95	1,548	1,575	1,557	1,569	1,523	1,503	1,452	1,416	1,339	1,253
0.90	0.90	1,548	1,582	1,535	1,540	1,476	1,446	1,372	1,336	1,245	1,149
0.85	0.85	1,565	1,591	1,543	1,504	1,466	1,440	1,339	1,273	1,193	1,100
<u>With OFA</u>											
1.10	1.05	1,535	1,539	1,535	1,524	1,506	1,478	1,434	1,342	1,323	1,236
	1.00	1,529	1,534	1,510	1,492	1,466	1,417	1,363	1,244	1,218	1,134
	0.95	1,493	1,488	1,415	1,382	1,324	1,270	1,198	1,031	1,010	935
	0.90	1,494	1,490	1,426	1,371	1,318	1,265	1,176	1,113	1,024	948
	0.85	1,510	1,492	1,414	1,364	1,310	1,276	1,158	1,062	963	898
1.05	1.00	1,469	1,489	1,446	1,357	1,330	1,280	1,197	1,129	994	926
	0.95	1,512	1,537	1,549	1,512	1,524	1,493	1,444	1,393	1,318	1,228
	0.90	1,493	1,517	1,507	1,448	1,452	1,400	1,343	1,291	1,184	1,097
	0.85	1,459	1,484	1,407	1,320	1,301	1,245	1,162	1,095	969	884
1.00	0.95	1,514	1,560	1,536	1,512	1,502	1,481	1,430	1,339	1,316	1,238
	0.90	1,493	1,534	1,484	1,451	1,418	1,384	1,337	1,213	1,162	1,111
	0.85	1,462	1,489	1,388	1,347	1,298	1,266	1,188	1,018	1,007	949

**Table 78 – T<sub>c</sub> profiles of co-firing 90-10 PRB-DB blend**

ER <sub>mb</sub>	ER <sub>oa</sub>	Thermocouple Number (Distance from the burner exit in mm)									
		TC 1 (179)	TC 2 (331)	TC 3 (636)	TC 4 (788)	TC 5 (941)	TC 6 (1,093)	TC 7 (1,246)	TC 8 (1,398)	TC 9 (1,550)	TC 10 (1,703)
<u>Without OFA</u>											
1.10	1.10	N/A	1,516	1,533	1,516	1,518	1,472	1,427	1,384	1,314	1,237
1.05	1.05	N/A	1,492	1,512	1,483	1,482	1,416	1,363	1,291	1,240	1,148
1.00	1.00	N/A	1,449	1,440	1,379	1,342	1,257	1,183	1,117	1,072	1,021
0.95	0.95	N/A	1,483	1,440	1,398	1,352	1,281	1,199	1,135	1,123	1,048
0.90	0.90	N/A	1,506	1,534	1,515	1,501	1,440	1,374	1,321	1,281	1,198
0.85	0.85	N/A	1,468	1,459	1,416	1,370	1,292	1,217	1,152	1,140	1,068
<u>With OFA</u>											
1.10	1.05	N/A	1,463	1,416	1,364	1,301	1,226	1,139	1,096	1,058	989
	1.00	N/A	1,454	1,455	1,406	1,311	1,249	1,175	1,093	1,074	996
	0.95	N/A	1,456	1,469	1,422	1,335	1,273	1,210	1,158	1,123	999
	0.90	N/A	1,484	1,511	1,479	1,444	1,399	1,360	1,314	1,263	1,164
	0.85	N/A	1,444	1,437	1,383	1,303	1,252	1,183	1,132	1,103	1,034
1.05	1.00	N/A	1,508	1,544	1,531	1,496	1,460	1,427	1,371	1,342	1,236
	0.95	N/A	1,495	1,522	1,499	1,437	1,396	1,348	1,282	1,262	1,138
	0.90	N/A	1,446	1,443	1,391	1,305	1,250	1,191	1,120	1,114	1,009
	0.85	N/A	1,489	1,516	1,492	1,443	1,407	1,360	1,307	1,275	1,154
1.00	0.95	N/A	1,444	1,451	1,390	1,344	1,267	1,208	1,142	1,098	1,007
	0.90	N/A	1,495	1,535	1,511	1,467	1,450	1,380	1,344	1,284	1,172
	0.85	N/A	1,463	1,482	1,448	1,377	1,342	1,265	1,199	1,160	1,066

**Table 79 – T<sub>w</sub> profiles of co-firing 90-10 PRB-DB blend**

ER <sub>mb</sub>	ER <sub>oa</sub>	Thermocouple Number (Distance from the burner exit in mm)									
		TC 1 (179)	TC 2 (331)	TC 3 (636)	TC 4 (788)	TC 5 (941)	TC 6 (1,093)	TC 7 (1,246)	TC 8 (1,398)	TC 9 (1,550)	TC 10 (1,703)
<u>Without OFA</u>											
1.10	1.10	1,523	1,537	1,561	1,511	1,522	1,494	1,435	1,382	1,306	1,224
1.05	1.05	1,476	1,499	1,478	1,428	1,427	1,362	1,327	1,263	1,167	1,081
1.00	1.00	1,463	1,492	1,441	1,352	1,320	1,263	1,165	1,108	973	889
0.95	0.95	1,482	1,497	1,434	1,403	1,323	1,315	1,192	1,122	1,038	986
0.90	0.90	1,523	1,544	1,528	1,508	1,478	1,475	1,383	1,324	1,242	1,171
0.85	0.85	1,503	1,511	1,461	1,412	1,353	1,334	1,198	1,158	1,054	989
<u>With OFA</u>											
1.10	1.05	1,510	1,489	1,396	1,355	1,286	1,273	1,123	1,083	968	940
	1.00	1,453	1,489	1,501	1,461	1,345	1,309	1,229	1,160	1,004	1,003
	0.95	1,458	1,496	1,514	1,471	1,375	1,335	1,258	1,180	1,052	1,009
	0.90	1,491	1,517	1,544	1,516	1,475	1,432	1,372	1,344	1,306	1,205
	0.85	1,466	1,477	1,466	1,412	1,311	1,266	1,181	1,118	1,099	1,038
1.05	1.00	1,496	1,542	1,577	1,564	1,452	1,451	1,420	1,394	1,338	1,252
	0.95	1,484	1,533	1,558	1,542	1,456	1,423	1,347	1,294	1,265	1,161
	0.90	1,451	1,490	1,488	1,449	1,299	1,263	1,191	1,141	1,037	1,010
	0.85	1,483	1,524	1,541	1,517	1,432	1,424	1,383	1,328	1,258	1,169
1.00	0.95	1,443	1,488	1,473	1,434	1,325	1,255	1,107	1,123	1,023	1,012
	0.90	1,485	1,538	1,564	1,547	1,480	1,458	1,369	1,364	1,316	1,211
	0.85	1,460	1,509	1,518	1,488	1,386	1,326	1,249	1,190	1,200	1,073

**Table 80 – Maximum temperature of firing PRB and co-firing 90-10 PRB-DB blend**

ER <sub>mb</sub>	ER <sub>oa</sub>	PRB		90-10 PRB-DB	
		Center	Wall	Center	Wall
<u>Without OFA</u>					
1.10	1.10	1,508	1,530	1,533	1,561
1.05	1.05	1,555	1,610	1,512	1,499
1.00	1.00	1,500	1,554	1,449	1,492
0.95	0.95	1,545	1,575	1,483	1,497
0.90	0.90	1,537	1,582	1,534	1,544
0.85	0.85	1,545	1,591	1,468	1,511
<u>With OFA</u>					
1.10	1.05	1,554	1,539	1,463	1,510
	1.00	1,523	1,534	1,455	1,501
	0.95	1,467	1,493	1,469	1,514
	0.90	1,463	1,494	1,511	1,544
	0.85	1,473	1,510	1,444	1,477
1.05	1.00	1,448	1,489	1,544	1,577
	0.95	1,559	1,549	1,522	1,558
	0.90	1,516	1,517	1,446	1,490
	0.85	1,447	1,484	1,516	1,541
1.00	0.95	1,546	1,560	1,451	1,488
	0.90	1,492	1,534	1,535	1,564
	0.85	1,448	1,489	1,482	1,518

**Table 81 – Equations of  $T_c$  profiles,  $T_{\infty,hg}$  and  $U_{oa}$  from firing PRB**

ER <sub>mb</sub>	ER <sub>oa</sub>	Equation of the Trend Line	R <sup>2</sup>	T <sub>∞,hg</sub> (K)	U <sub>oa</sub> (W/m <sup>2</sup> ·K)
<u>Without OFA</u>					
1.10	1.10	$T(y) = -0.0002y^2 + 0.1864y + 1,468.9$	0.9904	1,420	41
1.05	1.05	$T(y) = -0.0002y^2 + 0.1475y + 1,535.4$	0.9935	1,447	40
1.00	1.00	$T(y) = -0.0001y^2 - 0.1012y + 1,564$	0.9898	1,342	44
0.95	0.95	$T(y) = -0.0002y^2 + 0.2243y + 1,477.8$	0.9890	1,468	39
0.90	0.90	$T(y) = -0.0002y^2 + 0.1093y + 1,528$	0.9897	1,401	41
0.85	0.85	$T(y) = -0.0002y^2 + 0.0683y + 1,550.5$	0.9915	1,382	42
<u>With OFA</u>					
1.10	1.05	$T(y) = -0.0002y^2 + 0.2308y + 1,486$	0.9943	1,482	39
	1.00	$T(y) = -0.0002y^2 + 0.1268y + 1,505.8$	0.9891	1,397	42
	0.95	$T(y) = -(8 \times 10^{-5})y^2 - 0.1655y + 1,543.9$	0.9908	1,280	47
	0.90	$T(y) = -(9 \times 10^{-5})y^2 - 0.1284y + 1,530.7$	0.9855	1,293	46
	0.85	$T(y) = -(8 \times 10^{-5})y^2 - 0.1872y + 1,553.8$	0.9894	1,268	47
1.05	1.00	$T(y) = -0.0001y^2 - 0.064y + 1,502.2$	0.9811	1,318	45
	0.95	$T(y) = -0.0003y^2 + 0.3219y + 1,441.5$	0.9892	1,412	41
	0.90	$T(y) = -0.0002y^2 + 0.1944y + 1,460.6$	0.9819	1,420	41
	0.85	$T(y) = -(9 \times 10^{-5})y^2 - 0.1199y + 1,509.7$	0.9864	1,281	46
1.00	0.95	$T(y) = -0.0002y^2 + 0.2206y + 1,473.9$	0.9875	1,460	39
	0.90	$T(y) = -0.0002y^2 + 0.0705y + 1,494.3$	0.9878	1,328	44
	0.85	$T(y) = -(7 \times 10^{-5})y^2 - 0.1607y + 1,523.6$	0.9849	1,277	47
Average					43

**Table 82 – Equations of  $T_w$  profiles,  $T_{w,hg}$  and  $U_{oa}$  from firing PRB**

$ER_{mb}$	$ER_{oa}$	Equation of the Trend Line	$R^2$	$T_{w,hg}$ (K)	$U_{oa,w}$ (W/m <sup>2</sup> ·K)
<u>Without OFA</u>					
1.10	1.10	$T(y) = -0.0003y^2 + 0.2321y + 1,478.1$	0.9942	1373	38
1.05	1.05	$T(y) = -0.0003y^2 + 0.2217y + 1,551.7$	0.9948	1437	36
1.00	1.00	$T(y) = -0.0003y^2 + 0.2y + 1,484.3$	0.9877	1349	39
0.95	0.95	$T(y) = -0.0002y^2 + 0.2281y + 1,515.5$	0.9923	1514	34
0.90	0.90	$T(y) = -0.0002y^2 + 0.1652y + 1,535.8$	0.9920	1475	35
0.85	0.85	$T(y) = -0.0002y^2 + 0.1208y + 1,561$	0.9953	1459	35
<u>With OFA</u>					
1.10	1.05	$T(y) = -0.0002y^2 + 0.19y + 1,502.7$	0.9874	1466	35
	1.00	$T(y) = -0.0002y^2 + 0.1489y + 1,509.7$	0.9875	1434	36
	0.95	$T(y) = -0.0002y^2 - 0.024y + 1,512.1$	0.9834	1274	42
	0.90	$T(y) = -0.0002y^2 - 0.0532y + 1,518.7$	0.9981	1253	43
	0.85	$T(y) = -0.0002y^2 - 0.0402y + 1,542.6$	0.9944	1289	41
1.05	1.00	$T(y) = -0.0002y^2 + 0.0666y + 1,477.5$	0.9923	1324	40
	0.95	$T(y) = -0.0002y^2 + 0.2896y + 1,465.2$	0.9899	1522	34
	0.90	$T(y) = -0.0003y^2 + 0.214y + 1,465.3$	0.9918	1343	39
	0.85	$T(y) = -0.0002y^2 + 0.0054y + 1,479.7$	0.9925	1269	42
1.00	0.95	$T(y) = -0.0002y^2 + 0.1956y + 1,498.4$	0.9811	1467	35
	0.90	$T(y) = -0.0002y^2 + 0.1112y + 1,497.3$	0.9827	1386	38
	0.85	$T(y) = -0.0002y^2 - 0.0623y + 1,500$	0.9732	1226	44
				Average	<u>38</u>



**Table 83 – Equations of T<sub>c</sub> profiles, T<sub>∞,hg</sub> and U<sub>oa</sub> from co-firing 90-10 PRB-DB blend**

ER <sub>mb</sub>	ER <sub>oa</sub>	Equation of the Trend Line	R <sup>2</sup>	T <sub>∞,hg</sub> (K)	U <sub>oa,c</sub> (W/m <sup>2</sup> ·K)
<u>Without OFA</u>					
1.10	1.10	$T(y) = -0.0002y^2 + 0.2953y + 1,443.9$	0.9965	1506	38
1.05	1.05	$T(y) = -0.0003y^2 + 0.2706y + 1,437.1$	0.9926	1355	43
1.00	1.00	$T(y) = -0.0001y^2 - 0.0849y + 1,515.1$	0.9796	1310	45
0.95	0.95	$T(y) = -(9 \times 10^{-5})y^2 - 0.1605y + 1,562.6$	0.9822	1292	46
0.90	0.90	$T(y) = -0.0002y^2 + 0.2414y + 1,464.3$	0.9840	1472	39
0.85	0.85	$T(y) = -0.0001y^2 - 0.0788y + 1,530.8$	0.9718	1332	44
<u>With OFA</u>					
1.10	1.05	$T(y) = -(7 \times 10^{-5})y^2 - 0.2285y + 1,566.5$	0.9849	1251	48
	1.00	$T(y) = -0.0001y^2 - 0.1135y + 1,537.2$	0.9704	1303	45
	0.95	$T(y) = -0.0002y^2 + 0.004y + 1,498.2$	0.9744	1264	47
	0.90	$T(y) = -0.0002y^2 + 0.1979y + 1,451.2$	0.9895	1414	41
	0.85	$T(y) = -(9 \times 10^{-5})y^2 - 0.1475y + 1,528.4$	0.9758	1271	47
1.05	1.00	$T(y) = -0.0002y^2 + 0.2695y + 1,451.7$	0.9845	1488	38
	0.95	$T(y) = -0.0002y^2 + 0.1802y + 1,473.1$	0.9773	1418	41
	0.90	$T(y) = -0.0001y^2 - 0.1074y + 1,518.8$	0.9723	1290	46
	0.85	$T(y) = -0.0002y^2 + 0.2119y + 1,452.8$	0.9825	1430	40
1.00	0.95	$T(y) = -0.0002y^2 + 0.0059y + 1,481.5$	0.9854	1249	48
	0.90	$T(y) = -0.0003y^2 + 0.3022y + 1,431.4$	0.9873	1381	42
	0.85	$T(y) = -0.0002y^2 + 0.1081y + 1,468.9$	0.9837	1341	44
Average					44

**Table 84 – Equations of  $T_w$  profiles,  $T_{w,hg}$  and  $U_{oa}$  from co-firing 90-10 PRB-DB blend**

ER <sub>mb</sub>	ER <sub>oa</sub>	Equation of the Trend Line	R <sup>2</sup>	T <sub>w,hg</sub> (K)	U <sub>oa,w</sub> (W/m <sup>2</sup> ·K)
<u>Without OFA</u>					
1.10	1.10	$T(y) = -0.0002y^2 + 0.2738y + 1,477.1$	0.9898	1,519	34
1.05	1.05	$T(y) = -0.0002y^2 + 0.176y + 1,455.8$	0.9932	1406	37
1.00	1.00	$T(y) = -0.0002y^2 + 0.0647y + 1,477.2$	0.9931	1322	40
0.95	0.95	$T(y) = -0.0002y^2 + 0.0064y + 1,503$	0.9880	1293	41
0.90	0.90	$T(y) = -0.0002y^2 + 0.2216y + 1,491.9$	0.9915	1485	35
0.85	0.85	$T(y) = -0.0002y^2 + 0.0268y + 1,516.4$	0.9901	1326	40
<u>With OFA</u>					
1.10	1.05	$T(y) = -0.0001y^2 - 0.1451y + 1,546.6$	0.9859	1302	41
	1.00	$T(y) = -0.0003y^2 + 0.1803y + 1,456.5$	0.9647	1302	41
	0.95	$T(y) = -0.0003y^2 + 0.2349y + 1,447.7$	0.9797	1345	39
	0.90	$T(y) = -0.0002y^2 + 0.2097y + 1,471.8$	0.9772	1453	36
	0.85	$T(y) = -0.0001y^2 - 0.0708y + 1,512.7$	0.9635	1338	40
1.05	1.00	$T(y) = -0.0002y^2 + 0.2118y + 1,486.5$	0.9236	1470	35
	0.95	$T(y) = -0.0003y^2 + 0.2409y + 1,473.5$	0.9624	1376	38
	0.90	$T(y) = -0.0002y^2 + 0.0342y + 1,490.1$	0.9532	1306	41
	0.85	$T(y) = -0.0002y^2 + 0.2274y + 1,465.7$	0.9779	1464	35
1.00	0.95	$T(y) = -0.0002y^2 - 0.0111y + 1,497.9$	0.9313	1272	42
	0.90	$T(y) = -0.0002y^2 + 0.2576y + 1,468.6$	0.9549	1495	34
	0.85	$T(y) = -0.0002y^2 + 0.1131y + 1,482.9$	0.9393	1374	38
				Average	<u>38</u>

## APPENDIX L

### BURNT FRACTION CALCULATION

Burnt fraction (BF) is the mass fraction of the fuel burned during the combustion process to the input fuel as shown in equation (L.1). BF is useful for estimating and adjusting the amount of heat output from burning the fuel more accurately.

For a steady open system, equation (L.1) becomes equation (L.2). Then, Lawrence, et al. (2009) used equation (L.3) as a rough estimation of burnt fraction where ER is the measured ER,  $X_{O_2,flue,dry}$  is the measured mole fraction of O<sub>2</sub> in flue gas on dry basis, and  $X_{O_2,air}$  is the mole fraction of O<sub>2</sub> in air. In case air is used as an oxidizer,  $X_{O_2,air}$  is always 0.21. The results of BF estimation are given in Table 85.

$$BF = \frac{\text{Burnt Fuel}}{\text{Fuel Input}} \quad (\text{L.1})$$

$$BF = \frac{Y_{f,in} - Y_{f,out}}{Y_{f,in}} \quad (\text{L.2})$$

$$BF \approx \frac{1}{ER} \left( 1 - \frac{X_{O_2,flue,dry}}{X_{O_2,air}} \right) \quad (\text{L.3})$$

**Table 85 – Results of burnt fraction estimation**

ER <sub>mb</sub>	ER <sub>oa</sub>	BF	
		PRB	90-10 PRB-DB
<u>Without OFA</u>			
1.10	1.10	0.85	0.87
1.05	1.05	0.90	0.91
1.00	1.00	0.92	0.90
0.95	0.95	0.92	0.94
0.90	0.90	0.96	0.96
0.85	0.85	0.96	1.01
<u>With OFA</u>			
1.10	1.05	0.85	0.90
	1.00	0.88	0.94
	0.95	0.91	0.95
	0.90	0.91	0.96
	0.85	0.94	0.97
1.05	1.00	0.91	0.91
	0.95	0.91	0.94
	0.90	0.93	0.93
	0.85	0.95	0.96
1.00	0.95	0.91	0.91
	0.90	0.91	0.94
	0.85	0.94	0.99

## APPENDIX M

### FUEL NITROGEN CONVERSION EFFICIENCY CALCULATION

Fuel-bound nitrogen (or fuel N) conversion efficiency ( $N_{conv}$ ) is used to estimate the amount of fuel N converted to  $NO_x$ . In other words,  $N_{conv}$  is used to estimate how much  $NO_x$  are generated by fuel-bound mechanisms. Equation (M.1) given by Annamalai and Puri (2007) is used to calculate  $N_{conv}$  of fuel at various ER as shown in Table 86.

$$N_{conv} = \left(\frac{c}{n}\right) \frac{X_{NO_x}}{(X_{CO} + X_{CO_2})} \times 100\% \quad (M.1)$$

Because coal-fired power plants are typically operated in the lean combustion regime, the average  $N_{conv}$  will take only the values in the fuel-lean regime into account. Table 87 shows the results of averaging.

**Table 86 – Results of fuel N conversion efficiency calculation**

ER <sub>mb</sub>	ER <sub>o</sub>	N <sub>conv</sub>	
		PRB	90-10 PRB-DB
<u>Without OFA</u>			
1.10	1.10	7.34	4.36
1.05	1.05	10.47	5.69
1.00	1.00	12.63	7.48
0.95	0.95	15.94	12.88
0.90	0.90	18.76	14.63
0.85	0.85	23.80	15.58
<u>With OFA</u>			
1.10	1.05	12.26	5.44
	1.00	11.74	7.71
	0.95	13.60	9.47
	0.90	15.08	11.04
	0.85	16.31	12.52
1.05	1.00	12.19	12.61
	0.95	15.92	12.82
	0.90	17.59	14.38
	0.85	19.44	14.95
1.00	0.95	16.85	16.15
	0.90	18.25	16.55
	0.85	20.54	17.38

**Table 87 – N<sub>conv, avg</sub> of lean combustion (ER ranged from 0.85 to 0.95)**

Fuel Type	Without OFA	With OFA		
		1.00	1.05	1.10
PRB	19.50	18.55	17.65	15.00
90-10 PRB-DB	14.36	11.01	14.05	16.69

## APPENDIX N

### RESPIRATORY QUOTIENT (RQ) CALCULATION

Respiratory quotient, RQ, is defined as the ratio of moles of CO<sub>2</sub> produced by the combustion process to moles of O<sub>2</sub> consumed during the combustion as shown in equation (N.1). RQ could be estimated by fuel composition or empirical formulae (RQ<sub>comp</sub>) or by flue gas composition (RQ<sub>flue</sub>) as defined in equation (N.2) and (N.3) respectively. Please note that equation (N.3) is applied for the stoichiometric condition or ER is equal to one, and the mole fraction of N<sub>2</sub> at the exit (X<sub>N<sub>2</sub>,e</sub>) could be estimated by assuming all of the gases that are not reported in Appendix J is N<sub>2</sub>.

$$RQ = \frac{CO_{2,produced} \text{ (in moles)}}{O_{2,consumed} \text{ (in moles)}} \quad (N.1)$$

$$RQ = \left[ 1 + \left( \frac{H}{4C} \right) - \left( \frac{O}{2C} \right) + \left( \frac{S}{C} \right) \right]^{-1} \quad (N.2)$$

$$RQ = \frac{X_{CO_2,e} \left( \frac{X_{N_2,i}}{X_{N_2,e}} \right) - X_{CO_2,i}}{X_{O_2,i} - X_{O_2,e} \left( \frac{X_{N_2,i}}{X_{N_2,e}} \right)} \quad (N.3)$$

## APPENDIX O

### BENEFIT OF NO<sub>x</sub> REDUCTION FROM TRADING IN EMISSIONS MARKETS

As mentioned in the Introduction section that NO<sub>x</sub> could be traded in the emissions markets, each g/GJ of NO<sub>x</sub> reduction could be converted into money. The benefit of NO<sub>x</sub> reduction from the current research will become clear when it is presented in financial terms. The calculation is based on the following assumptions.

First, in order to maximize the benefit, PRB and DB should be mixed and ground within the same mill. This method could save both processing time and expenses. So, it is not necessary to buy a new mill for DB. Second, NO<sub>x</sub> were traded at \$15.89 per short ton in 2011 (U.S. EIA 2012). Third, average plant efficiency is 35%. Lastly, the power plants run continuously for 330 operating days per year and have 35-day period for maintenance.

By using the above assumptions, the proposed operating condition could decrease NO<sub>x</sub> by 159 g/GJ of heat input or 5.03 short tons per year per MW of heat input. Hence, adopting the proposed operating condition the techniques explained in the thesis could make benefit approximately \$228 per year per MW of heat output. For instance, if a 500 MW coal-fired power plant with conventional burners adopts the proposed techniques and operating condition, this plant could make a profit on selling NO<sub>x</sub> credit to another plant by approximately \$114,181 per year. Some other scenarios of NO<sub>x</sub> reduction are presented in Table 88.



**Table 88 – Benefit of NO<sub>x</sub> reduction in various scenarios**

Description	Base Case	Scenario 1	Scenario 2	Scenario 3
Fuel Type	PRB	90-10 PRB-DB	90-10 PRB-DB	90-10 PRB-DB
ER <sub>mb</sub>	0.85	0.85	0.95	1.10
ER <sub>oa</sub>	0.85	0.85	0.95	0.95
SN <sup>2</sup> <sub>sa</sub>	1.42	1.42	1.42	1.42
OFA Injection	No	No	No	Yes
NO <sub>x</sub> Emissions in g/GJ of Heat Input				
- g/GJ of heat input	330	256	212	171
- Short ton per year per MW of heat input	10.4	8.05	6.66	5.37
NO <sub>x</sub> Reduction in Short Ton/Year/MW of Heat Input	-	2.35	3.74	5.03
Benefit in U.S. Dollars per Year (for 500 MW Plants)	-	53,345	84,898	114,181

## APPENDIX P

### UNCERTAINTY ANALYSIS

This section provides the summary of standard errors (or uncertainties) from air flow measurement, flue gas measurement, and temperature measurement. Table 89 shows the overall uncertainties of airflow measurement whilst Table 90 and Table 91 show the standard errors in measuring flue gas composition from firing PRB and co-firing 90-10 PRB-DB blend.

**Table 89 – Overall uncertainties of airflows and temperature components**

Description	Overall Uncertainty
Primary air	$\pm 0.61\%$
Secondary air	$\pm 1.8\%$
OFA	$\pm 14\%$
T <sub>c</sub>	$\pm 1.8\%$
T <sub>w</sub>	$\pm 1.5\%$

**Table 90 – Standard errors in measuring flue gas composition from firing PRB**

ER <sub>mb</sub>	ER <sub>oa</sub>	O <sub>2</sub> (%)	CO (%)	CO <sub>2</sub> (%)	NO (%)	NO <sub>2</sub> (%)	NO <sub>x</sub> (%)
<u>Without OFA</u>							
1.10	1.10	1.32	2.27	0.33	1.16	N/A	1.16
1.05	1.05	1.83	5.54	0.39	2.65	N/A	2.65
1.00	1.00	1.40	3.38	0.15	1.29	N/A	1.29
0.95	0.95	1.36	9.08	0.14	1.72	44.24	1.72
0.90	0.90	1.44	9.67	0.22	0.44	9.45	0.44
0.85	0.85	0.65	18.97	0.18	0.25	2.12	0.26
<u>With OFA</u>							
1.10	1.05	1.98	9.04	0.56	2.91	N/A	2.91
	1.00	2.15	10.56	0.16	1.79	N/A	1.79
	0.95	1.66	7.90	0.26	0.79	57.41	0.79
	0.90	0.86	5.49	0.24	0.35	13.25	0.36
	0.85	0.81	11.46	0.20	0.23	16.06	0.22
1.05	1.00	0.53	5.16	0.06	0.30	N/A	0.30
	0.95	1.52	6.70	0.21	0.62	21.59	0.63
	0.90	1.19	9.75	0.22	0.32	12.60	0.33
	0.85	0.76	9.66	0.18	0.23	2.11	0.24
1.00	0.95	0.84	5.53	0.12	0.21	15.38	0.22
	0.90	2.02	11.30	0.19	2.42	N/A	2.42
	0.85	0.58	10.42	0.30	0.13	13.57	0.14

**Table 91 – Standard errors in measuring flue gas composition from co-firing 90-10 PRB-DB blend**

ER <sub>mb</sub>	ER <sub>oa</sub>	O <sub>2</sub> (%)	CO (%)	CO <sub>2</sub> (%)	NO (%)	NO <sub>2</sub> (%)	NO <sub>x</sub> (%)
<u>Without OFA</u>							
1.10	1.10	0.70	1.98	0.14	2.04	N/A	2.04
1.05	1.05	3.48	3.43	0.32	2.00	N/A	2.00
1.00	1.00	1.64	5.53	0.10	2.05	N/A	2.05
0.95	0.95	1.81	7.98	0.19	1.23	21.53	1.24
0.90	0.90	1.13	7.59	0.18	0.66	6.79	0.67
0.85	0.85	1.34	8.38	0.21	0.52	10.66	0.52
<u>With OFA</u>							
1.10	1.05	1.83	3.75	0.26	1.54	N/A	1.54
	1.00	1.90	6.46	1.71	2.23	N/A	2.23
	0.95	2.77	8.48	0.23	1.17	N/A	1.17
	0.90	1.18	9.52	0.18	0.76	N/A	0.76
	0.85	0.92	8.04	0.23	0.62	30.74	0.62
1.05	1.00	1.49	6.89	0.13	0.67	100.00	0.67
	0.95	1.22	5.43	0.33	0.56	N/A	0.56
	0.90	1.52	9.44	0.29	0.69	15.88	0.70
	0.85	1.32	17.30	0.23	0.49	N/A	0.49
1.00	0.95	1.75	12.68	0.17	0.68	8.49	0.69
	0.90	0.93	9.82	0.14	0.31	4.29	0.31
	0.85	0.78	14.63	1.03	0.25	2.73	0.25